Study and optimization of a compact X-ray source

Alexandre Moutardier

université PARIS-SACLAY

Study and optimization of a compact X-ray source

Étude et optimisation d'une source compacte de Rayons X

Thèse de doctorat de l'université Paris-Saclay

École doctorale n° 576, particules hadrons énergie et noyau : instrumentation, imagerie, cosmos et simulation (**PHENIICS**)
Spécialité de doctorat: **physique des accélérateurs**
Graduate School : **Physique**, Référent : **Faculté des sciences d'Orsay**

Thèse préparée dans l'unité de recherche **IJCLab (Université Paris-Saclay, CNRS)**, sous la direction de **Nicolas DELERUE**, chargé de recherches

Thèse soutenue à Paris-Saclay, le 20 septembre 2022, par

Alexandre MOUTARDIER

Composition du jury

Achille STOCCHI Professeur des universités, Université Paris-Saclay	Président
Marie-Laure GALLIN-MARTEL Directeur de recherche, LPSC (Grenoble)	Rapporteur & Examinatrice
Frank ZIMMERMANN Cadre scientifique, CERN	Rapporteur & Examinateur
Marica BIAGINI Professeure émérite, INFN-FNL (Italie)	Examinatrice
Patrick PUZO Professeur des universités, Université Paris-Saclay	Examinateur
Nicolas DELERUE Chargé de recherches, Université Paris-Saclay	Directeur thèse

THESE DE DOCTORAT
NNT : 2022UPASP093

université PARIS-SACLAY

ÉCOLE DOCTORALE
Particules, hadrons, énergie et noyau : instrumentation, imagerie, cosmos et simulation (PHENIICS)

Titre: Étude et optimisation d'une source compacte de Rayons X
Mots clés: Dynamique Faisceau, Accélérateur de particules, Rayonnement Compton, Diagnostics

Résumé: Dès leurs découvertes, les rayons-x se sont trouvés être un atout majeur pour les scientifiques, puis les médecins, les biologistes, et même les conservateurs d'art. Différentes sources de rayon-x existent (tube de Crookes, synchrotron, ...), et plus récemment un nouveau type de source se développe : les sources Compton. Dans ce cas, un échange d'énergie cinétique entre des électrons et des photons permet d'augmenter l'énergie de ces derniers. Cette thèse retrace les travaux réalisés sur l'accélérateur d'électrons à 50 MeV du prototype de source Compton ThomX. Des simulations de l'accélérateur et notamment de l'injection des électrons dans un anneau de stockage sont présentées et ont permis, notamment, une étude des risques de perte le long de la ligne de transfert et du premier tour dans l'anneau. L'injection dans l'anneau étant un moment critique, un code de correction de l'injection se basant sur des mesures de la position du faisceau à l'entrée de l'anneau et rétroagissant sur les déviateurs à la fin de la ligne de transfert a été développé et testé sur simulateur. Ce code se base sur des calculs linéaires de matrice de transfert. Enfin, lors du démarrage de la machine, des études sur les diagnostics du faisceau d'électrons (écrans scintillants, moniteurs de position, moniteurs de charge, ...) ont été réalisées et sont discutées ici.

Title: Study and optimization of a compact X-ray source
Keywords: Beam dynamics, Particle accelerator, Compton Radiation, Diagnostics

Abstract: From physics to medicine, biology, or art, x-rays have a wide spectrum of applications. X-ray sources are legion (Crookes tube, synchrotron accelerator, ...) and recently the Compton sources. Compton's back-scattering effect occurs when an electron gives a part of its kinetic energy to a photon. This thesis describes works done on the 50 MeV electron accelerator of ThomX, a prototype of a compact Compton source. The transfer line and the storage ring of the accelerator, especially the injection process, have been simulated. It has allowed a study of beam loss risks during injection as well as a test for the injection feedback code developed. This code, based on linear transfer matrix computation, uses beam position measured at the entrance of the ring to correct steerer magnetic strength at the exit of the transfer line. Eventually, a study of electron beam diagnostics during linac commissioning is also discussed.

Acknowledgement

Mes remerciements vont tout d'abord à Nicolas Delerue, mon directeur de thèse, qui avant même de m'avoir proposé cette thèse m'a fait découvrir le domaine de la physique des accélérateurs de particules qui est maintenant devenu une de mes passions. Nicolas, a toujours été bienveillant, en me poussant lorsqu'il fallait et en m'aidant en cas de besoin. Je le remercie aussi de m'avoir fait découvrir le musée science ACO et les joies de la vulgarisation et de la pédagogie.

En parlant de science ACO, merci à Jack, Pierre, Marie-Pauline, Anne-Fleur et tout les autres membres de l'association pour leur accueil et d'avoir partagé leurs savoir et leurs anecdotes sur ACO.

Au laboratoire, ce sont tous les membres de ThomX qui ont toujours été là en cas de besoin, que ce soit pour travailler ou pour se changer les idées. Ainsi, je voudrais remercier les autres doctorants et stagiaires - Coline, Emmanuel, Ezgy, Muath, Scott, ... - pour les échanges plus ou moins sérieux que l'on a pu avoir. Pour ce qui est des permanents, je remercie Vincent C. pour les longues mais très intéressante conversations sur le fonctionnement de la synchro ou les propositions de livres et films à voir, Hayg pour son aide sur la prise en main de la création d'interfaces, Sophie pour l'aide apportée pour faire fonctionner la machine, Cristelle pour l'aide bureaucratique apportée et beaucoup d'autres tels que Alexandre G., Christelle, Hayg, Hugues, Iryna, Kevin, Marie, Philippe, Slava, et tous ceux que j'oublie.

Que ce soit pour mon stage d'avant ma thèse ou l'obtention de mon post doc, un très grand merci à Vincent L. Que la force soit avec toi.

Enfin, une thèse est probablement beaucoup plus compliquée à vivre sans le soutient de sa famille et de ses amis. En effet, les moments de détentes sont cruciaux et ce rôle à très bien été tenu par Émeline, Emmanuel, Théo et Théophile et nos parties de maître des ténèbres. Bien sûr, je remercie chaleureusement mes parents, grands-parents, sœurs, tantes, cousins et tous les autres membres de ma famille et belle famille pour toutes les conversations, repas et vacances durant ces 3 années.

Merci tout particulièrement à Mathilde de partager ma vie, de m'avoir supporté et aidé dans les moments compliqués.

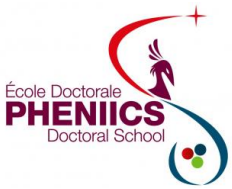

Glossary

ACO	:	*Anneau de Collisions d'Orsay* Collision ring of Orsay, France
ADC	:	*Analog to Digital Converter*
AOCS	:	*All-Optical inverse Compton Scattering source* Tsinghua University (China)
ASN	:	*Autorité de Sûreté Nucléaire* French nuclear safety authority
BLM	:	*Beam Loss Monitor*
BPM	:	*Beam Position Monitor*
BW	:	*BandWidth*
CAD	:	*Computer-Aided Design*
CBS	:	*Compton BackScattering effect*
CCD	:	*Charge Coupled Device* Camera sensor
CCS	:	*Compact Compton Source*
CERN	:	*Conseil Européen pour la Recherche Nucléaire* European Organization for Nuclear Research
CLS	:	*Compact Light Source*
DG	:	*Diagnostics*
DP	:	*Dipole*
DPI	:	*Injection Dipole*
DS	:	*Device Server*
ECR	:	*Electron Cyclotron Resonance*
EL	:	*Extraction Line*
FC	:	*Faraday Cup*
FODO	:	*FOcus/DefOcus* classical accelerator line with thee quadrupoles
FP	:	*Fabry-Perrot cavity*
GUI	:	*Graphical User Interface*
IBS	:	*Intra-Beam Scattering* A collective effect

ICT	:	*Integrating Current Transformer*
INFN	:	*Laboratori Nazionali di Frascati* National laboratory of Frascati , Italia
IP	:	*Interaction Point*
LAL	:	*Laboratoire de l'Accelerateur Linéaire d'Orsay* Laboratory of the linear accelerator of Orsay, France
LEP	:	*Large Electron-Positron collider* Ancestor of the LHC at CERN
LHC	:	*Large Hadron Collider* CERN
Li	:	*Linac*
LIL	:	*LEP Injection Linac*
Linac	:	*Linear accelerator*
MadX	:	*Methodical Accelerator Design X* 10^{th} version of the CERN accelerator's design code
MuCLS	:	*Munich Compact Light Source* Build by the Technical University of Munich and Lyncean Technologies
OC	:	*Optical Cavity*
OTR	:	*Optical Transition Radiation*
PC	:	*Photo-Cathode*
ph	:	*Photon*
QP	:	*Quadrupole*
RF	:	*Radio-Frequency*
Ri	:	*Ring* ThomX is split in two : Ri-C1 and Ri-C2
RMS	:	*Root Mean Square*
ROI	:	*Region Of Interest*
SOLEIL	:	*Source Optimisée de Lumière d'Énergie Intermédiaire du LURE* French synchrotron accelerator
SP	:	*Sextupole*
SST	:	*Screen STation*
STR	:	*Steerer*
TL	:	*Transfer Line*
UHV	:	*Ultra-High Vacuum*

USAF1951 : *U.S. Air Force 1951*
Resolution test chart made by U.S. Air Force in 1951

WAC : *WaveCAtcher*
Homemade current monitor

YAG : *YAG:Ce*

YAG:Ce : *Yttrium Aluminum Garnet crystal doped with Cerium*

Yb:KGW : *ytterbium crystal doped with potassium gadolinium tungstate*

Contents

Introduction

Electrons and X-rays have been linked to accelerators since their discoveries, as Crookes tubes can be considered as the first electron accelerators and permitted the discovery of both the electrons by Joseph John Thomson in 1897 [1] and the X-rays by Wilhelm Röntgen in 1895 [2].

Applications of hard X-rays are countless; hence, a broad range of X-rays sources exist, from X-rays to synchrotrons. X-rays tube are updates of Crookes tubes commonly used as large spectrum X-rays sources like for standard medical radiography. Synchrotron accelerators are electron accelerators used to generate high-intensity monochromatic X-rays.

Both have interesting properties depending on the needs, but a significant gap exists between their performances. New X-ray sources have been developed over the past few decades to fill this gap. Those machines are based on Compton Backscattering (CBS), corresponding to a momentum transfer between energetic electrons and photons. These new sources can create high-intensity quasi-monochromatic X-rays, unlike X-ray tubes. Moreover, they require less space, are potentially movable and are cheaper than synchrotron accelerators. Hence, they can be used for many applications.

Even if CBS sources are approximately one hundred times larger than X-ray tubes, they are often denoted as Compact Light Source (CLS) or Compact Compton Source (CCS) in comparison to synchrotron accelerators - that have closer structure and performances - roughly one hundred times larger.

This thesis takes place in a prototype of CCS, named ThomX, at Orsay, in France. ThomX is aimed to generate a high X-ray flux by the interaction of an electron beam stored in a small storage ring and a laser beam stored in a high finesse Fabry-Perrot cavity. My work focuses on electron beam diagnostics, beam propagation simulations - especially during the ring injection - simulations of electron loss and the creation of a feedback system for the ring injection.

1 - Accelerators and X-rays

Contents

1.1 . History

During the XIXth century, scientists studied the electrical conductivity of low-pressure gases. The protocol consisted in having a high voltage applied between two plates - the cathode (negative voltage) and the anode (positive voltage) - inside a pressurised vacuum tube, as shown in Fig. 1.1, and measuring the potential differences needed to create electrical arcs. Several major discoveries and technologies came out of those experiments.

In the middle of the century, some experimenters noticed light emissions from the tube. By creating holes inside the cathode and the anode, they noticed that this light is produced between them and may exist after the anode, but never before the cathode. Moreover, phosphorescence may be induced in a phosphorescent screen placed behind the anode. William Crookes has developed his own kind of tubes - the Crookes' tubes - with which he can decrease more the gas pressure [3]. At some point, he noticed a disappearance of the light emission from the gas, but the phosphorescence remains. Those observations show that something - named "cathode rays" - comes out of the cathode and goes toward the anode.

By adding an electric and magnetic field around the tube in 1896-1897, Joseph John Thomson showed that these rays are composed of negative charge particles much lighter than the hydrogen - the lightest element known at that time - and

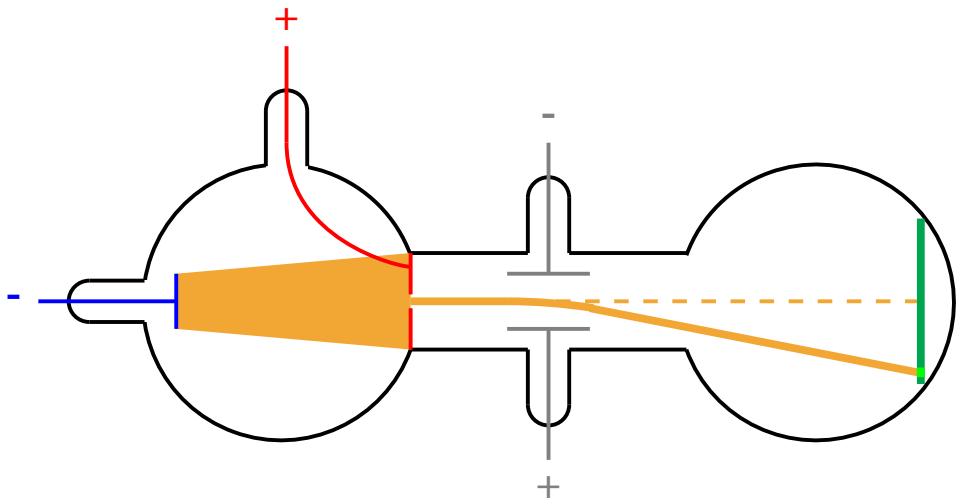

Figure 1.1: Sketch of a Crookes tube, a type of vacuum tubes used to study the electrical conductivity of low-pressure gases. The black line symbolises the glass tube inside which the gas pressure is around 10^3-10^5 mbar [3]. In blue is the cathode, in red is the anode, in grey is a capacitor made of two charged plates used to show the deflection of cathodic rays and in dark green is a phosphorescent plate. The light emitted by those rays - hence electrons - is represented in orange in case of gas ionisation and green for phosphorescent. The orange dashed line represents the propagation of the electron with the uncharged capacitor, while the plain one corresponds to the charged case.

independent of the cathode's composition [1]. The electron was discovered, and cathode rays' tubes may be considered as accelerator's ancestor as some electrons are extracted from the cathode and accelerated by the high voltage between the plates. The light emission is explained by collisions between electrons and atoms that ionise the gas and excite phosphorescent atoms.

In 1895, during studies of Crookes tubes, Wilhelm Röntgen identified a radiation emission coming from the tube [2].

Röntgen also noticed two other valuable properties of X-rays. First, even if X-rays pass through matter, some absorption occurs, and the denser and the thicker the matter, the more X-rays are absorbed. Second, the X-ray exposes photographic plates. Hence, by combining those two effects, one may create photography of the shadow of an object but also identify inner density change inside it. Röntgen use this method on his wife's hand to create the first radiography of human body on December 22^{th}, 1895 (Fig. 1.2).

Thanks to studies of low-pressure gases' electrical conductivity, scientists have discovered the first elementary particles - the electron - and very high energetic photon - the X-ray - but have also created the first electron accelerator and X-ray

Figure 1.2: First human body radiography ever made. The hand is that of Wilhelm Röntgen's wife on December 22th, 1895, while the large dark circle on the second finger is her wedding ring [4].

source. Nowadays, accelerators, electrons and X-rays are always linked together as most of the X-rays sources use accelerated electrons to generate them.

1.2 . Particle accelerators

A particle accelerator comprises several elements that may be grouped into four parts: particle source, accelerating section, transport line and potentially ring (see Fig. 1.3). The essence of an accelerator is the source that allow particles extraction from matter and the accelerating systems that provide energy to the extracted particles. The transport line allows beam transport, characterisation and shaping, while rings mainly store a beam and either use it at some point each turn and/or increase its energy.

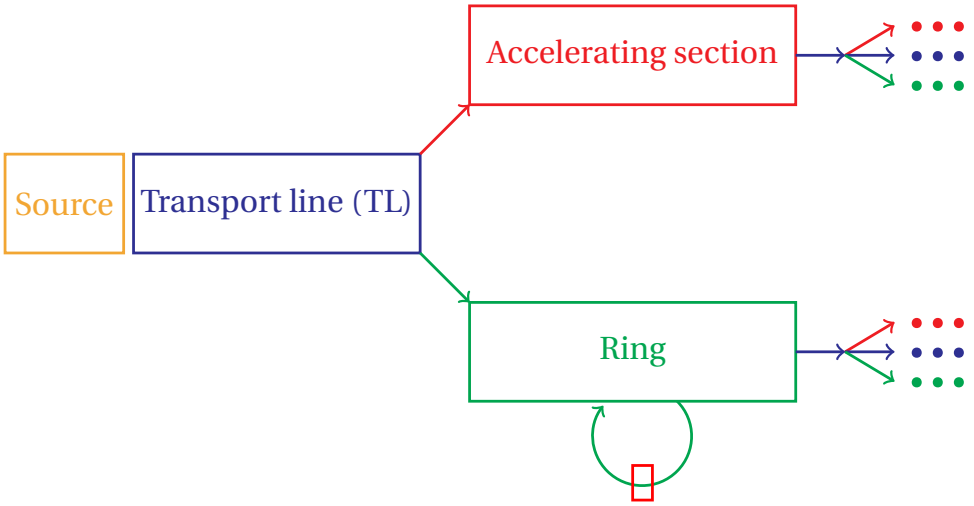

Figure 1.3: General sketch of an accelerator. Four main components may be encountered : a source to create the beam, a transport line to transport, characterise and shape it, an accelerating section to accelerate it and some times a ring to let the beam loops.

1.2.1 . Sources

Several kinds of sources exist depending on the type of particles. A few of them are presented here.

1.2.1.1 Electron sources

The first discovered way to extract electrons from matter is to apply a high voltage between two metal plates - the anode (+) and the cathode (-) - under vacuum, as it is done in Crookes tubes (see Fig. 1.1). This phenomenon is named field emission [5].

An upgrade of this device consists of heating the cathode - often thanks to a current-carrying filament - to provide some thermal energy to the electrons. This so-called thermionic effect [5] alone is enough to create free electrons, but an electrical voltage must guide those electrons away from the source. With a high voltage, the Schottky effect [5] implies that the electric field enhances the thermionic emission.

Another widespread method to extract electrons from matter is to use the photoelectric effect [6, 7]. If one illuminates a metal plate with photons of energy above a certain threshold, some electrons will be kicked out of the metal. A beam may be created during illumination time and guided away with an additional electric field which starts the electrons acceleration.

The choice of the method depends on the beam parameters wanted. All methods can deliver continuous beam, but only the photoelectric effect allows the production of extremely short bunches ($\approx$ fs). Other parameters like the beam current,

emittance (size and divergence), and spin polarisation can weight in favour of one specific electron source. For the ThomX accelerator, the choice has been made to have a photo-injector, using the photoelectric effect to generate a very short beam. See section 2.1.1 for more details.

1.2.1.2 Ion sources

For Ions sources, there exists even more methods. According to the element properties (matter state, electronic shell, ...), the source is more or less complicated. Still, the key is always to create ions by taking/giving one or several electrons from/to an atom and accelerating it with an electric field as soon as possible.

For liquids and solids, the first step is often to evaporate the liquid or sublime the solid and use the gas created to generate ions. The state transition may be done by heating the matter, decreasing the pressure, bombarding with a laser beam or an electron beam for example.

As for gas, ionisation through electrical discharge may be used, but often nowadays, a plasma is created as it is the case with ECR (Electron Cyclotron Resonance) sources [8]. As shown Fig. 1.4, in ECR sources, some gas is injected into a cavity filled with radio-frequency (RF) waves. The power of the RF resonates with some electrons and increases their energy. At the centre of the plasma - called the ECR zone - the "hot" electrons might kick out atoms' electrons and create ions. Some ions may follow the magnetic line and be extracted from the source.

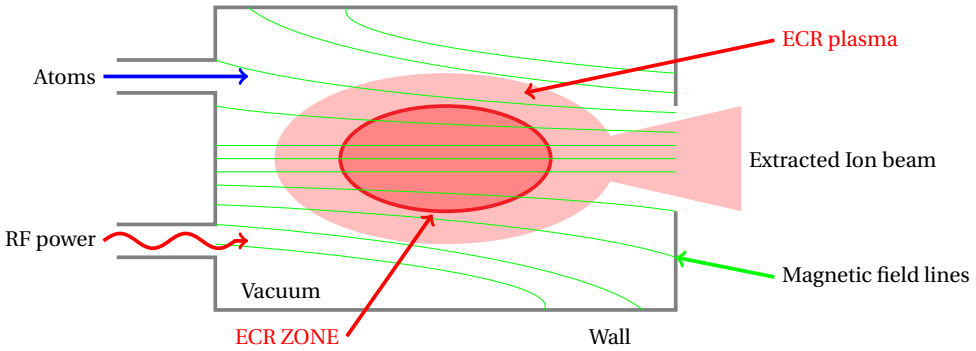

Figure 1.4: Sketch of an ECR source adapted from [8].

1.2.1.3 Anti-matter sources

Accelerators are used for hundreds of purposes, and some of them need anti-matter. Those anti-elements cannot be found in large amounts in nature, but with enough energy, one can create them.

For example, during the sixties, an electron-positron collider - named ACO (Anneau de Collisions d'Orsay, LAL, France, Fig. 1.5) - was created to study the collision between electrons' and positrons' beams and the creation of new particles

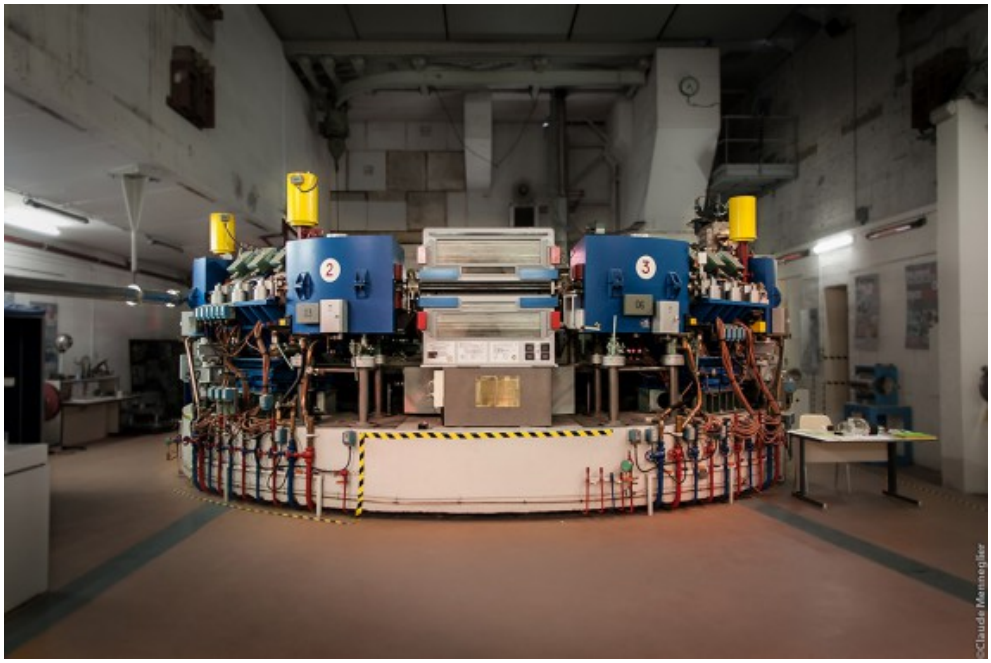

Figure 1.5: The "Anneau de Collisions d'Orsay" (ACO) is one of the world's first collider and synchrotron sources. It is a $7\,\mathrm{m}$ diameter ring that was fill of electrons and positrons using the linear accelerator of Orsay from 1967 to 1988.

[9]. A $750\,\mathrm{MeV}$ electron beam was led to a thin plate of tungsten. Within the metal, some electrons will interact with the nucleus of tungsten, be deflected and emit a photon via bremsstrahlung. If the photon has enough energy and interacts with another nucleus, it might annihilate into an electron-positron pair. As the tungsten sheet is thin enough, some of those positrons go out of the matter, and a magnetic field is used to separate electrons and positrons and create the positrons' beam.

1.2.2 . Accelerating section

Most of the accelerators use a device to increase the particles' energy, hence its momentum. An electric field parallel to the beam propagation axis is used for that purpose. For continuous beams, a constant electric field must be used. The simplest device is two charged plates with a hole to let the beam pass. The potential difference V between the two plates will increase the energy of the beam by qV if q is the particles' charge. To increase further the energy gain of electrostatic accelerators, two main types of electrostatic' generators are used [10] :

- **Van der Graaff generator**: A belt mechanically brings charges from the ground to an isolated electrode to generate a high voltage between the ground and the electrode (see Fig. 1.6a)

- **Cockcroft-Walton generator**: A voltage multiplier using capacitors and diodes to pass from low electrical power source to high voltage (see Fig. 1.6b)

(a) The small Van der Graaff generator used at the museum "Science ACO" (Orsay, France) to create high voltage and demonstrate air breakdown.

(b) $1\,\mathrm{MeV}$ Cockcroft-Walton generator at the "Laboratori Nazionali di Frascati" INFN, Italy.

The high voltage is limited to a few mega-volts by the insulation breakdown which create electrical arc. Some alternatives allow to increase the energy gain like the use of highly charged particles or tandem accelerators - two top-to-tail Van de Graaff with beam polarity inversion system between them - but the voltage limitation always restricts the energy gain at the end.

Nevertheless, it is possible to go over this limitation using a radio-frequency (RF) electric field. In the case of pulsed voltage between plates under vacuum, the breakdown process has an initiating time t proportional to maximum voltage squared V^2 [11], hence if the electric field variations are fast enough, the breakdown cannot establish itself. It is the principle of RF cavities.

RF cavities are metallic - often copper - devices such that an RF electromagnetic field can be established within it with the electric component co-linear to the particle's trajectory as shown Fig. 1.7. The goal is to send the beam at the right time so that the electric field accelerates the particles. When several cavities are one after the other, the phase difference between two successive cavities must equal the time needed for the particles to pass from one cavity to the next. If the particles are relativistic, this time can be considered constant as the particles' velocity does not increase so much. Still, for non-relativistic particles, the speed of

particles must be taken into account, which may lead to the use of several cavity sizes. On ThomX (see section 2), as the gun delivers a 5 MeV electron beam, the accelerating section can be composed of several identical cavities.

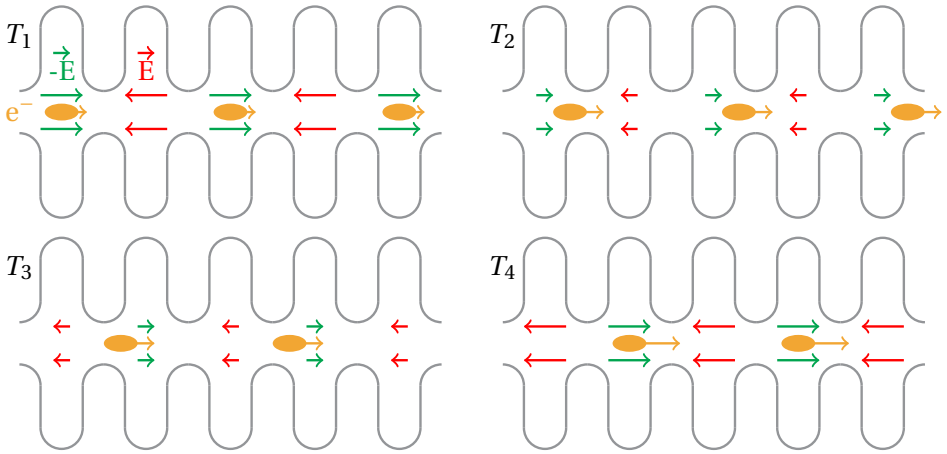

Figure 1.7: Sketch of relativistic electron beam propagation inside an RF section for different time : T1 < T2 < T3 < T4.

During the fill-up of the section of the RF gun, the imperfections or impurities on the cavities' wall may drastically increase the electric field locally. It explains why before using the RF cavity at nominal power, one must commission it with a slow increase of the RF power until the first breakdown. As this breakdown is just above the limits - thanks to the slow power increase - the risk of damage is small. Still, the sparks might burn the impurities or erase the imperfection and allow to increase furthermore the power in the cavity. By repeating this back and forth process slowly, one can achieve nominal power with few breakdowns.

The use of RF cavities implies using a pulsed beam and controlling the arrival time of the particles as the electric field is decelerating half of the time but allows the creation of very high accelerating gradients. Moreover, one may use as many successive cavities as wanted which theoretically permits to increase the energy gain to infinity. To reduce the energy losses, one may use superconducting RF cavities. The RF power may be provided by a klystron or solid state RF power amplifier and transported using waveguides.

Other accelerating systems exist like the cyclotron (see Fig. 1.8) composed of two half-circles filled with a magnetic field and separated by an alternative electric potential. A source creates charged particles at the centre of the electric gap, where they start their acceleration. Once in the magnetic field, the particles' trajectory is deflected. The particles return to the electric region that has used the propagation time to change its polarity. Again the particles are accelerated, then travel in the magnetic field along an arc of a circle with a larger radius - as particles have higher momentum - and return to the accelerating gap. After several turns, the particles

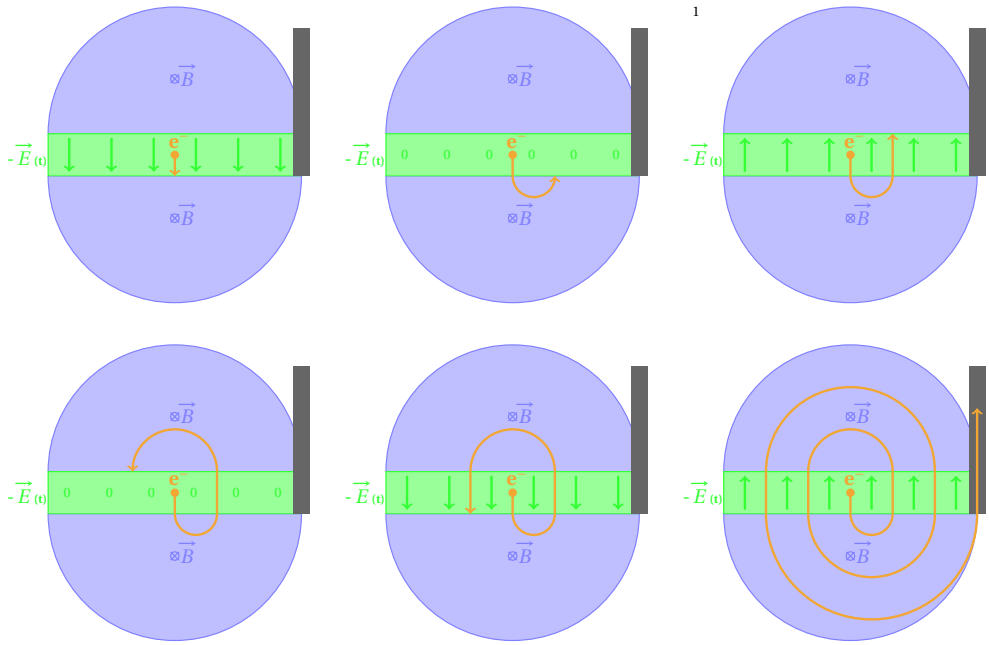

Figure 1.8: Sketch of the behaviour of a cyclotron during electron acceleration. From left to right and top to bottom: electron injection, first rotation in the magnetic field, first beam acceleration, rotation with larger radius as particles have higher momentum, new acceleration, ..., beam extraction.

will have the energy that leads them to an extracting pipe. Those devices are compact and robust which is perfect for medical purposes - like proton therapy - to reduce failure time and space requirements.

1.2.3 . Transport lines

Once a beam is created, it must be led from the source to places of interest. To avoid interaction with gas - which induces particle losses - the beam will travel within a vacuum chamber with typical pressure as low as $10^{-10}\,\mathrm{mbar}$. Along this pipe, several pieces of equipment may be added.

To curve the beam trajectory, one usually uses a magnetic field provided either by a permanent magnet or an electromagnet - classical or superconducting - with a magnetic field perpendicular to the rotation plane. The remaining part of the accelerator is composed of straight lines where there is diagnostics to characterise the beam properties, steerers to correct the particles' trajectories, quadrupoles to focalise/defocalise the beam and every other equipment needed like vacuum pump, vacuum gauge, cooling system...

The main hardware systems of transport lines are describe in section 1.2.5.

1.2.4 . Rings

Rings - or circular accelerators - are structures composed of elements similar to those found in transfer lines (TL) but the whole structure loops on itself. Dipoles are essential for that purpose as the beam should turn of $360°$ each turn. The quadrupoles, sextupoles and other multipoles are often found too to control the beam properties during rotations. Non-destructive diagnostics are privileged to permit beam characterisation without beam perturbation. To correct beam trajectory, some feedback systems can use diagnostics and simulations to compute the strength needed in the steerers. A more detail description of those hardware systems is provide in section 1.2.5.

In rings, to my knowledge, there is at least one accelerating cavity. It can be use for two purpose.

First, the storage ring uses the cavity to compensate the energy loss of particles. The energy loss can have different origins, and for electrons or positrons the main one is the synchrotron radiation. Because of the RF structure, the energy gain for particles at the head and tail of the beam would not be the same. For particles ahead of the beam the energy gain must be slightly higher to increase their energy as well as their radius of curvature - hence travelling length - into dipoles which will increase their propagation time for next turns and lead them to the tail of the beam. Inversely, tail's particles have lower energy gain, which means lower travelling length into dipoles, hence they achieve a turn quicker and go ahead of the beam.

Second, booster ring uses the cavity to increase the energy of the particles. At the same time, one must increase the strength of the magnetic element to keep particles on the same path, else because of Eq. (1.1), the particles will travel in larger and larger orbits that may lead to beam loss. Those boosters are commonly used to reach very high-energy beams.

1.2.5 . Accelerator hardware

Description of the main hardware systems of transport line and ring.

1.2.5.1 Magnetic element

1.2.5.1.1 Dipole Dipoles - or bending magnets - are magnets used to bend the beam's trajectory. A magnetic field perpendicular to the rotation plane is used for that purpose. To generate it, one may use two coils through which an electric current flows, as seen on Fig. 1.9. The iron core channels the magnetic field to avoid parasitic fields outside the dipole. Some permanent magnets could also be used, but electromagnets allow changing the magnetic field easily.

In first approximation, one can consider the trajectory outside of dipoles straight and inside them curved such that the radius of curvature ρ follow the Eq. (1.1) with B the magnetic strength, p the particle momentum and q its charge.

$$|B\rho| = \left|\frac{p}{q}\right| \tag{1.1}$$

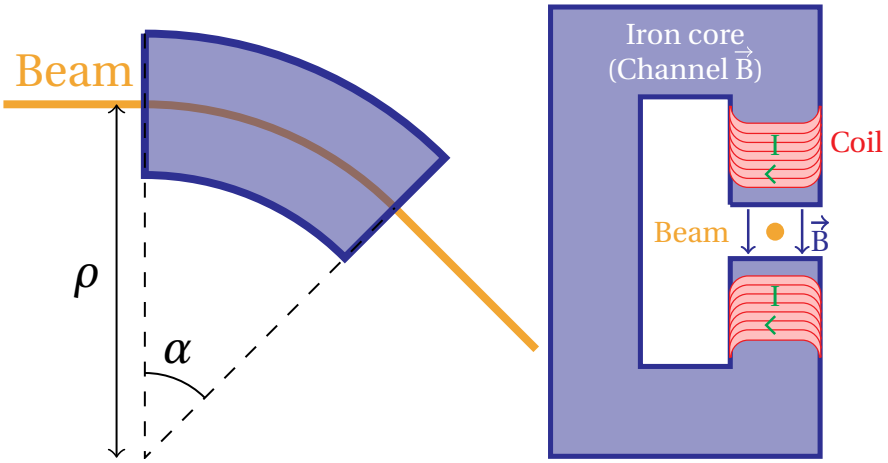

Figure 1.9: Simplified sketch of dipoles seen from above (left) and by side (right).

As reaching a very high magnetic field (above several Tesla) can be complicated, to be able to increase the particles' energy - hence momentum - one must use a higher radius of curvature, which means a larger accelerator. This explains why some facilities like the Large Hadron Collider (LHC) at CERN are so large.

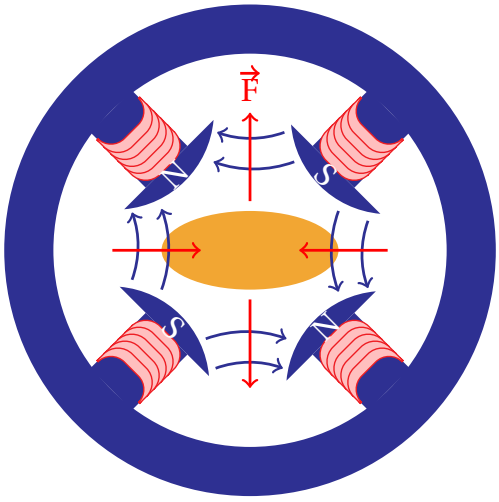

Figure 1.10: Sketch of a quadrupole in the transverse plane. The blue arrows represent the magnetic field, while the red arrows represent the force that feel the beam in orange.

1.2.5.1.2 Quadrupole The quadrupoles are magnetic elements composed of four poles at 90° each (see Fig. 1.10) with polarity inverted from one pole to the next. This element is used to focalise or defocalise the beam. Because of its

structure, the magnetic field at the centre of a quadrupole is null, and gradually increases when one moves away from the centre.

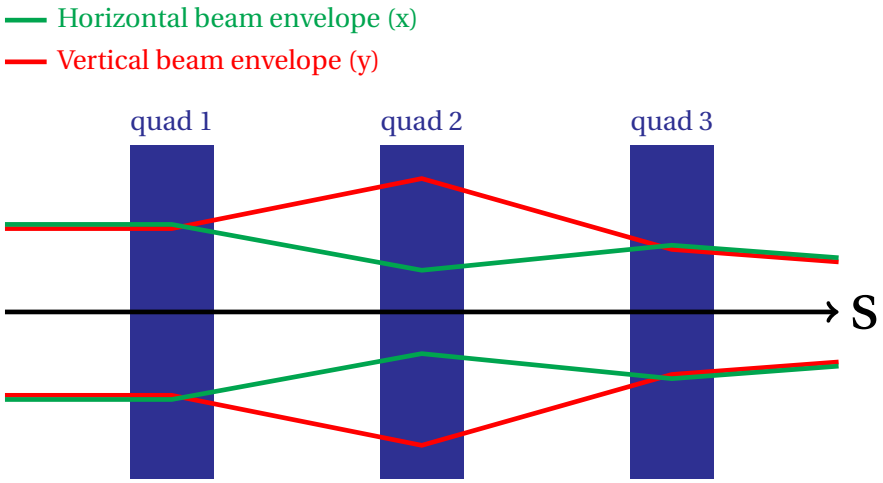

Figure 1.11: Sketch of a FODO cell with three quadrupoles. The green (red) line corresponds to the horizontal (vertical) beam envelope. S is the axis of propagation.

A quadrupole can be considered as a lens, but contrary to classical optical lens, it focuses in one transverse plane and defocuses in the other. To obtain a global focalisation of the beam, one must use several quadrupoles - often three - one after the other with inverted polarity. A classical structure used in accelerators is a FODO (FOcus/DefOcus) cell structure composed of three identical quadrupoles.The Fig. 1.11 show an example of the FODO cell with the first and third quadrupole that focalise in the horizontal plane while the second one focalises in the vertical plane. Because, in the second quadrupole, the beam is smaller horizontally, the defocalisation is smaller than the focalisation in the first quadrupole, and vice versa in the vertical plane, which permits to achieve global focalisation at the end.

1.2.5.1.3 Sextupole Sextupoles are elements similar to quadrupoles but with six poles, as shown in Fig. 1.12. Like higher multipoles - octupoles, ... - sextupoles are used to compensate for some non-linearities. For instance, a sextupoles can be used to suppress the coupling between both transverse planes. These elements can be found in TL but are more often used in rings where a very small non-linearity can lead to a significant effect because of the accumulation of turns.

1.2.5.1.4 Steerer The steerers - or correctors - are either electric or magnetic elements used to deflect the beam slightly. For relativistic particles, the choice of magnetic steerers is often made as the ratio between magnetic and electric force

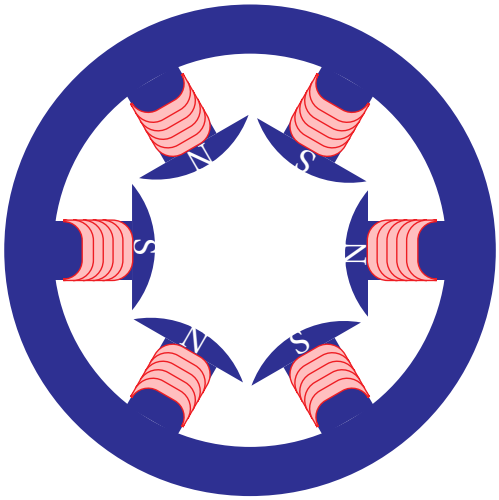

Figure 1.12: Sketch of a sextupole in the transverse plane.

can be expressed as $\frac{F_B}{F_E} = \frac{qvB}{qE} = v \approx c\frac{B}{E}$ which mean that a $1\,\mathrm{T}$ electromagnet have the same impact than a MV plan capacitor with a gap of a few centimetres.

Contrary to dipoles, magnetic steerers are only used to correct the beam trajectory regarding the ideal one - often the centre of the beam pipe - but is not meant to bend this ideal trajectory. Moreover, steerers are often used in both planes at the same time. This may be done with a device like the one on Fig. 1.13.

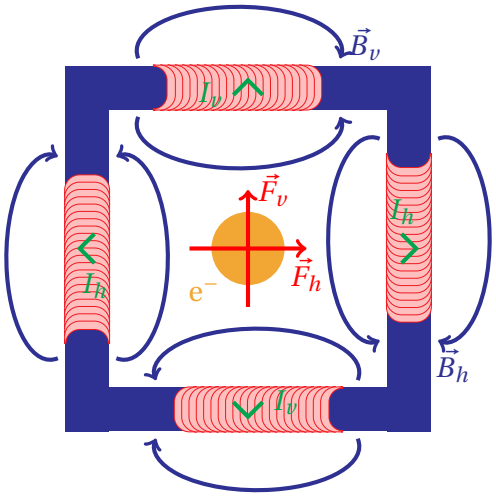

Figure 1.13: Sketch of a magnetic steerer in the transverse plane. Electrons are going outside the paper. Two bipolar generators allow deflection in every direction.

1.2.5.2 Diagnostics

Many diagnostics exist depending on the properties one wants to measure and on the particle type. Some common diagnostics are presented in the following section.

1.2.5.2.1 Scintillator screen A scintillator screen is a material that will emit light when a beam passes through it. Many materials and physical principles can be used. The light can come from an energy deposition in the matter and then deexcitation of the atoms with a photon emission as for Yttrium aluminium garnet (YAG) crystals [12]. The optical transition radiation (OTR) screen emits light by the OTR effect [13], which corresponds to an emission of light from charged particles travelling in an inhomogeneous medium. Both effects can be used to identify the shape of the beam or its position.

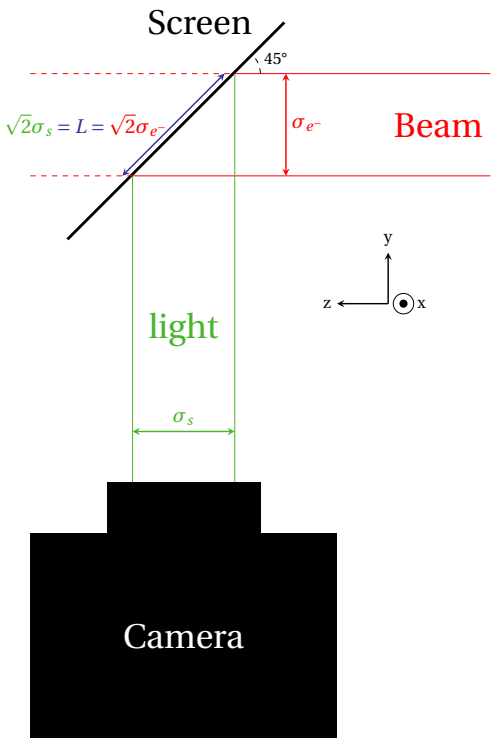

Figure 1.14: Sketch of a simple scintillator screen station.

The longitudinal length of the beam can be measured using a phenomenon that emits light when and only when there is a beam. The Cherenkov radiation is one of such physical principles. It correspond to an emission of light by particles travelling in a medium faster than light in this medium. A streak camera can be used for very short beam to measure the longitudinal length of the light emission. For electrons, the synchrotron radiation can also be used similarly.

1.2.5.2.2 Beam position monitor Beam position monitors (BPM) are non-destructive diagnostics composed of 4 electrodes around the beam trajectory. When the beam passes between them, it induces a current in the electrode. The closer the beam to an electrode, the higher the induced current. Hence by comparing the current of two opposite electrodes, one may deduce where is the centre of charge of the beam. At first order, one may compute the position of the beam using the BPM of Fig. 1.15 with Eq. (1.2) and Eq. (1.3).

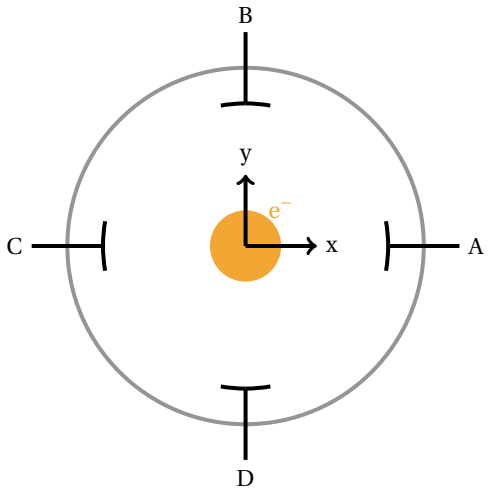

Figure 1.15: Sketch of a simple beam position monitor. Electrons are going outside the paper.

$$x = k_x \times \frac{V_A - V_C}{V_A + V_C} \tag{1.2}$$

$$y = k_y \times \frac{V_B - V_D}{V_B + V_D} \tag{1.3}$$

With k_x and k_y some calibration factors, and V_i the potential read on the electrode i.

1.2.5.2.3 Integrating current transformer Integrating current transformer - or ICT - is a coil wrapped around the beam trajectory as shown Fig. 1.16. A current proportional to the beam charge is induced in the coil when the beam passes through it. The calibration factor can be tabulated beforehand, and ICT gives a non-destructive measure of the beam charge.

1.2.5.2.4 Faraday cup Another charge diagnostics is the Faraday Cup (FC). This destructive device is often made of a grounded piece of conductor - often copper or graphite - aimed to stop the beam and recover all the charges. One can directly measure the beam charge by measuring the charge flux from the FC to

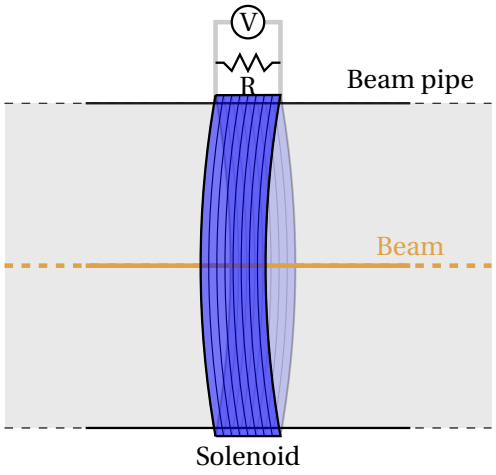

Figure 1.16: Sketch of an Integrating Current Transformer. The current is measured by measuring a voltage at the terminal of some known resistor.

the ground. This measure may be very precise as no calibration is needed, but for that purpose, special care for the device design must prevail over the loss of beam charge or secondary particles induced by the collision of the beam particles on the conductor. An example of FC with a magnet to avoid charge losses is shown in Fig. 1.17.

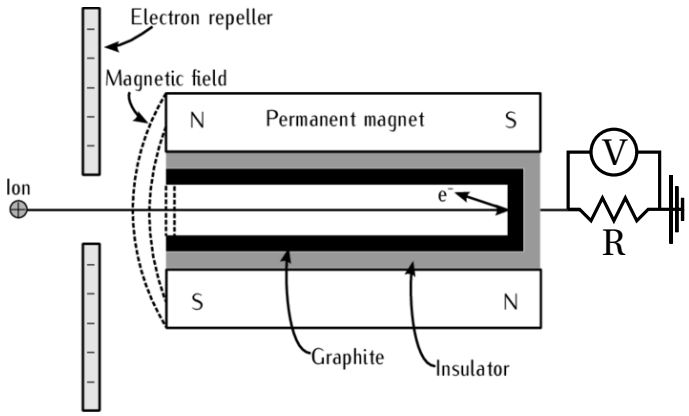

Figure 1.17: Sketch of a Faraday cup adapted from [14]. The measure of the current flux is made by measuring a voltage at the terminal of some known resistor.

1.2.6 . Applications of accelerators

Many methods exist to create a beam, accelerate it and control it, and so are their use.

If one considers cathodic tubes as small accelerators, it was used to discover the electron, to measure alternative current in analogical oscilloscopes, and even in old televisions when they were deeper than wider. But even without considering cathodic tubes, the usefulness of particle beams is countless.

From fundamental experiments - to understanding the infinitely small and physics laws - to medicine or even art conservation, examples of applications of accelerators are presented in the following sections.

1.2.6.1 Large Hadron Collider

One of the most famous accelerators in the world is the Large Hadron Collider (LHC). LHC is - today - the accelerator of all superlatives. The longest - $27\,\mathrm{km}$ of circumference -, the most energetic per nucleon - $7\,\mathrm{TeV}$ per proton -, the most complex - two Linacs, 7 booster rings, 1232 dipoles cooled down to less than $2\,\mathrm{K}$ for the main ring, 4 main experiments (Alice, Atlas, CMS and LHCb), ... - the most prolific - $60\,\mathrm{TB}$ of data generated per second (only a few is saved but they must be well selected) -, etc. [15] Its principle is to circulate two beams - often protons but sometimes heavier ions like lead - in 2 different pipes in opposite directions and, at some point, let them collide. During this process, beams will interpenetrate, and potentially some parts of the nucleus will interact with others. Lots of energy may be released at this instant, allowing heavy particles like Z bosons, quarks, gluons, muons or even Higgs bosons to appear. Around the interaction point, giant detectors of several tons allow one to recover all information about particles passing through them which permits the reconstruction of what happened during the interaction.

Among other things, this machine has permitted the discovery of the Higgs boson in 2012 [16], the last missing piece of the standard model of particles. An upgrade of the accelerator - named HL-LHC for High Luminosity LHC - aim to increase the luminosity - hence the number of events per second - to continue the studies of the Higgs' properties and try to find new physics like supersymmetry or string theory to understand the slight differences between standard model's predictions and measurements.

Another project - FCC-ee for Future Circular Collider of electron-positron - plans to switch back from hadron to electron-positron collider - as was the LEP, the LHC ancestor - and continue heavy particles studies.The energy may be adapted depending on the desired studies. For instance, $120\,\mathrm{GeV}$ allows studying the pair Z-Higgs boson creation, while a $175\,\mathrm{GeV}$ or $182.5\,\mathrm{GeV}$ beam permits creation of $t\bar{t}$ pairs [17]. Using elementary particles and not composed ones allows for a more precise measurement of particle properties as the primal interaction is less complex to reconstruct. Research for new particles, dark matter and other actual mysteries of the known physics is also on topic.

Those domains of physics are also studied with other less energetic accelerators all around the world, like at Caen (France), Frascati (Italia), Chicago (USA),

Stanford (USA) or Tsukuba (Japan).

1.2.6.2 Accelerators for medicine

Another application of accelerators is to treat cancer. The goal is to damage tumour cells without killing healthy ones. Accelerators are used to deliver a certain energy to "burn" the tumour. This dose delivered to the inner part of the tumour is high enough to kill them, but to protect the normal cell, the borders of the tumour are often just damaged. As a unique tumour cell may multiply enough to regenerate the whole tumour, several sessions of irradiation must be performed. Hopefully, normal cells heal quicker than tumour ones; hence, if one chooses the correct delay between two sessions, the damage to the tumour tissue increases while healthy ones heal each time.

Several ways to provide energy deposition can be used. It can be done using X-rays - radiotherapy or K-edge cancer therapy (see section 1.3.2.3) - or particles like proton, neutron or heavier positive ions. All of these methods use accelerators. Proton and ion therapy directly use accelerated particles, neutrons can be provided by proton beam colliding onto a target, and X-rays are commonly generated by the bremsstrahlung effect (see section 1.3.1.1.1) using energetic electrons colliding onto a target.

An X-ray beam may be used for superficial cancer as energy deposition in the matter is maximum after some centimetre and then decrease. Still, one can see on Fig. 1.18 that after $30\,\mathrm{cm}$ a quarter of the maximal energy is always deposited, which can be too much for fragile tissue.

Such a method is too dangerous for tumours around the spinal cord, eyes or brain. Luckily, the Bragg peak of proton energy deposition in the matter can be used to palliate this issue. When a mono-energetic proton beam enters a medium, it will deposit energy following the red curve on Fig. 1.18. In the beginning, only a small amount of energy is deposited. The beam is stopped at the Bragg peak, depositing all its remaining energy, and almost no energy is deposited beyond. For a large-scale tumour, one may modify the Bragg peaks - like for the blue curve of Fig. 1.18 - either by increasing the beam energy spread, delivering several proton beams at different energy or using several identical beams but adding some absorber between the accelerator and the body to decrease the depth of the Bragg peak artificially.

For medical purposes, other kinds of accelerators can be found, like accelerators aimed at generating radioisotope for therapeutic goals or health diagnostic but also X-rays generators for radiography, for instance.

1.2.6.3 New AGLAE

Not only do humans need to have health checks at some point, but works of art need it too. Different methods exist to do so using an accelerator. It explains

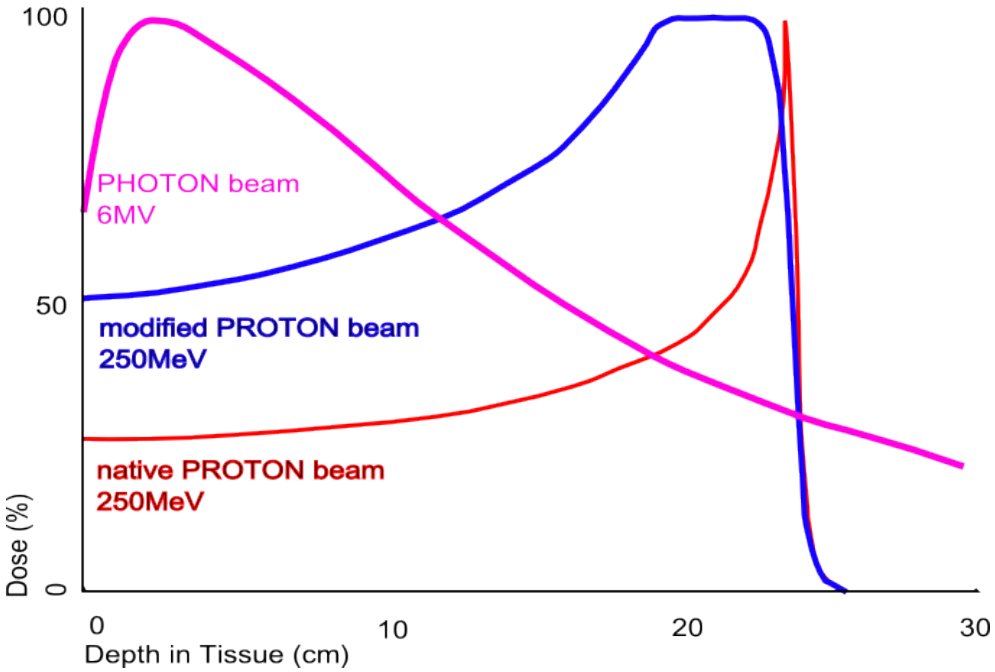

Figure 1.18: Plot of energy deposition within a body for X-photon beam (pink) $250\,\mathrm{MeV}$ proton beam (red) and $250\,\mathrm{MeV}$ proton beam with high energy spread (blue) [18].

why a museum like the Louvre has in its underground an accelerator named New AGLAE [19] for "Accélérateur Grand Louvre d'Analyses Elémentaires".

This machine is a proton or alpha particles accelerator that provides beams of 4 and $6\,\mathrm{MeV}$ respectively. The beam goes out of the accelerator, passes through the air and then impinges on the piece of art under study. Several detectors around the target will detect secondary particles emitted after the beam's interaction with the object. From the signal recorded, one may find the atomic constitution of the masterpiece even for trace elements.

X-rays may also be used to probe the interior of sculptures. Nowadays, synchrotron accelerators are the most potent X-ray generators (see section 1.3.1.2.1), but other generators could be used.

1.3 . X-rays

X-rays correspond to high energy photons in the range of $10\,\mathrm{nm}$ - $0.1\,\mathrm{keV}$ - to $5\,\mathrm{pm}$ - $1\times10^{2}\,\mathrm{keV}$ - as shown in Fig. 1.19. The photon wavelength is in the range of the size of atoms, hence X-ray can be used to scan the atoms' or molecules' structures. Moreover, as first noticed by Wilhelm Röntgen when he discovered X-rays, they can pass through matter and expose photographic plates, which permits radiography.

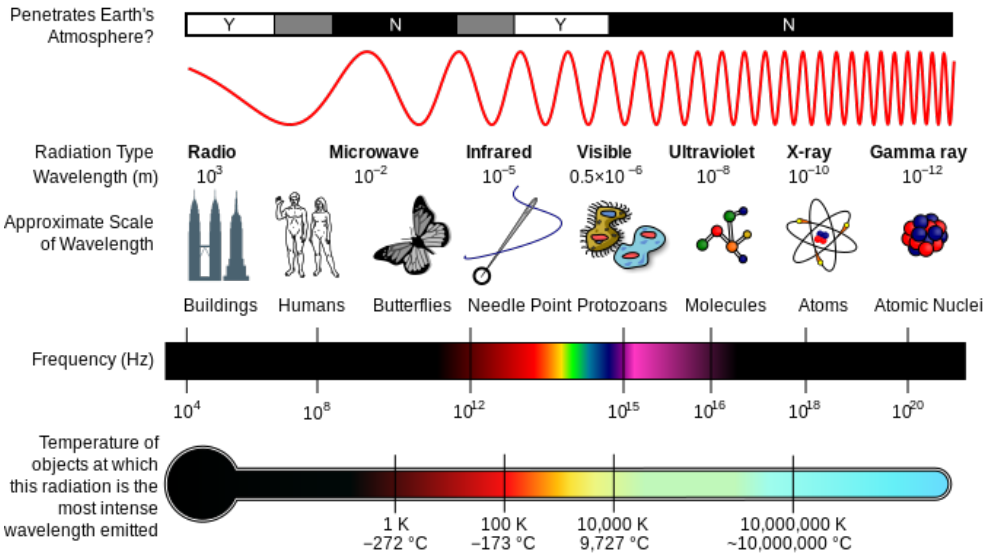

Figure 1.19: Electromagnetic spectrum of light [20].

1.3.1 . X-ray sources

Several methods can be used to generate X-rays. Some of them are presented in the following sections.

1.3.1.1 X-rays tube

X-ray tubes are devices similar to Crookes' tubes section 1.1 where some electrons are extracted from a cathode, accelerated by a high voltage and sent to a plate. Within the plate, the bremsstrahlung effect creates the X-rays.

1.3.1.1.1 Bremsstrahlung effect Bremsstrahlung can be translated as deceleration radiation. When an electron beam enters matter - like the anode of the Crookes tube - the velocity of a few electrons is affected by the electric field of the nucleus, which induces electron deceleration and photon emission. The closer the electron is to the nucleus, the higher the photon energy. This phenomenon leads to emission of a continuous spectrum as seen on Fig. 1.20. On the image, the two largest peaks above the continuous spectrum correspond to the rhodium's K lines. They are located at the energy needed to extract inner electrons from the atom.

1.3.1.1.2 Example of X-rays tube Crookes' tubes are one example of X-ray tubes. Nowadays the devices are based on the same principle, but enhancement of the electron production has led to a new limitation: overheating risk because of energy deposition within the plate. To palliate overheating, some tubes use

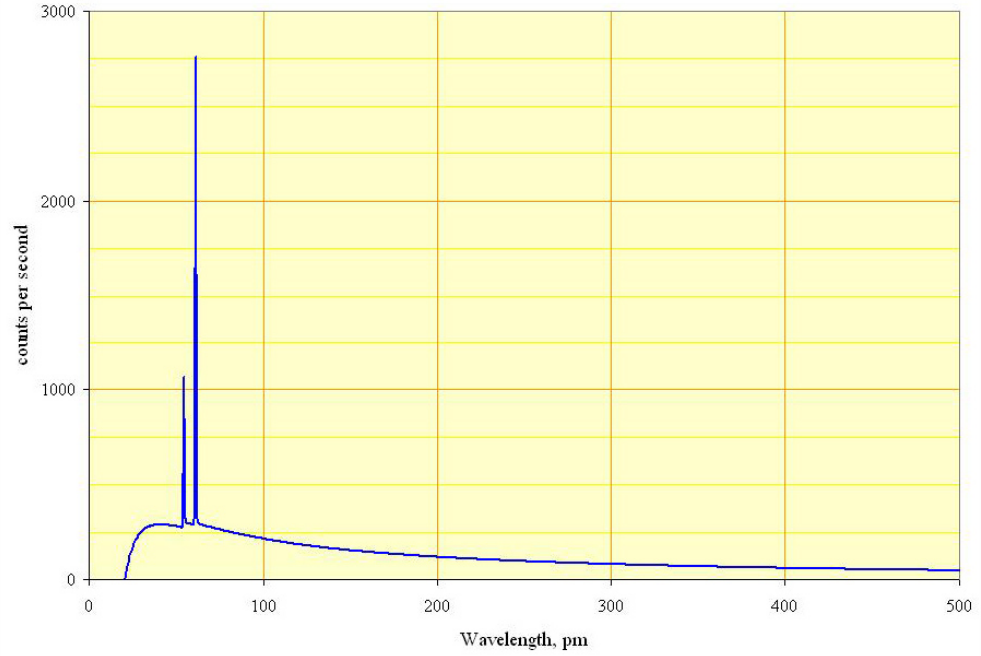

Figure 1.20: The spectrum of a rhodium target tube operated at 60 kV, showing continuous spectrum - Bremsstrahlung - and K lines of the rhodium (see section 1.3.2.2).

rotating anodes such that the energy is not deposited at only one place but all along a circle. Even so, the yield of X-ray sources is limited.

1.3.1.2 Synchrotron radiation sources

A synchrotron accelerator is an electron storage ring using synchrotron radiation to generate light.

1.3.1.2.1 Synchrotron effect Synchrotron radiation occurs when a charged particle's trajectory is not uniform, like during rotations into a magnetic field (see Fig. 1.21). In that case, the light is emitted with energy proportional to the fourth power of the Lorentz factor (γ^4). This power four on the Lorentz factor and the fact that γ is inversely proportional to the rest mass of the particle explain why electrons and positrons are most subject to synchrotron radiation. It permits the creation of synchrotron accelerators, but also may become a nightmare in the electrons or positrons storage ring of very high energy accelerators as energy loss can be huge.

1.3.1.2.2 Example of synchrotron accelerator SOLEIL - Source Optimisée de Lumière d'Énergie Intermédiaire du LURE - facility is one example of

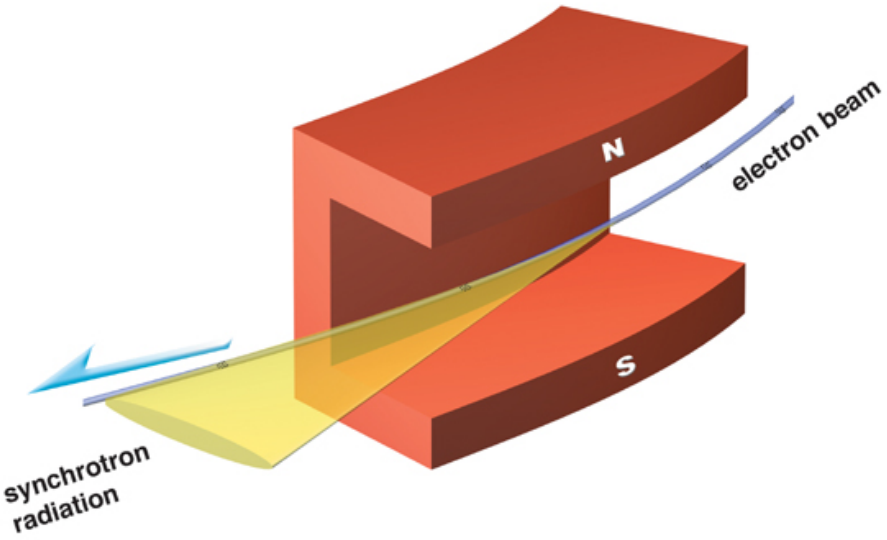

Figure 1.21: Sketch of the synchrotron radiation - in yellow - emitted by an electron beam into a dipole [21].

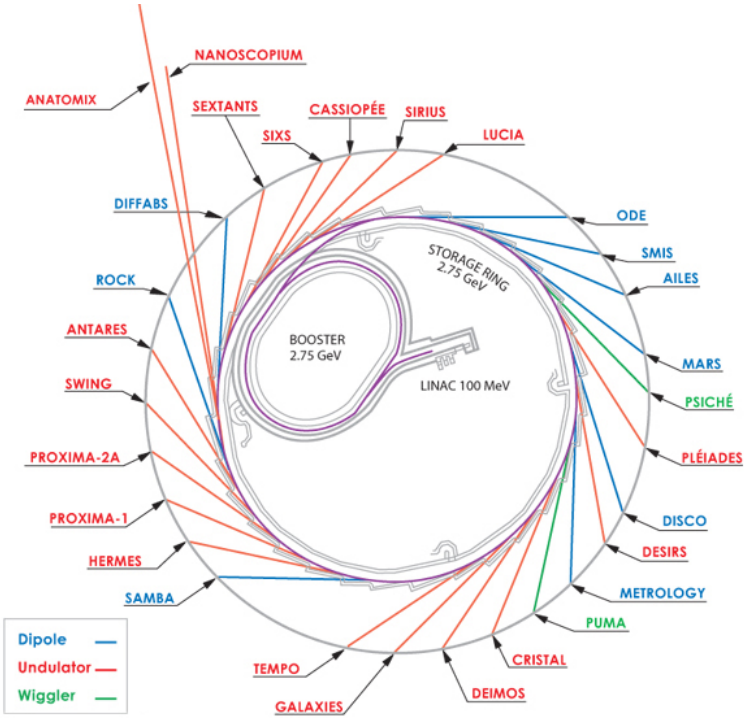

Figure 1.22: Maps of SOLEIL see from above. In blue are lines where the light comes from dipoles, in red from undulators and in green from wigglers [22].

a synchrotron accelerator located a few tens of kilometres South-West of Paris in France. This facility is a $3\,\mathrm{GeV}$ electron accelerator composed of a Linac, a booster and a storage ring as shown on Fig. 1.22. In normal operations, the storage ring often works in a top-up mode where some bunch - from one to 416 - travels in the storage ring, and at regular time intervals the Linac and the booster quickly start to replace the lost electrons. This method allows keeping a nearly constant current, which means a constant light power delivered at each light line.

To increase the range of possible light emission, not only dipoles are used, but also some other devices named undulator and wiggler. Both use a succession of magnets to force the bunch trajectory to undulate and permit the generation of light with characteristics depending on the geometrical structure of the device. Undulator has the particularity to create coherent light with countless uses.

Synchrotron radiation sources may be used to do fundamental and applied research. The techniques used involve tomography, spectroscopy, the study of proteins, viruses, cell chemistry in action, etc.

1.3.1.3 Compact Compton sources

Compact Compton Sources (CCS) are X-ray sources using the Compton backscattering effect. The main goal is to create intense, cheap and compact sources that can be installed in laboratories, museums or hospitals.

Several experiments of Compton backscattering effect have been made with success all around the world. For example, in the gamma range there is a source at NewSUBARU in Japan [23] and the HIGS facility at Duke in the US [24], while in the X-ray range, there is the Munich Compact Light Source (MuCLS) build by Lyncean Technologies [25] that have obtained light.

1.3.1.3.1 Compton backscattering effect The Compton BackScattering effect (CBS) refers to a momentum transfer from an electron to a photon coming backwards regarding to the electron trajectory.

The photon-electron scattering effect was first encountered with small energy photons scattered on a free electron. In this case - studied and explained by Joseph John Thomson - the energy lost by the photon during the scattering is null or negligible, and the process is considered elastic scattering. This phenomenon is named Thomson scattering.

The Compton scattering is a generalisation of this effect where one may consider whether a high energy photon is scattered on a bound electron or not. In most cases, the Compton scattering is an inelastic effect as the photon energy decreases.

The inverse process where a low-energy photon is scattered on a high-energy electron - which increases the photon energy and decreases the electron one - is named the inverse Compton scattering or Compton backscattering (CBS). CBS is the most efficient photon energy amplifier [26].

On ThomX (see section 2), with a $50\,\mathrm{MeV}$ electron beam and a $1.2\,\mathrm{eV}$ photon beam, the maximum energy of the photon created by CBS is $46\,\mathrm{keV}$ which actually corresponds to hard X-rays.

1.3.1.3.2 Example of Compact Compton sources

The ThomX project is one of the Compact Compton Sources (CCS) prototypes under development. Currently, the most advance industrial project in the X-ray range is the Munich Compact Light Source (MuCLS) [25] which is a CCS developed by Lyncean Technologies, Inc. [27]. An example of measurement obtained by this machine is presented in section 1.3.2.4. Thanks to the high photon energy amplification, all those facilities are much smaller than synchrotron accelerators, as shown Fig. 1.23.

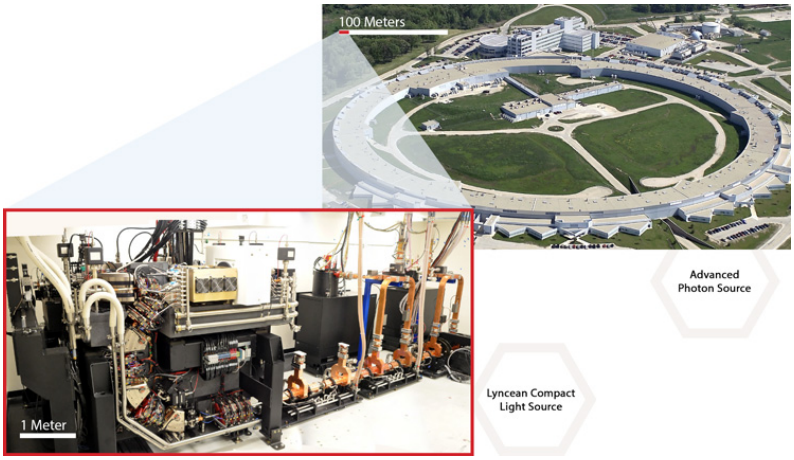

Figure 1.23: Comparison of Lyncean compact light source (CLS) and conventional synchrotron light sources [27].

1.3.1.4 Comparison of X-rays sources

X-ray sources can be compared using their brightness. This observable corresponds to the number of photons per second - hence flux - divided by the x beam size, the x beam divergence, and the bandwidth at a level of 10^{-3} of the maximum amplitude - denoted to 0.1%BW. Hence the units of the brightness B is $\mathrm{photon/s/mm^2/mrad^2/0\,1\%BW}$.

On the Fig. 1.24 one may see that rotating X-tubes are limited to a brightness of $10^{10}\,\mathrm{ph/s/mm^2/mrad^2/0\,1\%BW}$. ThomX expects to deliver around $5\times10^{11}\,\mathrm{ph/s/mm^2/mrad^2/0\,1\%BW}$, and synchrotron facilities may achieve $5\times10^{15}\,\mathrm{ph/s/mm^2/mrad^2/0\,1\%BW}$ in the $45\,\mathrm{keV}$ range. Some superconducting RF gun's CCS plan to deliver up to $1\times10^{15}\,\mathrm{ph/s/mm^2/mrad^2/0\,1\%BW}$ which is equivalent to synchrotron accelerators. According to those values, synchrotron accelerators are far brighter than ThomX, itself brighter than x tubes, but several other parameters must be investigated.

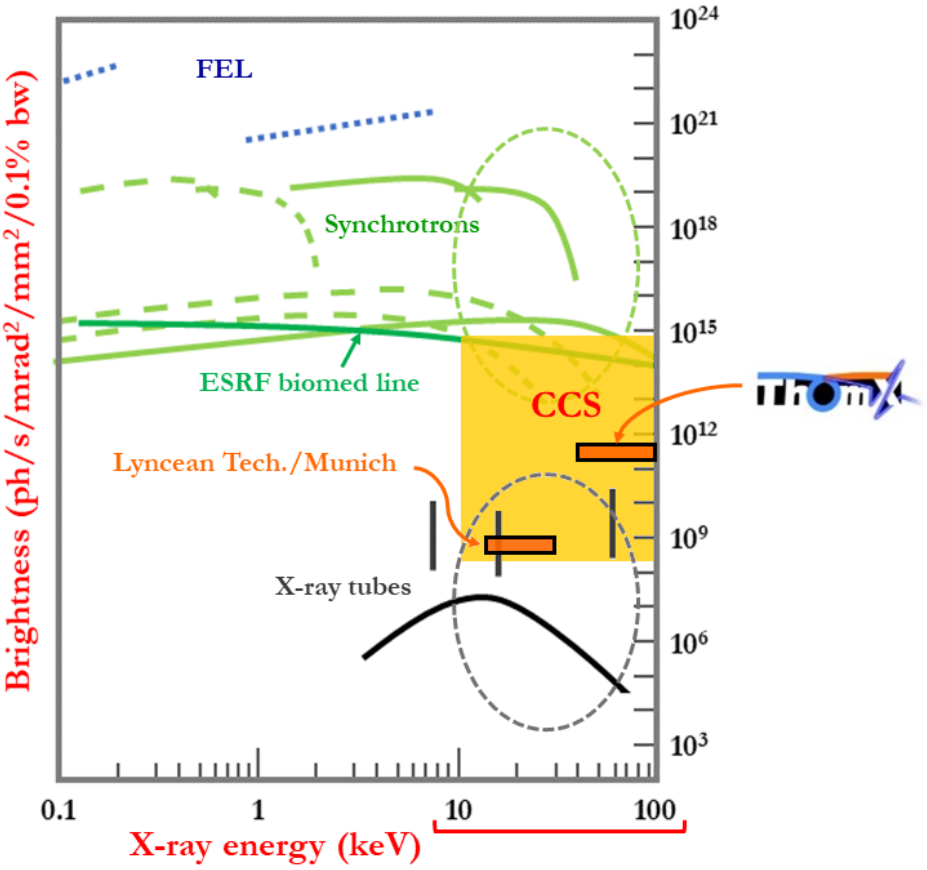

Figure 1.24: Brightness - hence performances - of different X-rays sources against the photon energy, adapted from [28]. The CCS region corresponds to Compact Compton Sources while grey and green ellipse correspond to X-ray tubes and synchrotron accelerators range. FEL mean free electron laser. Vertical lines in the X-ray range correspond, from left to right, to sources using copper, molybdenum and tungsten targets.

For instance, the radio-frequency accelerating structure in both synchrotron and Thomx imposes the X beam to be pulsed - at 17 MHz for ThomX - while the tubes may deliver a continuous beam that might be needed for some experiment. Inversely, tubes cannot deliver quasi-monochromatic light with very high flux while both other sources can. Furthermore, the complexity of the device must be considered. An X-ray tube needs only a high voltage function, while an accelerator like SOLEIL is a complex machine with a Linac, a booster, a storage ring and dozens of light's lines. ThomX is between them, a complex structure but small enough to be replicated in museums, hospitals or laboratories.

Table 1.1: Comparison of three X sources: X tubes, synchrotron (based on SOLEIL) and ThomX. The brightness is expressed in $\mathrm{ph/s/mm^2/mrad^2/0\,1\%BW}$.

	X-ray tubes	**SOLEIL**	**THOMX**
Behaviour	Continuous	Pulse	Pulse
X emission in	All directions	Cones : opening < 1 mrad	Cones : opening ≈ 10 mrad
Brightness	10^4-10^{10}	10^{14}-10^{18}	5×10^{11}
Spectrum	Wide	Wide to monochromatic	quasi-monochromatic
Construction cost	< 10k€	≈300M€	≈10M€
Needed surface	$1\,\mathrm{m^2}$	$30\,000\,\mathrm{m^2}$ for 29 lines	$300\,\mathrm{m^2}$
Nuclear safety requirements	Small	Huge	Medium

The Tab. 1.1 sums up differences in these three kinds of sources. This table shows that those three sources have their own advantages and drawbacks.

To summarise, CCS and synchrotron radiation sources are complementary, and both allow several kinds of measurements impossible with X-ray tubes. Moreover, the large beam size of ThomX permits saving time during analyses of large objects such as a complete masterpiece, liver or dinosaurs' eggs. In this last case, ThomX can detect embryos in the eggs by tomography. If a more precise analysis is needed, ThomX primary results can be used to draw a short list of interesting pieces for synchrotron radiation sources experiments. For patients hardly movable or requiring a specific medical environment, ThomX replica may be installed directly in hospitals.

1.3.2 . Usage of X-rays

Applications of X-rays are plentiful, from simple radiography to studies of proteins evolving during biological's processes. Four applications of X-ray available on ThomX - among others - are presented here.

1.3.2.1 Tomography

A few months after one of the first pieces of evidence of X-rays generated by Crookes tube, the first radiography ever made was realised by Wilhelm Röntgen. Since then, radiography has been shown to be an efficient way to "see-through" opaque matter such as skin, muscles, and clothes, but also concrete or metal with

a strong enough X-ray beam.

But radiography is a 2D projection of a 3D object. If one sees a hole at the centre of an object's radiography, he cannot know if it is a small vacuum hole close to the front, the back or at the centre of it, or even a longer hole with density close to the object. By taking a second radiography after a rotation of 90° of the object, one may discriminate all those cases for simple shapes. The goal of the tomography is precisely that, doing radiography under different angles to reconstruct the inner 3D structure of an object by concatenating all those projections.

An example of tomography using CBS is shown Fig. 1.25. This experiment has been made at Tsinghua University (China) with a laser-plasma accelerator denoted as all-optical inverse Compton scattering source (AOCS) [29].

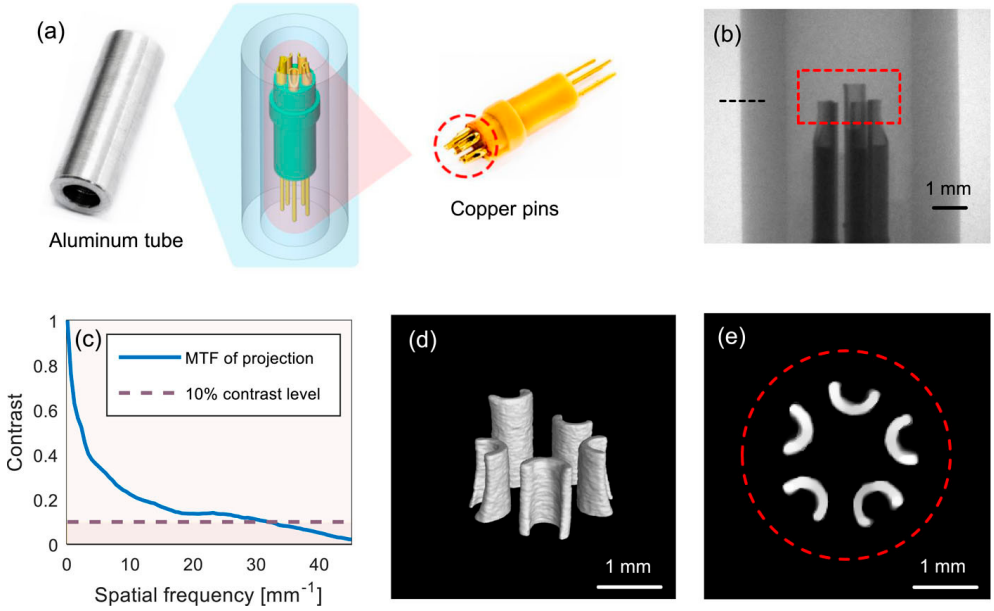

Figure 1.25: AOCS-based region-of-interest (ROI) micro-focus computed tomography (CT) imaging: (a) illustration of test object, with the ROI highlighted by a red dashed circle; (b) 60-shot accumulated projection image; (c) curve of modulation transfer function of tube edge marked by a black dashed line in the projection image (b); (d) three-dimensional reconstructed image within the ROI; (e) one slice of the tomographic image in (d). The ROIs in (b) and (e) are highlighted by a red dashed rectangle and circle, respectively [29].

1.3.2.2 X-ray fluorescence

When a target is illuminated by energetic photons - like X-rays - some atoms may be ionised by expulsing one of their inner electrons. As one of the electronic orbits

is empty, electrons from a higher orbit will complete it. Light is emitted at a specific wavelength - usually in the X-ray range - characteristics of the target's element and the vacant orbit. By identification of the peaks on a spectrum of emitted light, it is possible to find the composition of the target's atoms even for trace elements on a small sample.

This effect is behind the larges peaks often seen on the spectrum of X-ray tubes like the one of Fig. 1.20.

1.3.2.3 K-edge cancer therapy

X-rays may be used in the health domain as in radiotherapy (see section 1.2.6.2).

This method has long since proven its effectiveness, but the risk of killing healthy cells becomes too high in the case of fragmented tumours or fragile tissues. The K-edge cancer therapy [26] may be used to reduce the ratio of energy deposition in tumours cell over energy deposition in the normal tissue.

For that purpose, doctors can inject one heavy element - like gadolinium or iodine - into the tumour and irradiate it using a monochromatic X-ray beam. If the energy of the X-rays is just above the binding energy of the innermost electron shell - known as the K-shell - of the injected element, photons absorption is more likely to happen. As there is more photon absorption, the energy deposition inside the tumour is higher than outside. Hence the dose delivered to the tumour cells is higher than the dose delivered to the healthy cells.

Tumour tissues are more vascularised than normal cells as they need more resources; hence the elements may be introduced through sanguine circulation to simplify the delivery, but direct injection may also be considered.

1.3.2.4 Edge-enhancement radiography

Another possible application of X-ray is edge-enhancement radiography. This method aims to enhance the edge contrast of radiography and improve its sharpness by using phase contrast. Radiography are very efficient in discriminating between two media with large density differences like bones and muscle. Still, when the density is close, as it is between organs, the edge can be hard to visualise. Nevertheless, the medium differences impact the phase of the X-rays. If the coherence of X-rays is good enough at the source, this phase contrast can be measured and permits better edge reconstruction.

This technique has been tested on the Munich Compact Light Source (MuCLS) [30] with success. The comparison between conventional radiography (left) and edge-enhancement radiography (right) are shown Fig. 1.26. One sees the amelioration of the edge contrast in the trachea region (blue arrows) between conventional methods **C)** and enhanced ones **D)**.

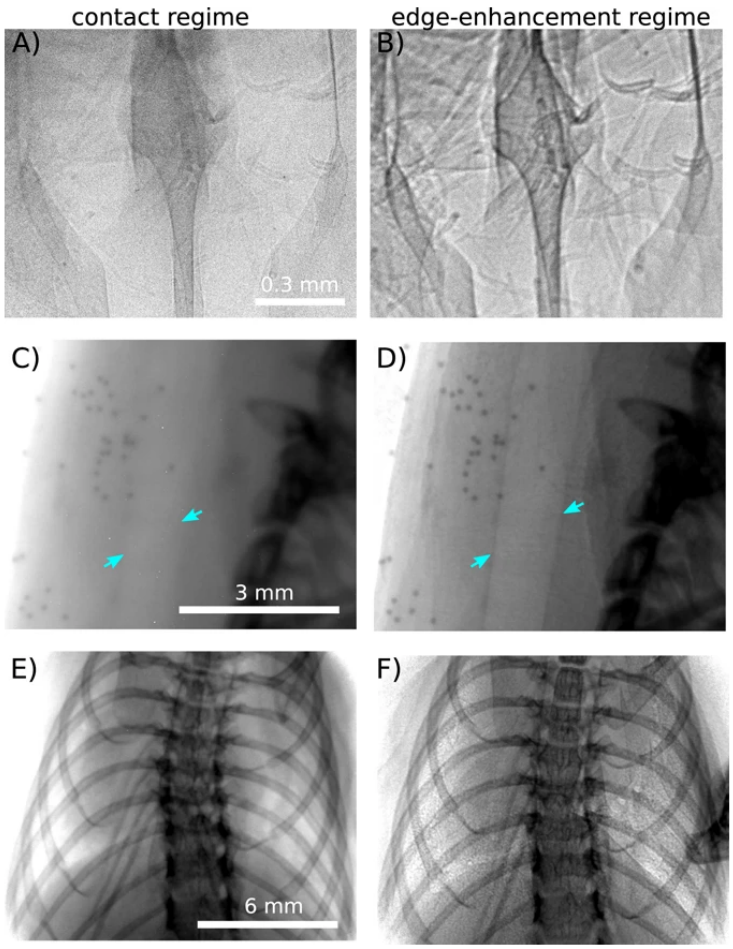

Figure 1.26: The contrast in all three regions of interest is increased by increasing the detector-sample distance to the edge-enhancement regime. A) and B) shows the nasal airways imaged with a detector pixel size of $0.65\,\mu\mathrm{m}$ and exposure time of $180\,\mathrm{s}$. In B) the sample-detector distance is increased to $30\,\mathrm{cm}$. In panels C) and D) the trachea region with a detector pixel size of $6.5\,\mu\mathrm{m}$ and exposure time of $1\,\mathrm{s}$ is shown. The sample-detector distance is $1.5\,\mathrm{m}$ in D). The blue arrows highlight the edges of the trachea. The lungs are displayed in E) and F) with a detector pixel size of $13\,\mu\mathrm{m}$ and exposure time of $1\,\mathrm{s}$. The sample-detector distance is increased to $1.6\,\mathrm{m}$ in F) and is less than $2\,\mathrm{cm}$ for A), C) and E) [30].

1.4 . Conclusion

Since their discovery, X-rays and electrons have been linked by the accelerators. Nowadays, the most common X-rays generators are X-ray tubes based on the same

principle that allowed their discovery, while the most potent sources are synchrotron accelerators. A new kind of device - complementary to synchrotron - begins to appear: compact X-rays sources based on Compton's backscattering effect. ThomX (see section 2) in one prototype of those Compact Compton Sources.

2 - ThomX, a Compton X-ray sources

Contents

ThomX [26] (see Fig. 2.1) is a prototype of Compact Compton Source (CCS) aiming at generating a high X-ray flux using Compton Back Scattering (CBS) effect (see section 2.4.1). The main goal of the ThomX project is to demonstrate the feasibility of creating a small ($300\,m^2$) cheap (about 10M€) machine that delivers a high flux of quasi-monochromatic hard X-rays.

The machine is composed of a 50-MeV-electron accelerator and a high finesse Fabry-Perrot cavity as shown in Fig. 2.2. Such a machine has numerous applications, some of which have been discussed in section 1.3.2. The main accelerator principles have already been described in section 1.2. This chapter focuses on the

properties of the ThomX component. Values and informations come mainly from the technical design report [26] or some internal notes.

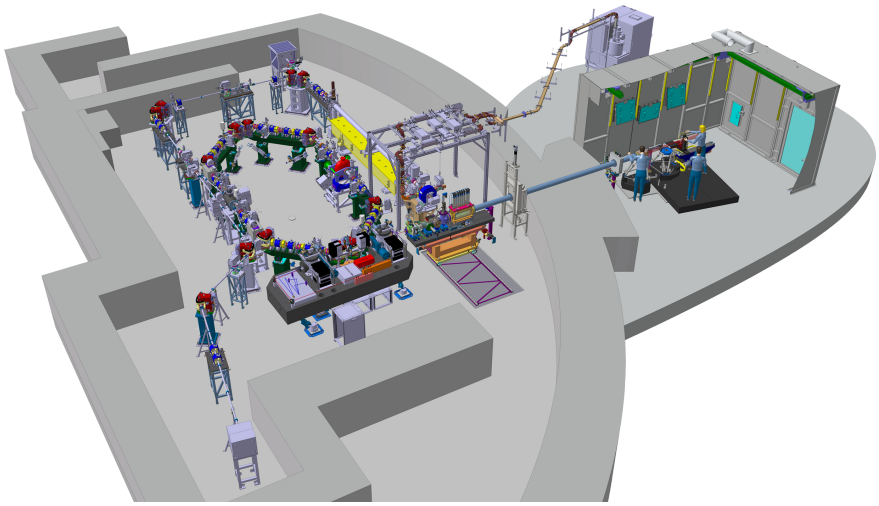

Figure 2.1: Drawing of ThomX accelerator's bunker and X-rays' experimental bunker.

2.1 . ThomX structure

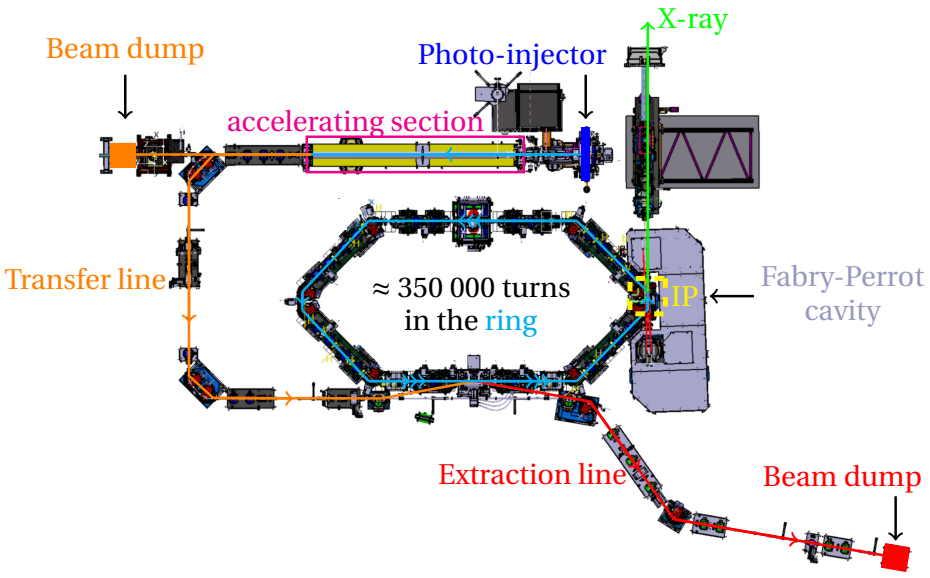

Figure 2.2: Drawing of ThomX seen from above.

ThomX is composed of many elements that may be summarised in 7 main parts highlighted in Fig. 2.2 and summarised here :

- Photo-injector
- Accelerating section
- Transfer line
- Ring
- Optical cavity
- X-ray line
- Extraction line

2.1.1 . Photo-injector

For ThomX, the electron beam source is a photo-injector. It is composed of a copper photo-cathode (PC) illuminated by a laser to initiate the beam extraction by the photoelectric effect (see Fig. 2.3).

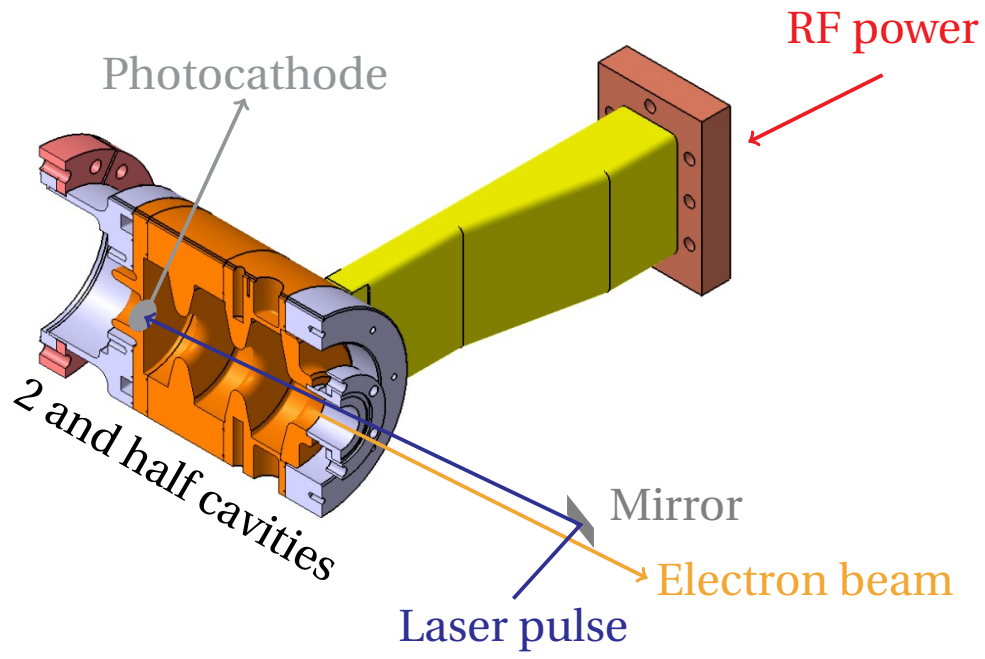

Figure 2.3: Sketch of the photo-injector of ThomX.

The PC laser uses an ytterbium-doped crystal with potassium gadolinium tungstate (Yb:KGW). It is an infrared laser ($1030\,\mathrm{nm}$) converted into UV range ($257\,\mathrm{nm}$) by a frequency quadrupler in an adjacent room. Its characteristics are summarised in Tab. 2.1.

Table 2.1: Characteristics of PC laser.

Wavelength	257 nm
Energy max	100 µJ
Pulse duration	5 ps
Trigger frequency	50 Hz

During the 5 ps illumination, the laser produces many free electrons - called photo-electrons - ready to go away. To start the acceleration of those photo-electrons and extract them from the source, the PC is inside two and a half copper radio frequency (RF) cells. The RF electric field is created by a klystron and delivered through a waveguide to the cavity around the PC. The RF power allows the beam's extraction from the PC with an energy up to 5 MeV. Even without the laser, electrons are extracted by the RF due to the Schottky effect, creating a dark current.

A summary of the properties of the electron source, named electron gun or simply gun, is given in Tab. 2.2.

Table 2.2: Characteristics of the electron gun.

RF frequency	2998.55 Hz
RF power	8 MW
Accelerating gradient	80 $MV m^{-1}$
Electron energy at the exit	5 MeV
Electron beam charge	1 nC
Electron beam length at the exit	5 ps×c
Repetition rate	50 Hz

A small transfer line with several diagnostics can be found just after the gun to characterise the beam. Those elements are described in section 2.2 with the other electron diagnostics of the machine.

2.1.2 . Accelerating section

The last component of the linac is an accelerating section of type "LIL" (LEP Injector Linac) [31] as shown Fig. 2.4. Its characteristics are summarised in Tab. 2.3. As for the RF gun, the section uses RF power delivered by the klystron to fill the cavities with electromagnetic power. The cavity is shaped to maximise the electric field along the beam trajectory. The cavities are grouped in a 4.5-meter-long section in which the RF power travels. The electric field on two by-side cavities is not in phase, but the time needed to go from one cavity to the next equals the phase difference. Hence if the beam enters the first cavity when the electric field is optimum, it will also be true for all following cavities. In summary, if the synchronisation is well done, the beam always fell an optimal accelerating

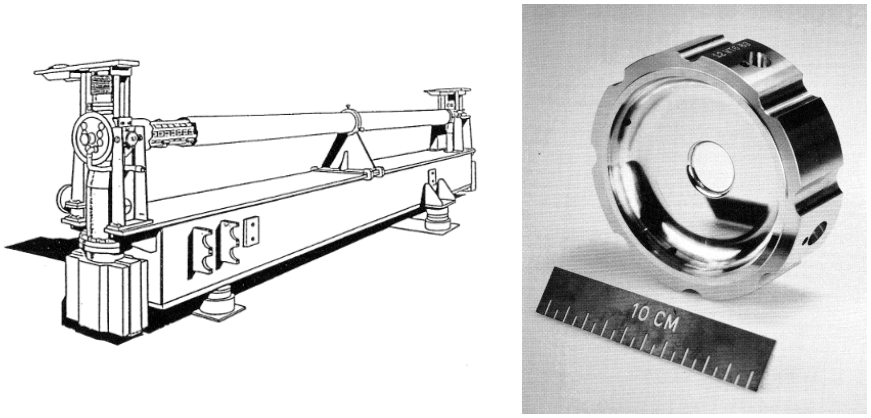

Figure 2.4: Sketch of the LIL section used at ThomX (left) and photo of the unit cell of the LIL accelerating structure (right) [31].

field and may be accelerated with a higher electric gradient than those provided by a static field limited by discharge risk.

Table 2.3: Characteristics of the accelerating section.

RF frequency	$2998.55\,\mathrm{Hz}$
Number of cavities	135
Total length	$4.5\,\mathrm{m}$
Operation mode	$2\pi/3$
Accelerating gradient	$12.5\,\mathrm{MV\,m^{-1}}$
Electron energy at the exit	$50\,\mathrm{MeV}$
Electron bunch length at the exit	$5\,\mathrm{ps}\times\mathrm{c}$
Repetition rate	$50\,\mathrm{Hz}$

2.1.3 . Transfer line

The transfer line (TL) - depicted in orange on Fig. 2.2 - starts at the exit of the accelerating section and is separated into two paths some meters after.

The straight path leads directly to a beam dump used to stop the beam properly during linac commissioning and machine restart. Three quadrupoles after the section are used to focalise the beam.

One $45°$ dipole provides the separation. Electrons go straight to the beam dump if it is off, and are deflected otherwise. A second identical dipole just after permits a $90°$ rotation according to the linac. The dipoles will disperse the beam according to its energy to analyse the energy dispersion. Two metal plates can be mechanically inserted by the side of the beam to cut off off-energy particles. Two other dipoles will recombine the beam and correct the dispersion given by the first pair.

Eventually, the TL ends with a new dipole - named injection dipole - that creates a new fork allowing to go either to the left in the ring or in a straight line to the extraction line and bypass the ring. The bypass will be used to study the beam before the injection in the ring to ensure better matching and avoid beam losses.

2.1.4 . Ring

The ThomX ring - depicted in cyan on Fig. 2.2 - is a very small ring of only $18\,\mathrm{m}$. It is used to store one electron bunch for roughly $350\,000\,\mathrm{turns}$. There is 8 dipoles of $45°$ to permit complete turn, 24 quadrupoles to shapes the beam and focalises it at the interaction point, 12 sextupoles to control the beam dispersion, and a $500\,\mathrm{MHz}$ RF cavity to recovered the energy lost on each turn.

All those elements may have tiny error of position or electromagnetic field that can impact the beam. Because of the number of turns, those error can add up to each other and create an enormous error that may lead to loss of the bunch and sometimes to material damage. To avoid that, the tune of the ring is chosen to be irrational. The tune is a value corresponding to the number of turns needed for a particle to coming back to the same position in the phase space (u,u'). If this number is irrational, one particles is never at the exact same place in the phase space inside a given element which avoid to have the exact same error each N turns. For ThomX ring, the tune is around 3.17 in the horizontal plane and 1.74 in the vertical.

A bunch orbit feedback system exit in the ring. It uses the bunch position measured by the beam position monitor (BPM) and correct it using extra electrodes of some the BPMs (see section 2.2.1).

The last but not the least part of the ring is the injection/extraction devices. It's composed of 3 elements, the septum, the injection kicker and the extraction kicker. Let's concentrate on the injection process first. The electron beam from the TL is deviated by the injection dipole and enters one of the septum's two cavities. In this cavity, a magnetic field corrects the beam trajectory such that the beam is at the centre of the ring's pipe in the injection kicker nearly $1.5\,\mathrm{m}$ after. The kicker is a fast magnetic dipole that will finish the trajectory correction by giving a small kick to the beam. If the injection is done correctly, the beam will continue in the ring, passing the eight $45°$ dipoles of the ring, travel in the second cavity of the septum where there is no magnetic field and come back in the kicker. The bunch is stored if after a certain number of turns the bunch pass the kicker in the same configuration; hence if periodic conditions are obtained.

One may think that only one kicker at the septum localisation may be enough to deflect the beam into the right direction but the magnetic field needed for such a deflection is so strong that the time to pass from the nominal field to 0 is much larger than the $60\,\mathrm{ns}$ needed for the beam to achieve the first ring turn. In this case, the remanent field after one turn would lead to beam loss, whereas with the septum/kicker method, the septum has time to go back to zero because the

beam passes through the field-free cavity. The magnetic field in the kicker is small enough to have a falling time of 50 ns, smaller than the revolution time of the bunch.

For the extraction, the bunch is deflected by the extraction's kicker - symmetric to the injection one according to the septum - and everything appends oppositely. The bunch is deflected and goes into the septum's first cavity, where a magnetic field leads it to the extraction line.

Previous simulations of the bunch propagation into the ring have been made by Illya Drebot [32] and Alexis Gamelin [33].

The extraction is planned to occur after 20 ms. This time is shorter than the damping time - 0.5 s [32] at least - of the beam in the ring. Hence, the beam is always in an undamped mode in the ring and cannot use the stability implied by the damping. A well-matched injection helps minimise the bunch oscillations. Some injection simulations have been made and are presented in section 3.2.3.

Some of the ring's and bunch's characteristics are presented in Tab. 2.4.

Table 2.4: Characteristics of the ring and the electron beam.

Ring length	$L \approx 18\,\mathrm{m}$
Revolution frequency	f = $\frac{c}{L}$ 16.7 MHz
Injection repetition rate	50 Hz
Storage time	20 ms
Transverse damping time	1 s
Longitudinal damping time	0.5 s
Bunch length at the injection (rms)	4 pm
Bunch length at the extraction (rms)	50 pm
Transverse bunch size at IP	σ_e = 70 µm
Bunch charge	1 nC
Kicker/septum pulse reproducibility	$<10^{-3}$

Even if using a ring - and not only a linear section - is adding lots of complexity - and even more with a so small ring and short storage time - the choice has been made to have one on ThomX to increase the beam interaction's frequency, hence the X-rays flux.

2.1.5 . Optical cavity

Thanks to the ring's revolution frequency, the CBS interaction occurs each 60 ns. Still, if only a few X-ray photons were created each time, the emitted flux would be negligible. To increase the number of photons generated at each interaction, the electrons' bunch and photons' beam are focused at the Interaction Point (IP). The photon density is also increased thanks to a Fabry-Perrot cavity (FP) that stores the laser. IP and FP are depicted in yellow and grey on Fig. 2.2.

The simplest FP cavity possible is two mirrors facing each other with one that possibly lets enter some photons. First, one has to deliver a first laser pulse into the cavity. The beam will go to the second mirror and come back. When the first beam is at the mirror location, one may add up a second laser pulse and then a third, a fourth, a fifth, etc. This method permits storing a photon beam and increases its power until the power losses during one turn equal the injection power.

The Optical Cavity (OC) of ThomX is composed of four mirrors that must be precisely positioned and with a high reflectivity surface to avoid as much as possible the losses that reduce the amount of power stored, but the principle is similar to the two mirrors case. The quality of such cavities is represented by a parameter named finesse. With a finesse of $30\,000$, the OC of ThomX is a very high-quality one.

The FP laser used to fill the OC is composed of several stages. The first is a fibre Ti:Sapphire laser that delivers some tenth of mW. The second amplification is done using a fibre laser pumped by three diodes. Other stages are used before and after it to stretch and compress the laser pulse temporally which allow the second amplification. The laser's and FP's characteristics are shown on Tab. 2.5.

Table 2.5: Characteristics of the Fabry-Perrot (FP) laser and the FP optical cavity (OC).

OC finesse	$30\,000$
OC repetition rate	$33.4\,\mathrm{MHz}$ (Twice the ring one)
FP laser wavelenght	$1030\,\mathrm{nm}$
FP laser type	Ti:Sapphire + fibre
Angle between electron and laser trajectory	$2 \times \varphi = 2°$
Transverse beam size at IP	$\sigma_\gamma = 70\,\mu\mathrm{m}$
OC beam energy	$28\,\mathrm{mJ}$

2.1.6 . X-ray line

Once the electron beam is created, shaped and injected into the ring, it encounters the photon beam stored in the FP cavity. Some photons may scatter on electrons and obtain enough energy to become X-ray. Those X-rays photons are emitted backwards, and the more energy they have, the more their trajectory will be closed to the electrons one. In the first dipole after the IP, the electrons rotate, whereas the X-ray photons continue straight and follow the green line on Fig. 2.2 toward the X-ray line.

The X-ray line is composed of two parts. The first one in the accelerator bunker (see Fig. 2.5a) is used to characterise the X-ray beam, and the second one in the experimental room (see Fig. 2.5b) allowing to shape and use of the beam. Between them, a X-rays and radiation shutter made of tungsten and lead allowed entering

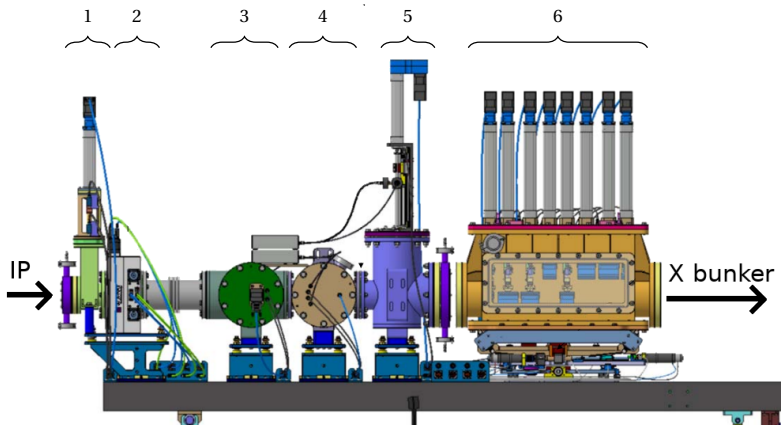

(a) X-ray line in the accelerator bunker. From left to right: 1 X-rays shutter, 2 selection slot, 3 fluorescent screen, 4 Kapton foil, 5 wire detector, and 6 transfocator.

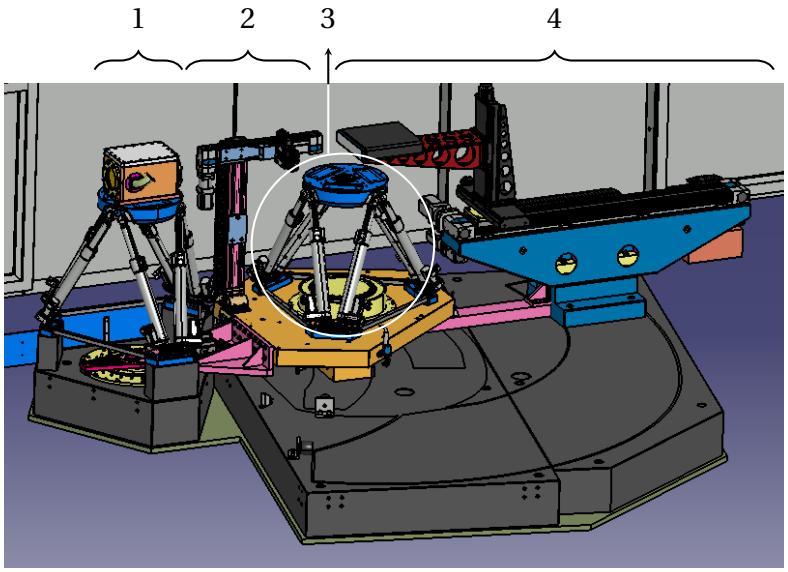

(b) X-ray line in the X-rays experimental room. From left to right: 1 monochromator, 2 selection slot, 3 hexapod, and 4 detectors support.

Figure 2.5: X-ray line of ThomX. The X-rays go from left to right. Most of the propagation is done under vacuum, and Kapton foil is used for the vacuum-air interface. Shutters and slots are made of tungsten.

the experimental room without stopping the accelerator. Tungsten is also used in shutters and selected slices to stop completely or partially the X-rays. Some part of the line is under vacuum, and Kapton foils are used for vacuum-air interface as it is transparent for X-rays.

In the first part of the X-ray line, a fluorescent screen and a camera are used to visualise the transverse shape of the beam. This device degrades the beam

properties, thus it is used only during beam characterisation. Similarly, a Kapton screen is used too. This foil is transparent for the X-rays except for the few impurities that induce the light emission. This method is not as accurate as a fluorescent screen, but the screen can be kept all the time to have a constant record. The wire detector is a second non-destructive diagnostic used to measure horizontal X-ray beam position. This device is made of two vertical metal wires. Some electrons are kicked out if the beam passes close to the wire, which creates a charge displacement. The closer the X-ray beam, the higher the current. Hence by comparing both currents, one may compute the horizontal beam position. The last element of this first part of the line is a kind of lens named the transfocator. It is composed of eight movable pieces of aluminium, allowing either collimation or focalisation of the beam.

The experimental room is composed of a monochromator used to reduce the energy dispersion of X-rays at a few 10^{-3}. A retractable slot allows the selection of desired beam part. The sample can be placed on a hexapod. This device allows to move the sample in all direction and permit controlled rotation for tomography. The monochromator is also on a hexapod to permit the displacement needed for energy selection. Depending on the experiment, several kinds of detectors can be placed around the sample. Both the sample's hexapod and diagnostic support are movable thanks to an air cushion.

2.1.7 . Extraction line

After $20\,\mathrm{ms}$ the beam is sent to the extraction line (EL) - depicted in red on Fig. 2.2 - where it can be stopped into the second beam dump. This line is mainly used for the cleanly stop the beam. Still, some diagnostic allows characterising it after ring propagation and permit some comparison - for example, beam charge - to evaluate the beam losses.

2.2 . Electron diagnostics

The characterisation of the electron beam is essential on an accelerator and even more on a prototype as no one may be sure of what will happen beforehand - and sometimes even after. Several kinds of diagnostics have been installed on ThomX as seen on Fig. 2.6 to acquire as much information as possible. Below, a general review of them is given, while a more detailed presentation and the commissioning of some of them are shown in section 6.

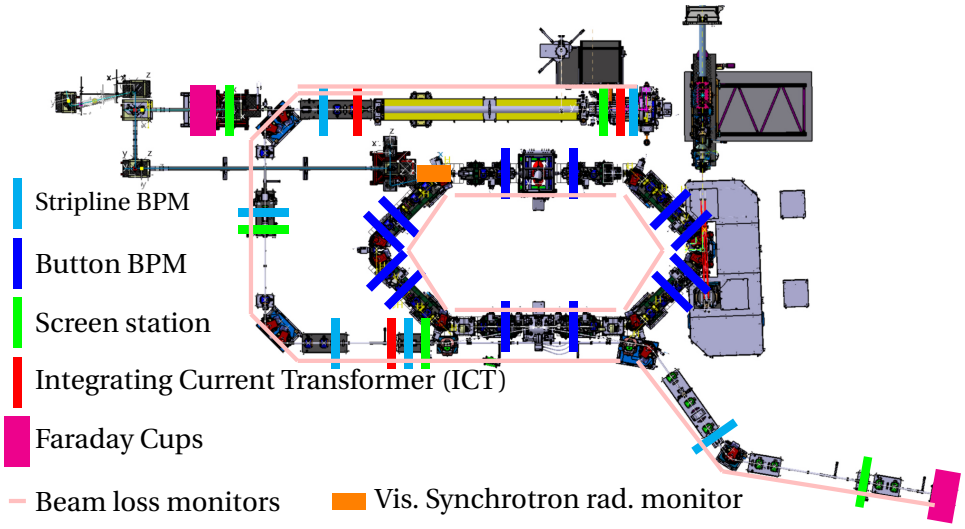

Figure 2.6: Drawing of diagnostics on ThomX sees from above.

2.2.1 . BPM

A Beam Position Monitor (BPM) is a device aimed at measuring the position of the beam's charge barycenter. It comprises four electrodes in which a current is induced by the beam passing nearby. The integral of this current is - in first approximation - proportional to the distance from the beam to each electrode. Hence by comparing them, one may find the beam position.

The BPMs are very common on the accelerator as it is a non-destructive accurate method to measure the beam position. This is why some industrial companies have developed dedicated electronics. ThomX has 5 "Libera Brilliance +" [34] (see Fig. 2.7) developed by "Instrumentation technology" to analyse all the 72 BPMs signals - 4 electrodes per BPM, 18 BPM - and deliver the beam position.

Figure 2.7: Image of one Libera Brillance+ developed by Instrumentation Technologies to acquire signal from four BPM at once [34].

On ThomX, two kinds of BPM may be found.

2.2.1.1 Stripline BPM

Striplines BPM (6 on ThomX) have long electrodes - $10\,\mathrm{cm}$ for the BPM of the linac and $15\,\mathrm{cm}$ for those of the TL (4) and EL (1) - at $90°$ from each other as show Fig. 2.8.

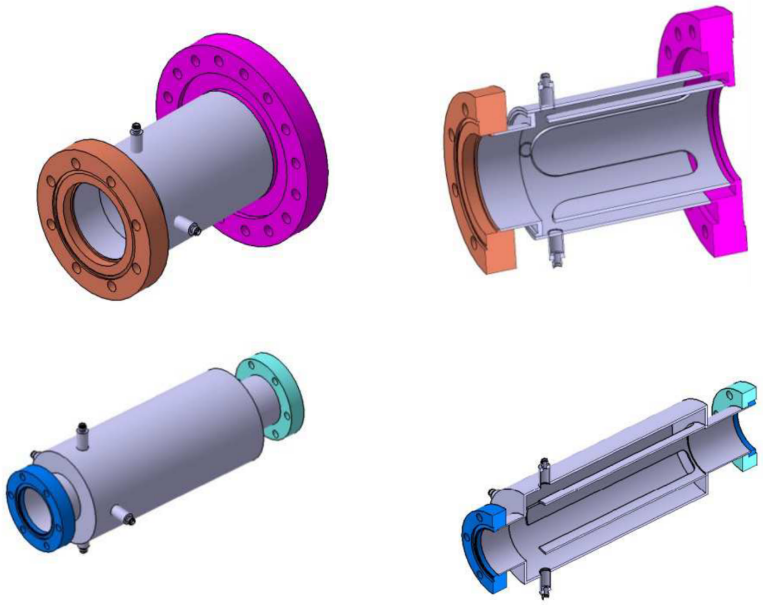

Figure 2.8: Drawing of ThomX stripline BPM. Top the linac one, bottom those of the TL and EL.

The electrode length allows a higher current to be generated, hence a more accurate measurement. Stripline BPMs are better for single pass or low-frequency measurement.

2.2.1.2 Button BPM

For the ring, other kinds of BPM are used. To avoid overlap of several turns, the electrodes must be short and look like a round button. Thus they are called button BPM (see Fig. 2.9). To avoid noise created by synchrotron radiation, the electrodes are usually two side by side, above and below the beam path.

There is 12 button BPM on the ThomX ring, four of them having four additional electrodes for ion cleaning and feedbacks. Those extra electrodes will be connected to high voltage - at most $200\,\mathrm{V}$ - to deflect the ions toward the vacuum chamber that else could shield the beam from the magnetic' elements and perturb it.

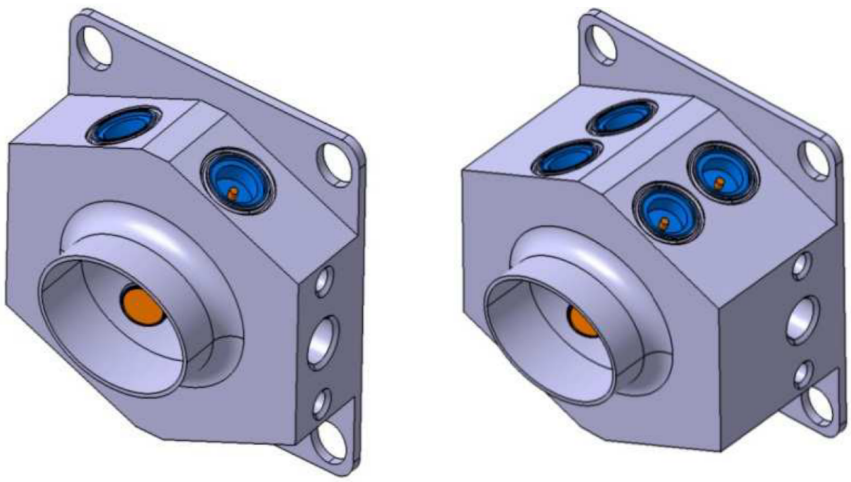

Figure 2.9: Drawing of ThomX button BPM. Left those with four electrodes, right those with four extra electrodes used for ion cleaning.

2.2.2 . Screen station

The screen stations - denoted as SSTs - are intercepting diagnostics composed of scintillator screens that emit light at the passage of the electron beam. A CCD camera is placed below those screens to visualise the emission. On ThomX, there are 5 SSTs located near the RF gun, at the end of the linac, in the transfer line (twice) and in the extraction line (Fig. 2.6). They are used to visualise the beam and measure its transverse profile but can also be used for energy measurement as reported in section 6.2.1.

To ensure ultra-high vacuum (UHV) inside the beam pipe, screens stations are made of a vacuum vessel with a UHV-compatible actuator on which is the mechanical arm with screens as shown on Fig. 2.10.

At least three screens are available on each station. A USAF1951 calibration chart allows measuring the optical system's resolution and magnification. Both Yttrium Aluminum Garnet crystal doped with Cerium [35] - YAG:Ce - and an Optical Transition Radiation - OTR - are used for beam visualisation. The first uses energy deposition by the electron beam and emission of light by atoms deexcitation, while the second uses photon emission because of electromagnetic discontinuity between vacuum and screen. On the station just before the TL beam dump, an additional fourth screen made of sapphire would be used to generate Cherenkov radiation - light emission by particles travelling faster than light in some medium - and allows longitudinal length measurement of the beam using a double-sweep streak camera.

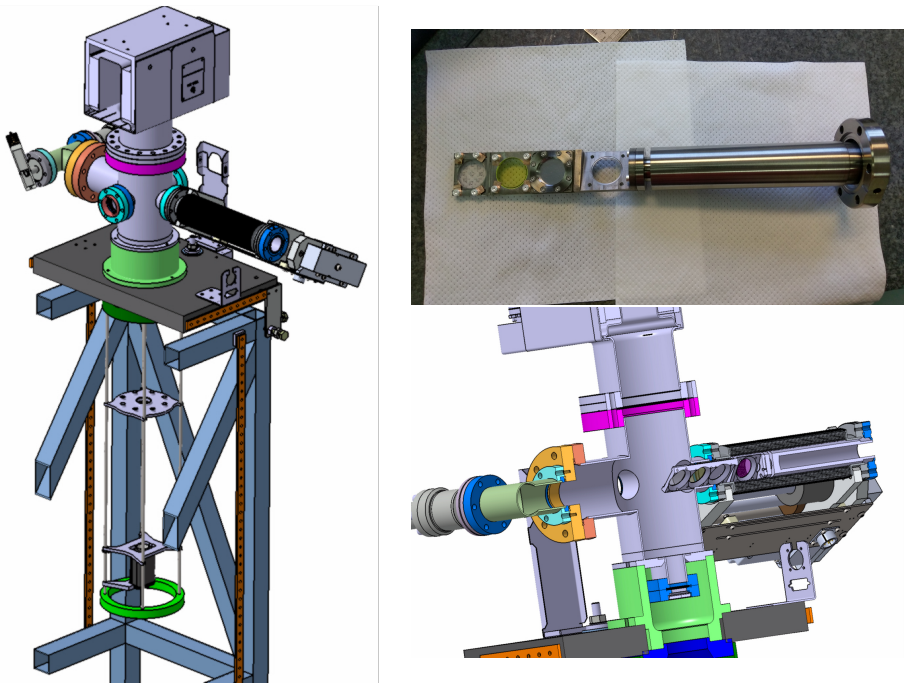

Figure 2.10: Left: CAD 3D view of one of the diagnostic stations. The beam travels from the front left to the back right on the image. The screen is inserted by the motorised UHV-actuator on the right. The observation camera is located below the station. On some stations, such as the one depicted here, a vacuum pump can be inserted on top of the station.
Right: Photo (top) and drawing (bottom) of the screen's mechanical arm. Three to four screens can be inserted via these mechanical arms. In this example, the 4th screen is the Cerenkov screen. It has a slightly different angle to allow Cerenkov light to go upward.

2.2.3 . Synchrotron light

The Synchrotron radiation (see section 1.3.1.2.1) can be used as a diagnostic. Adding a window on the pipe tangential to the beam trajectory in a dipole permits the extraction of the synchrotron radiation's photons. Like with the Cherenkov screen, the photon beam is led to the streak camera in the photocathode laser's room to measure its length corresponding to the electron beam duration. This device will permit checking the beam elongation during propagation in the ring.

2.2.4 . Faraday cup

The Faraday Cup (FC) is basically a graphite block encountered on both beam dumps used to stop the beam. The graphite absorbs the electron, and with an Ammeter between the plate and the ground - $0\,\mathrm{V}$ of the accelerator - one may

measure the beam charge, hence the number of electrons.

A simple piece of graphite won't be enough because of secondary electrons kicked out of the plate by incoming electrons. However, with a more complex device, one may recover all particles and accurately and directly measure the beam current.

The method's main drawback - but sometimes advantage - is that the beam has been stopped. This explains its localisation only in the beam dump on ThomX.

A homemade device called WaveCatcher - see section 2.3.3 - is used to measure FC's current.

2.2.5 . Integrating current transformer

Another way to measure the beam's current - hence beam charge - is to have a coil around the beam trajectory. When the beam passes through it, an inductive current is generated proportional to the beam one. With appropriate calibration, one may deduce beam charge from coil current. This device is named Integrative Current Transformer or ICT.

WaveCatchers - see section 2.3.3 - are also used to measure ICT's currents.

2.2.6 . Beam loss monitor

The Beam Loss Monitor (BLM) are optical fibre along the beam pipe linked to a photo-detector. When electron losses occur in the accelerator, they generate some secondary electrons in the pipe wall, which can cross it. Suppose those electrons travel through the fibre and have enough energy, they will emit some light by Cherenkov radiation - light emitted by particles travelling at speed higher than the speed of light in the medium.

The travel time needed for the light to go to the detector depends on where the losses occur. Hence it is possible to reconstruct the localisation of the losses with this method.

The photo-detector emits a current reading by WaveCatchers - see section 2.3.3.

2.3 . Accelerator control

2.3.1 . Synchronisation

Within ThomX, an heterodyne synchronisation is done between the linac $3\,\mathrm{GHz}$ HF and the ring $500\,\mathrm{MHz}$ RF. Mixing and comparison of those frequencies and their sub harmonics as PC laser oscillator or RF system frequencies, allow generating a unique trigger, which is synchronised with the $50\,\mathrm{Hz}$ general power supply. This trigger achieves a pico-second level synchronisation between the linac $3\,\mathrm{GHz}$ HF and the ring $500\,\mathrm{MHz}$ RF.

This trigger is then split in four $50\,\mathrm{Hz}$ sub-harmonic - depending on the needs - each passes to one of the four delay generators. Those generators generate many trigger signals that can be delayed separately according to the main one. Delays are essential to ensure that each system receives its trigger at the right time. For

instance, the BPM in the linac and the one in the extraction line could not be trigged simultaneously as there is 20 ms between beam passage into them, but they have a much shorter acquisition time.

A $100\,\mathrm{ps}$ jitters is achieved between each trigger and the PC laser pulse.

2.3.2 . Acquisition system and remote control

For all those diagnostics, some data are generated. One has to recover them to allow analysis after hand. It is the meaning - amount others think - of the acquisition system.

Each piece of equipment of ThomX comes with its own electronic and ways to exchange information. For example, two different kinds of cameras do not need the same signal to set the exposure time.

To normalise the command used, a layer of software converts the specific language of each piece of equipment into one common language. On ThomX, the choice was made to use the Tango software [36] that uses some Device Servers (DS) to do the bridge.

Some other levels can be added over Tango to create convenient interfaces. One of those levels is the application Jive [37]. It is a Java code that allows one to access every property of each device. All the accelerator could be controlled from its "ATKPanel" - the name of the panel of one specific device. The number of DS and properties require a good understanding and knowledge of the equipment and the ThomX nomenclature.

To efficiently operate ThomX, some GUI - Graphical User Interface - has been developed in Python and MatLab. Those interfaces may allow non-experts to do complex tasks by only clicking one button. I have developed several GUI that allow controlling the SST stations, the BPM or even the devices themselves.

For instance, one interface allows one to know the state of the complete machine by exchanging with all devices and summarizing everything into one value. If the value is OK, then everything works. Else there is some devices' error that has to be corrected. The GUI allows finding those devices, may give a usual solution if those are tabulated and provide access to the ATKPanel and server controller to investigate further.

There is also a device server to ensure data measurement synchronisation and avoid comparing data coming from two different bunches.

2.3.3 . WaveCatcher

On ThomX, three diagnostics (ICT, FC, BLM) use homemade modules named WaveCatcher [38] (WAC) to measure charges. WAC are $50\,\Omega$ voltage samplers with a 12 bits analogical ADC running at a $3.2\,\mathrm{GHz}$ sampling frequency with a 1024 points memory depth. There are three WAC modules with eight channels each for measurement. Each WAC module has its own trigger and trigger delay, but the eight channels of a module share the same one. hence, the diagnostics outputs should be dispatched such that all signals are within the $0.32\,\mu\mathrm{s}$ window

of its WAC. Each channel have a electrical noise of $0.7\,\mathrm{mV}$ effective.

2.4 . X-rays production with ThomX

2.4.1 . Compton Back-Scattering effect

The Compton BackScattering effect (CBS) refers to a momentum transfer from an electron to a photon.

CBS is the most efficient photon energy amplifier [26] with a maximum energy of the scattered photon given by Eq. (2.1).

$$E_{CBSmax} = 4\gamma^2 \times E_i = 4\left(\frac{E_e}{m_e c^2}\right)^2 \times E_i \tag{2.1}$$

Where E_{CBSmax} is the maximal energy of the photon generated by CBS, γ is the Lorentz factor, E_e is the electron's energy, m_e is the electron's mass, and E_i is the energy of the incoming photon [26].

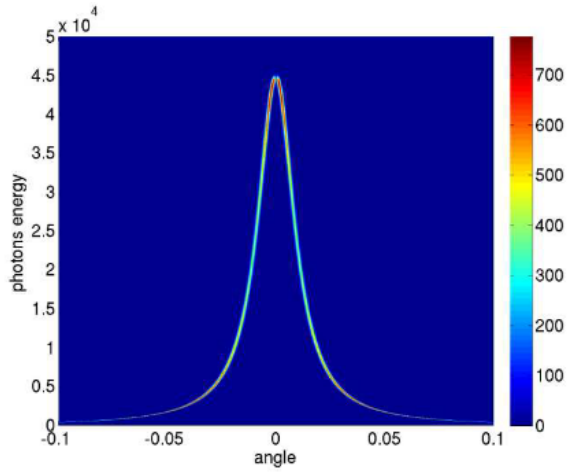

Figure 2.11: X-ray intensity as a function of the emission angle in mrad (horizontal axis) and their energy in eV (vertical axis). The colour bar indicates the number of X-ray photons [26].

This maximal energy corresponds to the photons that are scattered backwards and follow the same trajectories as the electrons ($\theta = 0$ in Fig. 2.12). The closer is the photon trajectory to the electron one, the higher is the photon energy. Hence the CBS emission corresponds - in the direction of electrons - to a cone emission with maximal energy at the centre and an energy diminution as the radius increase, as shown Fig. 2.11.

On ThomX, the electron energy is $50\,\mathrm{MeV}$, and the incoming photon has a wavelength of $1030\,\mathrm{nm}$ which means an energy of $1.2\,\mathrm{eV}$. Hence the maximal energy of the photon created by CBS is $E_{CBS} = 4 \times \left(\frac{50\,\mathrm{MeV}}{511\,\mathrm{keV}}\right)^2 \times 1.2\,\mathrm{eV} = 46\,\mathrm{keV}$ which

correspond to hard X-rays. A project of potential upgrades for ThomX plans to increase the electron energy to 70 MeV which would allow reaching 90 keV X-ray.

To evaluate - at first order - the flux of x-photon - N_x - produced per second, one can use Eq. (2.2) given in the ThomX TDR [26].

$$N_x = \frac{\sigma_{th} N_e N_\gamma f \frac{\cos\varphi}{2\pi}}{\sqrt{\sigma_{y,e}^2 + \sigma_{y,\gamma}^2}\sqrt{(\sigma_{x,e}^2 + \sigma_{x,\gamma}^2)\cos^2\varphi + (\sigma_{z,e}^2 + \sigma_{z,\gamma}^2)\sin^2\varphi}} \tag{2.2}$$

Where N_x is the flux of X-ray photon generated per second, $\sigma_{th} = 6.65 \times 10^{-29}\,\mathrm{m}^2$ is the Thomson cross section, N_e (N_γ) is the number of electrons (photons) per beam, f is the electron bunch revolution frequency, φ is half the collision angle, $\sigma_{u,v}$ are respectively the tree dimensional bunch rms sizes - represented by u = x,y or z - of the electron (v = e) or the laser pulse (v = γ). The nominal values of those parameters are summarised in Tab. 2.6.

Table 2.6: Electron bunch and photon beam's propeties at the interaction point (IP, see Fig. 2.12)

Thomson cross section	σ_{th}	$6.65 \times 10^{-29}\,\mathrm{m}^2$
Electron bunch charge	Q_e	1 nC
Number of electron	$N_e = \frac{Q_e}{e}$	6.2×10^9
Photon beam energy	E_γ	28 mJ
Number of photon	$N_\gamma = \frac{E_\gamma}{E_{\text{one }\gamma}}$	1.5×10^{17}
Electron bunch revolution frequency	f	16.7 MHz
Half collision angle	φ=$\alpha/2$	1°
Transverse RMS electron bunch size	$\sigma_{x,e}$, $\sigma_{y,e}$	70 µm
Longitudinal RMS electron bunch size	$\sigma_{z,e}$	$4 - 50\,\mathrm{ps} \times \mathrm{c}$
Transverse RMS photon beam size	$\sigma_{x,\gamma}$, $\sigma_{y,\gamma}$	70 µm
Longitudinal RMS photon bunch size	$\sigma_{z,\gamma}$	$10\,\mathrm{ps} \times \mathrm{c}$
X-ray flux	N_x	3.2×10^{11}-1.5×10^{12} ph/s

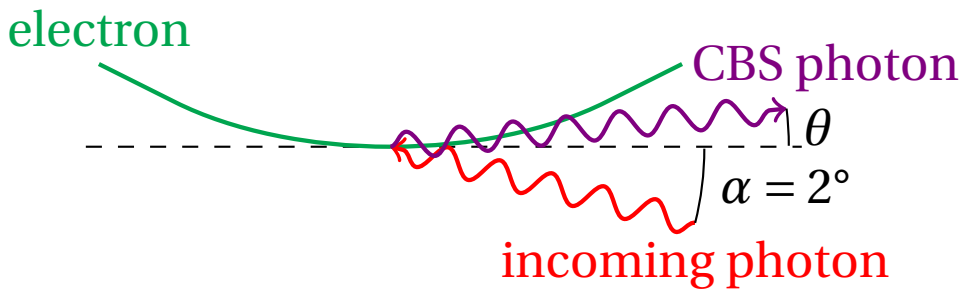

Figure 2.12: Schematic of Compton back-scattering collision at the interaction point.

2.5 . ThomX challenges

The ThomX project expects to generate a high flux of X-rays. For that purpose, two mains challenge as to be achieved. First, the $18\,\mathrm{m}$ long ring needs a high-speed injection system and cannot use the damping effect to stabilise the beam as damping time is larger than storing time. The second main challenge is the high finesse Fabry-Perrot (FP) cavity. To increase the number of photons stored in this device, one has to decrease the loss of photons by using mirrors as reflecting as possible. The property used to characterise the photon's lifetime inside the FP cavity is the finesse, and the ThomX FP cavity has a very high finesse (30000).

An estimation of X-ray generated by CBS is given by Eq. (2.2). It gives a flux around $10^{12}\,\mathrm{photon/s}$ but some correction - like electron bunch elongation - must be applied to accurately estimate the X-ray flux.

For instance, studies done by Illya Debrot [32] on early ThomX ring design and parameters show that CBS and intra-beam scattering (IBS) - a collective effect corresponding to the collision of electrons within the bunch - impact the flux of scattered photon. At the extraction - after $20\,\mathrm{ms}$ - $20\,\%$ less scattering occurred as one may see on Fig. 2.13.

Realistic simulation give a flux up to $7.8 \times 10^{12}\,\mathrm{photons/s}$ in nominal conditions.

The X-ray beam has a considerable divergence. Hence, even if it is emitted from a source of $70\,\mu\mathrm{m}$, its diameter is around $10\,\mathrm{cm}$ in the experimental room which allows keeping illumination of large samples at once.

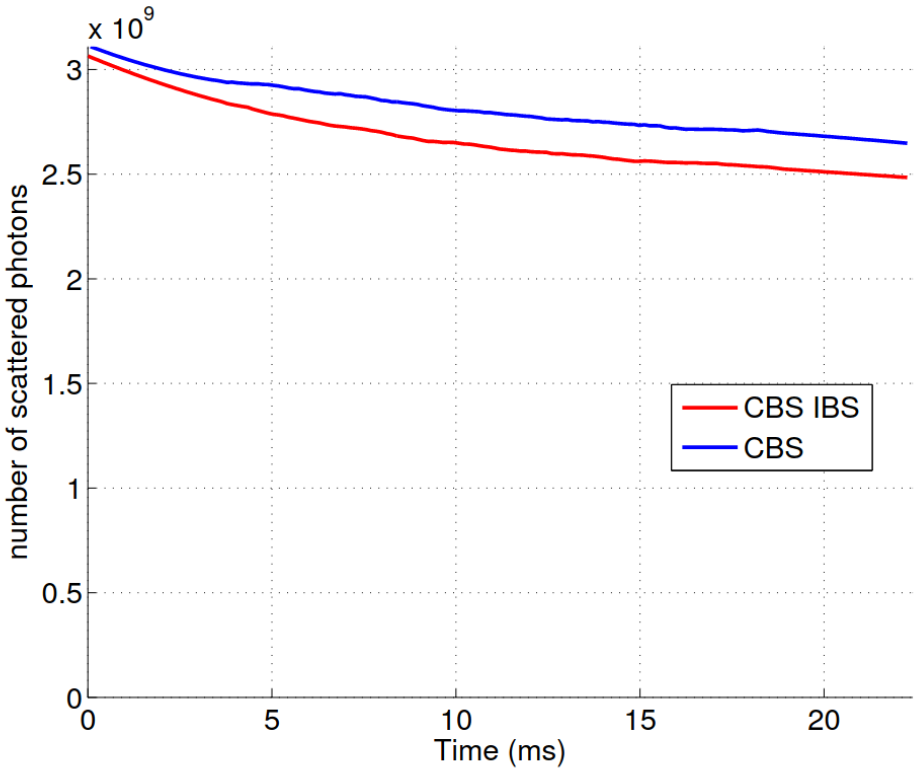

Figure 2.13: Evolution of the number of scattered photons during beam propagation into the ring. CBS: Compton BackScattering. IBS: Intra-Beam Scattering, a collective effect increasing the beam length because of intern collision between electrons. ([32]).

3 - Simulations

Contents

An accelerator is a complex machine that involves many different phenomena. To approach as much as possible the understanding of ThomX before commissioning, the behaviour of the beam has been simulated. This chapter presents the formalism used for particles representation and propagation within an accelerator (section 3.1) and simulations of ThomX done either using MadX (section 3.2) - a code developed by the CERN - or a homemade code (section 3.3) using the linear transfer matrix formalism.

3.1 . Generality

3.1.1 . Coordinates

A coordinate system must be created to localise a particle in the accelerator. A convenient way is to use a frame that follows the beam. Like that particle's positions are always of the order of beam size, even far away from the source. For that purpose, let's consider a mobile Cartesian frame attached to a hypothetical ideal particle - called reference particle - that follows the beam at the reference's speed, hence the particle's velocity at the nominal energy. This ideal particle propagates on the perfect path - an arc of a circle inside a dipole and straight outside them - onto the ideal machine. This perfect path is called $\vec{s}$ and defined the reference frame shown in Fig. 3.1 such that :

- $\vec{s}$ is the longitudinal axis of the reference frame

  - s > 0 : particles ahead of the reference
  - s < 0 : particles behind the reference

- $\vec{x}$ and $\vec{y}$ are transverses axis of the reference frame
  - $\vec{x}$ is horizontal, positive to the left when one looks downstream
  - $\vec{y}$ is vertical, positive to the up direction

- The ideal particles is always at (0,0,0)

- $\vec{z}$ is tangent to s at (0,0,0)
  - outside dipoles $\vec{z} = \vec{s}$

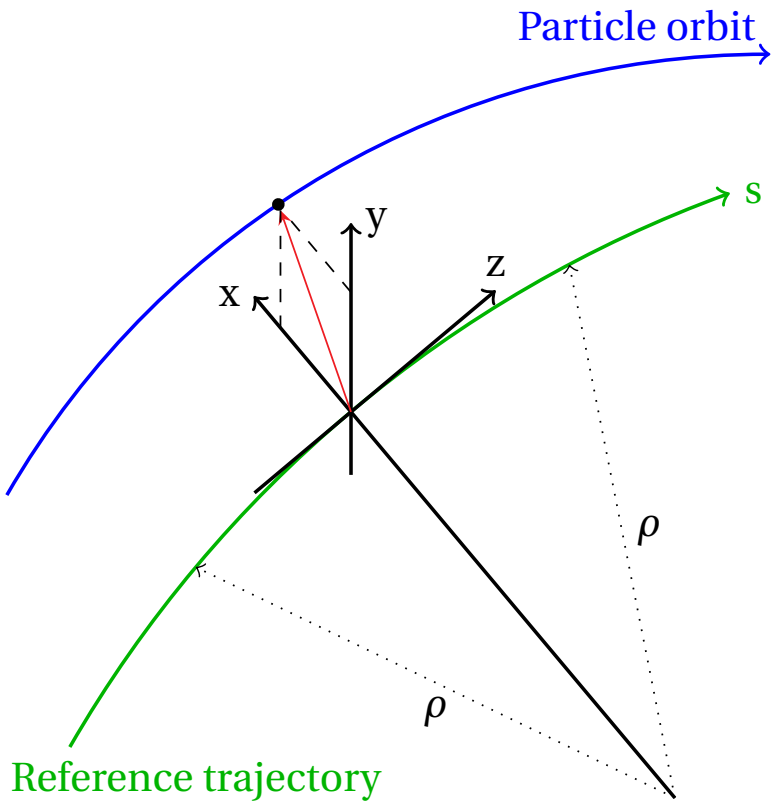

Figure 3.1: Sketch of the coordinate system used for positioning of particles within a bunch.

Those conventions will be used in this document if nothing else is defined.

3.1.2 . Linear transfer matrix calculation

3.1.2.1 Principle over drift space

Let's assume a classical particle travelling into the (z,y) plane in free space. The particle will follow a linear trajectory as no forces deflect it, as Fig. 3.2 shows.

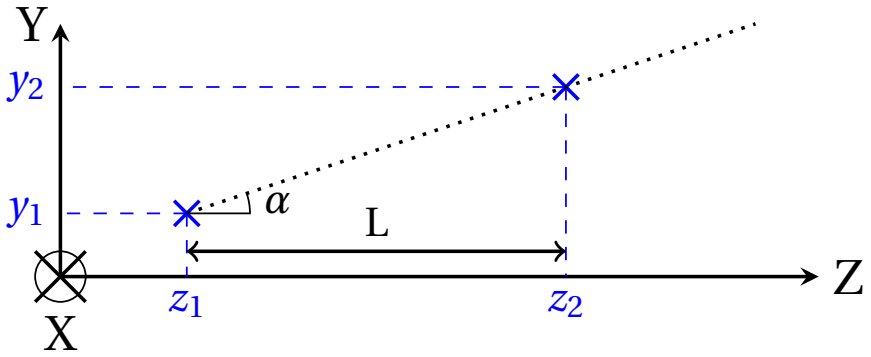

Figure 3.2: Propagation of a particle in a drift space of length L.

By knowing the transverse's particle position y_1 at the beginning and the angle α between the particle's trajectory and the $\vec{z}$ axis one may compute the position y_2 of the particle after a drift L along $\vec{z}$ axis. This position is given by the Eq. (3.1):

$$y_2 = y_1 + L \times \tan\alpha \tag{3.1}$$

For small α, one may linearise this equation by assuming $\tan\alpha \approx \alpha$. This approximation is called the paraxial approximation and is usually valid at accelerators where most angles are usually of a few mrad at most. As α is constant all along the trajectory, one may also write $\alpha_2 = \alpha_1$. Those 2 observations lead to a system of 2 linear equation that may be written using matrix formalism as follow :

$$\begin{pmatrix} y_2 \\ \alpha_2 \end{pmatrix} = \begin{pmatrix} 1 & L \\ 0 & 1 \end{pmatrix} \times \begin{pmatrix} y_1 \\ \alpha_1 \end{pmatrix} \tag{3.2}$$

The α angle may be linked to the particle property by noticing that :

$$\alpha \approx \tan\alpha = \frac{dy}{dz} = y' \tag{3.3}$$

Also :

$$\frac{dy}{dz} = \frac{dy/dt}{dz/dt} = \frac{p_y}{p_z} \tag{3.4}$$

And under paraxial approximation, $p_z >> p_y$, hence:

$$p = \sqrt{p_y^2 + p_z^2} = |p_z| \times \sqrt{1 + \frac{p_y^2}{p_z^2}} \approx |p_z| \tag{3.5}$$

By combining Eq. (3.3), Eq. (3.4) and Eq. (3.5), with appropriate assumptions, one may write :

$$\alpha \approx y' \approx \frac{p_y}{p} \tag{3.6}$$

Hence, one has :

$$\begin{pmatrix} y_2 \\ y_2' \end{pmatrix} = \begin{pmatrix} 1 & L \\ 0 & 1 \end{pmatrix} \times \begin{pmatrix} y_1 \\ y_1' \end{pmatrix} \tag{3.7}$$

This formalism - named linear transfer matrix formalism - is a convenient way to represent propagation into some devices as one only needs to know the initial position and direction of a particle and the transfer matrix of the section after to be able to compute - at the first order - the position of the particle after the device.

Similar reasoning may be done in the (z,x) plane and leads to similar results for $\begin{pmatrix} x \\ x' \end{pmatrix}$ propagation.

Several conventions may be used for the $\vec{z}$ axis's propagation. Let's use the convention of Trace3D [39] - a program created by the Los Alamos National Laboratory (University of California, U.S.A) to compute beam-dynamics - that provides all the transfer matrix used in section 3.3. The two coordinates used to characterise the propagation along $\vec{z}$ axis are z and $\frac{\Delta p}{p}$ where z is the relative position according to the position of the reference particle, and $\frac{\Delta p}{p}$ is the relative momentum of the particle according to the reference one, p.

As no reason exists for momentum to be modified in free space, one may write the Eq. (3.8):

$$\frac{\Delta p_2}{p} = \frac{\Delta p_1}{p} \tag{3.8}$$

For the z equation, special care must be taken with the movement of the reference frame. Let's call Ref_1 (Ref_2) the reference frame when the particle is at position 1 (2). By definition of L, one has $z_2|_{Ref_1} = z_1|_{Ref_1} + L$ but the equation needed is $z_2|_{Ref_2} = f(z_1|_{Ref_1})$, hence a change of frame must be done.

If v is the velocity of the referential particle, the change of frame correspond to a shift of $\vec{z}$ axis by a factor $R_{1\to2} = v \times t_{1\to2}$. The time of propagation may be expressed as function of L as, by convention, $L = v_{part} \times t_{1\to2}$ with v_{part} the velocity of the particle considered. Hence, the change of frame may be written $z_2|_{Ref2} = z_2|_{Ref1} + L \times \frac{v}{v_{part}}$ By substitution into $z_2|_{Ref1} = z_1|_{Ref1} + L$ one finds the following equation (Eq. (3.9)) :

$$z_2|_{Ref2} = z_1|_{Ref1} + L \times \frac{v_{part} - v}{v_{part}} \approx z_1|_{Ref1} + L \times \frac{\Delta v}{v} \tag{3.9}$$

The approximation $v \approx v_{part}$ comes from the assumption that the particle has a velocity close to the reference one.

One last step needs to be done, convert $\frac{\Delta v}{v}$ into $\frac{\Delta p}{p}$. Let's first compute $\frac{dp}{dv}$:

$$\frac{dp}{dv} = \frac{d}{dv}(\gamma m v) = \frac{d}{dv}\left(\frac{mv}{\sqrt{1-\left(\frac{v}{c}\right)^2}}\right) = \gamma^2 \times \frac{p}{v} \tag{3.10}$$

Hence, by integrating the Eq. (3.10) one finds that :

$$\frac{\Delta p}{p} = \gamma^2 \times \frac{\Delta v}{v} \tag{3.11}$$

Which leads to the Eq. (3.12) :

$$z_2|_{Ref2} = z_f|_{Ref1} + \frac{L}{\gamma^2} \times \frac{\Delta p}{p} \tag{3.12}$$

By identification with Eq. (3.12) and Eq. (3.8) one finds the matrix system Eq. (3.13) :

$$\begin{pmatrix} z_2 \\ \frac{\Delta p_2}{p} \end{pmatrix} = \begin{pmatrix} 1 & L/\gamma^2 \\ 0 & 1 \end{pmatrix} \times \begin{pmatrix} z_1 \\ \frac{\Delta p_1}{p} \end{pmatrix} \tag{3.13}$$

Eventually, one may summarise the particle behaviour into the full space in one 6 by 6 matrix as follow :

$$\begin{pmatrix} x_2 \\ x_2' \\ y_2 \\ y_2' \\ z_2 \\ \frac{\Delta p_2}{p} \end{pmatrix} = \begin{pmatrix} 1 & L & 0 & 0 & 0 & 0 \\ 0 & 1 & 0 & 0 & 0 & 0 \\ 0 & 0 & 1 & L & 0 & 0 \\ 0 & 0 & 0 & 1 & 0 & 0 \\ 0 & 0 & 0 & 0 & 1 & L/\gamma^2 \\ 0 & 0 & 0 & 0 & 0 & 1 \end{pmatrix} \times \begin{pmatrix} x_1 \\ x_1' \\ y_1 \\ y_1' \\ z_1 \\ \frac{\Delta p_1}{p} \end{pmatrix} \tag{3.14}$$

The zero elements added to complete the matrix denotes the independence of the 3 planes (x, x'), (y, y') and $(z, \frac{\Delta p_1}{p})$.

Similar reasoning may be done for other accelerator's elements.

3.1.2.2 Classical transfer matrix

In generality, the transfer matrix into the 6D phase space may be written as follow :

$$M = \begin{pmatrix} R_{xx} & R_{xy} & R_{xz} \\ R_{yx} & R_{yy} & R_{yzx} \\ R_{zx} & R_{zy} & R_{zz} \end{pmatrix} \tag{3.15}$$

Where R_{uv} is a 2-by-2 transfer matrix in plane (u, v).

As seen above, most elements are null in transfer matrices. In this section, only the non-zero components of the classical accelerator's elements based on Trace3D documentation [39] are given.

3.1.2.2.1 Drift space

Parameters :

- L : the length of the drift

$$R_{xx} = \begin{pmatrix} 1 & L \\ 0 & 1 \end{pmatrix} = R_{yy} \tag{3.16}$$

$$R_{zz} = \begin{pmatrix} 1 & \frac{L}{\gamma^2} \\ 0 & 1 \end{pmatrix} \tag{3.17}$$

Where γ is the Lorentz factor.

Another kind of elements use the same matrix: Markers. The goal of those element is to compute at some specific location the particles position to allow comparison between simulation and measurement or to impose some physical constraints on the particles. Marker are often used for diagnostics as they do not impact particles in simulations.

If one want to compute the particle properties at the centre of the marker, the drift matrix must be splited in two half ones.

3.1.2.2.2 Quadrupoles

Parameters :

- L : the length of the quadrupole
- $|k|$: the magnetic strength of the quadrupole

For positive k :

→ $F = \begin{pmatrix} \cos(\sqrt{k} \times L) & \frac{1}{\sqrt{k}} \sin(\sqrt{k} \times L) \\ -\sqrt{k} \times \sin(\sqrt{k} \times L) & \cos(\sqrt{k} \times L) \end{pmatrix}$: matrix in the transverse focusing plane

→ $D = \begin{pmatrix} \cosh(\sqrt{k} \times L) & \frac{1}{\sqrt{k}} \sinh(\sqrt{k} \times L) \\ \sqrt{k} \times \sinh(\sqrt{k} \times L) & \cosh(\sqrt{k} \times L) \end{pmatrix}$: matrix in the transverse defocusing plane

By considering that $\sqrt{-1} = i$, one may notice that :

$$D(-k, L) = F(k, L) \tag{3.18}$$

Hence, with special care on the sign of k - positive k for a focalisation in x plane -, one may write :

$$R_{xx} = F(k, L) \tag{3.19}$$

$$R_{yy} = D(k, L) = F(-k, L) \tag{3.20}$$

$$R_{zz} = \begin{pmatrix} 1 & \frac{L}{\gamma^2} \\ 0 & 1 \end{pmatrix} \tag{3.21}$$

3.1.2.2.3 Horizontal bending magnet without edges

Parameters :

- Δs : the magnetic length of the dipole
- α : the angle of deflection
- $\rho = \frac{\Delta s}{\alpha}$: the radius of curvature
- $n = -\left[\frac{\rho}{B_y}\frac{\partial B_y}{\partial x}\right]_{x=0,y=0}$: magnetic field index
- $h = \frac{1}{\rho}$
- $k_x = \sqrt{(1-n)h^2}$
- $C_x = \cos(k_x * \Delta s)$
- $S_x = \sin(k_x * \delta s)$
- $k_y = \sqrt{nh^2}$
- $C_y = \cos(k_y * \Delta s)$
- $S_y = \sin(k_y * \Delta s)$

$$R_{xx} = \begin{pmatrix} C_x & \frac{S_x}{k_x} \\ -k_x \times S_x & C_x \end{pmatrix} \tag{3.22}$$

$$R_{yy} = \begin{pmatrix} C_y & \frac{S_y}{k_y} \\ -k_y \times S_y & C_y \end{pmatrix} = \begin{pmatrix} 1 & \Delta s \\ 0 & 1 \end{pmatrix} \tag{3.23}$$

Let's suppose that the magnetic field is uniform along x, hence that $\frac{\partial B_y}{\partial x} = 0 = n$ Under this assumption, one may compute $\frac{S_y}{k_y} = \lim_{x\to 0}\left(\frac{\sin(x\Delta s)}{x}\right) = \Delta s$. We find back the matrix R_{yy} of a drift of length Δs hence the assumption corresponds to ignore the effect of the dipole toward the $\overrightarrow{y}$ axis.

$$R_{zz} = \begin{pmatrix} 1 & \frac{-k_x \Delta s \beta^2 + S_x}{\rho^2 k_x^3} + \frac{\Delta s}{\gamma^2}\left(1 - \frac{1}{\rho^2 k_x^2}\right) \\ 0 & 1 \end{pmatrix} \tag{3.24}$$

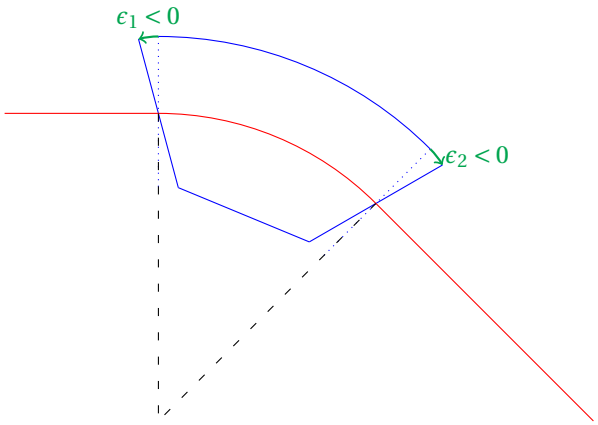

Figure 3.3: Definition and convention of the bending magnet's edges at the entrance and the exit of them. Blue dotted lines correspond to the 0 edges case. Black dashed lines symbolise the curvature radius.

$$R_{xz} = \begin{pmatrix} 0 & \frac{h(1-C_x)}{k_x^2} \\ 0 & \frac{hS_x}{k_x} \end{pmatrix} \tag{3.25}$$

$$R_{zx} = \begin{pmatrix} -\frac{hS_x}{k_x} & -\frac{h(1-C_x)}{k_x^2} \\ 0 & 0 \end{pmatrix} \tag{3.26}$$

3.1.2.2.4 Bending magnet's edges

Parameters :

- ϵ : the edges angle (see Fig. 3.3)
- $\rho = \frac{\Delta s}{\alpha}$: the bend's radius of curvature
- Higher orders of corrections (ψ) are neglected.

$$R_{xx} = \begin{pmatrix} 1 & 0 \\ \frac{\tan\epsilon}{\rho} & 1 \end{pmatrix} \tag{3.27}$$

$$R_{yy} = \begin{pmatrix} 1 & 0 \\ -\frac{\tan\epsilon}{\rho} & 1 \end{pmatrix} \tag{3.28}$$

$$R_{xx} = \begin{pmatrix} 1 & 0 \\ 0 & 1 \end{pmatrix} \tag{3.29}$$

The two transverse matrices correspond to the matrix of thin lens. Similar matrices may be found if one assumes a thin quadrupole ($L = 0$).

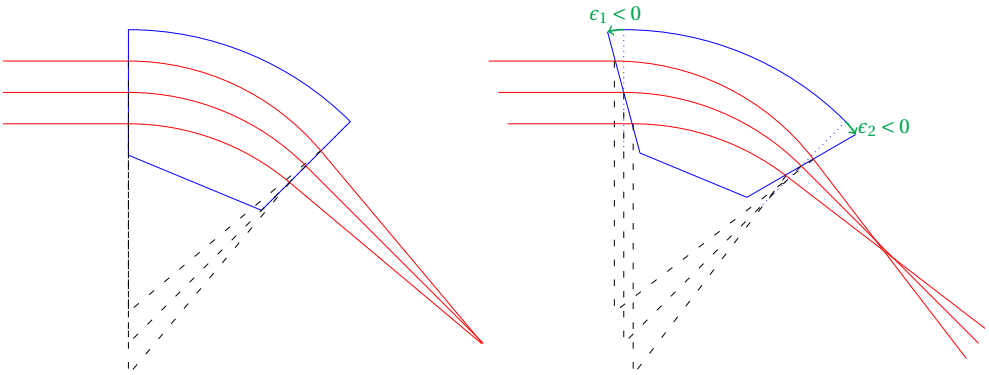

Figure 3.4: Geometric consideration of the focalisation effect of negative bend edges. The upper case corresponds to a sector bending magnet without edges. The lower case corresponds to a bending magnet with $-15°$ edges at the entrance and exit. Blue dotted lines correspond to the 0 edges case. Black dashed lines symbolise the curvature radius used to trace circle arc.

The sign of ϵ will define the focusing or defocusing effect of the dipole. Positive ϵ_1 (for the entrance face) or ϵ_2 (for the exit face) corresponds to reducing the external length - opposite to the centre of curvature - of the magnet as shown Fig. 3.3.

The focusing effect of negative edges can be shown by hand with the geometrical construction of Fig. 3.4. In this figure, the particles trajectories are straight outside the dipole. Inside them, the trajectory is an arc of a circle of curvature radius ρ - symbolised by the dashed lines - such that curved and straight trajectories are tangential. One may notice that the focal point for the sector bending magnet (up) occurred at the very end of the drawing, while the bending magnet with edges (down) has a focal point much closer. Moreover, one may notice that the three lines do not cross at the same distance in this last case. This effect may induce beam chromaticity and coupling between longitudinal and transverse planes.

3.1.2.2.5 Change of frame

A change of frame has no transfer matrix, but with the matrix formalism, one may compute it as follow :

Parameters :

- δx : change of position in x
- $\delta x'$: change of momentum in x'
- δy : change of position in y

- $\delta y'$: change of momentum in y'
- δz : change of position in z
- $\delta z'$: change of momentum in $\frac{\Delta p}{p}$

$$\begin{pmatrix} x_2 \\ x_2' \\ y_2 \\ y_2' \\ z_2 \\ \frac{\Delta p_2}{p} \end{pmatrix} = \begin{pmatrix} x_1 \\ x_1' \\ y_1 \\ y_1' \\ z_1 \\ \frac{\Delta p_1}{p} \end{pmatrix} + \begin{pmatrix} \delta x \\ \delta x' \\ \delta y \\ \delta y' \\ \delta z \\ \delta z' \end{pmatrix} \tag{3.30}$$

3.1.2.2.6 Steerer

Parameters :

- $\delta x'$: Horizontal kick
- $\delta y'$: Vertical kick

A steerer works like a small dipole used to deflect particles either vertically, horizontally or in both planes at the same time. Still, the dipole's matrix cannot be used as the reference particle should not be affected by this element to permit effective deflection in the transverse positioning of the particles according to the reference frame. In the first order, one may consider a steerer as an infinitely small element that changes the deflection angle by an amount $\delta x'$ - horizontally - and $\delta y'$ - vertically - depending on the strength of the steerer. This behaviour corresponds to a change of frame in x' and y'.

$$\begin{pmatrix} x_2 \\ x_2' \\ y_2 \\ y_2' \\ z_2 \\ \frac{\Delta p_2}{p} \end{pmatrix} = \begin{pmatrix} x_1 \\ x_1' \\ y_1 \\ y_1' \\ z_1 \\ \frac{\Delta p_1}{p} \end{pmatrix} + \begin{pmatrix} 0 \\ \delta x' \\ 0 \\ \delta y' \\ 0 \\ 0 \end{pmatrix} \tag{3.31}$$

3.1.2.2.7 Kicker

Parameters :

- L : Kicker's length
- $\delta x' = \chi$: horizontal kick

On ThomX, the kicker is a magnetic element that deflects the beam in (x,s) plane to correct the injection angle or allow beam extraction. This behaviour corresponds to the steerer's one with only horizontal deflection. Moreover, the kicker's length cannot be neglected ($L = 0.1\,\mathrm{m}$); hence it has been chosen to simulate ThomX kickers as two infinite small kickers at the beginning and the end of the real element with only half of the kicker's kick each.

$$\begin{pmatrix} x_2 \\ x_2' \\ y_2 \\ y_2' \\ z_2 \\ \frac{\Delta p_2}{p} \end{pmatrix} = M_{\mathrm{drift}}(L) \times \left(\begin{pmatrix} x_1 \\ x_1' \\ y_1 \\ y_1' \\ z_1 \\ \frac{\Delta p_1}{p} \end{pmatrix} + \begin{pmatrix} 0 \\ \chi/2 \\ 0 \\ 0 \\ 0 \\ 0 \end{pmatrix} \right) + \begin{pmatrix} 0 \\ \chi/2 \\ 0 \\ 0 \\ 0 \\ 0 \end{pmatrix} = \begin{pmatrix} x_1 \\ x_1' \\ y_1 \\ y_1' \\ z_1 \\ \frac{\Delta p_1}{p} \end{pmatrix} + \begin{pmatrix} L \times \chi/2 \\ \chi \\ 0 \\ 0 \\ 0 \\ 0 \end{pmatrix} \tag{3.32}$$

For totally linear computation, splitting the kick like that or having an infinity small kicker are the centre is equivalent. Still, this description is also use for others simulation where some non linearities are taken into account.

$$M = M_{\mathrm{drift}}(L) \tag{3.33}$$

3.1.2.2.8 Succession of elements

To compute propagation along a succession of n elements (drift, dipole, quadrupole,...), one has to know the initial condition and each element's transfer matrix.

Parameters :

- $\begin{pmatrix} x_1 \\ x_1' \\ y_1 \\ y_1' \\ z_1 \\ \frac{\Delta p_1}{p} \end{pmatrix}$: initial 6D vector of particle position in phase space
- M_1 : Transfer matrix of the first element encountered by the particle
- ...
- M_n : Transfer matrix of the n-th element encountered by the particle

The propagation may be computed using (Eq. (3.34)).

$$\begin{pmatrix} x_2 \\ x_2' \\ y_2 \\ y_2' \\ z_2 \\ \frac{\Delta p_2}{p} \end{pmatrix} = M_n \times M_{n-1} \times ... \times M_1 \times \begin{pmatrix} x_1 \\ x_1' \\ y_1 \\ y_1' \\ z_1 \\ \frac{\Delta p_1}{p} \end{pmatrix} \tag{3.34}$$

3.2 . MadX simulation

3.2.1 . MadX

MadX [40, 41] is a code developed by CERN to simulate beam dynamics and optimise beam optics. It is based on the linear transfer matrix for beams but with some higher-order correction to simulate beams or particles propagation as realistic as possible without increasing too much computing time. MadX allows either computation of the ring's orbit using periodical conditions between the beginning and the end of a ring, calculation of the beam propagation or tracking of single particles on defined sequences.

3.2.2 . ThomX representation in MadX

I have simulated the whole ThomX accelerator on MadX except for the linac (from the source to the end of the accelerating section) that has been simulated previously by Luca Garolfi [42] using another code named Astra.

As several paths exist on the accelerator, it was chosen to create several sequences - one for each path at least - and concatenate them after. This method avoids multiple definitions of elements, even for the definition of the ring's sequence with and without the septum and the injection or extraction kicker. Fig. 3.5 show all elementary sequences defined.

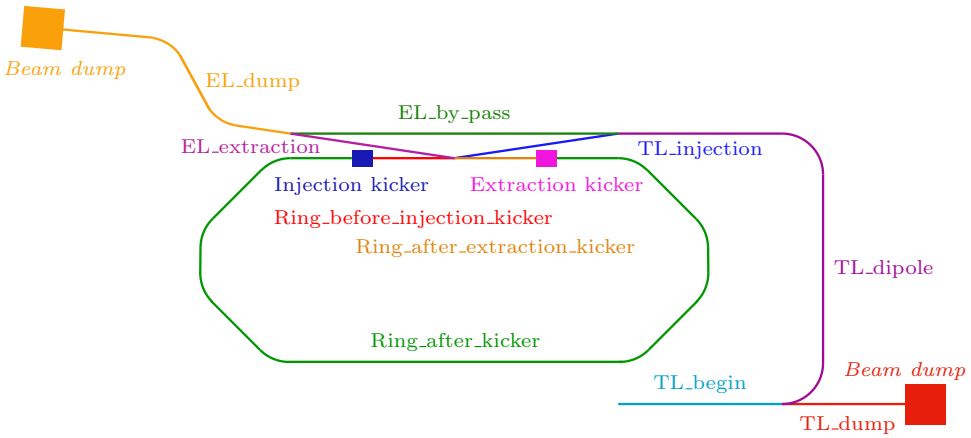

Figure 3.5: Elementary sequences of ThomX define in the MadX script.

Those sequences are concatenated to generate lines used in simulations. All combined sequences defined are :

- **TL_straight** = TL_begin + TL_dump
- **TL** = TL_begin + TL_dispersive + TL_injection
- **TL_EL** = TL_begin + TL_dispersive + EL_by_pass + EL_dump

- **Ring_with_injection_kicker** = Ring_before_injection_kicker + Injection kicker + Ring_between_kickers + drift at extraction kicker's place + Ring_after_extraction_kicker
- **Ring_with_both_kickers** = Ring_before_injection_kicker + Injection kicker + Ring_between_kickers + Extraction kicker + Ring_after_extraction_kicker
- **Ring_with_extraction_kicker** = Ring_before_injection_kicker + drift at injection kicker's place + Ring_between_kickers + Extraction kicker + Ring_after_extraction_kicker
- **Ring** = Ring_before_injection_kicker + drift at injection kicker's place + Ring_between_kickers + drift at extraction kicker's place + Ring_after_extraction_kicker
- **TL_1_turn** = TL + frame change + Ring_with_injection_kicker
- **TL_1_turn_EL** = TL + frame change + Ring_with_both_kickers + frame change + EL_extraction + EL_dump
- **TL_n_turn** = TL_first_turn + (n-1)*Ring
- **last_turn_EL** = Ring_with_extraction_kicker + frame change + EL_extraction + EL_dump
- **TL_n_turn_EL** = TL_first_turn + (n-2)*Ring + last_turn_EL

One may notice a change of frame in some sequence definitions. This computation artefact is used during injection or extraction to simulate beam propagation more accurately.

3.2.3 . Injection simulation

The injection in the ring is critical to ensure a good capture of the beam without oscillations. An incorrect injection could reduce overlap at the interaction point or lead to beam losses, both implying lower X-ray yield.

Let's study the injection mechanism and explain the change of frame applied during simulations.

Five main components have to be considered during the injection as shown in Fig. 3.6: The injection dipole, the septum, the kicker, but also both quadrupoles between the septum and the kicker.

When the beam arrives from the TL, it is deflected by the injection dipole with an angle of $-160\,\mathrm{mrad}$. This angle is corrected almost in full by the magnetic cavity of the septum with only a slight deflection $\theta \approx 10.7\,\mathrm{mrad}$ remaining. This deflection is calculated such that the beam is at the centre of the ring's pipe into

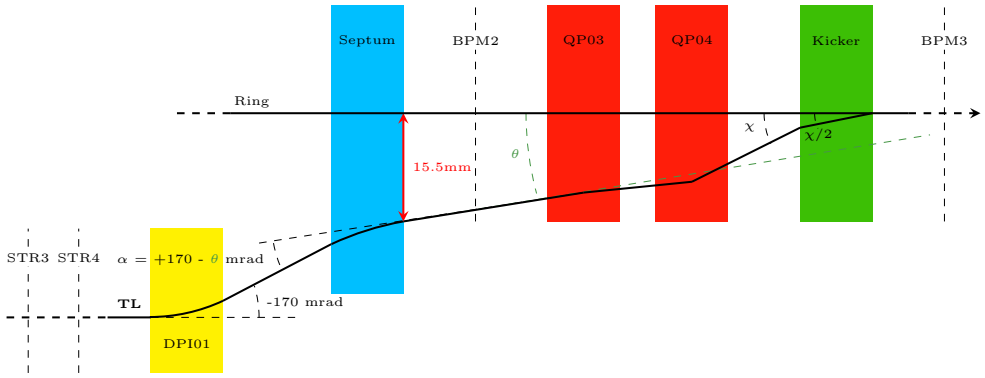

Figure 3.6: Drawing (not to scale) of the injection of ThomX. χ is the kick angle induced by the kicker. Acronym are the following : STR = Steerer; DPI = Injection Dipole; BPM = Beam Position Monitor; QP = Quadrupole. The associated numbers correspond to the ThomX nomenclature.

the kicker. Finally, the kicker finishes the angle correction to align the particle's trajectory along the ring's reference trajectory under periodic conditions.

During the propagation from the end of the septum to the kicker, the beam passes through two quadrupoles. As shown on Fig. 3.6, the reference trajectory during the injection does not pass through the magnetic centre of the quadrupoles that are aligned on the ring reference frame. This off-axis propagation induces a small beam deflection that must be considered.

To simulate off-axis propagation it has been chosen to compute a change of frame at the exit of the septum. Just after this change of frame, particles positioning are no longer expressed in the injection's reference frame but in the ring's reference frame.

To check the accuracy of the frame change, one may verify that, after the kicker, the new frame and the ring reference orbit agreed. For that purpose, one may track a particle with a null 6D-vector before the injection dipole and check that after the kicker, the particle vector's values return to zero as it should stay at zero anytime in the accelerator's reference frame.

Using this constraint and the mechanical layout, one may find the following parameters for change of frame :

- $\Delta X = -15.5\,\mathrm{mm}$: mechanical distance between the injection reference frame's origin and the ring's one at the exit of the septum
- $\Delta X' = \theta \approx 10.7\,\mathrm{mrad}$: angle between both frames

This change of frame and a kicker's kick of $\chi \approx -13.03\,\mathrm{mrad}$ allow agreement between both frames of less than $0.2\,\mathrm{mm}$ in x and less than $0.4\,\mathrm{mrad}$ in x' over, at least, the 20 first ring's turn. This behaviour is visible on Fig. 3.7 that corresponds

to the beam centroid propagation in x,y and x',y' planes from the beginning of the TL to the end of the 20^{th} turn in the ring. For y and y', both frame always stays equivalent as the change of frame do not impact them.

The θ and χ precision for this simulation correspond to the septum and kicker pulse reproducibility (see Tab. 2.4). Hence horizontal oscillation in the ring of the order of a few tenths of a millimetre is possible because of the magnetic reproducibility of the injection devices. For other simulations, some optimised values are used to achieve less than $0.3\,\mu\text{m}$ in x and less than $0.6\,\mu\text{rad}$ in x' over, at least, the 20 first ring's turn.

One may notice from the values above that the angle difference between both frames ($10.7\,\text{mrad}$) and the beam deflection needed inside the kicker ($13.0\,\text{mrad}$) are effectively different. This difference comes from the off-axis propagation in quadrupoles, therefore it must not be neglected.

Another method could have been used for simulation. One could have kept the particles in the reference frame and considered that the BPM and quadrupoles are off-axis and tilted. This method seems more natural but not simplest as one must compute the rotation and displacement of the elements according to the magnetic strength of the previous ones. Moreover, by keeping the quadrupoles at the normal localisation, the change of frame permit to avoid redefinition of elements of the section *Ring_before_injection_kicker* with and without displacement.

The process is similar during the extraction. Hence, the following frame change is applied at the entrance of the septum to pass from the ring's frame to EL's one :

- $\Delta X_{extraction} = -\Delta X_{injection}$
- $\Delta X'_{extraction} = \Delta X'_{injection}$

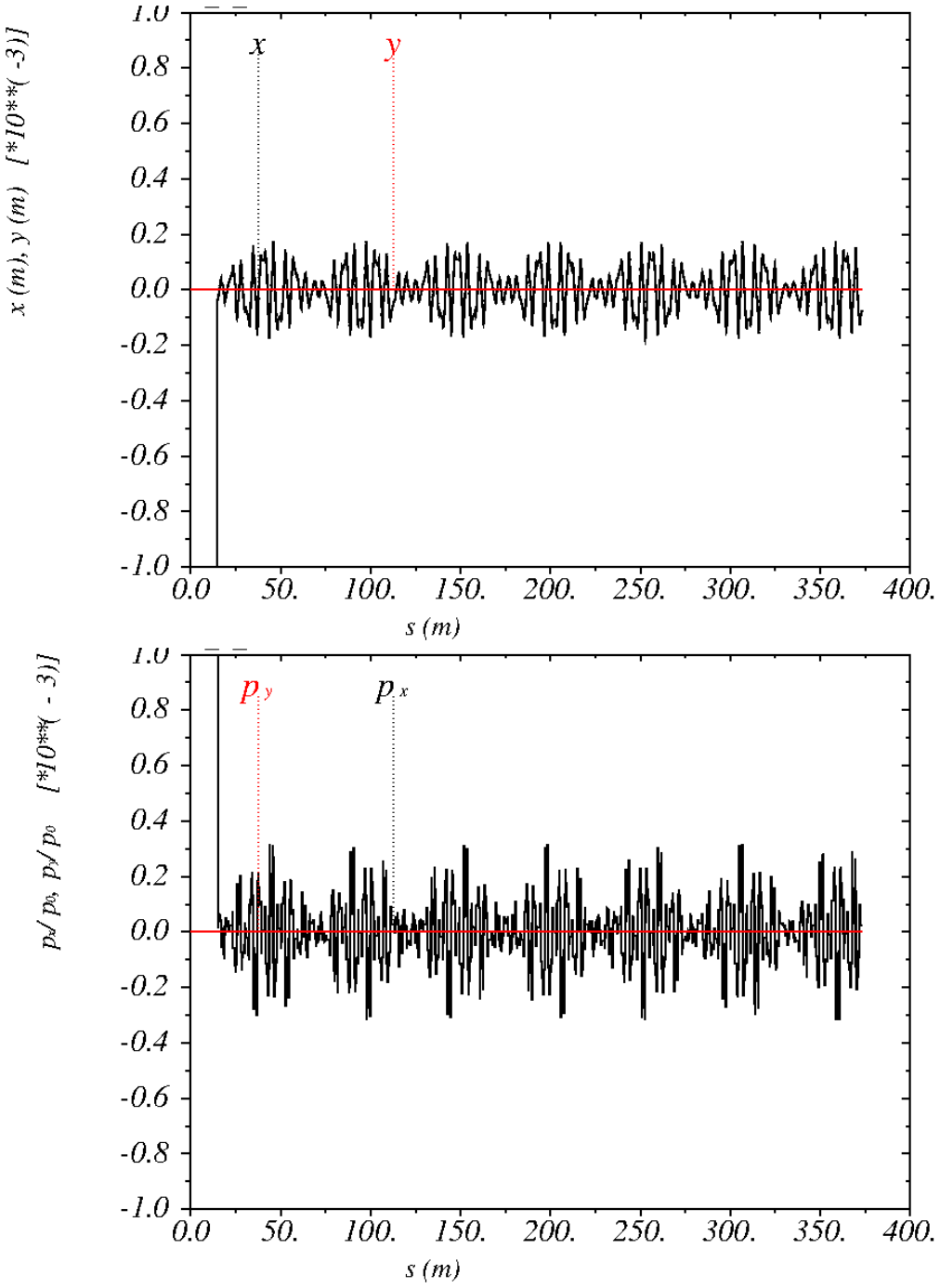

Figure 3.7: Tracking with MadX of the initially null beam centroid propagated along the TL and the 20 first ring's turn. In black are x (top) and x' (bottom) while in red are y (top) and y' (bottom). For y and y', oscillations do not exist throughout the propagation. The large peak at $15\,\mathrm{m}$ correspond to the change of frame. Before it, the beam position vector is always null. After, the oscillation amplitude characterises the fluctuation between the beam reference frame created with the change of frame and the periodical reference frame of the ring.

3.2.4 . Particles selection

MadX has a tracking mode that permits particle tracking along a sequence. The issue is that each initial particle's vector has to be defined manually. A python [43] code has been created to automatise particle selection within a beam's phase space. To define a beam one may use the beam emittance ϵ and the Twiss parameters [44] α, β and γ linked by the Eq. (3.35). From those parameters, one may extract the RMS transverse beam size σ_x and σ_y (Eq. (3.36)) and the RMS transverse beam momentum $\sigma_{x'}$ and $\sigma_{y'}$ (Eq. (3.37)).

$$\beta\gamma - \alpha^2 = 1 \tag{3.35}$$

$$\sigma_{x,y} = \sqrt{\epsilon_{x,y} \times \beta_{x,y}} \tag{3.36}$$

$$\sigma_{x',y'} = \sqrt{\epsilon_{x,y} \times \gamma_{x,y}} \tag{3.37}$$

The latest simulations of the ThomX linac give beam parameters at the exit of the accelerating section summarised in Tab. 3.1.

Table 3.1: Twiss parameters and emittance of the beam simulated at the end of the accelerating section.

	x	y
α	-10.95	-10.93
β	$43.25\,\mathrm{m}$	$43.13\,\mathrm{m}$
ϵ	$5 \times 10^{-2}\,\pi.\mathrm{mm.mrad}$	$5 \times 10^{-2}\,\pi.\mathrm{mm.mrad}$

Which give a beam size of :

- $\sigma_x \approx 1.5\,\mathrm{mm} \approx \sigma_y$
- $\sigma_{x'} \approx 0.4\,\mathrm{mrad} \approx \sigma_{y'}$

A particle within this beam's ellipse as to respect Eq. (3.38) and Eq. (3.39).

$$\gamma_x x^2 + 2\alpha_x x x' + \beta_x x'^2 < \epsilon_x \tag{3.38}$$

$$\gamma_y y^2 + 2\alpha_y y y' + \beta_y y'^2 < \epsilon_y \tag{3.39}$$

Particles respecting those two equations may be considered inside the 1-σ beam. If one thinks of the distribution of the particles as a Gaussian one, only $68\,\%$ of the actual beam's particles are simulated. To miss less than a particle in 10^{-6}, one may consider the 5-σ beam. In general, a k-σ beam in this thesis will refer to the beam defined above with an emittance multiplied by k^2, which means an RMS size multiplied by k.

For each particle, the python code selects randomly (x, x') - and then separately (y, y') - with a uniform random distribution until the beam ellipse's equations are met. An additional $35\,\mathrm{mm}$ long square cut on the x-y plane is added as the particles outside this square cut are well outside ThomX beam pipes. The Fig. 3.8 show an example of 400 particles selection inside the 1-σ beam. One may notice that nearly all particles' momenta are directed toward the outside of the beam. This behaviour is coherent with the negative sign of the Twiss parameter α.

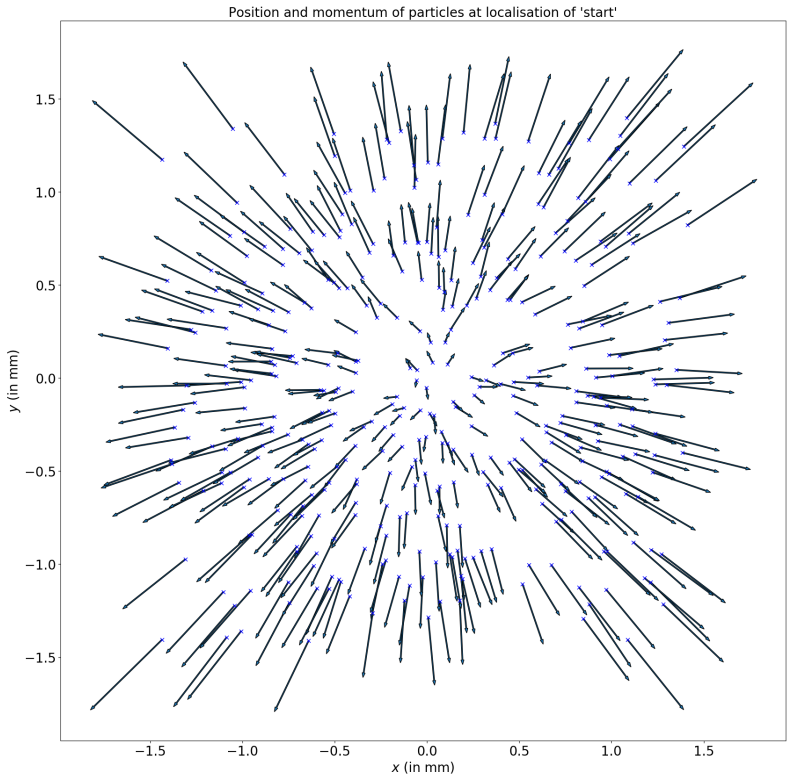

Figure 3.8: The plot of 400 particles selected inside the beam. The blue crosses represent particles' location in the (x,y) plane and the arrows - from (x,y) to (x+x′×1 m,x+x′×1 m) - represent the propagation of those particles on a hypothetical one meter long drift according to their transverse momentum.

The coherence of this particle selection may be shown by computing, on the one hand, the beam propagation in the accelerator and, on the other hand, selected particles inside the 1-σ beam and tracking them in the accelerator. In this case, the beam computation should give the beam envelope along the accelerator, and all particles shall stay inside this envelope.

Fig. 3.9 show the propagation of 400 particles selected for the Fig. 3.8 and the beam envelop. One may notice that particles stay inside the envelope as wanted. The only excursion visible is around $14\,\mathrm{m}$ in the x plane, but this peak is only a

computing artefact due to the change of frame at the injection (see section 3.2.3). One may also notice that the particles fill the envelope, which validates the selection and tracking of particles.

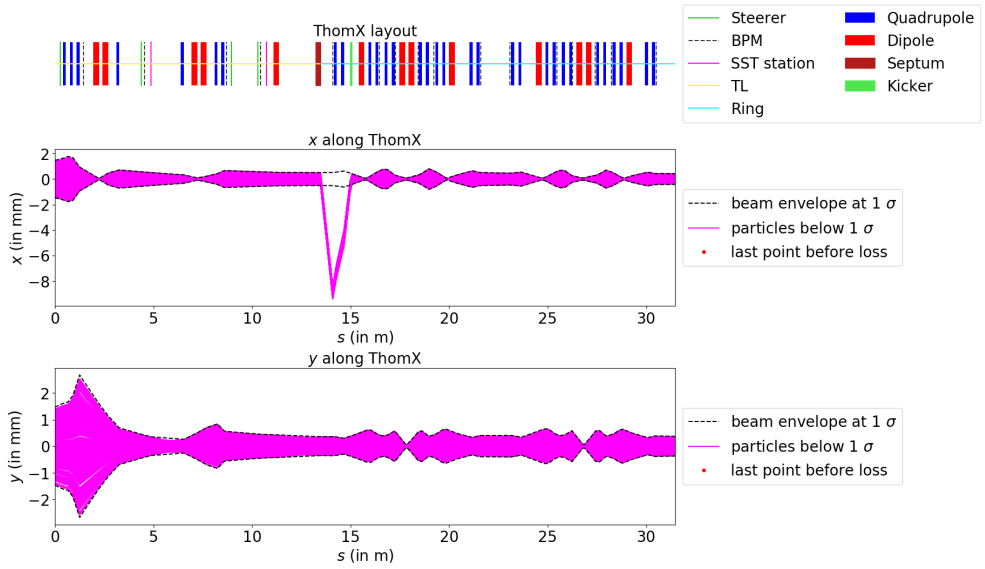

Figure 3.9: Comparison of the x (middle) and y (below) beam envelope propagation (in dashed line) and the propagation in those planes of 400 particles (in pink) selected inside the beam envelope at the beginning of the line. The upper part shows the layout of the TL_1_turn line used for those simulations. The large peak in x plane around $14\,\mathrm{m}$ corresponds to a change of frame used to simulate the beam propagation during the ring injection (see section 3.2.3)

This comparison has helped to understand how some elements parameters - like edges and fridge field of dipoles - are taken into account in MadX in beam propagation and tracking mode.

From Fig. 3.9 one may also notice a certain symmetry in the ring lattice. In fact, the ring is composed of four cells. Two opposite cells are identical and symmetric to the others two. At the interaction point (IP), around $18\,\mathrm{m}$, the beam is focused to a tiny size to increase beam density. By construction, a second focal point is at $27\,\mathrm{m}$ which is the symmetrical point of the IP in the ring.

For longitudinal coordinates, the particles are considered as on-time ($z = 0$) and on-momentum ($\frac{\Delta p}{p} = 0$). The on-time assumption come from the fact that the beam length is short ($5\,\mathrm{ps}$). The on-momentum assumption is not so true at the end of the accelerating section. Still, the line between the tow pair of $45°$'s dipoles in the transfer line is a dispersive line where the beam width correspond to the energy spread. At the middle of this line there is a slit used to select a specific energy and energy spread. Hence, a energy fluctuation or an high energy

spread before the slit are converted into an intensity fluctuation and the beam can be consider on momentum.

3.2.5 . Aperture

The Tracking mode of MadX let the opportunity to define some aperture. When the particle's position is calculated outside this aperture, the particle's propagation is stopped, and the loss is recorded. The position is checked at the entrance of every element except drift.

The TL and the EL beam pipes are circular with a diameter of $35\,\mathrm{mm}$ as is the aperture defined in the MadX code.

The ring's pipe shape is more complicated, as one may see on Fig. 3.10. The circular shape correspond to the TL aperture at scale.

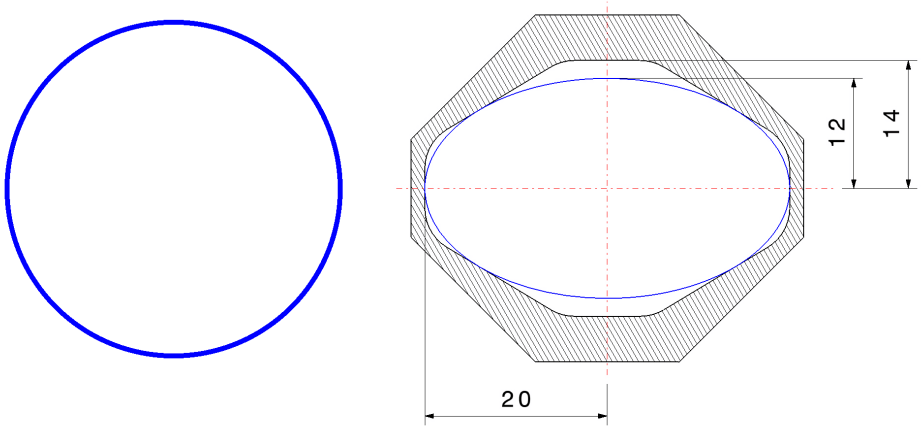

Figure 3.10: Drawing of the ThomX ring's tube (hatched) compared to the aperture defined in MadX for the ring (blue ellipse) and for the TL (blue circle) at scale.

In MadX, this shape was simplified by taking the largest ellipse fitting in the ring pipe. This ellipse has a semi-minor axis of $12\,\mathrm{mm}$ and semi-major axis of $20\,\mathrm{mm}$ as shown on Fig. 3.10 in blue line. The beam losses are thus slightly overestimated in the ring.

3.3 . Linear transfer matrix computation on MatLab

3.3.1 . Code details

The transfer matrix formalism is a convenient way to compute, in the first order, the propagation of a particle into an accelerator. Several simulation codes are based on that formalism - like MadX or Trace3D - but to my knowledge, none of them allows extracting propagation's equations with parametrisation of some elements' characteristics - like steerer deflection - to characterise analytically the

impact of those elements on the particle position at some points. For that purpose, a homemade linear transfer matrix code has been developed on MatLab [45]. The language MatLab has been chosen because of the possibility of creating variables - named *sym* for symbolic variable - and computing equations with them. This homemade code is composed of two classes :

- ***acc_el***: a class that represents one component of the accelerator
- ***accelerator***: a class that represents a full line of an accelerator with several components

An *accelerator* object is composed of :

- ***name***: the name of the accelerator line considered
- ***energy***: the energy (MeV) of the particle considered
- ***list_el***: a list of *acc_el* object

An *acc_el* object is composed of :

- ***name***: the name of the element
- ***type_el***: a string representing the type of element considered
  Possible type are:
  - "quad": a quadrupole
  - "bend": a bending magnet without edges
  - "edge": a bend edges (must be just before or after a bend)
  - "bend-edge": a bending magnet with 2 edges
  - "septum": a septum (similar to bending magnet for the injection)
  - "frame_change": a change of frame in the 6D phase space
  - "steerer": a steerer (treat as change of frame in x' and y')
  - "kicker": a kicker (treat as change of frame in x')
  - "screen": a screen's station (is transparent for the beam, but allow to compute propagation from station to station)
  - "BPM": a BPM (transparent)
  - "start": specific element corresponding to the beginning of the line (transparent)
  - "end": specific element corresponding to the ending of the line (transparent)
  - else: element considered as transparent

- ***at***: the position of the beginning of the element
- ***length***: the length of the element
- ***variables***: a list of the parameters needed to compute the transfer matrix of the element (ex: k for quadrupoles)
- ***save_calc***: a boolean to save the analytic computation at the end of the element and begin a new calculation after

Each class also has methods like ***matrix*** that allows one to compute the transfer matrix of the given *acc_el*'s object. Several methods enable splitting the accelerator's line, concatenating two accelerators, or inverting the propagation's direction for the accelerator's class. Still, the main method is ***calcul_propagation***, which computes the propagation of a particle represented by $(x, x', y, y', z, z')^t$ - where the "t" subscribe mean transpose - from the first element of the *acc_el*'s list to the last one. Each time the properties *save_calc* of an element is true, the script saves the propagation equation after the element and starts a new equation.

3.3.2 . Example with FODO line

To understand the meaning of this code, let's consider the line of 3 quadrupoles drawn on the Fig. 3.11, named FODO lattice. For the exemple let's parametrize the strength of the first quadrupole k_1 and let's use $k_2 = -2\,\mathrm{m}^{-2}$ and $k_3 = 1\,\mathrm{m}^{-2}$ for the second and the third quadrupole.

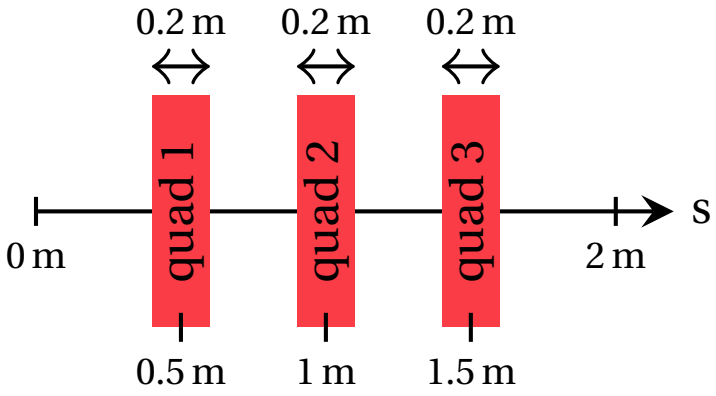

Figure 3.11: FODO line of 3 quadrupoles.

The computation along the line returns the Eq. (3.40) in this configuration.

$$\begin{cases} X_2 = 1.46 * X_1' * cos(0.2 * \sqrt{k_1}) + 1.29 * cos(0.2 * \sqrt{k_1}) * (0.4 * X_1' + X_1) + \\ \qquad (1.29 * X_1' * sin(0.2 * \sqrt{k_1}))/\sqrt{k_1} - 1.46 * \sqrt{k_1} * sin(0.2 * \sqrt{k_1}) * (0.4 * X_1' + X_1) \\ X_2' = 0.97 * X_1' * cos(0.2 * \sqrt{k_1}) + 0.17 * cos(0.2 * \sqrt{k_1}) * (0.4 * X_1' + X_1) \\ \qquad +(0.17 * X_1' * sin(0.2 * \sqrt{k_1}))/\sqrt{k_1} - 0.97 * \sqrt{k_1} * sin(0.2 * \sqrt{k_1}) * (0.4 * X_1' + X_1) \\ Y_2 = 1.33 * Y_1' * cosh(0.2 * \sqrt{k_1}) + 0.69 * cosh(0.2 * \sqrt{k_1}) * (0.4 * Y_1' + Y_1) \\ \qquad +(0.67 * Y_1' * sinh(0.2 * \sqrt{k_1}))/\sqrt{k_1} + 1.33 * \sqrt{k_1} * sinh(0.2 * \sqrt{k_1}) * (0.4 * Y_1' + Y_1) \\ Y_2' = 1.01 * Y_1' * cosh(0.2 * \sqrt{k_1}) - 0.23 * cosh(0.2 * \sqrt{k_1}) * (0.4 * Y_1' + Y_1) \\ \qquad -(0.23 * Y_1' * sinh(0.2 * \sqrt{k_1}))/\sqrt{k_1} + 1.01 * \sqrt{k_1} * sinh(0.2 * \sqrt{k_1}) * (0.4 * Y_1' + Y_1) \\ Z_2 = 2 \times 10^{-4} * Z_1' + Z_1 \\ Z_2' = Z_1' \end{cases} \tag{3.40}$$

Thanks to the parametrisation of k_1, one may analyse the impact of the first quadrupole's strength on the behaviour of a FODO line. Unfortunately, the equation's length quickly overgrows for more complex lines or parametrisations.

To palliate managing those larges equation, the results are written in a file as python's function and is directly imported in python's codes.This feature has allowed us to compare MadX's tracking results with MatLab's one on very simple lines - one element between 2 drift spaces - and validate MatLab's computation with reasonable accuracy. The slight differences found come from non-linearity taken into account in MadX computation.

4 - Loss maps

Contents

Beam losses on accelerators may have several impacts on the accelerator's performances as it may reduce the number of interactions - hence the luminosity - or damage some pieces of hardware. This chapter presents a study of particle losses. The consequences of particles losses is discussed in section 4.1. Both section 4.2.2 and section 4.2.3 show representations of the losses either longitudinally or transversely at some specific point of the accelerator.

4.1 . Consequences of particles losses

The more energetic is the beam, the worst the losses. ThomX is a low-energy electron accelerator, hence physical damage is unlikely. Nevertheless, beam losses risks exist and must be prevented.

The material activation depends on the beam energy and the material used to build the accelerator. The activation risk is more important above $10\,\mathrm{MeV}$ [46] as some elements - like metals - may become radioactive, involving an activation risk on the transfer line (TL), the ring (RI) and the extraction line (EL).

The electronics is particularly sensitive to radiation [46]. When possible, electronic devices are placed outside the bunker to avoid damage. Electronics close to the accelerator have to be shielded.

One specific piece of equipment had to be inside the bunker but may suffer from radiation damage: the Fabry-Perrot (FP) laser and especially the optical fibre of this device. It has been well known since at least 1994 that optical fibre may darken because of radiation exposure [47] which reduces the laser intensity. To protect fibres, one may use some shielding.

ThomX's goal is to generate a high X-ray flux. This flux is proportional to the number of electrons and photons at the interaction point (see Eq. (2.2)). A partial - uncontrolled - electron beam loss may lead to a reduction of the X-ray photon produced. Similarly, a reduction of stored laser power reduces the X-ray flux too.

The injection in the ring is one critical moment that could induce beam losses if it is not performed correctly. The study of losses in the TL and the first ring turn permits to understand the beam injection process and the risks of losses to optimise the injection.

4.2 . Loss maps

To simulate the possible beam losses inside the accelerator, some particles have been tracked using MadX (see section 3.2).

4.2.1 . Particles selection

The particle selection is described in section 3.2.4 and we remind here the main features. It is done by random uniform selection of (x,x') and (y,y') couples separately until points in the phase space x-x' or y-y' are within a particular beam ellipse. Previous simulations of the linac define these beam properties. Their values at the end of the accelerating section - or beginning of the TL - are given by Tab. 3.1. Beam with those parameters is denoted as 1-σ beam. A larger beam can also be considered by multiplying the transverse beam emittance ϵ by a factor k^2, which means multiplying both beam size and beam divergence in transverse phase space planes by k. Such a beam is denoted as a k-σ beam .

Although normal beams are usually gaussians, this flat beam selection is sufficient to identify the parts of phase space where losses occur. It is a convenient way to simulate lots of particles with large variations of properties around nominal parameters. For instance, increasing the beam emittance gives similar selections to those obtained by changing the Twiss parameters or moving the beam centroid. To demonstrate that, lets consider a selected quadruplet (x,x',y,y') representing the transverse position of a particle. This particle must respect Eq. (4.1) as the maximum transverse beam size is σ_x (σ_y) in x (y) plane, while the maximal beam divergence is $\sigma_{x'}$ ($\sigma_{y'}$).

$$\begin{cases} x < \sqrt{\beta_x \epsilon_x} = \sigma_x \\ y < \sqrt{\beta_y \epsilon_y} = \sigma_y \\ x' < \sqrt{\gamma_x \epsilon_x} = \sigma_{x'} \\ y' < \sqrt{\gamma_y \epsilon_y} = \sigma_{y'} \end{cases} \tag{4.1}$$

On the one hand, increasing ϵ increase the x,x',y and y' range of possibilities while on the other hand, increasing β (resp. γ) allows increasing x and y (resp. x' and y') too. Hence, for the selection - if one ignores the reality of the beam distribution - modifying ϵ is equivalent to modify β and γ by a similar amount.

For global beam offset, one may consider selecting two quadruplets, one characterising the beam's centroid (b subscript), the second representing the particle's position according to this centroid (p subscript). The position of the particle is

then $(x,x',y,y') = (x_b + x_p, x'_b + x'_p, y_b + y_p, y'_b + y'_p)$. Once again, the maximum range of possible values is increased as does an augmentation of ϵ.

In summary, I choose to select particles in larger beam ellipse characterised by the same Twiss parameters but a higher emittance to simulate more realistic particles.

Some special k-values are common in this work. If one sees beams as Gaussian distribution, the 1-σ beam can be interpreted as the standard deviation of the beam, while the 5-σ beam is the confidence interval outside which only one particle out of 10^6 is out of the distribution. For a $100\,\mathrm{pC}$ beam that is around 600 electrons. The 12-σ beam represents the case where particles can be selected at the edge of the pipe. Eventually, the case $k = 20$ is an arbitrary upper limit to emittance augmentation. To avoid too many particles selected outside the beam pipe - hence, being lost immediately - a $35\,\mathrm{mm}$ long square cut on the x-y plane is added. This means that the 20-σ beam is used to increase only the particles divergence according to the 12-σ beam case, as allowing the particles position to increase furthermore does not make sense.

4.2.2 . Maps along the accelerator

Several methods to represent particle losses exist. To know the location of the loss, a convenient way is to plot the losses alongside the machine. I choose to represent the particles' propagation in the x or y plane along the machine and add - above the curve - a red dot when a particle is lost. As MadX does not deliver the positioning of the particles once it is lost, the red dot is, in reality, at the location of the last valid s position before the loss.

The Fig. 4.1 is one of those losses representation along the transfer line (TL) and the ring first turn. The 600 particles are selected uniformly within the 5-σ perfectly centred ThomX beam (see section 4.2.1). To be more precise, a third of them are selected within the 1-σ beam. Another third imposed is within the 3-σ beam but outside the 1-σ beam. The last third of then is thus within the 5-σ beam and outside the $3\,\mathrm{s}$ one.

One may notice that no loss are visible on the Fig. 4.1. Hence, if the beam corresponds to the simulation and is well centred at the exit of the accelerating section, no losses must occur in the TL and the first ring's turn according to this simulation.

Unfortunately, in reality, beams are never exactly as predicted because of simulation approximation, elements misalignment or deflection of the beam created by external causes like parasitic magnetic field.

The Fig. 4.2 shown the tracking of 600 particles within the 12-σ beam. A third of them are selected within the 1-σ beam while a second third is restricted to the 5-σ beam. The remaining 200 particles are forced to be selected outside the 5-σ beam.

One may notice significant losses in the first meter of the TL. Those losses are explained by particles selected close to the beam pipe with a transverse momentum

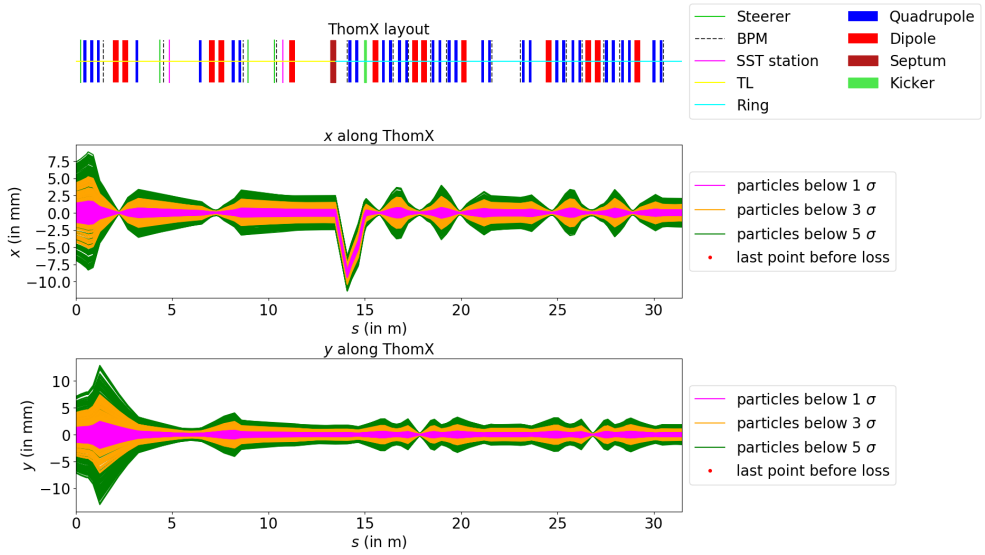

Figure 4.1: Tracking of particles along the accelerator. The upper part shows the layout of ThomX, and the middle (lower) part corresponds to the x (y) positioning of particles alongside the accelerator. The particle's trajectories are coloured according to their initial parameters, within 1-σ beam in pink, within 3-σ beam and outside 1-σ beam in orange and within 5-σ beam and outside 3-σ beam in green. For each random selection, 200 particles are generated; therefore, 600 particles are tracked. Losses should be represented as red dots, but not any loss occurs for those parameters. The peak around $14\,\mathrm{m}$ in the x plane is just a computing artefact due to the change of frame between the septum and the kicker (section 3.2.3).

directed toward it. But, once the third quadrupole of the TL is passed, the beam is focalised in the transverse plane, and losses do not occur anymore, even in the first ring turn where the beam pipe is smaller (see section 3.2.5).

Moreover, the losses at the beginning of the TL are unlikely to happen as the accelerating section is composed of some irises ($\varnothing 22$-$18\,\mathrm{mm}$) smaller than the TL beam pipe ($\varnothing 35\,\mathrm{mm}$). So in fact these losses would occur inside the accelerating section.

The transverse beam size does not seem to cause electron losses after the beginning of the TL. Even particles selected near the pipe - improbable because of the accelerating section's iris - achieved the first ring turn if they pass the first dipole. Nevertheless, particles with higher transverse momentum may have worse comportment. To check, let's select some particles over the 12-σ beam. The Fig. 4.3 show a new particles tracking with the same selection's parameters as the Fig. 4.2 and an additional fourth category of selection: 200 particles inside the 20-σ beam but outside the 12-σ one.

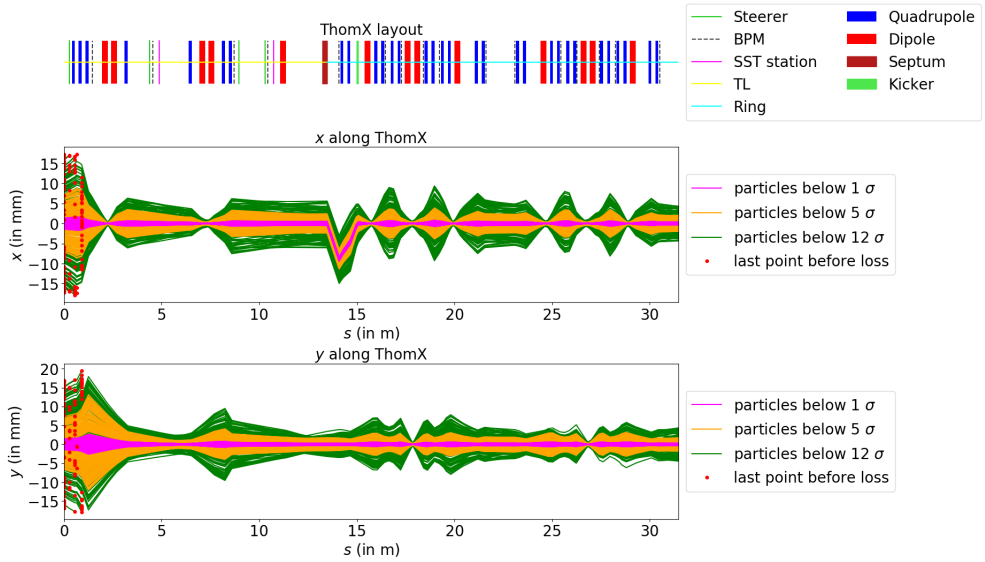

Figure 4.2: Tracking of particles along the accelerator. The upper part shows the layout of ThomX, and the middle (lower) part corresponds to the x (y) positioning of particles alongside the accelerator. The particle's trajectories are coloured according to their initial parameters. Within 1-σ beam in pink, within 5-σ beam and outside 1-σ beam in orange and within 12-σ beam and outside 5-σ beam in green. For each random selection, 200 particles are generated; therefore, 600 particles are tracked. The last position of particles recorded before being lost is represented as red dots. The peak around $14\,\mathrm{m}$ in the x plane is just a computing artefact due to the change of frame between the septum and the kicker (section 3.2.3).

The majority of the losses are always at the beginning of the TL, but several other locations of losses may be seen this time. Those extra losses occur at the injection of the beam ($14\,\mathrm{m}$), before the interaction point ($16\,\mathrm{m}$, $17\,\mathrm{m}$) and just after it ($20\,\mathrm{m}$), but not in the second half of the ring. Tracking along more turns is needed to be confident, but if the next turns are like the last half one, not so many losses must occur during the first few turns, and then the ring's transverse feedback system must ensure good comportment of the beam. Even if only a few unlikely losses may happen, their location is concerning, especially those at the injection and before the IP, as they are directed toward the Fabry-Perrot cavity where there are some sensitive pieces of equipment. Some mechanical options, like shielding, may be applied to avoid damage, but a good knowledge of the beam properties before trying to go in the ring and an injection feedback system (see section 5) to correct beam injection's mistakes will also help.

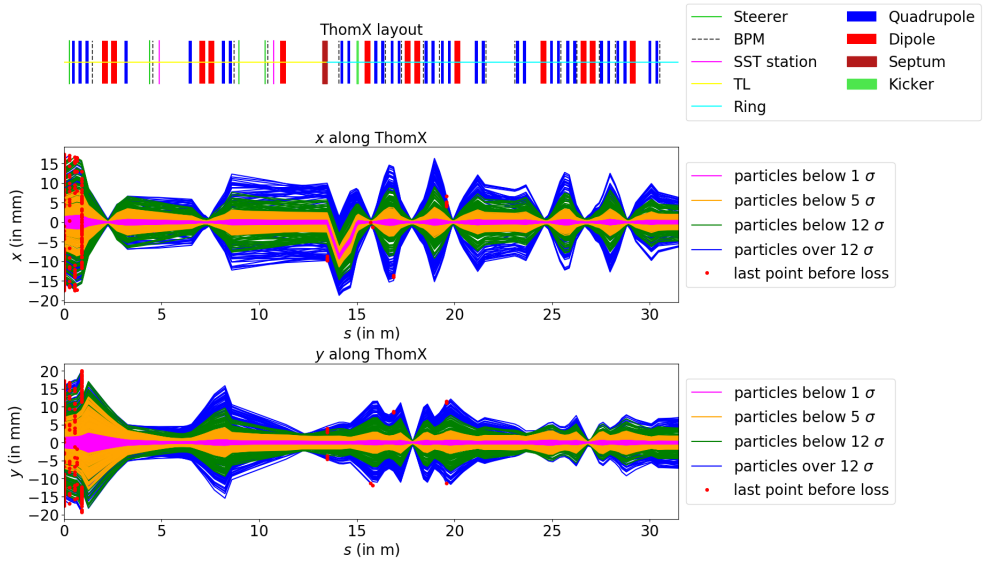

Figure 4.3: Tracking of particles along the accelerator. The upper part shows the layout of ThomX, and the middle (lower) part corresponds to the x (y) positioning of particles alongside the accelerator. The particle's trajectories are coloured according to their initial parameters, within 1-σ beam in pink, within 5-σ beam and outside 1-σ beam in orange and within 12-σ beam and outside 5-σ beam in green and in blue are represented particles above 12-σ with as upper limit the 20-σ beam. For each random selection, 200 particles are generated; therefore, 800 particles are tracked. The last position of particles recorded before being lost is represented as red dots. The peak around $14\,\mathrm{m}$ in the x plane is just a computing artefact due to the change of frame between the septum and the kicker (section 3.2.3).

4.2.3 . Projected maps

4.2.3.1 At the beginning of the TL

To minimise the losses, it is helpful to back-project the locations of the predicted beam losses to upstream screens before letting the beam go into the remaining part of the accelerator. For that purpose, let us consider 10000 particles selected within the 20-σ beam, propagate them using MAdX and record the particles' losses as before. To visualise the losses, let's plot the initial particle's position in the x-y plane with different colours depending on the losses location as done in the Fig. 4.4.

On Fig. 4.4 one may notice that particles are effectively selected within a square with x and y between $\pm 17.5\,\mathrm{mm}$. A large part of the losses - those in red - occurred since the very first element of the TL as some particles are selected too close - or even slightly outside - of the circular pipe. Because of beam divergence at the beginning, losses continue to appear in the following elements - in green - until

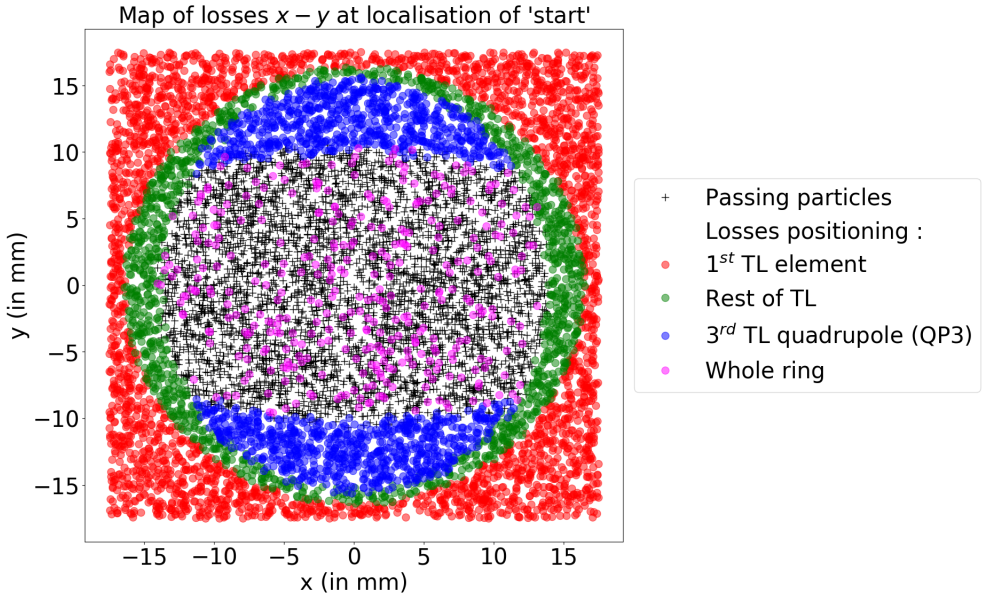

Figure 4.4: Map of losses of 10000 particles tracked alongside the TL and the first ring turn, projected at the beginning of the TL (named 'start') in the x-y plane. The black crosses represent the position of particles at 'start' which successful travel from there to the end of the first ring's turn without being lost. Dots are particle's positions at 'start' which are lost during the propagation, and the colours represent the lost location. Those locations are: in the very first element of the TL in red, in the 3^{rd} quadrupole of the TL in blue, in the remaining part of the TL (mostly before the 3^{rd} quadrupole) in green and in the ring in pink.

the third quadrupole of the TL (TL/DG/QP.03). There, the beam shape is not quasi-circular anymore but wider in the y plane, which explains the losses - in blue - in the upper and lower part of the remaining particles.

As seen previously, with loss maps along the accelerator (see section 4.2.2), after the 3^{rd} quadrupole of the TL, no losses occur until the ring. For the ring, the losses - in pink - seem random within a window of passing particles named acceptance window. This is likely to be losses due to particles that are selected with a higher transverse momentum at the beginning of the TL in the 20-σ beam case than in the 12-σ beam case.To check that, one may look at other transverse plane than just x-y, like x'-y' (Fig. 4.5), x-x' (Fig. 4.6) or y-y' (Fig. 4.7).

Fig. 4.5, in x'-y' plane, look much like Fig. 4.4, in x-y plane. The borders of the losses zone are less sharp. Still, one may find the rectangular shape of particles instantaneously lost - that is induced by the square cut in the x-y plane - as well as the circular the losses at the beginning of the TL and the losses mostly in the upper and lower part of the third quadrupole because of the wide vertical beam.

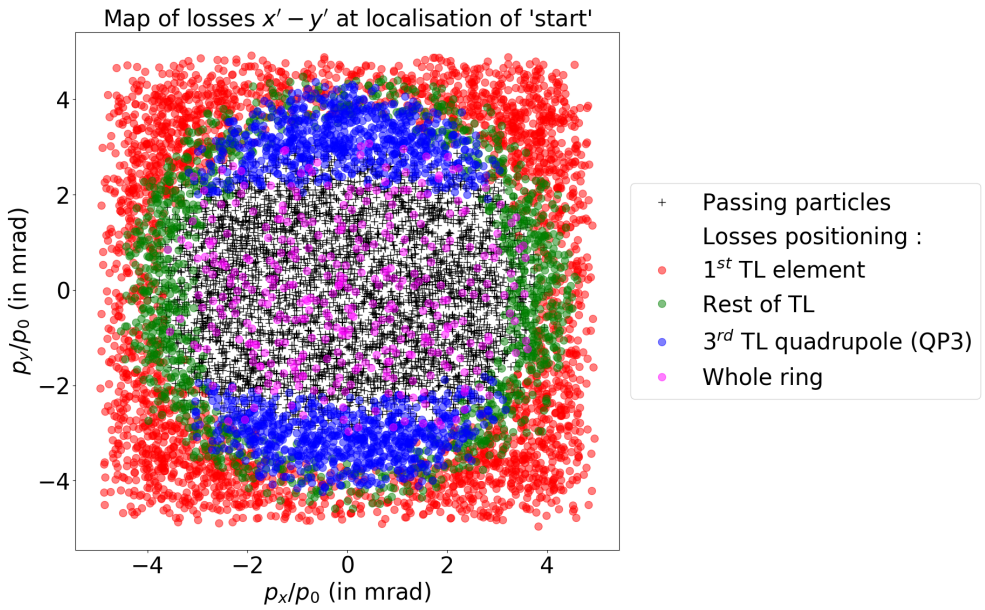

Figure 4.5: Map of losses of the identical 10000 particles than Fig. 4.4 tracked along the TL and the first turn in the ring, projected at the beginning of the TL (named 'start') in x'-y' plane. Black crosses represent the position of particles at 'start' which complete the first ring turn without being lost. Dots are particles' positions at 'start' which are lost during the propagation, and the colours represent the lost location. Those locations are: in the very first element of the TL in red, in the 3^{rd} quadrupole of the TL in blue, in the remaining part of the TL (mostly before the 3^{rd} quadrupole) in green and in the ring in pink.

Even the acceptance window is similar - slightly larger than higher - with a random distribution of the ring's losses. Those observations lead to the conclusion that not only high divergence alone can explain the losses inside the ring but a combination of position and divergence.

In x-x' (Fig. 4.6) and y-y' (Fig. 4.7), the visualisation of losses is more complex as the beam ellipse on those two planes are thin, tilted and cut at the border because of the square cut in x-y plane. In x-x' plane, the correction of the tilde is done by computing the slope a_x of the ellipse by linear regression with the least squares method on all the points and then plot $x' - a_x \times x$ as function of x (Fig. 4.6b). The same method is applied in y-y' plane (Fig. 4.7b), and they both give the same slopes $a_{x,y} = 0.254\,\mathrm{mm}^{-1}$. Once the correction is applied, one may notice that some clusters of ring's losses are form at the ellipse's edge. In the y-y' plane, two symmetrical clusters are visible in the upper and lower part of the corrected ellipse. Still, in the x-x' plane, only one smaller cluster at the bottom of the tilted ellipse exists. Hence, first, the vertical divergence seems to

imply slightly more losses in the ring. Second, it is preferred to have horizontal transverse momentum directed toward positive x than negative.

The complete study of losses projected at the beginning of the TL permits us to understand beam propagation and loss reason.

4.2.3.2 At screen stations location

The acceptance window corresponds to the location where particles have to be if one wants to propagate them until the end of the first ring's turn. Unfortunately, in reality, it is impossible to compare the beam position at the beginning of the TL to this window as there is no diagnostic to measure the beam position there. But one may use the same principle of projection of losses at location of diagnostics of the accelerator.

The Fig. 4.8 represents the projection of losses at the first screen station of the TL. As this station is not in the line leading to the ring, one must first select the particles, propagate them to the end of the first ring's turn with losses record, and then do a second propagation of the same particles, this time toward the straight line leading to the screen station.

Once again, no one may discriminate particles lost in the ring by their location, but the acceptance window permits knowing where the beam must be if one wants to lead it to the ring. The risk of losses may be evaluated by comparing actual beam positioning to this beam acceptance window.

According to the Fig. 4.8, the dimension of the acceptance window ($\pm 7.5\,\mathrm{mm} \times \pm 4\,\mathrm{mm}$) are within the YAG or OTR screen ($25\,\mathrm{mm} \times 17.7\,\mathrm{mm}$), hence checking that the beam is at the centre of the first screen station of the TL and not at the edge must provide a first essential verification before going into the remaining part of the TL.

Similar studies may be done for each accelerator element, especially screen stations (SST) and beam position monitors (BPM), to constrain the risk of losses. On the second SST of the TL (Fig. 4.9a), the acceptance window is similar to the first SST. Still, some lost-free regions seem to form. In the third SST of the TL, the lost-free region, in the middle, continues growing with a square window defined by x between $-5\,\mathrm{mm}$ and $10\,\mathrm{mm}$ and y within $\pm 2\,\mathrm{mm}$. This phenomenon corresponds to a migration of the soon-to-be-lost particles toward the edge of the beam.

Once the beam enters the ring, BPMs can also be used as a warning for further losses as the acceptance window is well defined there (Fig. 4.10) in the upper-right and lower-right part of the first BPM passing by the beam and in the upper-left and lower-left portion of the second one. One may also notice that in the first BPM of the ring - during the injection - the acceptance window is not centred on the BPM but rather centred around $x = 9\,\mathrm{mm}$, $y = 0\,\mathrm{mm}$. This BPM is between the septum and the kicker, where the injected beam does not follow the reference trajectory of the ring, on which is centred the BPM.

This method is less accurate on BPMs as those types of equipment only measure the position of the charge centre of the beam and not its size. Still, if the beam centroid is outside the acceptance window, a large part of the beam will be certainly lost.

Prolonging this study on more turns could provide more accurate acceptance and reduce the risk of beam losses even more.

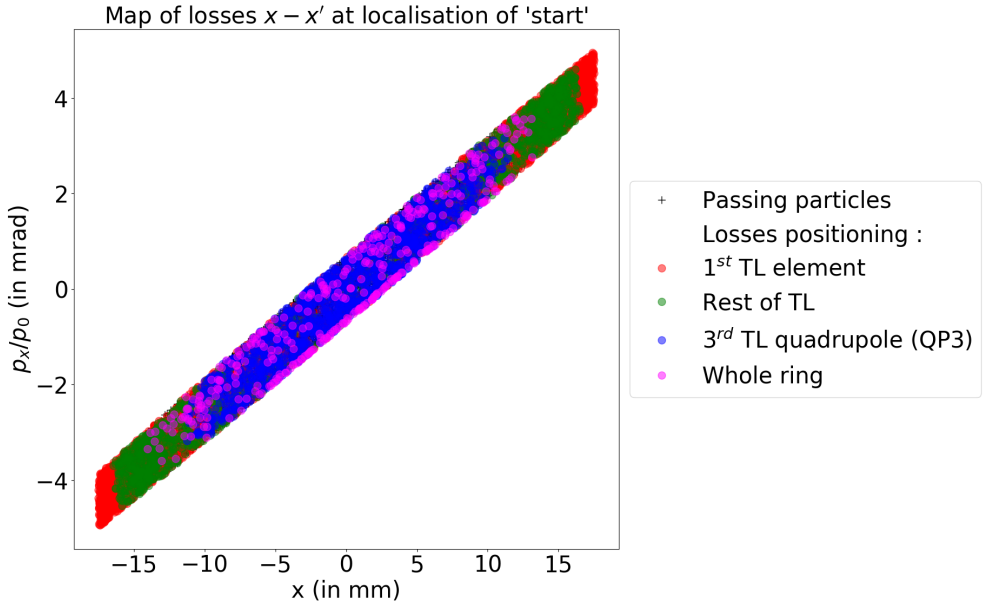

(a) Maps of losses in x-x' plane.

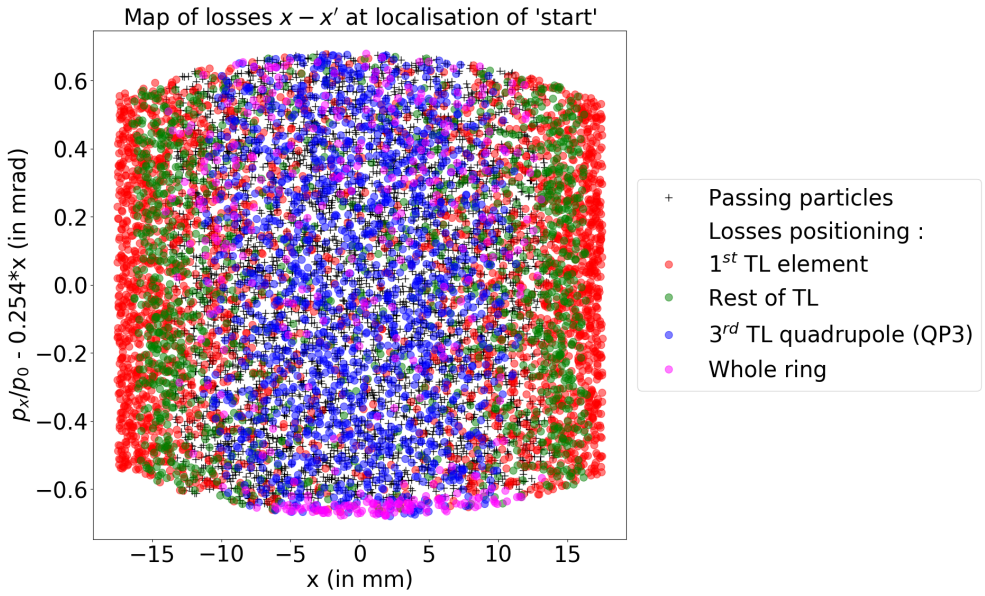

(b) Maps of losses in x-x' plane tilted to visualise the losses easily.

Figure 4.6: Map of losses of the identical 10000 particles than Fig. 4.4 tracked along the TL and the first turn in the ring, projected at the beginning of the TL (named 'start') in x-x' plane. Black crosses represent the positions of particles at 'start' which complete the first ring turn without being lost. Dots are particles' positions at 'start' which are lost during the propagation, and the colours represent the lost location. Those locations are: in the very first element of the TL in red, in the 3^{rd} quadrupole of the TL in blue, in the remaining part of the TL (mostly before the 3^{rd} quadrupole) in green and in the ring in pink.

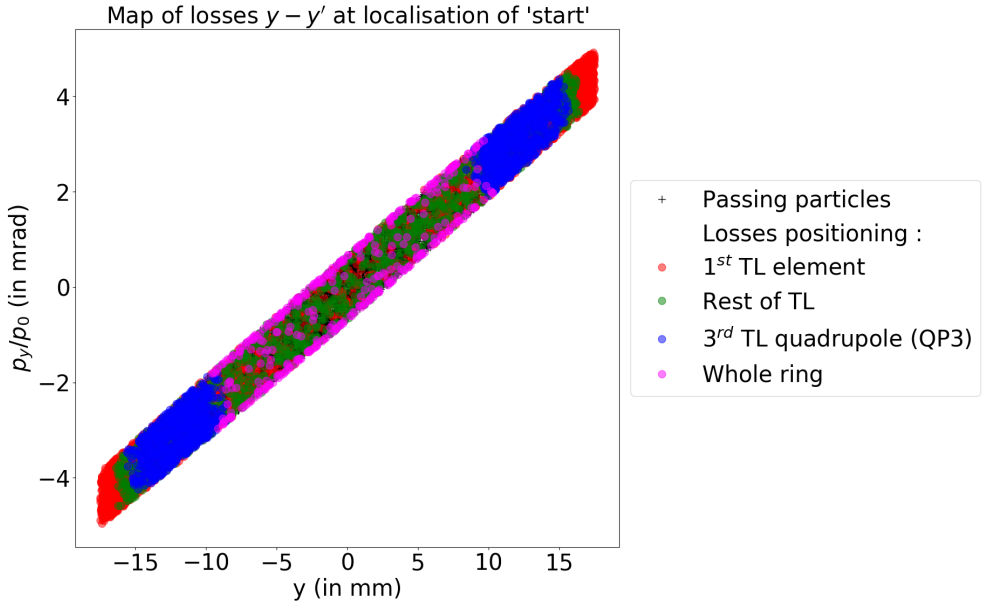

(a) Maps of losses in y-y' plane.

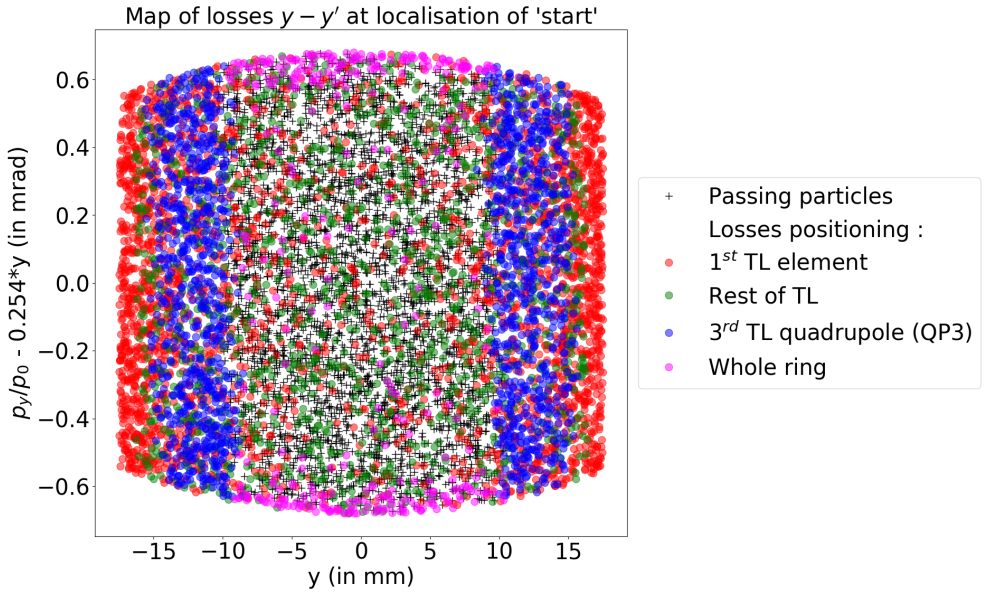

(b) Maps of losses in y-y' plane tilted to visualise the losses easily.

Figure 4.7: Map of losses of the identical 10000 particles than Fig. 4.4 tracked along the TL and the first turn in the ring, projected at the beginning of the TL (named 'start') in the y-y' plane. Black crosses represent the position of particles at 'start' which complete the first ring turn without being lost. Dots are particles' positions at 'start' which are lost during the propagation, and the colours represent the lost location. Those locations are: in the very first element of the TL in red, in the 3^{rd} quadrupole of the TL in blue, in the remaining part of the TL (mostly before the 3^{rd} quadrupole) in green and in the ring in pink.

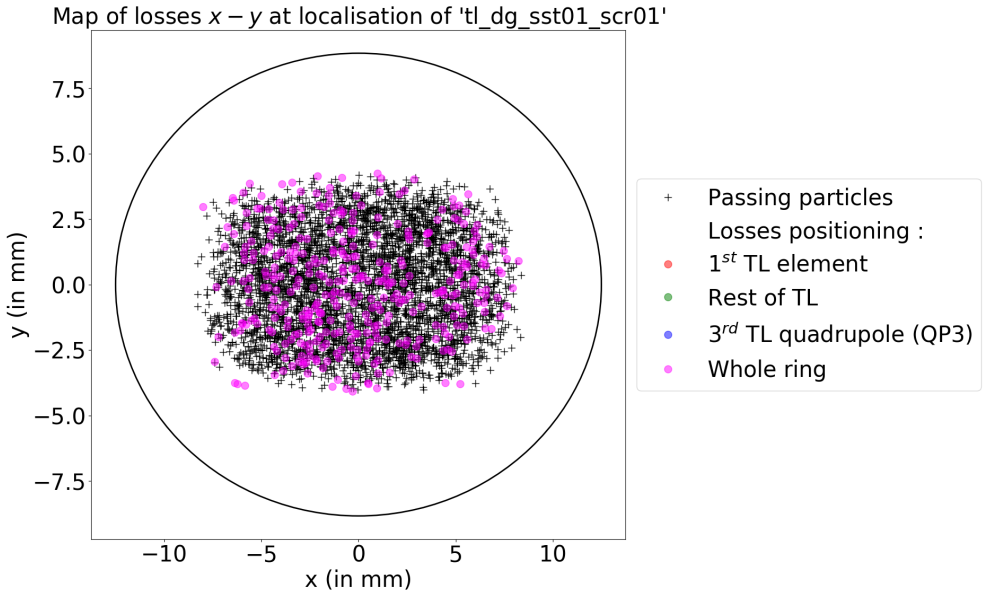

Figure 4.8: Map of losses of the identical 10000 particles than Fig. 4.4 tracked along the TL and the first turn in the ring, projected at the first screen station of the transfer line (TL/DG/SST.01), represented in black line. The station is in a different line than the ring; hence two simulations are needed: one to record the losses and one to project the particles to the screen station. Black crosses represent the position of particles at screen location that should have achieved to travel from the beginning of the TL to the end of the first ring turn without being lost if they had followed this path. Pink dots are particles' positions at screen location that should have been lost in the ring if they had followed this path.

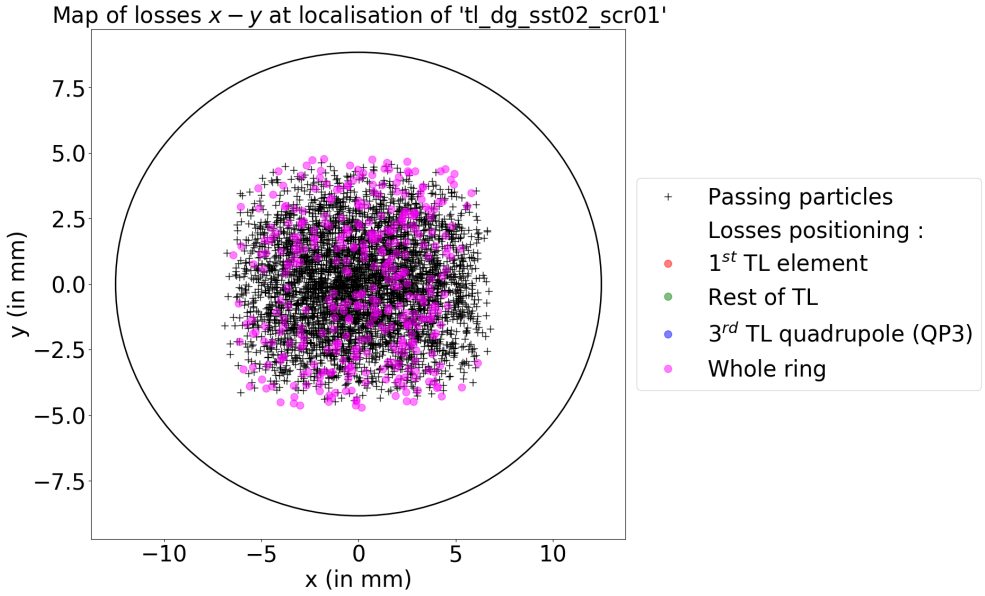

(a) Maps of losses in x-y plane projected on TL/DG/SST.02.

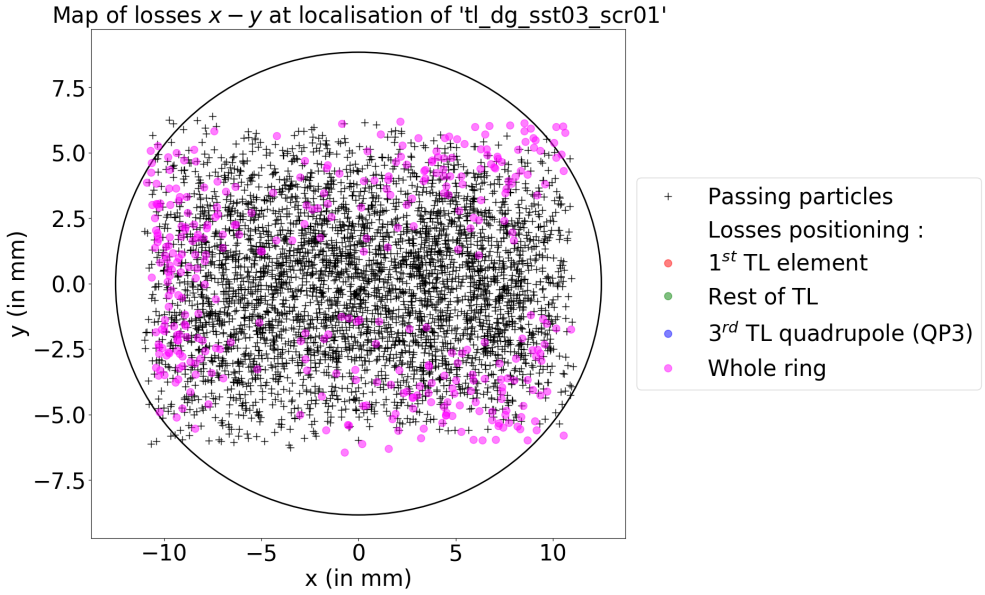

(b) Maps of losses in x-y plane projected on TL/DG/SST.03.

Figure 4.9: Map of losses of the identical 10000 particles than Fig. 4.4 tracked along the TL and the first turn in the ring, projected at the second (TL/DG/SST.02) and third (TL/DG/SST.03) screen station of the transfer line, represented in black line. Black crosses represent the position of particles at the screen location that complete the first ring turn without being lost. Pink dots are particles' positions at the screen location that are lost in the ring.

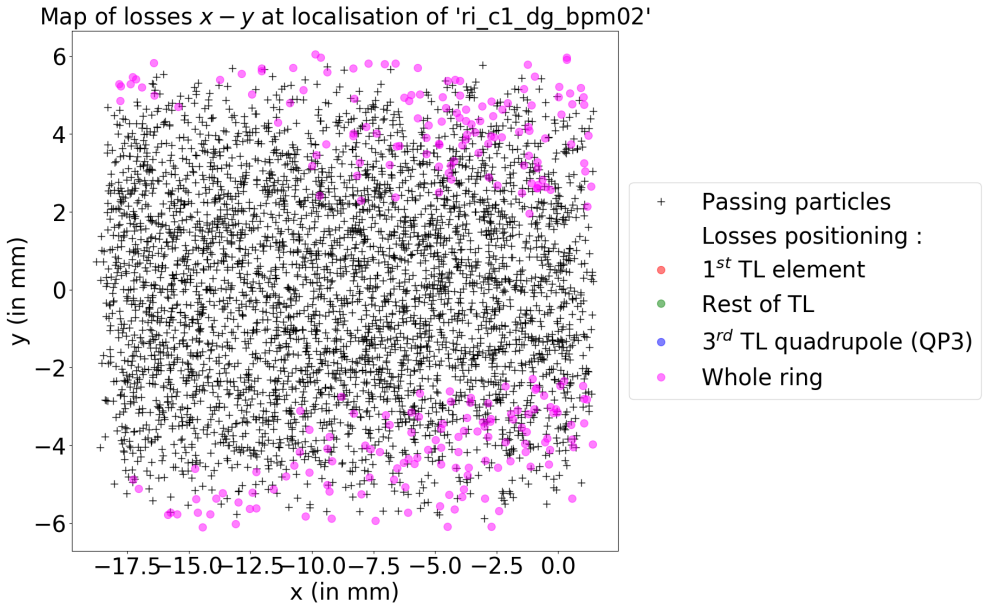

(a) Maps of losses in x-y plane projected on RI-C1/DG/BPM.02.

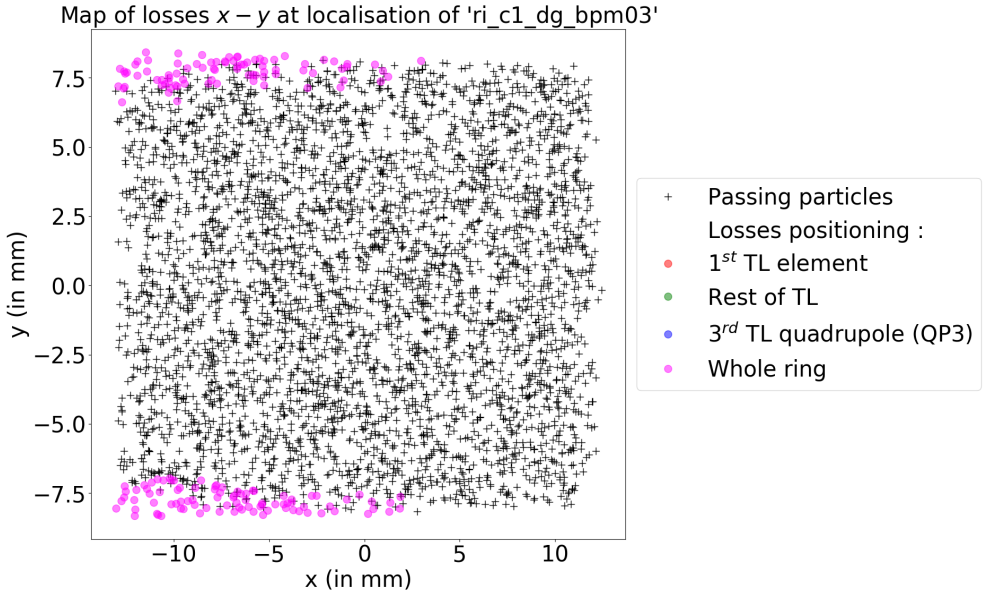

(b) Maps of losses in x-y plane projected on RI-C1/DG/BPM.03.

Figure 4.10: Map of losses of the identical 10000 particles than Fig. 4.4 tracked along the TL and the first turn in the ring, projected at the first (RI-C1/DG/BPM.02) and second BPM (RI-C1/DG/BPM.03) seen by the beam in the ring. Black crosses represent the position of particles at the BPM's location that complete the first ring turn without being lost. Pink dots are particles' positions at the screen location that are lost in the ring.

4.3 . Conclusion

An electron losses study has been done on the TL and ring first turn of ThomX. Some possible damages caused by losses has been pointed out, and the main risk seems to be a diminution of the X-rays flux. Nevertheless, the risk of beam loss is small because, according to simulation, only particles very far from simulated beam characteristics may be lost. Finally, a comparison of beam positioning at diagnostics location with the acceptance window at this location is done to decrease even more losses risk. The last screen station of the TL can be used to check that the beam is inside the completely free-losses zone before try to inject the beam in the ring.

Now that the code to study the losses is developed, new studies with non-zero steerers strength or element misalignment can be done easily and could be used for a better understanding of the beam propagation.

5 - Injection feedback

Contents

Electrons injection into the ring is one of the critical moments for the beam propagation. An incorrect injection induces oscillations of the bunch in the ring that may reduce the electron bunch's and photon beam's overlap, which diminishes the production of X-rays. If the oscillation is large, the bunch can even be lost, implying damage to components like electronics because of radiation emission. This chapter focuses on an injection feedback code (section 5.1) and its test on MadX simulations (section 5.2 and section 5.3).

5.1 . Ring injection

5.1.1 . Reminder on the injection simulation

As explained in section 3.2.3, the injection on ThomX uses an injection dipole to deflect the beam toward the ring. Then, a septum corrects a large part of this deflection such that the beam is at the centre of the beam pipe inside the injection kicker. Finally, this kicker finishes deflection correction to set the beam on the ring orbit.

Between the septum and the kicker, the beam passes through two quadrupoles (RI-C1/AE/QP.03 hereafter called QP3 and RI-C1/AE/QP.04 hereafter called QP4) but not at their magnetic centre (see Fig. 5.1). This off-axis propagation kicks the beam. To simulate this kick, it has been chosen to do a change of frame at the exit of the septum and let the beam propagate as if the reference trajectory was already the ring one. The change of frame is as follows :

- $X \rightarrow X + \Delta X$

  $\Delta X = -15.5\,\mathrm{mm}$: distance between the injection reference frame's origin and the ring's one at the exit of the septum

- $X' \rightarrow X' + \Delta X'$

  $\Delta X' = \theta = 10.72948\,\mathrm{mrad}$: angle between both frames at the exit of the septum

This change of frame and a kicker's kick of $\chi = -13.0345\,\mathrm{mrad}$ allow a nearly perfect injection in the ring.

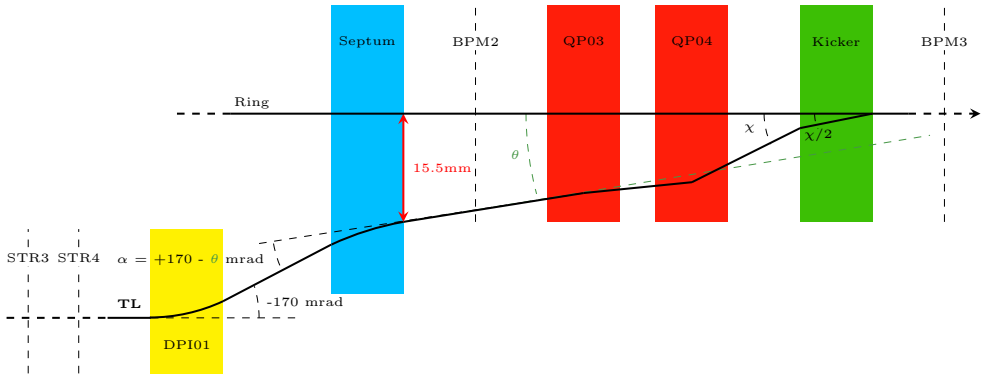

Figure 5.1: Drawing (not to scale) of the injection of ThomX. χ is the kick angle induced by the kicker. Acronym are the following : STR = Steerer; DPI = Injection Dipole; BPM = Beam Position Monitor; QP = Quadrupole. The associated numbers correspond to the ThomX nomenclature.

With those parameters, the beam does not pass at the centre of the first beam position monitor during the injection but rather at a position x $= -8.9\,\mathrm{mm}$. For the other BPMs, the nominal ring path passes through their centre. An estimation of the quality of injection may be done by comparing the beam position measured by BPMs with theoretical positions.

5.1.2 . Injection feedback principle

An injection feedback code has been developed to improve the injection from one beam to the next. The principle of this injection feedback system is to measure

the position of the beam at the localisation of the two firsts Beam Position Monitors (RI-C1/DG/BPM.02 hereafter called BPM2 and RI-C1/DG/BPM.03 hereafter called BPM3) of the ring and to compute the deflection on the two last steerers (TL/AE/STR.03 hereafter called STR3 and TL/AE/STR.04 hereafter called STR4) of the Transfer Line and the kicker's kick that should have been needed to enter the ring ideally, as shown Fig. 5.2.

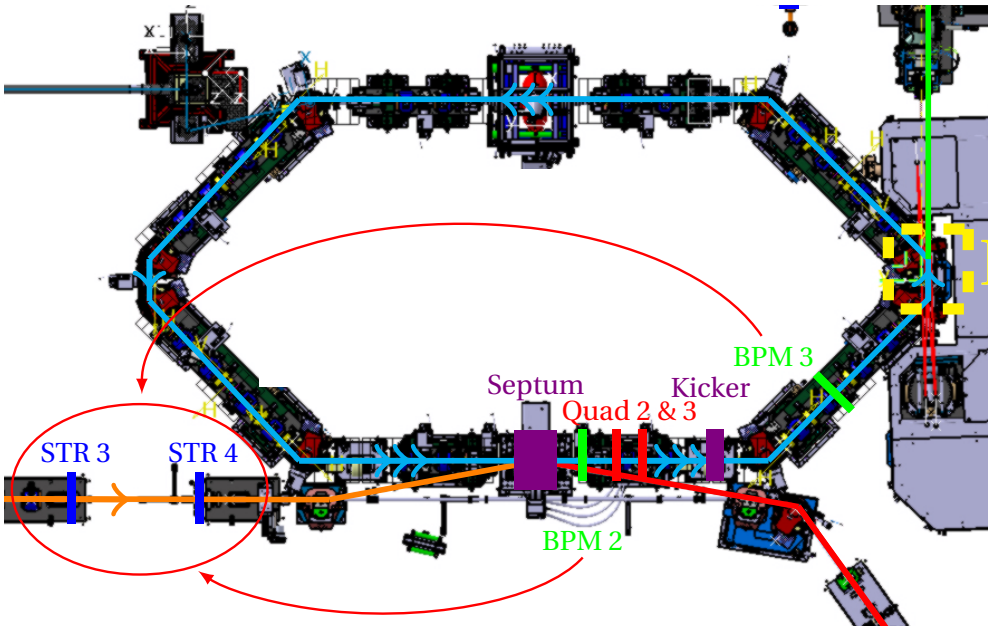

Figure 5.2: Zoom on Fig. 2.2 around the ThomX ring injection devices to show the main elements used for injection feedback. Acronym are the following : STR = Steerer; BPM = Beam Position Monitor; QP = Quadrupole. The associated numbers correspond to the ThomX nomenclature.

To be more precise, the BPM3 position is used to compute - using the equation of propagation from BPM2 to BPM3 - the momentum of the beam centroid inside the BPM2. A back-propagation of the 4D vector (x,x',y,y') from BPM2 to STR3 allows knowing the 4D beam vector before the first steerer. Similar computations are done with the desired parameters summarised in Tab. 5.1. With both the initial and the desired vector before the steerers, one may compute the steerers' strength needed to achieve desired positions knowing the initial ones.

The additional x' = 0 condition ensures a smooth injection in the ring. At least five degrees of freedom are needed to have a solution with five constrains. The steerers' strength gives four, and the kicker's kick is used for this additional fifth condition.

To compute the propagation equation with a parametrisation of the steerers' strength and the kicker's kick, a homemade code of linear transfer matrix has been

Table 5.1: Desired position inside the two first BPMs of the ring: BPM2 and BPM3. The condition X'_d = 0 is added to ensure a smooth injection and is provided by the kicker's kick.

	BPM2	BPM3
X_d	$-8.9\,\mathrm{mm}$	0
X'_d		0
Y_d	0	0

developed on MatLab. More details about the code are available in section 3.3.

From the linearity of this method, one must be sure to obtain linear equations for either downstream or upstream propagation. Because of the change of frame, steerers and kicker's kick, those equations cannot be written as a transfer matrix time a vector as several constant terms appear. In full generality, the equation of propagation from 1 to 2 should be as defined in the Eq. (5.1).

$$\begin{cases} X_2 &= f_X(X_1, X'_1, Y_1, Y'_1, Z_1, Z'_1, \text{parameters}) \\ X'_2 &= f_{X'}(X_1, X'_1, Y_1, Y'_1, Z_1, Z'_1, \text{parameters}) \\ Y_2 &= f_Y(X_1, X'_1, Y_1, Y'_1, Z_1, Z'_1, \text{parameters}) \\ Y'_2 &= f_{Y'}(X_1, X'_1, Y_1, Y'_1, Z_1, Z'_1, \text{parameters}) \\ Z_2 &= f_Z(X_1, X'_1, Y_1, Y'_1, Z_1, Z'_1, \text{parameters}) \\ Z'_2 &= f_{Z'}(X_1, X'_1, Y_1, Y'_1, Z_1, Z'_1, \text{parameters}) \end{cases} \tag{5.1}$$

Where f_i, for i = X,X',Y,Y',Z,Z', is a linear function of the variables X_1, X'_1, Y_1, Y'_1, Z_1, Z'_1.

The kicker's kick and steerers' strength are the only parameters considered for those equations. As their computation adds a parametrised constant in the x or y plane to the equation, the f_i's functions are also linear regarding those parameters. The change of frame only adds a constant term in the x plane by definition.

By assuming no coupling between x and y planes nor between y and z planes but one between x and z planes because of bending magnets, one may rewrite the Eq. (5.1) into the Eq. (5.2).

$$\begin{cases} \mathbf{X}_2 &= a_{x,x}\mathbf{X}_1 + a_{x,x'}\mathbf{X'}_1 + a_{x,z}\mathbf{Z}_1 + a_{x,z'}\mathbf{Z'}_1 + \sum_{param} a_{x,param}\mathbf{param} + a_{x,cst} \\ \mathbf{X'}_2 &= a_{x',x}\mathbf{X}_1 + a_{x',x'}\mathbf{X'}_1 + a_{x',z}\mathbf{Z}_1 + a_{x',z'}\mathbf{Z'}_1 + \sum_{param} a_{x',param}\mathbf{param} + a_{x,cst} \\ \mathbf{Y}_2 &= a_{y,y}\mathbf{Y}_1 + a_{y,y'}\mathbf{Y'}_1 + a_{y,z}\mathbf{Z}_1 + a_{y,z'}\mathbf{Z'}_1 + \sum_{param} a_{y,param}\mathbf{param} \\ \mathbf{Y'}_2 &= a_{y',y}\mathbf{Y}_1 + a_{y',y'}\mathbf{Y'}_1 + a_{y',z}\mathbf{Z}_1 + a_{y',z'}\mathbf{Z'}_1 + \sum_{param} a_{y',param}\mathbf{param} \\ \mathbf{Z}_2 &= a_{z,x}\mathbf{X}_1 + a_{z,x'}\mathbf{X'}_1 + a_{z,z}\mathbf{Z}_1 + a_{z,z'}\mathbf{Z'}_1 \\ \mathbf{Z'}_2 &= a_{z',x}\mathbf{X}_1 + a_{z',x'}\mathbf{X'}_1 + a_{z',z}\mathbf{Z}_1 + a_{z',z'}\mathbf{Z'}_1 \end{cases} \tag{5.2}$$

As we consider the propagation of the beam's centroid, let us consider that it is on time with the reference particles - $Z = 0$ - and stays so all along the injection

- $Z' = 0$. We can keep only the four transverse equations of Eq. (5.3) from those assumptions.

$$\begin{cases} \mathbf{X}_2 &= a_{x,x}\mathbf{X}_1 + a_{x,x'}\mathbf{X'}_1 + \sum_{param} a_{x,param}\mathbf{param} + a_{x,cst} \\ \mathbf{X'}_2 &= a_{x',x}\mathbf{X}_1 + a_{x',x'}\mathbf{X'}_1 + \sum_{param} a_{x',param}\mathbf{param} + a_{x',cst} \\ \mathbf{Y}_2 &= a_{y,y}\mathbf{Y}_1 + a_{y,y'}\mathbf{Y'}_1 + \sum_{param} a_{y',param}\mathbf{param} \\ \mathbf{Y'}_2 &= a_{y',y}\mathbf{Y}_1 + a_{y',y'}\mathbf{Y'}_1 + \sum_{param} a_{y',param}\mathbf{param} \end{cases} \tag{5.3}$$

Two equations must be separately considered: the downstream equation from BPM2 to BPM3 and the upstream equation from BPM2 to STR3. The $a_{u,v}$'s constants are delivered by the linear matrix code and are considered known values in this chapter.

5.1.2.1 Equation from BPM2 to BPM3

Between the BPM2 and the BPM3 there is no change of frame to consider, which means that constant terms of the Eq. (5.3) $a_{x,cst}$ and $a_{x',cst}$ are null. Moreover, the only parameter to consider is the kicker's kick that impacts only the x plane. Hence the Eq. (5.3) may be written as :

$$\begin{cases} \mathbf{X}_{BPM3} &= a_{x,x}\mathbf{X}_{BPM2} + a_{x,x'}\mathbf{X'}_{BPM2} + a_{x,kick}\mathbf{kick} \\ \mathbf{X'}_{BPM3} &= a_{x',x}\mathbf{X}_{BPM2} + a_{x',x'}\mathbf{X'}_{BPM2} + a_{x',kick}\mathbf{kick} \\ \mathbf{Y}_{BPM3} &= a_{y,y}\mathbf{Y}_{BPM2} + a_{y,y'}\mathbf{Y'}_{BPM2} \\ \mathbf{Y'}_{BPM3} &= a_{y',y}\mathbf{Y}_{BPM2} + a_{y',y'}\mathbf{Y'}_{BPM2} \end{cases} \tag{5.4}$$

5.1.2.1.1 Initial propagation If one considers the actual beam - denoted with an i subscript for initial - we know the kicker's kick as it is the one used at this instant, but also the initial positions $(X_{BPM2,i}, Y_{BPM2,i}, X_{BPM3,i}, Y_{BPM3,i})$ as they are measured. Therefore, the remaining unknowns are $(X'_{BPM2,i}, Y'_{BPM2,i})$. After inverting Eq. (5.4), one may compute these unknowns thanks to Eq. (5.5).

$$\begin{cases} \mathbf{X'}_{BPM2,i} &= \frac{\mathbf{X}_{BPM3,i} - a_{x,x}\mathbf{X}_{BPM2,i} - a_{x,kick}\mathbf{KICK}_i}{a_{x,x'}} \\ \mathbf{Y'}_{BPM2,i} &= \frac{\mathbf{Y}_{BPM3,i} - a_{y,y}\mathbf{Y}_{BPM2,i}}{a_{y,y'}} \end{cases} \tag{5.5}$$

5.1.2.1.2 Desired propagation Similarly, one may compute the desired momentum $(X'_{BPM2,d}, Y'_{BPM2,d})$ from the desired position $(X_{BPM2,d}, Y_{BPM2,d}, X_{BPM3,d}, Y_{BPM3,d})$. This time another constrain is added - $X'_{BPM3,d} = 0$ - to smooth the injection. A third unknown has to be realised to permit this third degree of freedom. It way choose to use the kicker's kick $kick_d$. From the Eq. (5.4), one may compute unknowns using Eq. (5.6).

$$\begin{cases} \mathbf{X'}_{BPM2,d} = \frac{a_{x,kick}\times\mathbf{X}_{BPM3,d}-(a_{x',kick}\times a_{x,x}-a_{x',x}\times a_{x,kick})\times\mathbf{X}_{BPM2,d}}{a_{x',x'}\times a_{x,kick}-a_{x,x}\times a_{x',kick}} \\ \mathbf{KICK}_d = \frac{a_{x',x'}\times\mathbf{X}_{BPM3,d}-(a_{x',x'}\times a_{x,x}-a_{x',x}\times a_{x,x'})\times\mathbf{X}_{BPM2,d}}{a_{x,x}\times a_{x',kick}-a_{x',x'}\times a_{x,kick}} \\ \mathbf{Y'}_{BPM2,d} = \frac{\mathbf{Y}_{BPM3,d}-a_{y,y}\mathbf{Y}_{BPM2,d}}{a_{y,y'}} \end{cases} \quad (5.6)$$

This calculation may be done once and for all as the nominal parameters - quadrupole strength, septum angle, elements positioning, ... - should not change but must be recomputed if they do.

5.1.2.2 Equation from BPM2 to STR3

Once the transverse 4D vector is known at the localisation of BPM2, one must compute the reverse propagation from BPM2 to STR3. This time, the frame change occurred during the propagation, ensuring a constant term on the x-x' plane. The parameters to be considered are the deviations induced by the steerers. Four parameters must be considered. Dev_{x3} (resp. Dev_{x4}) correspond to the horizontal deflection created by STR3 (resp. STR4) and will impact only the x plane - as no coupling x-y is considered - whereas the vertical deflection is symbolised by Dev_{y3} (resp. Dev_{y4}).

As the invert propagation stops just after the steerer STR3, the last computation consists of adding Dev_{x3} and Dev_{y3} to X' and Y' without propagation to permit those parameters to impact beam position X and Y. Hence, one may consider $a_{x,dev_{x3}} = 0 = a_{y,dev_{y3}}$.

Under those considerations, Eq. (5.3) can be rewritten as Eq. (5.7).

$$\begin{cases} \mathbf{X}_{STR3} = a_{x,x}\mathbf{X}_{BPM2} + a_{x,x'}\mathbf{X'}_{BPM2} + a_{x,dev_{x3}}\mathbf{Dev}_{x3} + a_{x,dev_{x4}}\mathbf{Dev}_{x4} \\ \mathbf{X'}_{STR3} = a_{x',x}\mathbf{X}_{BPM2} + a_{x',x'}\mathbf{X'}_{BPM2} + a_{x',dev_{x3}}\mathbf{Dev}_{x3} + a_{x',dev_{x4}}\mathbf{Dev}_{x4} \\ \mathbf{Y}_{STR3} = a_{y,y}\mathbf{Y}_{BPM2} + a_{y,y'}\mathbf{Y'}_{BPM2} + a_{y,dev_{y3}}\mathbf{Dev}_{y3} + a_{y,devy4}\mathbf{Dev}_{y4} \\ \mathbf{Y'}_{STR3} = a_{y',y}\mathbf{Y}_{BPM2} + a_{y',y'}\mathbf{Y'}_{BPM2} + a_{y',dev_{y3}}\mathbf{Dev}_{y3} + a_{y',dev_{y4}}\mathbf{Dev}_{y4} \end{cases} \quad (5.7)$$

This system of equations is true for both the initial parameters (i subscript) and the desired parameters (d subscript). To ensure physical coherence, one may write $(X,PX,Y,PY)_{str3,i} = (X,PX,Y,PY)_{str3,d}$ which gives a system of four equations with four unknowns, the desired deviations of the steerers : Dev_{x3}, Dev_{y3}, Dev_{x4}, Dev_{y4}. One may solve this system and obtain the Eq. (5.8) as the solution for the deflections needed in the steerers.

$$\begin{cases} \mathbf{Dev}_{x4,d} = \frac{a_{x,x}\mathbf{X}_i + a_{x,px}\mathbf{PX}_i + a_{x,devx4}\mathbf{Dev}_{x4,i} - a_{x,x}\mathbf{X}_d - a_{x,px}\mathbf{PX}_d}{a_{x,devx4}} \\ \mathbf{Dev}_{y4,d} = \frac{a_{y,y}\mathbf{Y}_i + a_{y,py}\mathbf{PY}_i + a_{y,devy4}\mathbf{Dev}_{y4,i} - a_{y,y}\mathbf{Y}_d - a_{y,py}\mathbf{PY}_d}{a_{y,devy4}} \\ \mathbf{Dev}_{x3,d} = \frac{a_{px,x}\mathbf{X}_i + a_{px,px}\mathbf{PX}_i + a_{px,devx3}\mathbf{Dev}_{x3,i} + a_{px,devx4}\mathbf{Dev}_{x4,i} - a_{px,x}\mathbf{X}_d - a_{px,px}\mathbf{PX}_d - a_{px,devx4}\mathbf{Dev}_{x4}}{a_{px,devx3}} \\ \mathbf{Dev}_{y3,d} = \frac{a_{py,y}\mathbf{Y}_i + a_{py,py}\mathbf{PY}_i + a_{py,devy3}\mathbf{Dev}_{y3,i} + a_{py,devy4}\mathbf{Dev}_{y4,i} - a_{py,y}\mathbf{Y}_d - a_{py,py}\mathbf{PY}_d - a_{py,devy4}\mathbf{Dev}_{y4}}{a_{py,devy3}} \end{cases} \tag{5.8}$$

Where $\mathbf{U}_v = \mathbf{U}_{BPM2,v}$, with $\mathbf{U} = \mathbf{X}, \mathbf{Y}, \mathbf{PX}, \mathbf{PY}$ and $v = i, d$.

By computing Eq. (5.5), Eq. (5.6) and then Eq. (5.8), one can know which correction should have been used to have a better injection. As this correction is applied to the next beam - which is different to this one - only a fraction of the difference between the initial deflection and the desired one should be applied to avoid over-correction.

Even if the equation of propagation has been computed on MatLab to parameterise the properties of ThomX's elements, this feedback system is developed on python as ThomX control command uses python-based graphical user interface (GUI). The exchange of equation of propagation is done by saving once and for all the MatLab's equation in a file read then by the python code.

Simulations of this injection feedback code applied to the MadX tracking code are presented in the following sections and a a tabular resuming parameters tested is given A .

5.2 . Main injection feedback simulations

5.2.1 . Simulation principle

The injection feedback code is applied to the MadX simulation of the TL and the ring first turn to validate its behaviour.

The idea of this simulation is to select randomly one particle within a particular beam's ellipse (see section 3.2.4) that will represent a beam's centroid. This particle is then tracked inside the MadX simulation with zero steerers' strength and nominal kicker's kick. Those parameter values are denoted as "initial parameters". From MadX results, one may extract beam position on the BPMs of the ring during the first turn. Those beam positions allow computing an estimation of the injection quality using Eq. (5.9).

$$E_U = \sqrt{\frac{1}{\#BPM - 1} \sum_{BPM \neq BPM2} U^2} \tag{5.9}$$

With $U = x,\ x',\ y$ or y'.

This estimator corresponds to the quadratic mean of one of the beam centroid transverse positions regarding the nominal ones for all 23 BPM of the first ring turn. The first BPM - RI-C1/DG/BPM.02 - is excluded as the nominal beam position depends on injection properties, while all other BPMs have a nominal

transverse position of 0. On the real machine, the BPM measures x and y only, but as simulators give access to x' and y', I have chosen to estimate them too. The simulation provides access to the particle's position and momentum at the entrance of each element, which has permitted the creation of a second estimator based on Eq. (5.9) but with a sum of positions in all elements of the ring after the injection. This second estimator gives results similar to the first one, which validates using only BPMs to estimate the ring injection quality. It has been chosen to keep only the first estimator in this study because it is a physical observable that could be compared with measurements when the code would be tested on ThomX.

Then, BPM2 and BPM3 values are used to compute the desired strength of the steerer using the injection feedback code. Finally, a fraction - by default always $10\,\%$ - of the computed correction - hence the difference between the used value and computed ones - is applied to the next iteration. This fraction corresponds to the coefficient of correction. The new MadX tracking can be done with either the same beam (perfect case, section 5.2.3) or a slightly different one (fluctuation case, section 5.2.4). The reference case (section 5.2.2) corresponds to a perfect case where the beam centroid is chosen to be the reference one, i.e. 4D null transverse vector. The longitudinal 2D vector is always taken null in order to consider that the beam centroid is on time with the reference particle.

Those simulations of the injection feedback are done 100 times - which corresponds to 10 secon at $10\,\mathrm{Hz}$ - and one may consider that the simulation has converged to a solution when at least once during the simulation E_x and E_y are both below $0.1\,\mathrm{mm}$ (BPM precision [26]) while at the same time x' and y' are both below $0.1\,\mathrm{mrad}$. The threshold of divergence has been empirically chosen and also seems to fit the BPM precision as there is slightly more than one BPM per meter in the ring and a $1\,\mathrm{m}$ long propagation with $0.1\,\mathrm{mrad}$ divergence corresponds to a $0.1\,\mathrm{mm}$ displacement.

5.2.2 . Reference case

First, let's consider the injection feedback simulation with the reference beam centroid. The initial vector of this specific case correspond to $x = y = 0\,\mathrm{m}$ and $x' = y' = 0\,\mathrm{rad}$.

From the discussion of the injection simulations (section 3.2.3), we know that the injection in the ring is not entirely perfect in the horizontal plane, but it is in the vertical one. This behaviour can be noticed on the first iteration of Fig. 5.3. This figure represents the injection's estimators against the number of iterations, and the first one is always done with nominal parameters, i.e. zero steerers' strength and nominal kicker's kick.

One may notice that both E_y and $E_{y'}$ remain null all along the iterations, which means that the injection code would not modify a perfect injection in the vertical plane. For the horizontal plane, both estimators E_x and $E_{x'}$ increase to reach a limit plateau at $E_x = 6.1\,\mu\mathrm{m}$ and $E_{x'} = 6.3\,\mu\mathrm{rad}$. This non-zero plateau seems

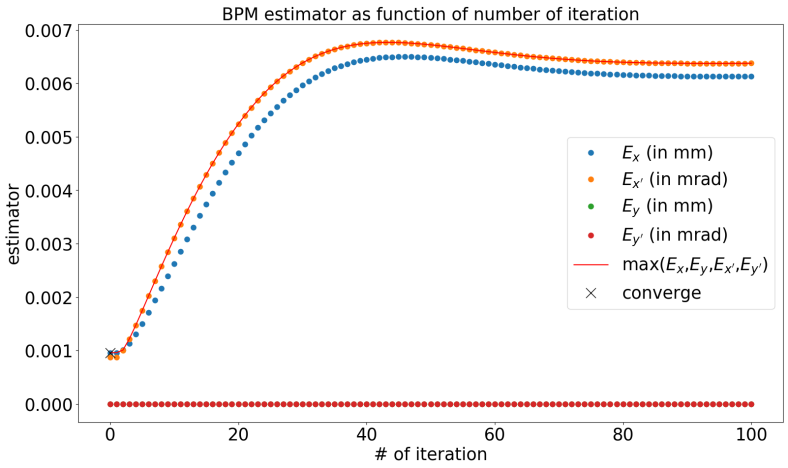

Figure 5.3: Estimation of the ring injection against iterations of the injection feedback for the reference beam centroid (null 4D transverse vector at start of the TL).

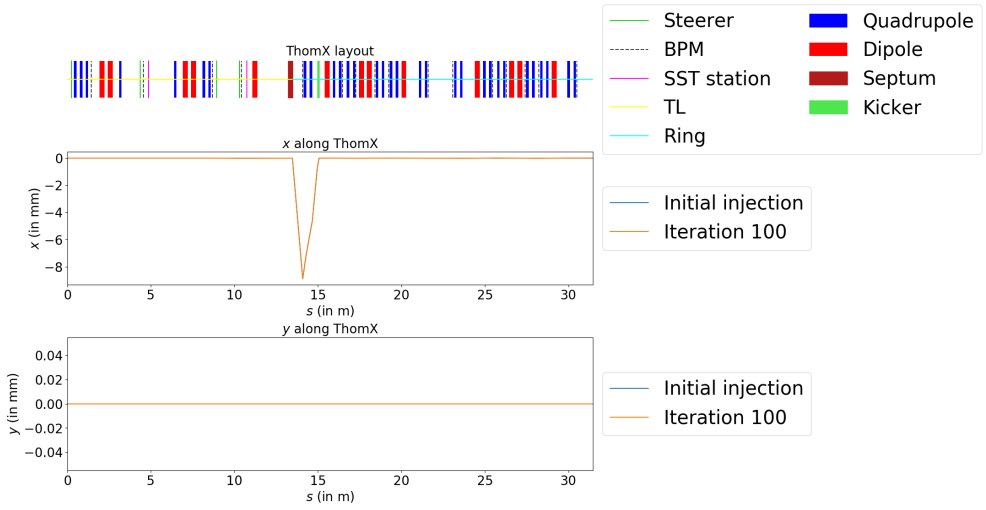

Figure 5.4: ThomX layout (top) and tracking of particles along ThomX TL and first ring turn in x plane (middle) and y plane (bottom). Particles represent the reference beam centroid before applying the injection feedback and after 100 iterations. Both curves are so close that they cannot be distinguished. The peak around $14\,\mathrm{m}$ in the x plane is a computing artefact due to the change of frame between the septum and the kicker (section 3.2.3).

to come from the difference between the MadX tracking code - which considers some non-linearities - and the linear matrix computation done for the feedback system. One may interpret it as a failure of the injection feedback because the

injection is worse after the feedback. Still, even the worse estimation stays well below thresholds of convergence ($100\,\mu\mathrm{m}, 100\,\mu\mathrm{rad}$) based on the precision of the BPM. Hence those differences can be neglected. The tracking of the centroid with initial and last computed parameters (Fig. 5.4) also leads to this conclusion of no noticeable differences as both curves superimpose.

The convergence point is the first iteration where all estimators are below a certain convergence threshold. If those conditions are achieved at least once during the iterations - and iterations do not lead to loss of the beam centroid - the simulation is considered convergent. In the reference case, this criterion of convergence seems weird because if one sets the threshold at $3\,\mu\mathrm{m}$ and $3\,\mu\mathrm{rad}$, the simulation would have been considered convergent even if the limits in x-x' planes are twice higher than the threshold. Nevertheless, ignoring cases where the convergence point is obtained before the first feedback corrections are applied may give a sense to the convergence criterion. If the convergence occurred after the second iteration, then the injection feedback has improved the injection at least once.

5.2.3 . Perfect case

In this section, the simulations are done with the same particle representing the same beam centroid at each iteration. This particle is randomly selected within the 1-σ beam ellipse.

5.2.3.1 One simulation example

An example of particle propagation with initial parameters is shown Fig. 5.5. This particle is used to represent a beam centroid during the injection feedback and Fig. 5.6 shows the injection estimation at each iteration, while Fig. 5.7 compares the initial propagation with the one after 100 iterations of the injection feedback.

The initial injection (Fig. 5.5) clearly shows a bad injection as the beam centroid oscillates a lot in the ring. This behaviour is corroborated by the estimator (Fig. 5.6) of iterations 0 - initial particle selection - and 1 - first injection feedback iteration computation, not yet applied to MadX tracking - which give $E_x = 0.22\,\mathrm{mm}$, $E_{x'} = 0.20\,\mathrm{mrad}$, $E_y = 0.32\,\mathrm{mm}$ and $E_{y'} = 0.43\,\mathrm{mrad}$. Hence, there is an oscillation of the order of some hundreds of micrometers in the ring first turn. At first, all estimators decrease, until the 10^{th} iteration, where E_x start to increase. Given that other estimators continue to improve and E_x does not grow too much, this behaviour is not an issue. According to the steerer strength computed at each iteration (Fig. 5.8), an inversion with large variations of both vertical steerers strength occurred when E_x increases. Those two phenomena seem correlated but have yet to be completely understood. One possible explanation is that, for small steerer strength computed, the difference between MadX simulation and linear matrix calculation is larger, which means a less accurate correction of the injection.

Finally, around the 20^{th} iteration, E_x decreases again and the convergence

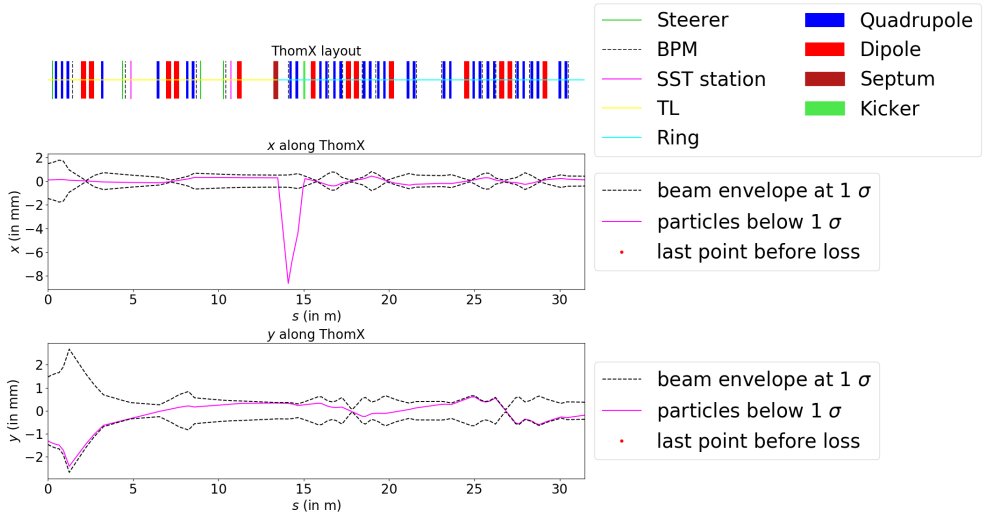

Figure 5.5: ThomX layout (top) and tracking of particles along ThomX TL and first ring turn in x plane (middle) and y plane (bottom). Particles represent the beam centroid randomly selected within 1-σ beam ellipse before applying the injection feedback. The steerers' strengths are null and the kicker's kick is nominal. The peak around $14\,\mathrm{m}$ in the x plane is a computing artefact due to the change of frame between the septum and the kicker (section 3.2.3).

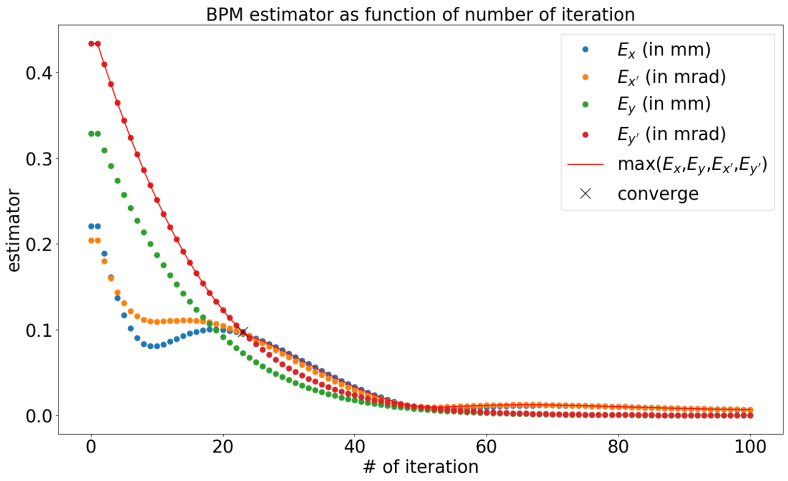

Figure 5.6: Estimation of the ring injection against iterations of the injection feedback. The particle used for this simulation of the injection feedback is the one of Fig. 5.5, randomly selected within the 1-σ beam ellipse. The convergence iteration is defined as the first iteration where E_x and E_y are below $0.1\,\mathrm{mm}$ and $E_{x'}$ and $E_{y'}$ are below $0.1\,\mathrm{mrad}$.

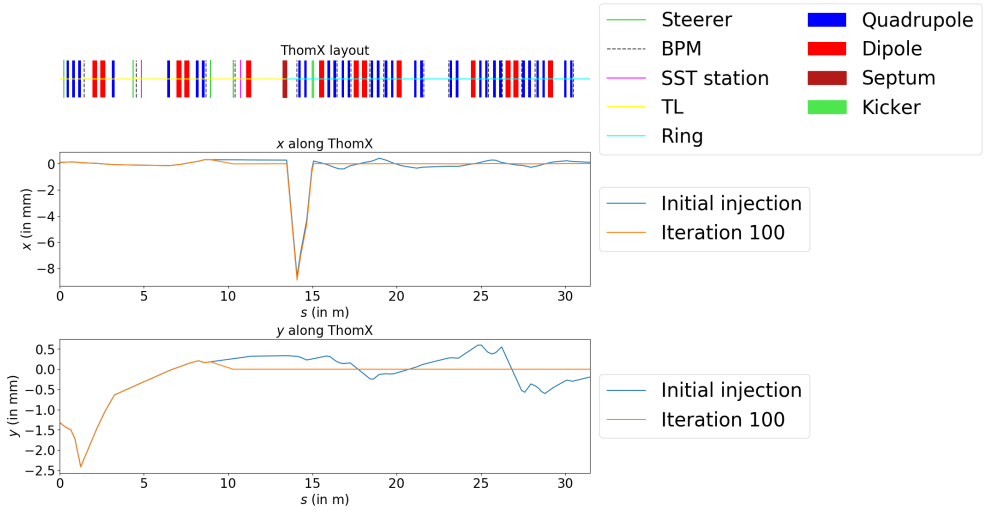

Figure 5.7: ThomX layout (top) and tracking of particles along ThomX TL and first ring turn in x plane (middle) and y plane (bottom). Particles represent the beam centroid randomly selected within 1-σ beam ellipse before applying the injection feedback (blue) and after 100 iterations (orange). The only difference between the two cases is the strength of the steerers (green line on the ThomX layout) around $10\,\mathrm{m}$ and the kicker's kick (thick green rectangle) around $15\,\mathrm{m}$. The peak around $14\,\mathrm{m}$ in the x plane is a computing artefact due to the change of frame between the septum and the kicker (section 3.2.3).

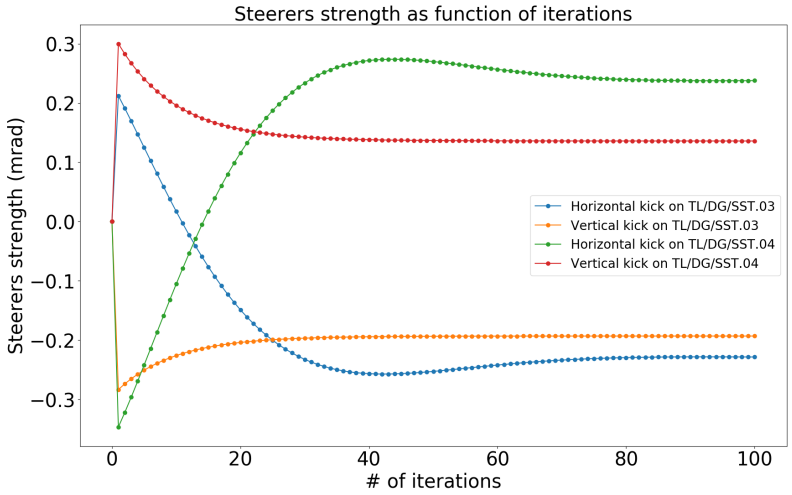

Figure 5.8: Steerer strength computed at each iterations of the simulation Fig. 5.6

criterion is obtained at the iteration 23 (black cross). At the end, a zero plateau in y-y' plane seems to be reached while x and x' estimators are around $E_x = 6.6\mu\mathrm{m}$

and $E_{x'} = 6.7\mu\text{rad}$ and seems to continue decreasing slowly.

5.2.3.2 Simulation of 1000 beam centroids

The above section shows only one particular example. To go further, let's select randomly 1000 particles - that represent as many beam centroids - and simulate the injection feedback for each of them separately.

Results of those simulations are summarised in the histogram of the first iteration where the convergence criterion is obtained (Fig. 5.9a) and the histogram of number of time estimators are below the criterion of convergence (Fig. 5.9b) over 100 iterations. One notices that on the 1000 simulations, no particle loss occurred, which would have meant that the injection feedback had created huge oscillations. Moreover, the convergence is always obtained, and this in less than 38 iterations.

Fig. 5.9a is nearly a perfect mirror of Fig. 5.9b with a symmetry axis at 50.5. This means that when the convergence is obtained for the first time at the iteration i, $101 - i$ iterations are below the convergence threshold, corresponding to the remaining - i including - number of simulations. Hence, once the convergence is obtained at some point, the convergence criterion remains valid nearly each time afterwards.

In short, in the perfect case with an initial selection of a beam centroid within the 1-σ beam, the convergence criterion is always reached in less than 38 iterations and stays reached after.

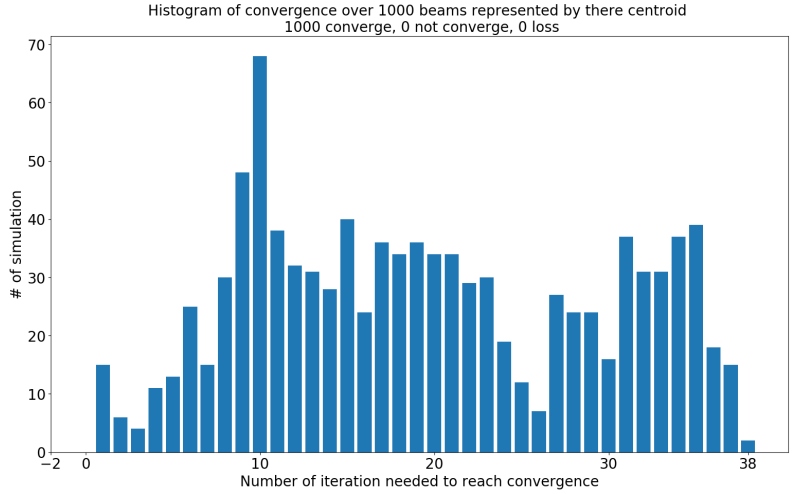

(a) Histogram of the number of iterations needed to reach the convergence for the first time.

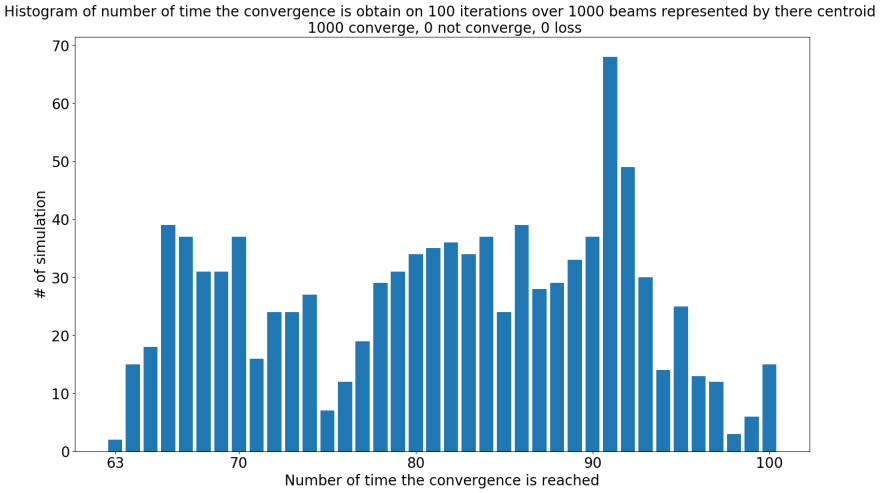

(b) Histogram of the number of time the convergence is reached.

Figure 5.9: One thousand particles have been selected within the 1-σ beam to represent as many beam centroids. The 100 iterations of the injection feedback are done using the same particle each. The case -2 corresponds to particles lost during the iteration of the feedback, while the case -1 correspond to particles that never reached the convergence criterion : E_x, $E_y < 100\mu m$ and $E_{x'}$, $E_{y'} < 100\mu rad$.

5.2.4 . Fluctuation case

In this section, the beam centroid is slightly different from one iteration to the next. To do so a particle representing the beam centroid is selected at first within the 1-σ beam ellipse. Then, each time that a new iteration is done, the actual particle parameters are those of the selected particle plus a uniform random

fluctuation of ever $1\,\%$ - small fluctuation - or $10\,\%$ - large fluctuation - of the ThomX nominal 1-σ beam size - $\sigma_x \approx 1.5\,\mathrm{mm} \approx \sigma_y$ - and momentum - $\sigma_{x'} \approx 0.4\,\mathrm{mrad} \approx \sigma_{y'}$ - at the exit of the accelerating section (see section 3.2.4).

5.2.4.1 1% fluctuations

5.2.4.1.1 One simulation example The initial - blue - and final - orange - particle propagation for an example of $1\,\%$ initial fluctuation injection feedback are given on Fig. 5.10. The slight difference between both propagation since the beginning of the TL - especially in the y plane - is due to the beam-to-beam fluctuations.

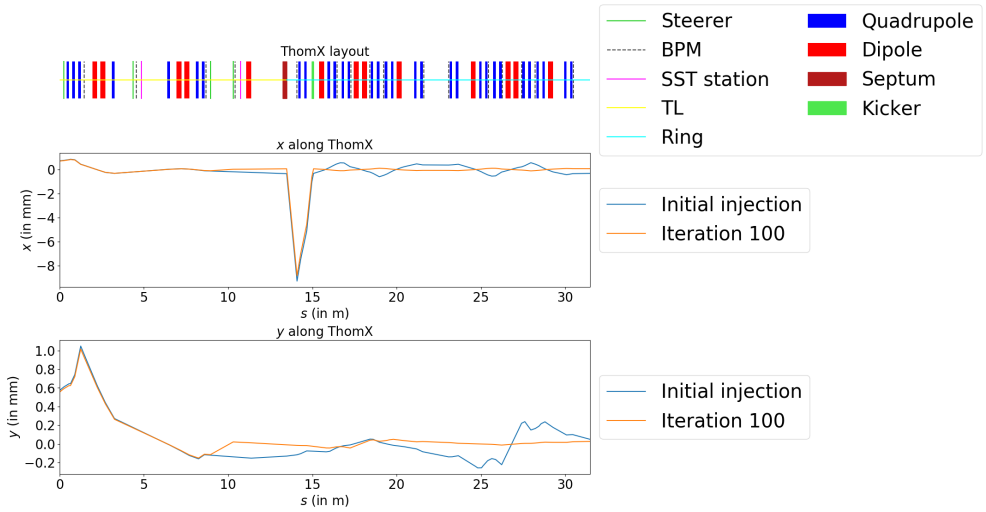

Figure 5.10: ThomX layout (top) and tracking of particles along ThomX TL and first ring turn in x plane (middle) and y plane (bottom). Particles represent the beam centroid randomly selected within 1-σ beam ellipse before applying the injection feedback (blue) and after 100 iterations (orange). A random beam-to-beam fluctuation of $1\,\%$ of the beam size at the beginning of the TL explains the slight difference in beam propagation since the beginning of the line. Around $10\,\mathrm{m}$, the difference in propagation is due to optimisation of the strength of steerers (green line on the ThomX layout). The peak around $14\,\mathrm{m}$ in the x plane is a computing artefact due to the change of frame between the septum and the kicker (section 3.2.3).

One may notice small oscillations in the ring for the final injection. They are corroborated by the 100^{th} iteration visible on the estimator plot (Fig. 5.11) that give estimators of $E_x = 0.07\,\mathrm{mm}$, $E_{x'} = 0.06\,\mathrm{mrad}$, $E_y = 0.03\,\mathrm{mm}$ and $E_{y'} = 0.03\,\mathrm{mrad}$. Those values are still below the convergence criterion, but it is not the case of the 74^{th} iteration that as a x estimator slightly higher than $0.1\,\mathrm{mm}$. Nevertheless,

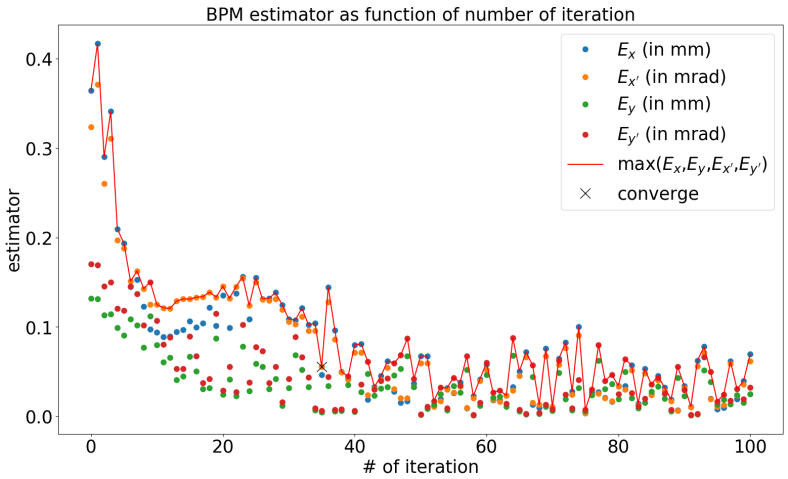

Figure 5.11: Estimation of the ring injection against iterations of the injection feedback. The particle used for this simulation of the injection feedback is the initial one of Fig. 5.10 - randomly selected within the 1-σ beam ellipse - with a random beam-to-beam fluctuation of $1\,\%$ of the beam size at the start of the TL. The convergence iteration is defined as the first iteration where E_x and E_y are below $0.1\,\mathrm{mm}$ and $E_{x'}$ and $E_{y'}$ are below $0.1\,\mathrm{mrad}$.

in this particular case, there is a factor 4 of gain on the injection estimation. Moreover, maximal estimation after the iteration of convergence is of the order of the convergence criterion which mean good injection nearly each time.

5.2.4.1.2 Simulation of 1000 beam centroids To certify the behaviour seen in the abovementioned example, 1000 particles are selected randomly - representing as many beam centroids - and the $1\,\%$ initial fluctuated injection feedback is applied to each of them separately.

Histogram of the iteration of convergence (Fig. 5.12a) is similar to that of the perfect case (Fig. 5.9a). No losses, convergence always reached. Even the maximal number of iterations needed to reach the convergence (39) is similar.

The main difference, in this case, is with the histogram of the number of times the convergence criterion is reached (Fig. 5.9b). An approximate symmetry of both histograms is still visible, but with a minor shifting of the axe of symmetry to a lower value. For extreme cases - 39 in the first histogram and 58 in the second - the worst number of iterations passing over the convergence threshold after the first iteration of convergence is $101-39-58=4$ iterations.This value is only an approximation but give an order of magnitude of the number of iterations over the convergence threshold after the iteration of convergence.

In short, even with $1\,\%$ beam-to-beam fluctuations of the beam centroid, the injection feedback permits the improvement of the injection, reaching the conver-

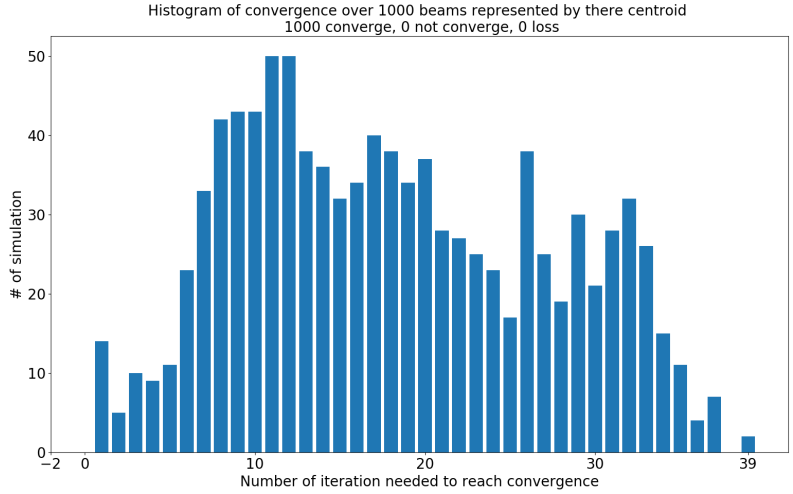

(a) Histogram of the number of iterations needed to reach the convergence for the first time.

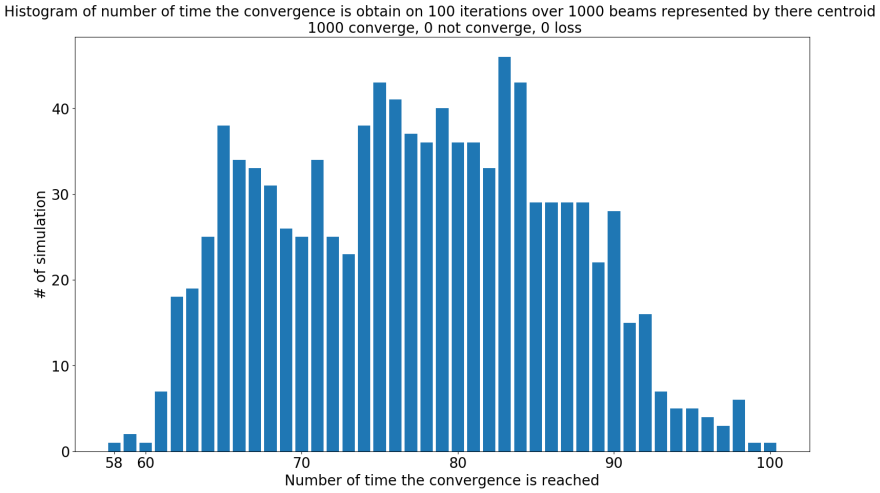

(b) Histogram of the number of time the convergence is reach.

Figure 5.12: One thousand particles have been selected within the 1-σ beam to represent as many beam centroids. A random beam-to-beam fluctuation of $1\,\%$ of the beam size at the start of the TL is applied to each of the 100 iterations. The case -2 corresponds to particles lost during the iteration of the feedback, while the case -1 correspond to particles that never reach the convergence criterion : E_x, $E_y < 100\mu\text{m}$ and $E_{x'}$, $E_{y'} < 100\mu\text{rad}$.

gence criterion in less than 39 iterations and this criterion stays verified most of the time afterwards.

5.2.4.2 10% fluctuations

A $1\,\%$ fluctuation of the beam centroid according to the beam size induces some oscillation of the beam in the ring of the order of convergence criterion. This section shows what happened for higher fluctuation with particles selected within the 1-σ beam ellipse.

5.2.4.2.1 Simulation of 1000 beam centroids The histograms of iteration needed to reach convergence (Fig. 5.13a) and nuber of time the convergence criterion is reach (Fig. 5.13a) are much different from the $1\,\%$ beam fluctuation. The main difference is that nearly 120 simulations have not reached the convergence - not even once by change - and those that have got it once have at most eight iterations under the convergence criterion. Hence, the criterion of convergence does not make sense in this case. Still, the injection feedback implies no particle loss, which is good news.

The small number of iterations where the convergence is reached and the nearly random distribution of the iteration number of the first convergence seems to show that the convergence criterion is obtained nearly by chance. Verification on an example is presented below.

5.2.4.2.2 One simulation example Here presents a case of injection feedback with $10\,\%$ beam-to-beam fluctuation. Fig. 5.14 show the initial particle propagation as well as the 5^{th}, 10^{th}, 15^{th}, 30^{th}, 100^{th} iterations ones. The 10^{th} iteration in x and both initial and 30^{th} iterations in y show a large fluctuation of the beam propagation in the beginning of the TL because of the $10\,\%$ fluctuation of the centroid position.

This fluctuation in position explains why the correction computed for one iteration does not match those needed for the next. This lead to incorrect correction, and the beam injection does not improve as shown Fig. 5.15, the plot of estimators against iterations.

Even if some injection - like the 46^{th} - are nearly twice worse than initial one, a fluctuation around $(0.5 \pm 0.4)\,\text{mm}$ and $(0.5 \pm 0.4)\,\text{mrad}$ seems to be keep, and excursion outside $1\,\text{mm}$ and $1\,\text{mrad}$ never occurred.

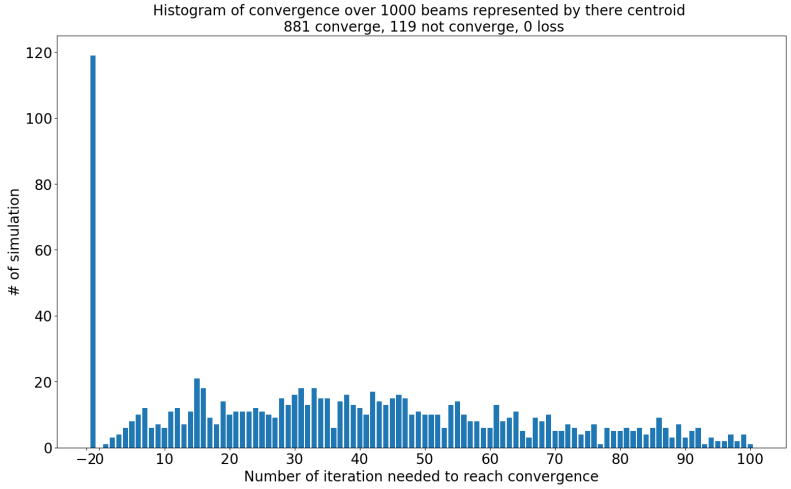

(a) Histogram of the number of iterations needed to reach the convergence for the first time.

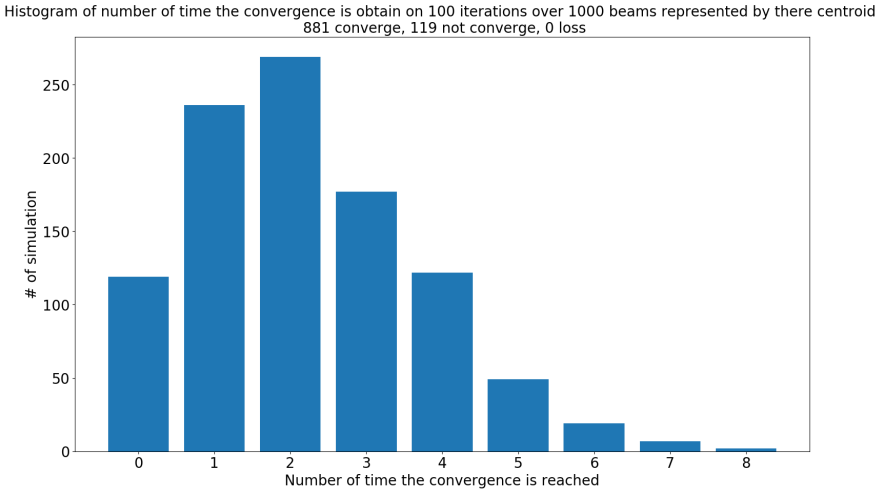

(b) Histogram of the number of time the convergence is reach.

Figure 5.13: One thousand particles have been selected within the 1-σ beam to represent as many beam centroids. A random beam-to-beam fluctuation of $10\,\%$ of the beam size at the start of the TL is applied to each of the 100 iterations. The case -2 corresponds to particles loss during the iteration of the feedback, while the case -1 (where there is the large peak) correspond to particles that never reach the convergence criterion : E_x, $E_y < 100\,\mu\text{m}$ and $E_{x'}$, $E_{y'} < 100\,\mu\text{rad}$.

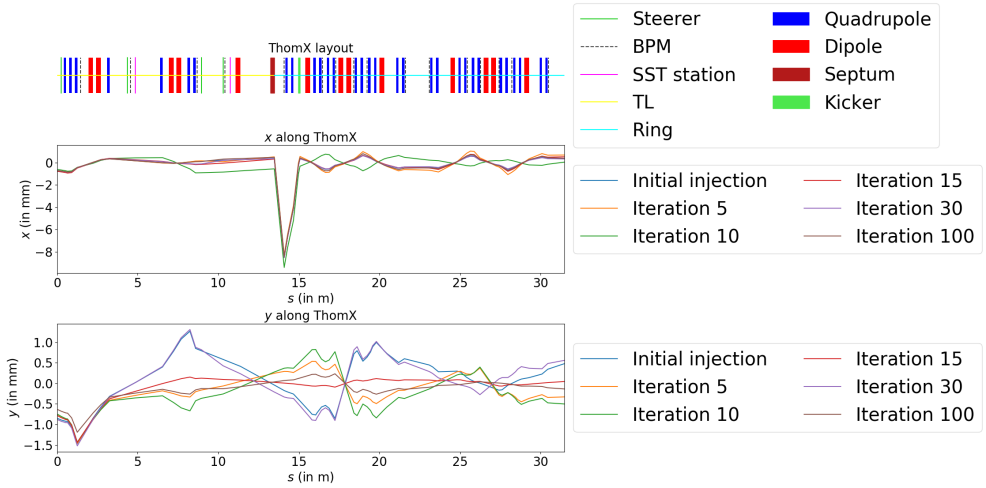

Figure 5.14: ThomX layout (top) and tracking of particles along ThomX TL and first ring turn in x plane (middle) and y plane (bottom). Particles represent the beam centroid randomly selected within 1-σ beam ellipse before applying the injection feedback (blue) and after 5 (orange), 10 (green), 15 (red), 30 (violet), and 100 (brown) iterations. A random beam-to-beam fluctuation of $10\,\%$ of the beam size at the beginning of the TL explains the significant difference in beam propagation since the beginning of the line. Around $10\,\mathrm{m}$, the difference in propagation is due to optimisation of the strength of steerers (green line on the ThomX layout). The peak around $14\,\mathrm{m}$ in the x plane is a computing artefact due to the change of frame between the septum and the kicker (section 3.2.3).

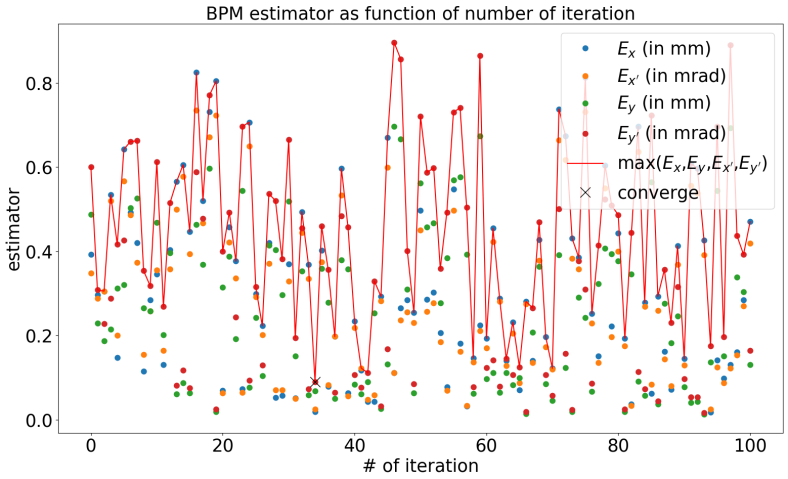

Figure 5.15: Estimation of the ring injection against iterations of the injection feedback. The particle used for this simulation of the injection feedback is randomly selected within the 1-σ beam ellipse with an additional random beam-to-beam fluctuation of $1\,\%$ of the beam size at the start of the TL. The convergence iteration is defined as the first iteration where E_x and E_y are below $0.1\,\mathrm{mm}$ and $E_{x'}$ and $E_{y'}$ are below $0.1\,\mathrm{mrad}$ but is reach here only by chance and does not make any sense.

5.2.5 . Summary

The injection feedback applied on particles - representing beam centroids - selected within a 1-σ beam ellipse gives good results for the reference case, perfect cases and even for fluctuated cases if the position's and momentum's beam-to-beam fluctuations of the particle representing the beam centroid is small enough. For significant fluctuation ($10\,\%$ of the 1-σ beam size), oscillation in the ring remains of the order of oscillations with the initial injection but at least does not increase to infinity and does not lead to loss of particles representing beam centroids.

5.3 . Studies of parameters' impact on simulations

This section focus on some studies of the injection feedback regarding modification of the beam positioning (section 5.3.1), modification of the coefficient of correction applied (section 5.3.2) and addition of the BPM uncertainty (section 5.3.3).

5.3.1 . Studies of larger off-axis and off-momentum beams

To select more exotic particles - representing beam centroids - a selection within the 5-σ beam is done in this section.

5.3.1.1 Perfect case

The propagation of one particle selected in the 5-σ beam is represented in blue in Fig. 5.16 as well as the particle propagation of the same particle at iterations 5, 10, 15, 30, and 100 of the injection feedback. In the ring (after $15\,\mathrm{m}$), the higher the iteration, the flatter the curve, which means that the injection improves.

The estimators against iteration of this simulation (Fig. 5.17) also demonstrate an improvement of the injection with a final estimation of the injection of $E_x = 3 \times 10^{-2}\,\mathrm{mm}$, $E_{x'} = 3 \times 10^{-2}\,\mathrm{mrad}$, $E_y = 2 \times 10^{-3}\,\mathrm{mm}$ and $E_{y'} = 3 \times 10^{-3}\,\mathrm{mrad}$. Those value are of the same order of magnitude of the 1-σ beam perfect case simulation shows in section 5.2.3.1. The general behaviour of the estimators is similar to those of the 1-σ beam perfect case but with five times higher initial estimation.

One thousand simulations with particles inside the 5-σ beam ellipse have been done to check this similarity observed in one case. Their results are resumed in the histogram of convergence iteration (Fig. 5.18a) and of the number of iteration below convergence threshold (Fig. 5.18b).

Once again, both histograms are nearly a perfect mirror to each other with symmetry around 50.5 which means that once the convergence is obtained, the convergence criterion stays verified.

A huge difference with the 1-σ beam case is the number of iterations needed to reach the convergence. Here, this number is much higher with nearly no con-

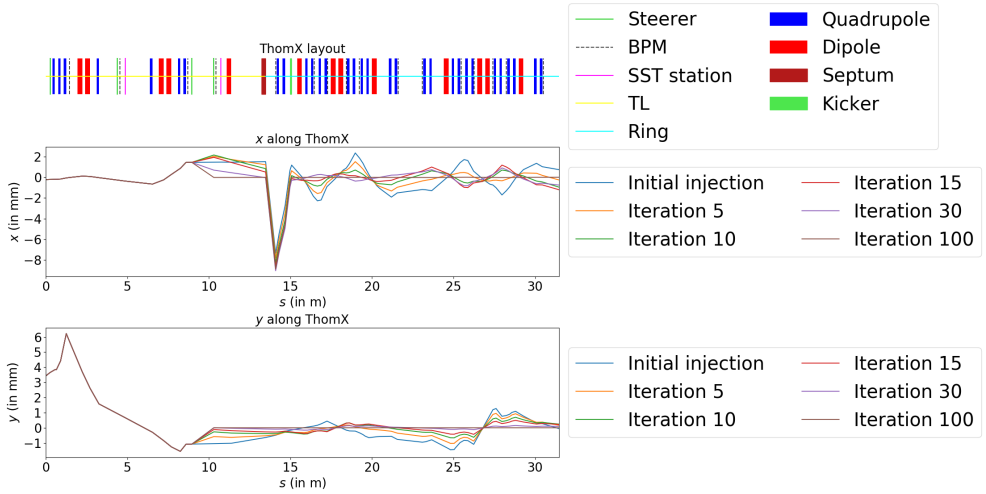

Figure 5.16: ThomX layout (top) and tracking of particles along ThomX TL and first ring turn in x plane (middle) and y plane (bottom). Particles represent the beam centroid randomly selected within 5-σ beam ellipses before applying the injection feedback (blue) and after 5 (orange), 10 (green), 15 (red), 30 (violet), and 100 (brown) iterations. The only differences in propagation are due to optimisation of the strength of steerers (green line on the ThomX layout) located around $10\,\mathrm{m}$. The peak around $14\,\mathrm{m}$ in the x plane is a computing artefact due to the change of frame between the septum and the kicker (section 3.2.3).

vergence at less than 20 iterations and a large peak around 50. After 53 iterations, the convergence is always obtained.

In short, the 5-σ beam perfect case is much like the 1-σ beam one with just an increase in the number of iterations needed to obtain the convergence. Hence, in a perfect world, the injection feedback would always permit convergence in less than 53 iterations, even for a beam with a centroid position far from the expected one.

5.3.1.2 Fluctuation case

In reality, the beam centroid is never precisely at the same position from one shot to the next. One thousand simulations of the injection feedback have been made with a random fluctuation of the particle - representing the beam centroid - position and momentum of maximum $1\,\%$ of the 1-σ beam size and momentum (see section 5.2.4). Results are represented by Fig. 5.19a, the histogram of the convergence iteration and Fig. 5.19b, the histogram of the number of time estimators are below the threshold of convergence.

Both histogram are closed to those of the reference case (Fig. 5.18a, Fig. 5.18b). The only difference remains in a global shifting to the left - of some iterations - of

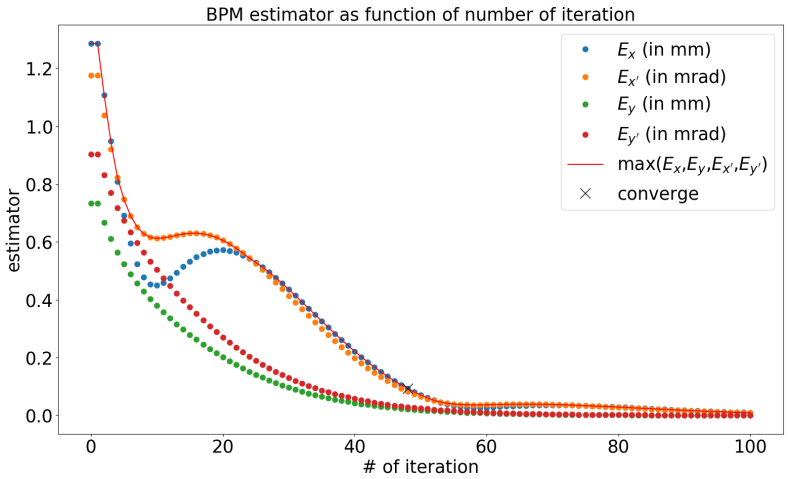

Figure 5.17: Estimation of the ring injection against iterations of the injection feedback. The particle used for this simulation of the injection feedback is the initial one of Fig. 5.16, randomly selected within the 5-σ beam ellipse. The convergence iteration is defined as the first iteration where E_x and E_y are below $0.1\,\mathrm{mm}$ and $E_{x'}$ and $E_{y'}$ are below $0.1\,\mathrm{mrad}$.

the histogram of the number of iterations below the convergence threshold.

This behaviour corresponds to the existence of some iteration after the convergence iteration with estimators above the convergence criterion. It can be visualised on the estimator against iterations' plot (Fig. 5.20) of one example of simulation where a plateau of estimators around $0.1\,\mathrm{mm}$, $0.1\,\mathrm{mrad}$ is reached after 50 iterations. Still, the beam's fluctuation sometimes induces higher oscillation in the ring.

A similar behaviour can be seen on Fig. 5.21, one example of simulation done with a $10\,\%$ beam centroid fluctuation. In this case, the oscillations after the 30^{th} iteration are around $(0.5 \pm 0.4)\,\mathrm{mm}$ and $(0.5 \pm 0.4)\,\mathrm{mrad}$ exactly like it was for the 1-σ beam case (section 5.2.4.2). This oscillation level is so large that it does not make sense to speak of convergence after the first iteration below the convergence threshold. Nevertheless, some improvement - a 2.5 factor here - of the injection is obtained in the 5-σ beam case and permits more significant oscillations to be lower than $1\,\mathrm{mm}$, $1\,\mathrm{mrad}$.

5.3.1.3 Summary

The 5-σ beam cases are much like 1-σ beam ones (section 5.2.3 and section 5.2.4) and both permit to reach the same plateau of convergence. The only difference is the number of iterations needed to reach the plateau that is larger in the 5-σ beam case. For both the perfect case and $1\,\%$ fluctuated case, maximum oscillations in

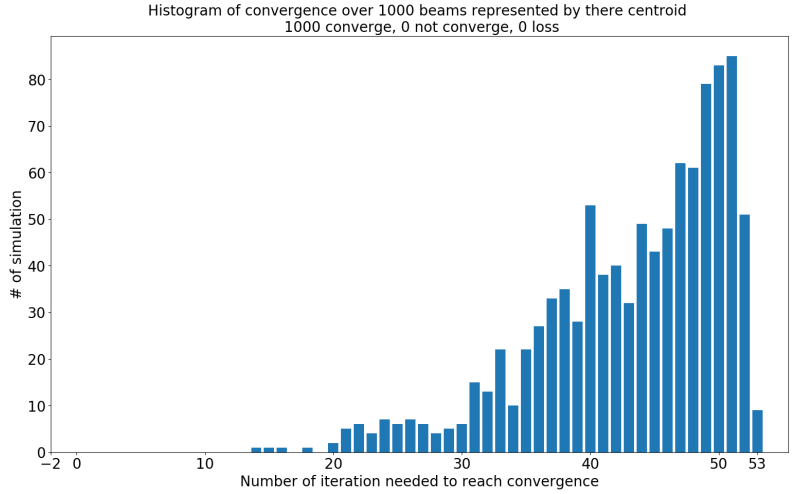

(a) Histogram of the number of iterations needed to reach the convergence for the first time.

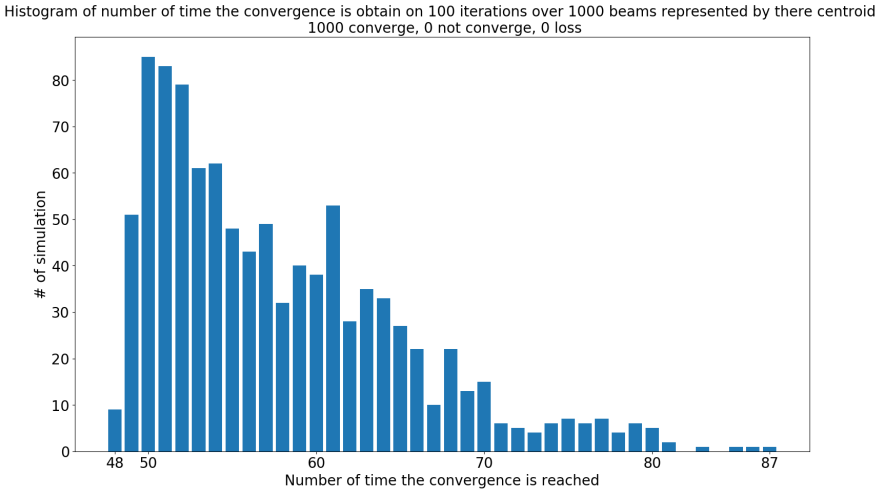

(b) Histogram of the number of time the convergence is reach.

Figure 5.18: One thousand particles have been selected within the 5-σ beam to represent as many beam centroids. The 100 iterations of the injection feedback are done using the same particle each. The case -2 corresponds to particles loss during the iteration of the feedback, while the case -1 correspond to particles that never reach the convergence criterion : E_x, $E_y < 100\,\mu\text{m}$ and $E_{x'}$, $E_{y'} < 100\,\mu\text{rad}$.

the ring are - in general - below the convergence threshold. For the case with $10\,\%$ fluctuated, the maximum oscillations in the ring are of the order of magnitude of $1\,\text{mm}$, $1\,\text{mrad}$, which is large, but still permit to improve the injection as initial estimators are even larger.

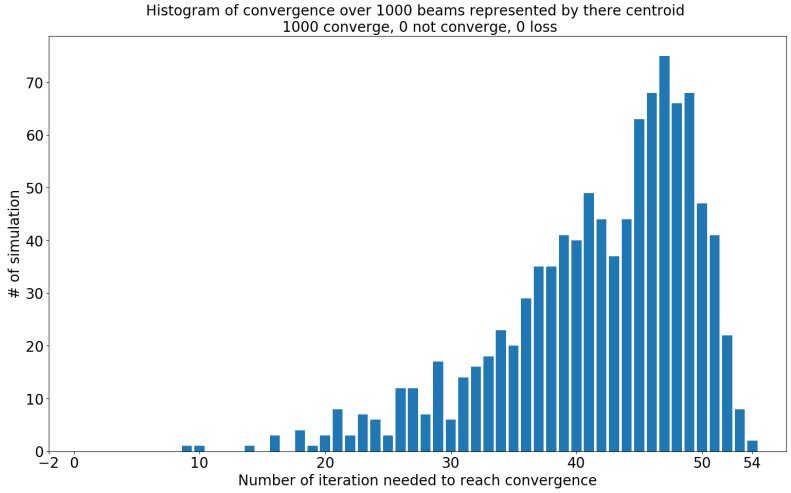

(a) Histogram of the number of iterations needed to reach the convergence for the first time.

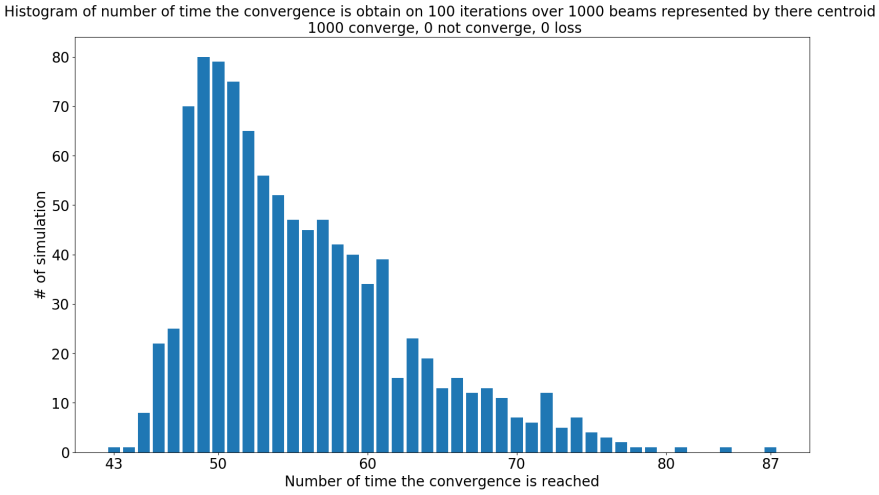

(b) Histogram of the number of time the convergence is reach.

Figure 5.19: One thousand particles have been selected within the 5-σ beam to represent as many beam centroids. A random beam-to-beam fluctuation of $1\,\%$ of the beam size at the start of the TL is applied to each of the 100 iterations. The case -2 corresponds to particles loss during the iteration of the feedback, while the case -1 correspond to particles that never reach the convergence criterion : E_x, $E_y < 100\mu\text{m}$ and $E_{x'}$, $E_{y'} < 100\mu\text{rad}$.

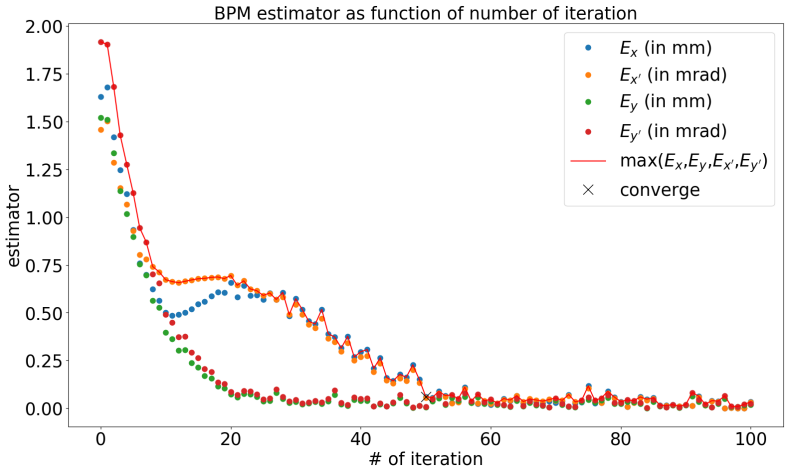

Figure 5.20: Estimation of the ring injection against iterations of the injection feedback. The particle used for this simulation of the injection feedback is randomly selected within the 5-σ beam ellipses with an additional random beam-to-beam fluctuation of $1\,\%$ of the 1-σ beam size at the start of the TL. The convergence iteration is defined as the first iteration where E_x and E_y are below $0.1\,\mathrm{mm}$ and $E_{x'}$ and $E_{y'}$ are below $0.1\,\mathrm{mrad}$.

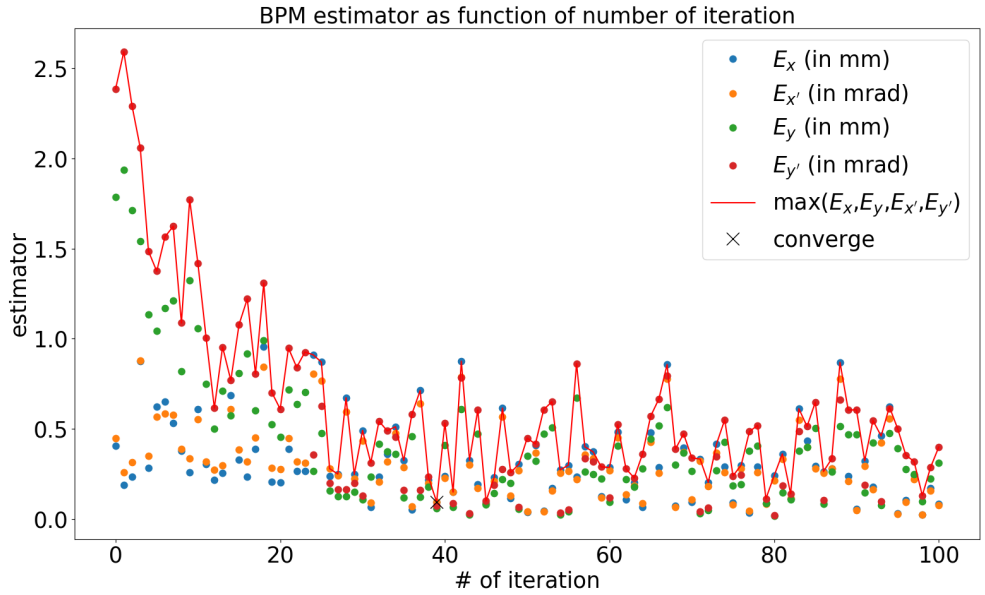

Figure 5.21: Estimation of the ring injection against iterations of the injection feedback. The particle used for this simulation of the injection feedback is randomly selected within the 5-σ beam ellipses with an additional random beam-to-beam fluctuation of $10\,\%$ of the 1-σ beam size at the start of the TL. The convergence iteration is defined as the first iteration where E_x and E_y are below $0.1\,\mathrm{mm}$ and $E_{x'}$ and $E_{y'}$ are below $0.1\,\mathrm{mrad}$ but is reach here only by chance and does not make any sense.

5.3.2 . Studies of feedback coefficient

In the injection feedback, the coefficient of the correction - the difference between steerers' strength values used and computed - is applied from one iteration to the next. By default, this coefficient has been arbitrary set a $10\,\%$ of the correction each time.

This section presents some tests with other coefficient defined. The same initial particle selected within the 5-σ beam ellipse is used for each comparison.

5.3.2.1 Perfect case

For this section, all figures come from simulations computed with the same particles selected in the 5-σ beam. The initial propagation of this particles is shown in Fig. 5.22.

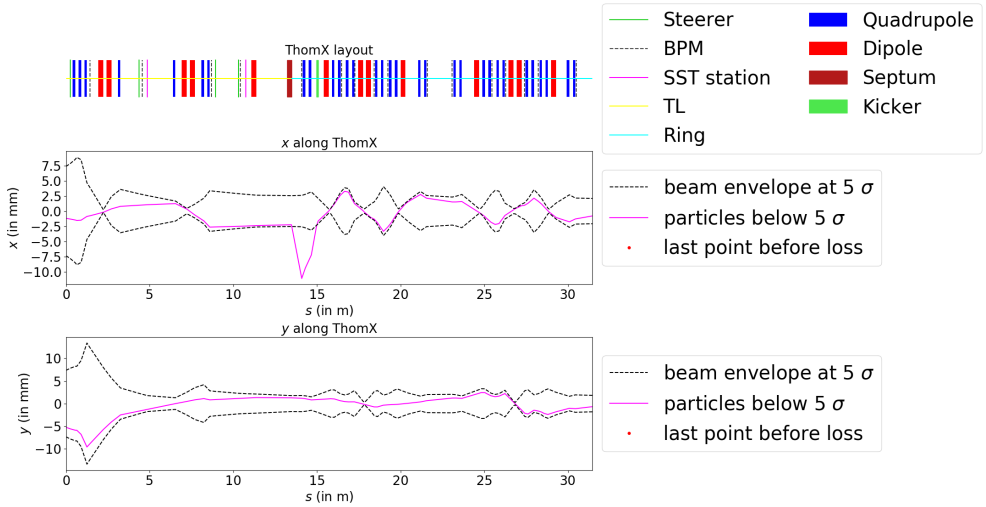

Figure 5.22: ThomX layout (top) and tracking of particles along ThomX TL and first ring turn in x plane (middle) and y plane (bottom). Particles represent the beam centroid randomly selected within 5-σ beam ellipses before applying the injection feedback. All steerers have null strength, and the injection kicker has the nominal kick. The peak around $14\,\mathrm{m}$ in the x plane is a computing artefact due to the change of frame between the septum and the kicker (section 3.2.3).

The coefficient tested and presented on Fig. 5.23 are $100\,\%$, $20\,\%$, $10\,\%$, $5\,\%$, $2\,\%$ and $1\,\%$.

One may notice that, except for the $100\,\%$ case (Fig. 5.23a), all plot are similar with only dilatation along the iteration number. A reduction of the coefficient seems only to affect the number of iterations needed to reach the convergence, but not the estimations curve in general.

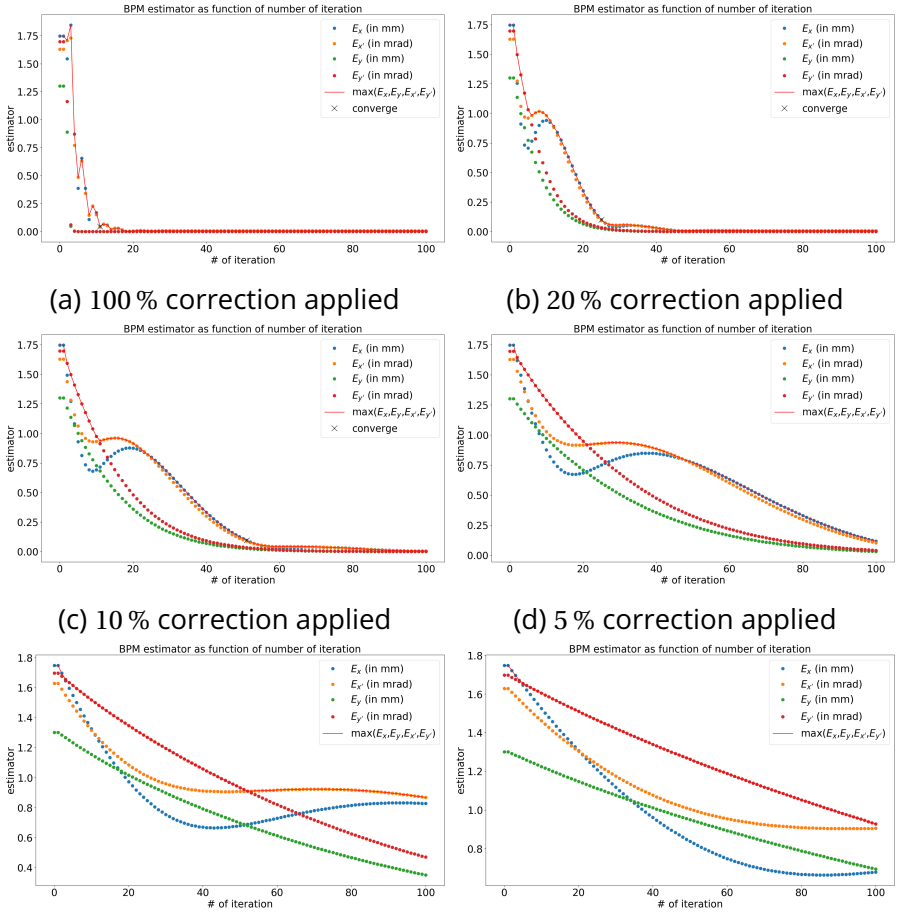

(a) 100 % correction applied (b) 20 % correction applied

(c) 10 % correction applied (d) 5 % correction applied

(e) 2 % correction applied (f) 1 % correction applied

Figure 5.23: Estimation of the ring injection against iterations of the injection feedback for different percentages of computed correction applied at each iteration. The unique particle used for each simulation of the injection feedback is the one of Fig. 5.22, randomly selected within the 5-σ beam ellipse. The convergence iteration is defined as the first iteration where E_x and E_y are below 0.1 mm and $E_{x'}$ and $E_{y'}$ are below 0.1 mrad.

For the 100 % case, 11 iterations are needed to reach convergence. This swift decrease of the estimators shows a good agreement between the MadX simulation and the linear transfer matrix used for correction calculation. Still, the correction calculation is not perfect else only one iteration would have been needed to reach the convergence.

Ten simulations have been done for each coefficient value with different initial particles. The means and standard deviation of the estimator after convergence has been calculated separately. Cases where the convergence is not reached are

excluded. Then, for each coefficient value, the mean of the mean estimators and the maximum of the standard deviation have been computed and are resumed in Tab. 5.2.

Table 5.2: Means over ten perfect case simulations of the means of estimators after the convergence. Cases where convergence is not reached are excluded. The standard deviation given is the maximum one on all simulations considered. All values are rounded to µm and µrad.

Coeff. applied	Simulations #	E_x[µm]	$E_{x'}$[µrad]	E_y[µm]	$E_{y'}$[µrad]
100 %	10	9 ± 21	9 ± 21	0	0
20 %	10	14 ± 19	15 ± 20	1 ± 13	2 ± 17
10 %	10	26 ± 20	27 ± 19	4 ± 17	6 ± 22
5 %	5	80 ± 18	72 ± 16	25 ± 18	34 ± 23
2 %	0	No convergence			
1 %	0	No convergence			

The table shows that the lower the coefficient applied, the fewer simulations converge. This observation can be explained by the increasing number of iterations needed to reach the convergence as visualised in the case described above. The increase of mean estimations when the coefficient decrease is also explainable by this phenomenon. In fact, a plateau of small estimation is reached soon after the convergence for large coefficient cases. In contrast, the transition between convergence and plateau dominates the mean calculation in small coefficient cases.

In a perfect case, the best correction factor seems to be 100 % as the correction is faster and sooner, leading to lower oscillation in the ring. Still, applying all the corrections at once is rarely a good idea in reality because of fluctuations and risks of over-correction. At the same time, smaller coefficients do not permit obtained convergence in every case in less than 100 iterations, which leads to many iterations with large oscillation and risk of particle losses. Both 10 % and 20 % give good enough results.

5.3.2.2 Fluctuations case

Let us study the correction coefficient applied for simulations with beam-to-beam fluctuations. Two cases are treated, one with a random fluctuation with maximum 1 % of the beam size and momentum as fluctuation, a second with maximum 10 %. For each coefficient comparison, a unique initial particle is selected within the 5-σ beam ellipse and used as a beam centroid. The fluctuation is added to this particle even for the initial estimator, which explains the change of this value on each plot.

5.3.2.2.1 1% fluctuations For beam position fluctuation of 1 % of the beam size, the coefficients tested and presented on Fig. 5.24 are 100 %, 20 %, 10 %, 5 %, 2 % and 1 %.

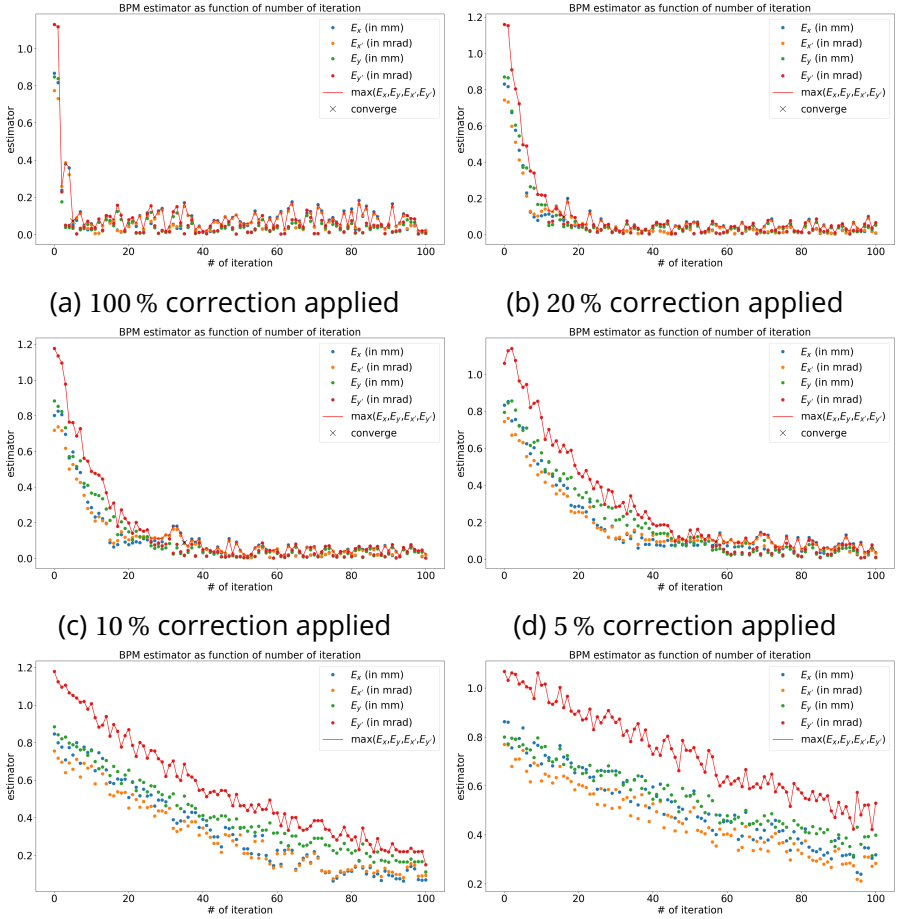

(a) 100 % correction applied (b) 20 % correction applied

(c) 10 % correction applied (d) 5 % correction applied

(e) 2 % correction applied (f) 1 % correction applied

Figure 5.24: Estimation of the ring injection against iterations of the injection feedback for different percentages of computed correction applied at each iteration. The unique particle used for each simulation of the injection feedback is randomly selected within the 5-σ beam ellipses. An additional random beam-to-beam fluctuation of 1 % of the 1-σ beam size at the start of the TL is applied at each iteration. The convergence iteration is defined as the first iteration where E_x and E_y are below 0.1 mm and $E_{x'}$ and $E_{y'}$ are below 0.1 mrad.

Figures of propagation are similar to those of the perfect case (see section 5.3.2.1), but three differences can be pointed out.

First, the local minimum in E_x and $E_{x'}$ has disappeared, which is an improvement of the injection feedback behaviour. This observation is not true for all

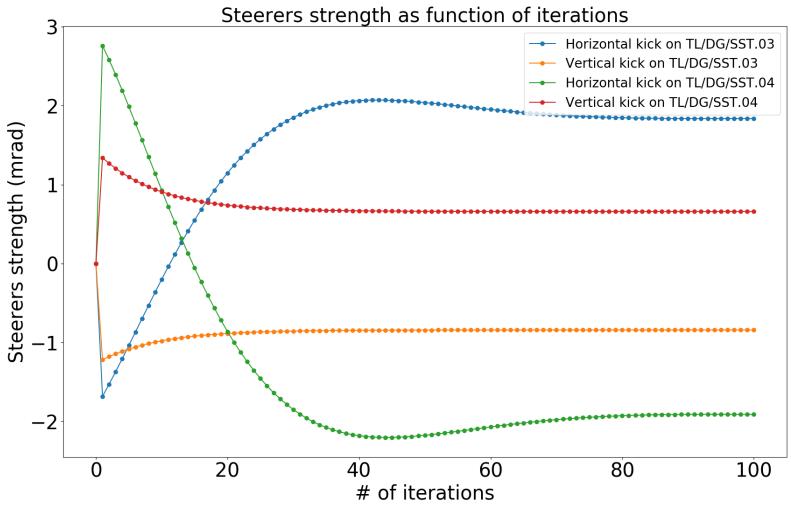

(a) Perfect case (Fig. 5.23c)

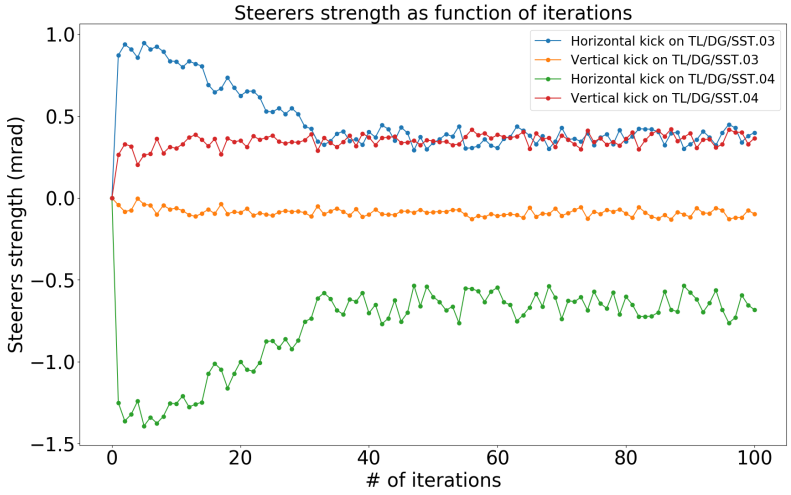

(b) Beam-to-beam fluctuated case (Fig. 5.24c)

Figure 5.25: Steerers' strength as a function of the iterations. The coefficient of correction applied from one iteration to the next is 10 %.

simulations with 1 % beam-to-beam fluctuations, but it is less systematic than with the perfect case. The hypothesis of a correlation between local minima and horizontal steerer strength inversion done in section 5.2.3 holds on as the disappearance of local minimal is accompanied by the disappearance of the inversion as it can be seen on Fig. 5.25 The truth of this correlation and its explication are not yet established. Still, this observation has been made on lots of examples. A specific study on this behaviour must provide a better comprehension of the injection feedback and of the injection process itself.

Second, simulation convergence is approximately 1.5 times faster in this case

than in the perfect one. It can be explained - at least in part - by the initial estimator that is smaller by a factor of 1.5 too. No significant modification of time to reach convergence can be pointed out.

Third, some fluctuation of the estimators exists. The maximum beam oscillation in the ring is of the order of $0.1\,\mathrm{mm}$ and $0.1\,\mathrm{mrad}$ after the first convergence iteration for all coefficient cases, except the $100\,\%$ one. This case has twice larger oscillations approximately.

Similar simulations have been done ten times, and the mean and standard deviation of estimators' values after the convergence iteration have been computed. The mean of those mean estimators and the maximum of those standard deviations for each coefficient case are given on Tab. 5.3.

Table 5.3: Means of the means of estimators after convergence over 10 feedback simulations with $1\,\%$ beam position fluctuation. Cases where convergence is not reach are exclude. The standard deviation given is the maximum one on all simulations considered. All values are rounded to $\mu\mathrm{m}$ and $\mu\mathrm{rad}$.

coeff. applied	Simulations #	E_x[µm]	$E_{x'}$[µrad]	E_y[µm]	$E_{y'}$[µrad]
$100\,\%$	10	68 ± 50	65 ± 44	39 ± 32	50 ± 42
$20\,\%$	10	40 ± 31	38 ± 29	28 ± 22	36 ± 28
$10\,\%$	10	43 ± 36	41 ± 31	27 ± 27	35 ± 35
$5\,\%$	10	74 ± 46	69 ± 39	37 ± 33	49 ± 44
$2\,\%$	1	155 ± 34	138 ± 29	98 ± 20	118 ± 24
$1\,\%$	0	No convergence			

Lower ring's oscillation after convergence iteration seems to be obtained for $10\,\%$ and $20\,\%$ corrections applied. The total correction case leads to higher fluctuation because of potential over-correction. The smaller correction factor seems to be under-corrected - at least for the first iteration after the convergence - which increases the time to reach stabilised oscillations.

In short, the injection feedback system is relevant for small fluctuation of the beam position and momentum at the beginning of the transfer line. Injection feedback seems optimum for $10\,\%$ and $20\,\%$ correction applied for which oscillations of the beam in the ring of the order of a few tens of micrometres can be achieved.

5.3.2.2.2 10% fluctuation We already have seen (section 5.2.4.2 that higher beam-to-beam fluctuation leads to higher beam oscillations in the ring. To check the optimum correction coefficient to apply for large beam-to-beam fluctuations, some coefficients have been tested with $10\,\%$ beam-to-beam fluctuation. Coefficient tested and represent in Fig. 5.26 are $100\,\%$, $20\,\%$, $10\,\%$, $5\,\%$, $2\,\%$ and $1\,\%$.

All figures are presented using a unique initial beam centroid on which is applied the fluctuation.

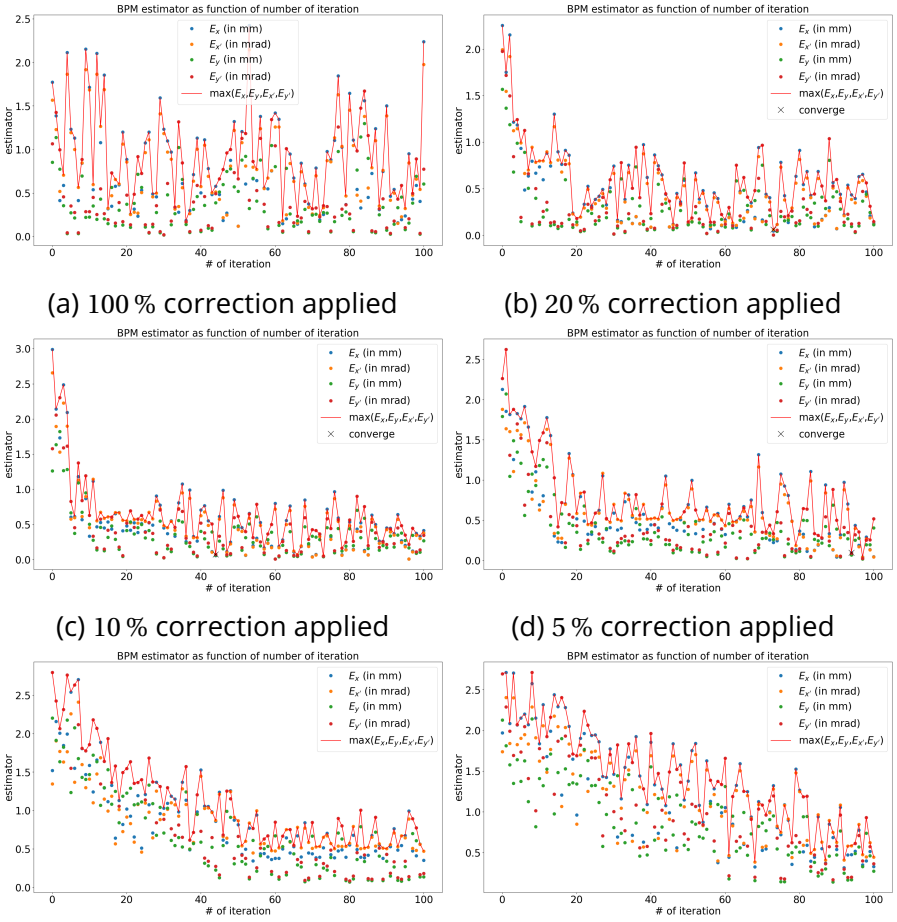

(a) 100 % correction applied (b) 20 % correction applied

(c) 10 % correction applied (d) 5 % correction applied

(e) 2 % correction applied (f) 1 % correction applied

Figure 5.26: Estimation of the ring injection against iterations of the injection feedback for different percentages of computed correction applied at each iteration. The unique particle used for each simulation of the injection feedback is randomly selected within the 5-σ beam ellipses. An additional random beam-to-beam fluctuation of 10 % of the 1-σ beam size at the start of the TL is applied at each iteration. The convergence iteration is defined as the first iteration where E_x and E_y are below 0.1 mm and $E_{x'}$ and $E_{y'}$ are below 0.1 mrad but does not make any sense here.

This time, the entire correction case cannot be used as it does not improve the injection in contrast to other cases. As for previous studies (section 5.3.2.1 and section 5.3.2.2.1), decreasing the correction applied elongates the estimation curve, which means that the lower the correction applied, the higher the time spent with high oscillation in the ring.

To find an optimum of the coefficient of correction to applied, 10 simulations

like the one of Fig. 5.26 have been done. As estimators stay large, the common convergence criterion does not make sense here. Nevertheless, the quality of the injection feedback has been measured by taking the mean and the standard deviation of estimators after the first iteration where E_x, $E_y < 1\,\mathrm{mm}$ and, $E_{x'}$, $E_{y'} < 1\,\mathrm{mrad}$. The mean of this quality factor over the ten simulations and the maximum standard deviation is given in Tab. 5.4.

Table 5.4: Means of the means of estimators after first iteration where E_x, $E_y < 1\,\mathrm{mm}$ and $E_{y'}$, $E_{y'} < 1\,\mathrm{mrad}$ over 10 feedback simulations with $10\,\%$ beam-to-beam fluctuation. Simulations where condition is not reach are exclude. The standard deviation given is the maximum one on all simulations considered. All values are rounded at $0.1\,\mathrm{mm}$ and $0.1\,\mathrm{mrad}$

coeff. applied	Simulations #	E_x[mm]	$E_{x'}$[mrad]	E_y[mm]	$E_{y'}$[mrad]
$100\,\%$	10	0.7 ± 0.6	0.7 ± 0.5	0.4 ± 0.3	0.5 ± 0.4
$20\,\%$	10	0.4 ± 0.4	0.4 ± 0.4	0.3 ± 0.2	0.3 ± 0.3
$10\,\%$	10	0.4 ± 0.4	0.4 ± 0.4	0.3 ± 0.3	0.4 ± 0.3
$5\,\%$	10	0.5 ± 0.4	0.5 ± 0.4	0.3 ± 0.3	0.4 ± 0.4
$2\,\%$	8	0.6 ± 0.3	0.6 ± 0.3	0.6 ± 0.3	0.7 ± 0.4
$1\,\%$	8	0.7 ± 0.4	0.7 ± 0.3	0.7 ± 0.3	0.9 ± 0.4

Like for the test of correction coefficient with smaller beam-to-beam fluctuation (section 5.3.2.2.1), best coefficient to applied are $10\,\%$ and $20\,\%$ as above there is an over-correction risk and below the correction is to slow.

5.3.2.3 Summary

The best correction coefficient to apply for perfect simulation is $100\,\%$ because correction computations are good enough to avoid over-estimation. Still, when the beam position and momentum fluctuate from one beam to the next, the over-correction is inevitable, which leads to large oscillations of the beam in the ring. On the contrary, a tiny coefficient applied implies a much longer time before reaching an acceptable injection. The optimum coefficient of correction to keep convergence reach in less than 100 iterations seems to be around 10-20 %.

Some test with coefficient definition depending on corrections values - higher coefficient for lower correction - have been done but does not seems to give better results. Nevertheless, the possibility to adapt the coefficients of correction desired is implemented. Once the injection feedback would be tested on the ThomX ring, the users could use it to optimise the injection.

5.3.3 . Studies of an error in the beam position measurement

The injection feedback is based on BPM to measure the beam position. Those diagnostics have a certain precision given by electronic noise, among others. On

the ring, it is planned to have $0.25\,\mathrm{mm}$ accuracy on one position measurement [26]. To take this error into account, some simulations of the injection feedback have been made with a random noise added to MadX results on the particle's positions in the RI-C1/DG/BPM.02 and RI-C1/DG/BPM.03 of the ring. The noise is selected within $\pm 0.1\,\mathrm{mm}$ uniform distribution on each measure for each iteration separately. These additional errors are not applied during the evaluation of the estimator to ensure accurate values.

All simulations are done with particles selected within the 1-σ beam beam ellipse at the end of the acceleration section.

5.3.3.1 Perfect case

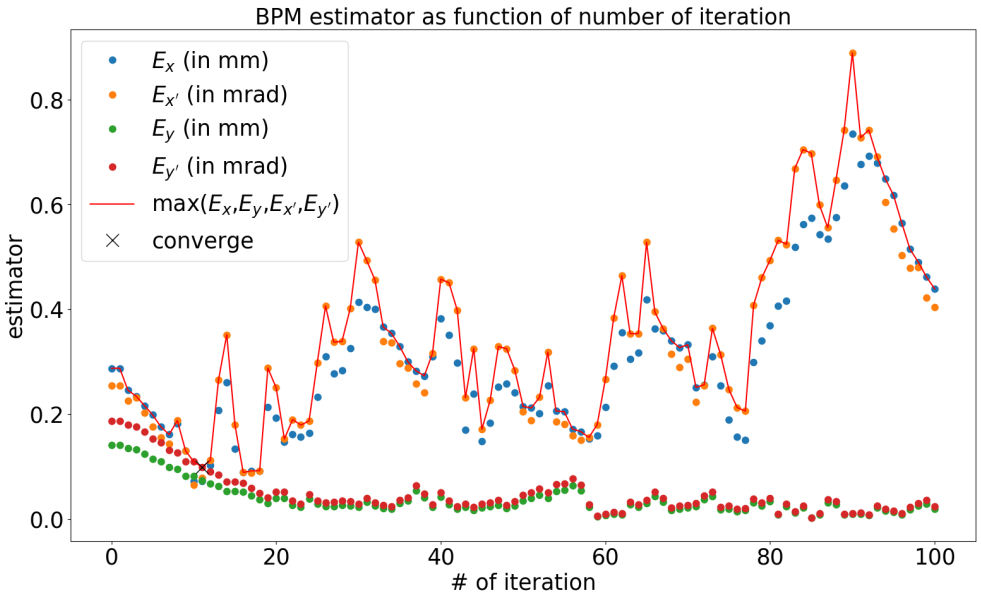

Figure 5.27: Estimation of the ring injection against iterations of the injection feedback. The particle used for this simulation of the injection feedback is randomly selected within the 1-σ beam ellipse. The coefficient of correction applied at each 1000 iterations is $10\,\%$. A random error of $\pm 100\,\mu\mathrm{m}$ is added to the beam position given by MadX tracking. The convergence iteration is defined as the first iteration where E_x and E_y are below $0.1\,\mathrm{mm}$ and $E_{x'}$ and $E_{y'}$ are below $0.1\,\mathrm{mrad}$ but does not make any sens here.

5.3.3.1.1 10% corrections applied Estimators of the injection against iteration of the injection feedback of one specific case of the perfect simulation are shown in Fig. 5.27. The injection slightly improved at first, but, after the 12^{th} iteration, the beam position error led to over-corrections that degraded the horizontal injection and created larger and larger oscillations in the ring.

This behaviour is not acceptable for a feedback system.

5.3.3.1.2 1% corrections applied To reduce the impact of the over-correction, the coefficient of correction applied from one perfect iteration to the next is diminished at $1\,\%$. As this tiny correction leads to a longer convergence time, simulation has been pushed to 1000 iterations.

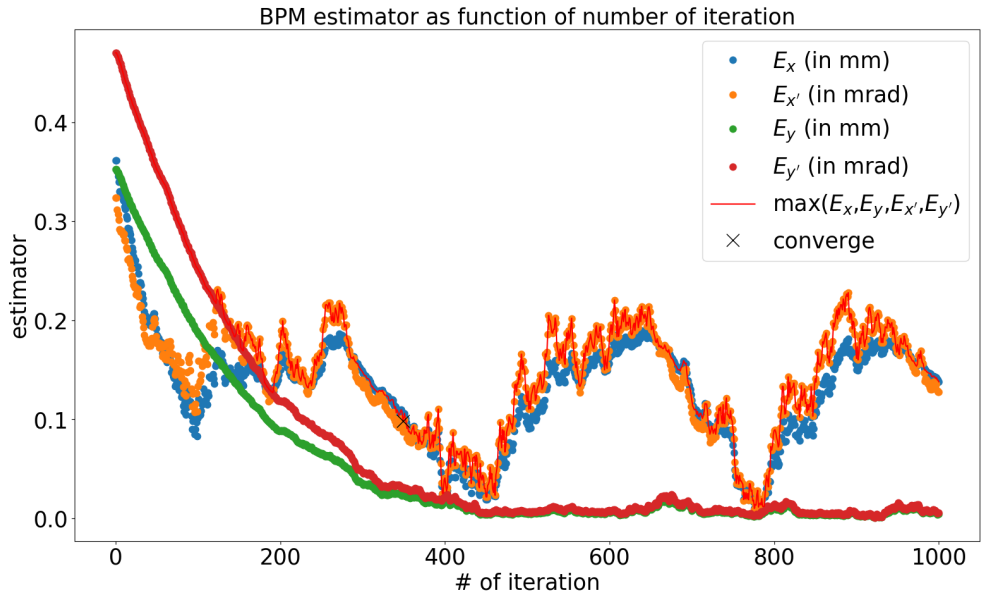

Figure 5.28: Estimation of the ring injection against iterations of the injection feedback. The particle used for this simulation of the injection feedback is randomly selected within the 1-σ beam ellipse. The coefficient of correction applied at each 1000 iterations is $1\,\%$. A random error of $\pm 100\,\mu\mathrm{m}$ is added to the beam position given by MadX tracking. The convergence iteration is defined as the first iteration where E_x and E_y are below $0.1\,\mathrm{mm}$ and $E_{x'}$ and $E_{y'}$ are below $0.1\,\mathrm{mrad}$.

With a smaller correction applied, the injection is improved as one cas see on Fig. 5.28 In the vertical plane, simulations tend to nearly perfect injection, while in the horizontal plane, the x estimator fluctuates between 0 and $0.2\,\mathrm{mm}$ which is better than the initial $0.36\,\mathrm{mm}$ oscillation.

Ten other similar simulations have been made. To evaluate the quality of the injection, the means and the standard deviation of these simulation estimators are summarised in Tab. 5.5. Only the last 800 iterations are considered to avoid the 200 first iterations that initial estimators may dominate.

By comparison with the others, simulation shown on Fig. 5.28 is slightly above the average.

The correction of the injection in the vertical plane is excellent, with maximum oscillations of the order of a few tens of micrometres in every case. For the

Table 5.5: Means and standard deviation of estimators on the last 800 iterations of perfect feedback simulation with random BPM error within $\pm 100\,\mu\mathrm{m}$.

Simulations #	E_x[µm]	$E_{x'}$[µrad]	E_y[µm]	$E_{y'}$[µrad]
0	86 ± 59	95 ± 66	8 ± 5	10 ± 7
1	133 ± 63	142 ± 66	7 ± 5	9 ± 6
2	103 ± 40	115 ± 51	11 ± 5	13 ± 6
3	119 ± 64	129 ± 68	7 ± 4	9 ± 5
4	98 ± 54	106 ± 57	15 ± 17	20 ± 23
5	183 ± 49	199 ± 59	14 ± 10	18 ± 13
6	109 ± 38	118 ± 39	12 ± 7	15 ± 9
7	81 ± 24	89 ± 33	17 ± 18	22 ± 24
8	125 ± 98	130 ± 95	18 ± 17	24 ± 23
9	75 ± 59	83 ± 64	15 ± 13	20 ± 18
10 (Fig. 5.28)	121 ± 49	134 ± 54	16 ± 20	21 ± 27
mean ± max	112 ± 98	122 ± 95	13 ± 20	16 ± 27

horizontal plane, oscillations are ten times larger with a mean ring oscillation of $(0.112 \pm 0.098)\,\mathrm{mm}$. This value is not so far away from the condition of convergence which means that the injection is not optimum but not outrageous too.

In short, with small corrections at each iteration in a perfect case, it is possible to improve the injection to a maximum oscillation of the order of $0.2\,\mathrm{mm}$.

5.3.3.2 Fluctuations case

As both errors of position measurement and fluctuation of the beam position at the beginning of the TL lead to an increase in the oscillation in the ring, considering both effects simultaneously can lead to unexpected results. This section present results of 10 simulations done with :

- Initial particle - representing the beam centoid - selected within 1-σ beam ellipse
- Beam-to-beam fluctuation of $1\,\%$ of the beam size and momentum at the beginning of the section
- $0.1\,\mathrm{mm}$ random BPM error
- over 1000 iterations

The estimators as function of the iterations is presented for two of them. One with a good injection (Fig. 5.29) and one with a bad one (Fig. 5.30).

On those two plots, one may notice that large oscillations are induced during a large number of iterations - which correspond to BPM error impact - on top

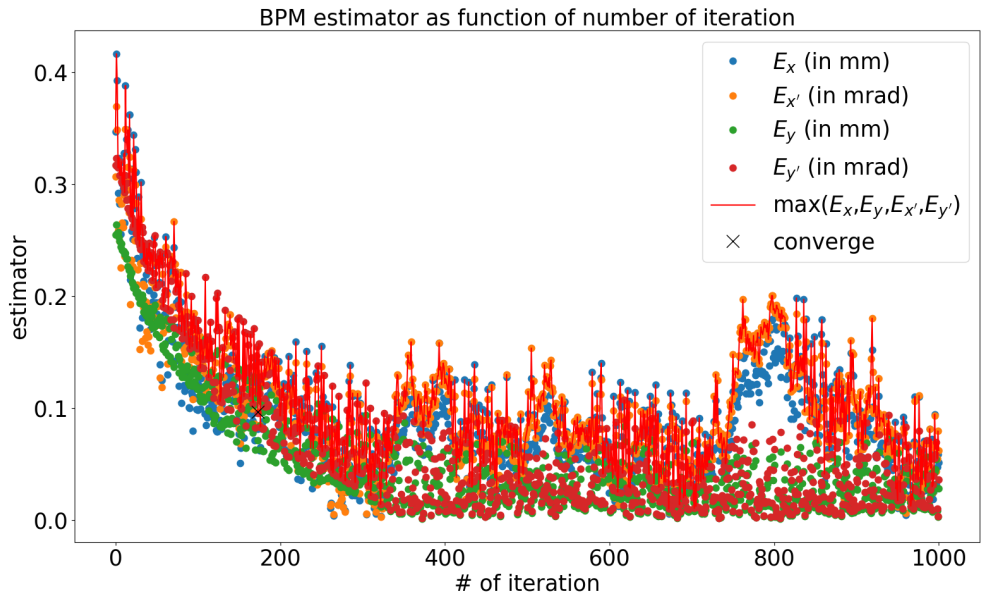

Figure 5.29: Estimation of the ring injection against iterations of the injection feedback. The particle used for this simulation of the injection feedback is randomly selected within the 1-σ beam ellipse with an additional random beam-to-beam fluctuation of $1\,\%$ of the beam size at the start of the TL. The coefficient of correction applied at each 1000 iterations is $1\,\%$. A random error of $\pm 100\,\mu\mathrm{m}$ is added to the beam position given by MadX tracking. The convergence iteration (190) is defined as the first iteration where E_x and E_y are below $0.1\,\mathrm{mm}$ and $E_{x'}$ and $E_{y'}$ are below $0.1\,\mathrm{mrad}$.

of which small fluctuations - characteristics of beam-to-beam fluctuation - are visible. Both effects add up to increase some time the oscillations in the ring, hence deteriorating the injection.

The mean and standard deviation of the last 800 iterations of the 10 simulations done are presented in Tab. 5.6. One may notice that the presented plots correspond to the worst and best simulations. In average, oscillation in the ring are of the order of $(0.15 \pm 0.11)\,\mathrm{mm}$ horizontally and $(0.03 \pm 0.02)\,\mathrm{mm}$ vertically, which correspond to 1.3 and 2.2 times larges respectively than perfect cases without beam-to-beam fluctuation (section 5.3.3.1.2).

In short, in this case, the convergence in the vertical plane is still reached with good precision. In the horizontal plane, the injection feedback induces some fluctuation of the oscillation amplitude above the convergence criterion. Still, some improvement in the horizontal injection is visible most of the time.

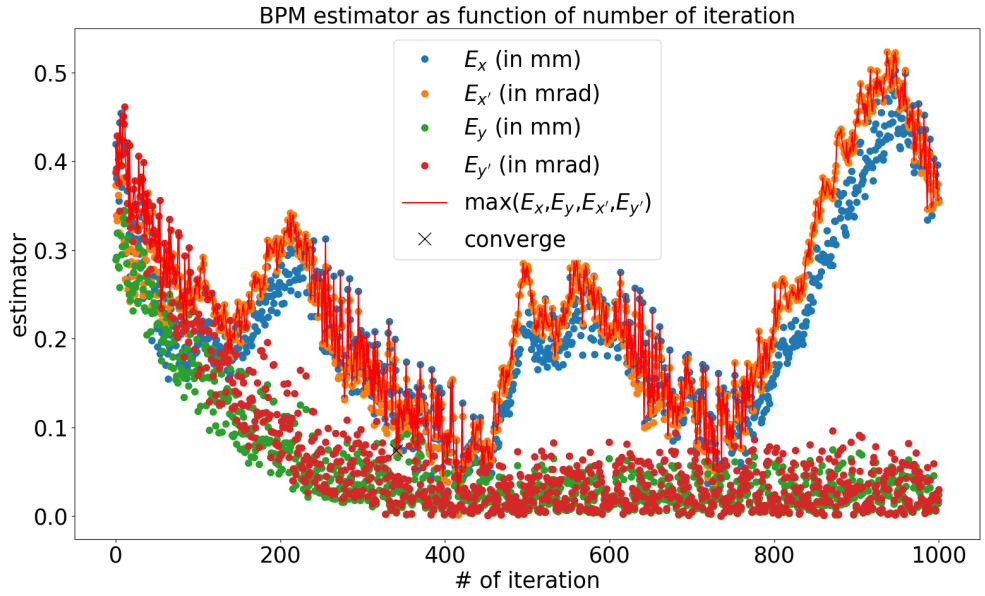

Figure 5.30: Estimation of the ring injection against iterations of the injection feedback. The particle used for this simulation of the injection feedback is randomly selected within the 1-σ beam ellipse with an additional random beam-to-beam fluctuation of $1\,\%$ of the beam size at the start of the TL. The coefficient of correction applied at each 1000 iterations is $1\,\%$. A random error of $\pm 100\,\mu\mathrm{m}$ is added to the beam position given by MadX tracking. The convergence iteration (190) is defined as the first iteration where E_x and E_y are below $0.1\,\mathrm{mm}$ and $E_{x'}$ and $E_{y'}$ are below $0.1\,\mathrm{mrad}$.

Table 5.6: Means and standard deviation of estimators on the last 800 iterations of $1\,\%$ beam-to-beam fluctuation feedback simulation with random BPM error within $\pm 100\,\mu\mathrm{m}$.

Simulations #	E_x[µm]	$E_{x'}$[µrad]	E_y[µm]	$E_{y'}$[µrad]
0	145 ± 44	158 ± 48	30 ± 20	38 ± 26
1	163 ± 92	175 ± 98	27 ± 18	35 ± 24
2	91 ± 50	98 ± 55	29 ± 19	37 ± 25
3	104 ± 40	112 ± 42	31 ± 21	40 ± 28
4 (Fig. 5.30)	206 ± 108	224 ± 121	29 ± 21	37 ± 28
5	206 ± 79	223 ± 87	26 ± 18	34 ± 23
6	200 ± 56	216 ± 57	29 ± 18	38 ± 24
7	160 ± 59	174 ± 63	29 ± 20	37 ± 26
8 (Fig. 5.29)	77 ± 38	85 ± 42	31 ± 21	40 ± 27
9	127 ± 66	140 ± 69	32 ± 20	42 ± 26
mean ± max	148 ± 108	161 ± 121	29 ± 21	38 ± 28

5.3.4 . Error correction

According to studies presented above, error in the BPM measurement seems to have one of the worse impacts on the injection feedback, with large beam-to-beam fluctuation for a potentially long time.

Some potential solutions - not yet tested - to minimise this effect are discussed here.

Without adding much new computation, one may calculate the steerer strength with measured values and some slightly modified values for each iteration. Those modified strengths give an idea of the sensitivity of the injection process. The higher the sensitivity, the lower should be the coefficient of correction applied to avoid large over-correction in case of significant measurement errors. Moreover, a potentially more accurate steerers' strength could be computed by taking a weighted mean of those new computed strengths.

Once a good injection is obtained, and the ring position measurement fluctuation is of the order of BPM uncertainties one may deactivate the feedback for a given duration.

In that case (good injection), the injection feedback could also be applied each N shots to reduce the statistical error on the BPM's value.

5.4 . Conclusion

To conclude, a feedback system has been developed to improve the electron beam injection in the ring of ThomX. This feedback is tested on simulations and gives promising results. The two primary sources of errors are BPM's measurement errors and large beam-to-beam fluctuations. Without taking them into account, one may obtain horizontal oscillations of the beam in the ring of less than $0.1\,\mathrm{mm}$ and even smaller vertical oscillations. When those two effects are considered, they add up to each other. One needs to have a small coefficient of correction from one iteration to the next to avoid large oscillations. In the horizontal plane, a mean oscillation below $0.2\,\mathrm{mm}$ could be achieved, while in the vertical plane, the correction stays nearly perfect with oscillations below $0.10\,\mathrm{mm}$ each time. Those values are of the same order of magnitude than the oscillations induced by the reproducibility of the injection devices (see section 3.2.3).

The injection feedback code must be tested on the actual machine once the commissioning of the ring begins to verify those affirmations.

6 - ThomX commissioning

Contents

In May 2021, the French nuclear safety authority (Autorité de Sûreté Nucléaire - ASN) delivered its authorisation for starting the operations for phase I of the ThomX project. This chapter recalls the phase I main parameters and presents a brief history of the commissioning and a few results of the electron beam diagnostics.

6.1 . Commissioning review

6.1.1 . Phase I parameters

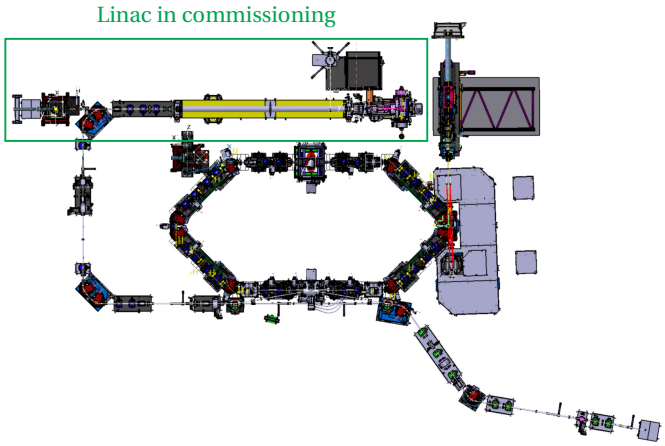

Figure 6.1: Drawing of ThomX seen from above. The green rectangle shows the part of the accelerator under commissioning during phase I.

Phase I of the ThomX project allows the commissioning of the straight part of the accelerator - denoted as *linac* from here onwards - shown in Fig. 6.1. Hence the dipoles found after the accelerating section cannot be turned on yet.

The beam energy tolerated for the commissioning is the nominal one - $50\,\mathrm{MeV}$ - while both the repetition rate and the charge are limited to $10\,\mathrm{Hz}$ and $100\,\mathrm{pC}$ respectively. With this smaller charge, the gun simulation predicts a geometrical transverse emittance of $2\pi.\mathrm{mm.mrad}$ in both planes.

6.1.2 . Timeline of the commissioning

The first months of the accelerator commissioning were reserved for the RF commissioning of the accelerating section and RF gun. Both RF systems were commissioned by the end of September 2021, and the first dark current was observed on the first screen station: on station LI/DG/SST.01 (Fig. 6.2). This electron emission comes from the field emission [5] of the gun (see section 2.1.1).

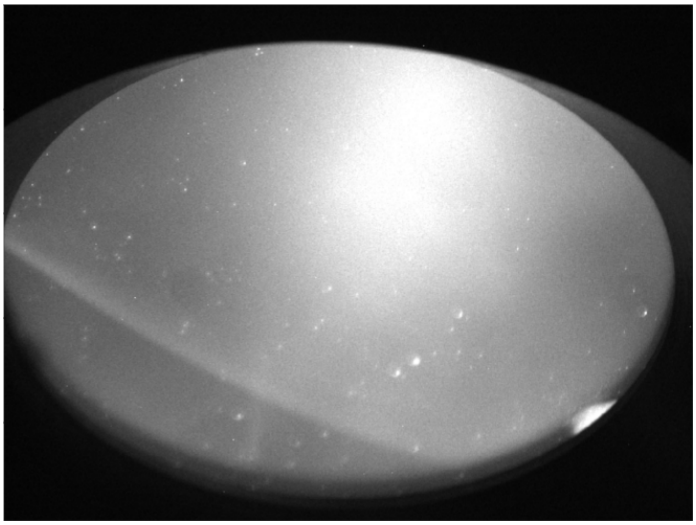

Figure 6.2: The first image of the dark current on the first screen station just after the gun: LI/DG/SST.01.

The 4^{th} of October 2021 the first photo-emitted electrons has been observed on the very same screen (Fig. 6.3).

In less than a month, the operators have achieved delivering a $50\,\mathrm{MeV}$, $100\,\mathrm{pC}$ electron beam at $10\,\mathrm{Hz}$. Other beam measurements were done the following months, like emittance measurement and optical transition radiation (OTR) light emission. Still, the main study was the alignment of the machine and the reduction of the parasitic magnetic field. A good alignment of the machine head must simplify the X-rays optimisation by reducing the beam displacement - hence transport modification - during optimisation of the gun focalisation [48].

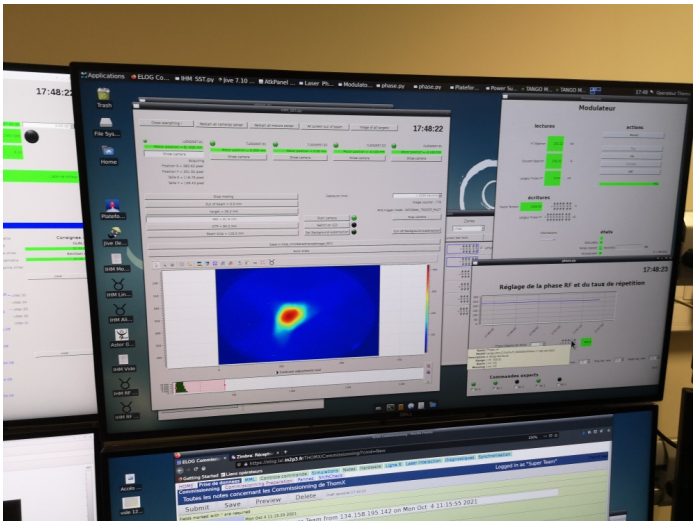

Figure 6.3: Image of the control room's screen of ThomX. I have developed the left interface that is used to visualise the beam. On the blue image, the red spot correspond to the first photo-emitted observed the 4^{th} of October 2021 on the LI/DG/SST.01 screen station just before the accelerating section.

6.2 . Diagnostic commissioning

Several diagnostics were commissioned during phase I to measure the electron beam properties. They are represented on the Fig. 6.4 with the other main elements of the line. From right to left (beam direction) in the linac, the beam passes thought elements resumed in Tab. 6.1.

Beam loss monitors seen on Fig. 2.6 will not be discussed in this chapter as they are not yet commissioned. The other diagnostics and a few results are presented in the following sections.

Table 6.1: Linac elements from the electron source (RF gun) to the beam dump (Faraday cup)

LI/RF/GUN.01	:	RF gun
LI/AE/STR.01	:	Steerer
LI/DG/BPM.01	:	Beam position monitor
LI/DG/ICT.01	:	Integrating current transformer
LI/DG/SST.01	:	Screen station
LI/HF/ACS.01	:	Accelerating section
TL/AE/STR.01	:	Steerer
TL/AE/QP.01	:	Quadrupole
TL/DG/ICT.01	:	Integrating current transformer
TL/AE/QP.02	:	Quadrupole
TL/AE/QP.03	:	Quadrupole
TL/DG/BPM.01	:	Beam position monitor
TL/DG/SST.01	:	Screen station
TL/DG/FC.01	:	Faraday cup

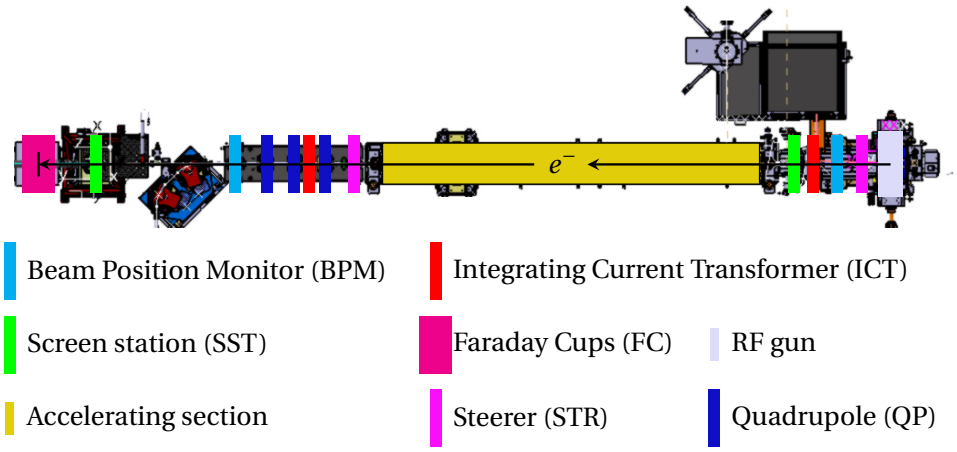

Figure 6.4: Drawing, from above, of the straight part of the ThomX accelerator - green rectangle on Fig. 6.1 - commissioned during phase I.

6.2.1 . Screen station

The screen stations - denoted as SSTs, see section 2.2.2 - are intercepting diagnostics composed of scintillator screens, that emit light at the passage of the electron beam, and a camera to visualise this emission. On ThomX, there are 5 SSTs located near the RF Gun, at the end of the linac, in the transfer line (twice) and in the extraction line (Fig. 6.4). This section focuses only on the 2 SSTs commissioned [49] : LI/DG/SST.01 and TL/DG/SST.01.

At least three screens are available on each station. First, a USAF1951 calibration chart [50] is used to measure the resolution and magnification of the optical

system. Yttrium Aluminum Garnet crystal doped with Cerium - YAG:Ce [35] - and an Optical Transition Radiation - OTR - screen are used for beam visualisation.

On TL/DG/SST.01, an additional fourth screen made of sapphire is used to generate Cherenkov radiation - light emission by particles travelling in some medium faster than light in this medium - and will allow longitudinal length measurement of the beam using a streak camera located in the photocathode laser room. The measure of the longitudinal length of the beam is not yet performed, but a first image of the Cherenkov emission at the exit of the accelerator bunker is shown in Fig. 6.5. The Cherenkov radiation is emitted at a specific angle depending on the particles energy. For the $50\,\mathrm{MeV}$ electron beam of ThomX, this Cerenkov angle is $\theta_{cr} = 55.63°$. For simplicity, screen is rotate of an angle $\theta_p = 114.75°$ such that the light is emitted upward emission like shown in Fig. 6.6.

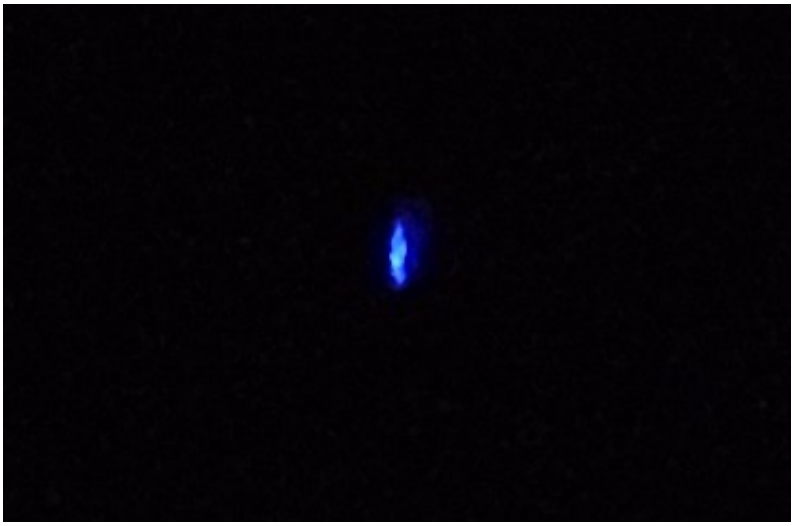

Figure 6.5: First image of the Cherenkov emission on the screen station TL/DG/SST.01 take the 21^{st} of July 2022. The image have been made with a phone camera at the exit of the accelerator bunker.

The other screens are rotated of $45°$ from both the beam trajectory and the camera axis as shown on Fig. 6.7, which means that light is emitted downwards perpendicular to the beam trajectory.

Cameras are “Basler scout scA640-70gm" CCD cameras [51] with “Tamron : 18-400mm F/3.5-6.3 Di II VC HLD" commercial lenses [52].

6.2.1.1 Calibration chart screen

The first screen on the mechanical arm is used for optical calibration. It is composed of glass engraved with 9 USAF-1951 resolution test chart [50] similar to the one shown on Fig. 6.8. This chart comprises triplets of calibrated horizontal and vertical lines denoted as elements. To discriminate each element, a group and an element

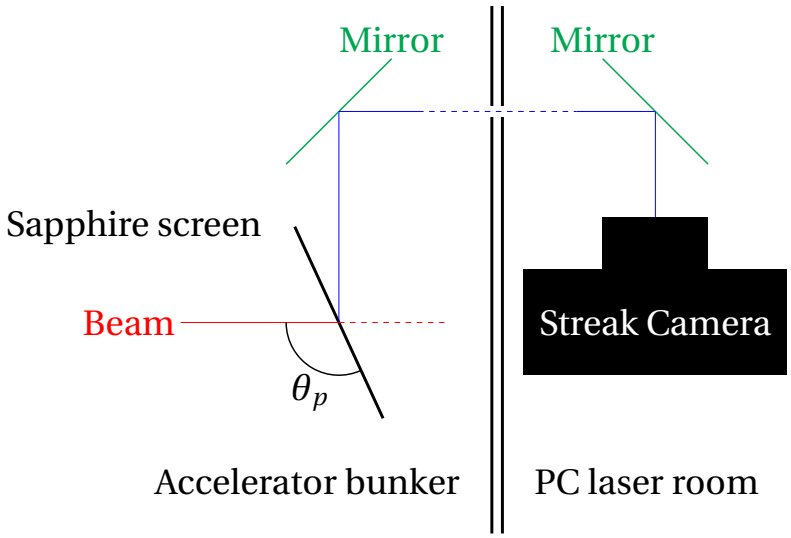

Figure 6.6: Sketch of the Cherenkov screen emission and propagation to the streak camera in the photocathode laser room used for length measurement.

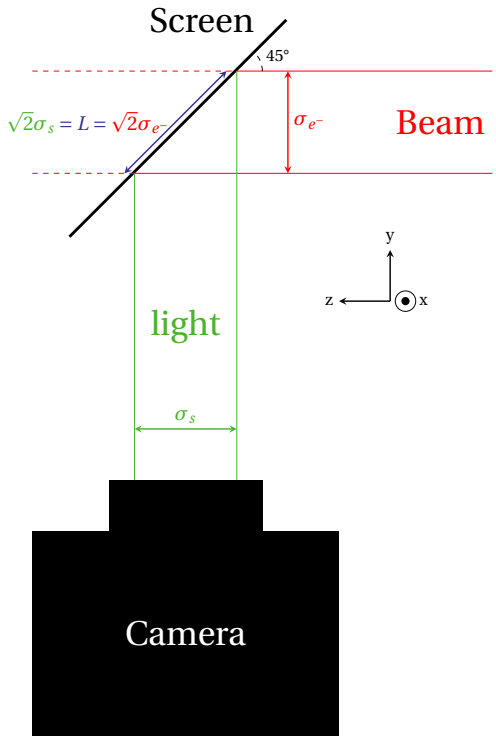

Figure 6.7: Drawing of screen station principle.

number are used. The element number can be found by the side of each element and goes from 1 to 6, while the group number is on top of them, and the value

depends on the line size.

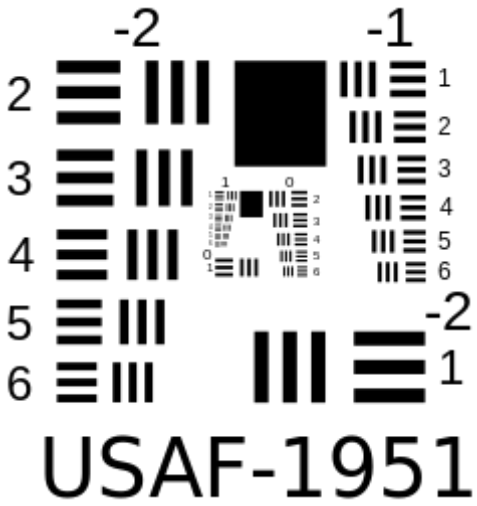

Figure 6.8: Example of one USAF-1951 resolution test chart [50].

To find the size of a line, one has to know the pair group-element number. From those value one can compute the width - or a fifth of the length - using the Eq. (6.1).

$$d[\mathrm{mm}] = 2^{-(1+group+(element-1)/6)} \tag{6.1}$$

From the size of the largest element, one may accurately compute the pixel/millimetre ratio needed to calculate the beam size - hence the magnification - while the resolution comes from the smallest element's triplet of lines that one can discriminate. To ensure reproducibility of the measurement, Scott Williams has developed a python code [53] that takes an image of the calibration target, like those of Fig. 6.9, and return resolution and magnification. Computation of Fig. 6.9 magnification and resolution are resumed in Tab. 6.2.

Table 6.2: Calibration parameters computed for images of Fig. 6.9. Resolution is given for the upper target, while other parameters are the mean for all targets detected by the analysis's code.

	Resolution [μm]		**Magnification** [μm/px]			
	Horz	**Vert**	**HX**	**VX**	**HY**	**VY**
Li/DG/SST.01	125	99	36	0	1	−36
TL/DG/SST.01	79	79	28	10	−5	27

The magnification computation gives a 2x2 matrix used to compute, from horizontal (h) and vertical (v) pixel length on the image, the horizontal (x) and vertical (y) physical length of the beam (in μm) by Eq. (6.2). This 2X2 matrix

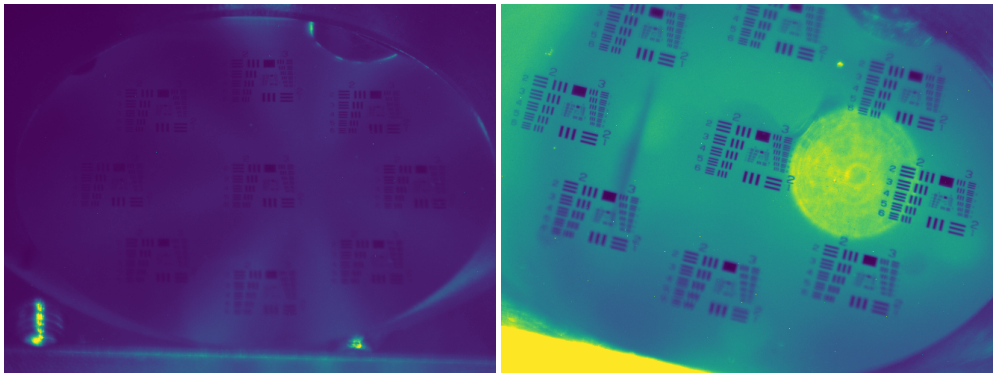

Figure 6.9: Image of LI/DG/SST.01 (left) and TL/DG/SST.01 (right) calibration's target.

corresponds to horizontal and vertical conversion factor times a rotation matrix, which explains why VX and HY are close to 0 in the case of LI/DG/SST.01 (screen horizontal) but not in the case of TL/DG/SST.01 (screen tilted).

$$\begin{pmatrix} x[\mu\mathrm{m}] \\ y[\mu\mathrm{m}] \end{pmatrix} = \begin{pmatrix} HX & VX \\ HY & VY \end{pmatrix} \times \begin{pmatrix} h[pixel] \\ v[pixel] \end{pmatrix} \tag{6.2}$$

6.2.1.2 YAG:Ce screen

The second screen on the mechanical arm of the screen stations is an Yttrium Aluminum Garnet doped with Cerium crystal.This YAG:Ce - hereafter denoted as YAG - is a scintillator crystal. When the electrons pass through the crystal, they deposit some energy through atoms' excitation. After a certain time, those atoms go back to the ground state by emitting photons.

The YAG screen permits visualising the transverse beam density, which can be used to measure the beam size or relative beam displacement. The light emission is - at first order - proportional to the electron density. Hence, by integrating the screen intensity, it is even possible to find back the beam charge if one knows the screen yield, the dark current and optical properties of the lens and camera.

The photon yield of the YAG screens before the beam dump - at $100\,\mathrm{pC}$ and $50\,\mathrm{MeV}$ - is of the order of 5×10^{12} photons per beam [54]. This emission is isotropic. Hence only a fraction of the light is directed toward the lens and the camera.

An example of a beam visualised with the YAG screen is given Fig. 6.10.

6.2.1.3 OTR screen

The optical transition radiation (OTR) screen uses the electromagnetic discontinuity between the vacuum and the aluminised screen to generate light. Like for the YAG screen, the OTR permits measurement of the beam size, the relative centroid

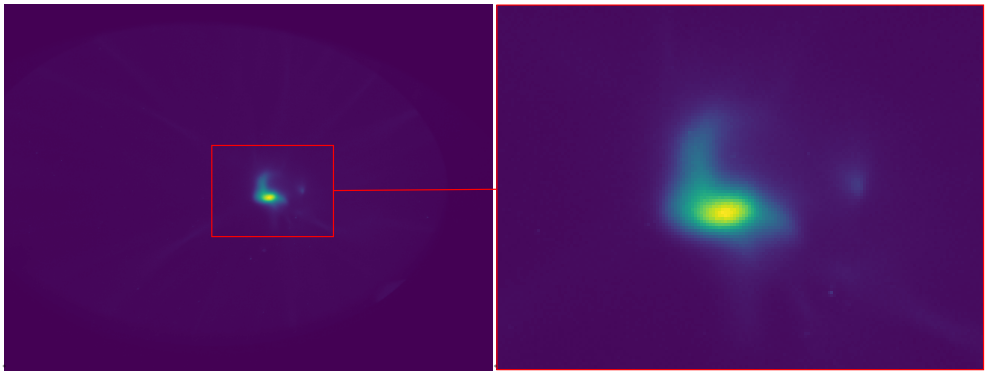

Figure 6.10: Image of one electron beam - in yellow - on the YAG screen of the station before the accelerating section (LI/DG/SST.01).

beam displacement, and the beam charge. The main reasons for having both OTR and YAG screens are, on the one hand, that the OTR screen gives more precise measurements because the thickness of the YAG screen and the blossoming of the energy deposition increases the spot size. On the other hand, the yield of the OTR screen is much smaller than the YAG one and having only OTR screen during the commissioning would have not being sufficient. On ThomX, it is planned to have a yield of 10^8 photons per beam emitted by the screen at $100\,\mathrm{pC}$ and $50\,\mathrm{MeV}$.

The OTR emission is directive with a cone of opening of $1/\gamma \approx 10\,\mathrm{mrad}$ where γ is the Lorentz factor. Hence, most of this emission will be directed toward the camera.

An example of a beam visualised with the OTR screen is given Fig. 6.11.

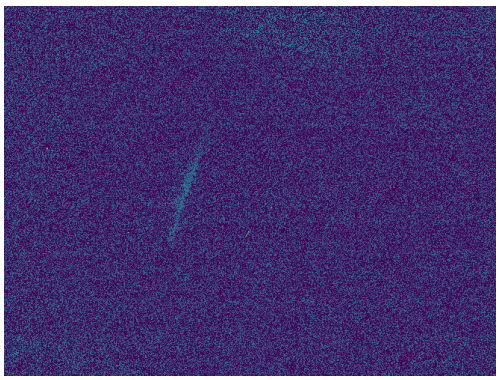

Figure 6.11: The first image of one electron beam - in yellow - on the OTR screen of the station before the beam dump (TL/DG/SST.01). This image was obtained with the subtraction of pictures with and without the beam.

6.2.1.4 YAG and OTR yields

The ratio of YAG yield over OTR yield is given by Eq. (6.3).

$$R_y = \frac{\text{yield}_{YAG}}{\text{yield}_{OTR}} = 5 \times 10^4 \tag{6.3}$$

This value shows a much more intense emission of YAG light than OTR light. Yet, on the camera sensors, the light intensity ratio R_I should be smaller as the optical aperture permits visualisation of nearly all the OTR emissions, but only a fraction of the $4\pi\text{sr}$ YAG emission.

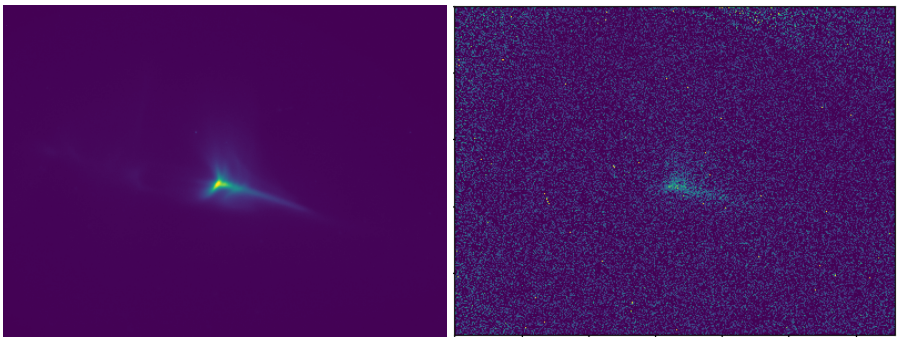

(a) YAG screen : exposition $1\,\text{ms}$.

(b) Subtraction of 2 images, one with a beam, one without. Images parameters are : exposition $10\,\text{s}$, beam repetition rate $10\,\text{Hz} \Rightarrow$ superposition of 100 shots.

Figure 6.12: Comparison of images taken on TL/DG/SST.01 screen station with YAG and OTR screens.

To check this assumption, several images of the beam have been taken with both screens on the TL/DG/SST.01 screen station.For the YAG screen, the raw image is shown Fig. 6.12a, and the sum of all pixels is equal to the beam intensity I_{YAG}. For the OTR screen, the intensity was too low. Hence, the exposure time has been increased to $10\,\text{s}$ to superimpose 100 shots signals. Moreover, a second image with the same exposure time but without the photo-emitted beam has been taken too. The Fig. 6.12b correspond to the subtraction of those two images, and 100 shots intensity I_{OTR} is computed by the sum of all pixels intensities of this image. Then, the intensity for one beam is this calculated intensity divided by 100.

The ratio R_I, in this case, is given by Eq. (6.4).

$$R_I = 100 \times \frac{I_{YAG}}{I_{OTR}} \approx 7 \times 10^3 \tag{6.4}$$

R_I is effectively smaller than R_y by a factor of 10. Still, this difference seems small by comparison with the small optical aperture and the isotropic YAG emission. Hence, only a part of the OTR light must be collected.

To check this and optimise the OTR intensity, a study of the optics (transmittance, aperture, optics direction, optics position, ...) is in progress.

6.2.1.5 Emittance measurement

6.2.1.5.1 Theory Besides measuring the beam size, a screen can be used to compute the transverse emittance of the beam. For that purpose, one can used the quadrupole scan - or quad-scan - method [55] which is aimed at extracting the transverse geometric beam emittance from beam size fluctuation when changing the strength of a quadrupole.

This technique is based on the linear transfer matrix propagation of a beam. Like a particle, a beam can be described by a matrix, and its propagation along a line is done using the same transfer matrix defined in section 3.1. Still, for a beam, the matrix is not a 1D vector but a 2D matrix Σ and the transport is computed using Eq. (6.5).

$$\Sigma_2 = M_{1\to 2}\Sigma_1 M_{1\to 2}^T \tag{6.5}$$

One may consider x-x', y-y', and z-z' planes independent because both the transport matrix of quadrupoles and drift are uncoupled which allows to focus on only one plane. The matrix elements of a beam in x-x' plane are linked to the Twiss parameters α, β, γ and the emittance ϵ by Eq. (6.6).

$$\Sigma = \begin{pmatrix} \sigma_{11} & \sigma_{12} \\ \sigma_{21} & \sigma_{22} \end{pmatrix} = \begin{pmatrix} \epsilon\beta & -\epsilon\alpha \\ -\epsilon\alpha & \epsilon\gamma \end{pmatrix} \tag{6.6}$$

The discriminant $\det(\Sigma) = \sigma_{11}\sigma_{22} - \sigma_{21}\sigma_{12}$ of this beam matrix is the geometric emittance squared ϵ^2 because of the relation between Twiss parameters (Eq. (3.35)).

Let us consider a quadrupole of length l, strength k at a distance D upstream of the screen. By using the thin length approximation, the transfer matrix of the quadrupole can be written as :

$$M_{QP} = \begin{pmatrix} 1 & 0 \\ kl & 1 \end{pmatrix} \tag{6.7}$$

Hence, the transfer matrix from the quadrupole to the screen is given by :

$$M = M_{drift}(D)M_{QP} = \begin{pmatrix} 1+Dkl & d \\ kl & 1 \end{pmatrix} \tag{6.8}$$

The beam matrix at SST is then equal to :

$$\Sigma^{SST} = M\Sigma^{quad}M^T = \begin{pmatrix} 1+Dkl & d \\ kl & 1 \end{pmatrix} \times \begin{pmatrix} \sigma_{11}^{QP} & \sigma_{12}^{QP} \\ \sigma_{21}^{QP} & \sigma_{22}^{QP} \end{pmatrix} \times \begin{pmatrix} 1+Dkl & d \\ kl & 1 \end{pmatrix} \tag{6.9}$$

After calculation, by identifications of the first coefficient, one obtains :

$$\sigma_{11}^{SST} = (1+Dkl)^2\sigma_{11}^{QP} + 2(1+Dkl)\sigma_{12}^{QP} + D^2\sigma_{22}^{QP} \tag{6.10}$$

Yet, $\sigma_{11}^{SST} = \beta\epsilon = \sigma^2$ is the beam size squared. After a last rewrite of the previous equation, one may find the quadratic equation (Eq. (6.11)) of the squared beam size as a function of k.

$$\sigma_x^2 = (\sigma_{11}^{QP} D^2 l^2)\mathbf{k^2} + (2Dl\sigma_{11}^{QP} + 2D^2 l\sigma_{12}^{QP})\mathbf{k} + \sigma_{11}^{QP} + 2D\sigma_{12}^{QP} + D^2\sigma_{22}^{QP} = A\mathbf{k^2} + B\mathbf{k} + C \tag{6.11}$$

Eventually, from a fit on the plot of σ_x^2 as function of k, one can find the constants A, B and C and compute the emittance using Eq. (6.12) and Eq. (6.13).

$$\begin{cases} \sigma_{11}^{QP} = \frac{A}{D^2 l^2} \\ \sigma_{12}^{QP} = \frac{B - 2Dl\sigma_{11}^{QP}}{2D^2 l} \\ \sigma_{22}^{QP} = \frac{C - \sigma_{11}^{QP} - 2D\sigma_{12}^{QP}}{D^2} \end{cases} \tag{6.12}$$

$$\epsilon_x = \sqrt{\sigma_{11}^{QP}\sigma_{22}^{QP} - (\sigma_{12}^{QP})^2} \tag{6.13}$$

The same demonstration can be done for the y-y' plane to compute the geometric emittance ϵ_y.

6.2.1.5.2 Measurement

On ThomX, the accelerator toolbox of Matlab Middle Layer [56] is used to provide transport matrices needed for the least mean square method. A measurement done using this code is shown Fig. 6.13. The quadrupole used is the last quadrupole of the triplet after the section (TL/AE/QP.03), and the beam size is measured using the screen station before the beam dump (TL/DG/SST.01).

This measurement gives a transverse geometric emittance of $\epsilon_x = 4.0 \times 10^{-2}\,\pi.\mathrm{mm.mrad}$ and $\epsilon_y = 2.7 \times 10^{-2}\,\pi.\mathrm{mm.mrad}$. The geometric emittance is not practical for comparing emittances of machines of different energy. Instead, the normalised emittance is computed by multiplying the geometric emittance by the relativistic β and γ factor.

For ThomX, $\beta \approx 1$ and $\gamma \approx 100$. Hence the normalised emittance is $\epsilon_x^N = \beta\gamma\epsilon_x = 4.0\,\pi.\mathrm{mm.mrad}$ and $\epsilon_y^N = \beta\gamma\epsilon_y = 2.7\,\pi.\mathrm{mm.mrad}$. The theoretical value of the transverse normalised emittance at $100\,\mathrm{pC}$ is $2\,\pi.\mathrm{mm.mrad}$ in both planes. The measurement is close to the theory, and some optimisation has permitted to reach nominal values after this measurement.

6.2.1.6 Energy measurement

6.2.1.6.1 Theory

To measure the beam's energy, the nominal method on ThomX will be to use the dipoles of the TL. The propagation in those dipoles has to respect Eq. (6.14).

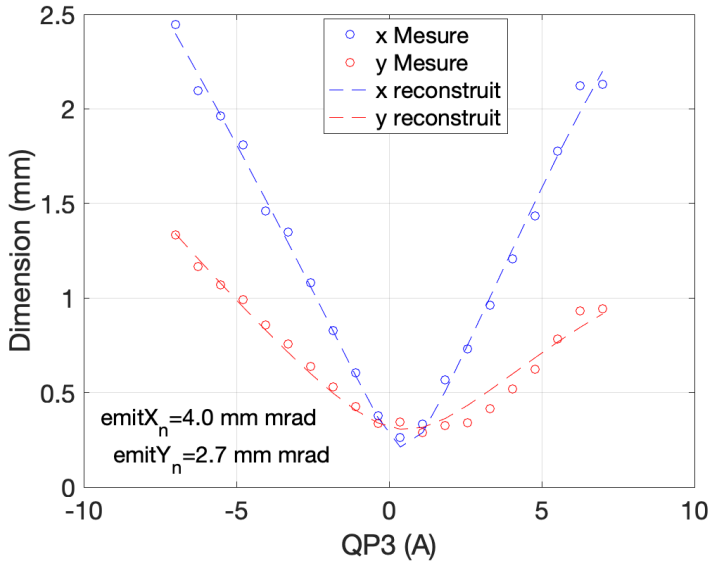

Figure 6.13: Results of the emittance measurement on the screen station TL/DG/SST.01 [57]. The dots correspond to the measurements, and the dashed line corresponds to the beam dimension found by the propagation of the computed beam matrix from the quadrupole TL/AE/QP.03 to the screen.

$$|B\rho| = \left|\frac{p}{q}\right| \tag{6.14}$$

The magnetic field B can be computed knowing the current in the dipole. The curvature radius ρ is implied by the geometry of the dipole, and the particles' charge is -e, the elementary charge. Hence the only unknown is the particles' momentum p linked to the particle's energy by Eq. (6.15) under relativistic approximation.

$$p = \gamma m v \approx \gamma m c = \frac{E}{mc^2} mc = \frac{E}{c} \tag{6.15}$$

One could compute the beam energy from the value of the magnetic field needed to pass from the linac to the TL rotated of 90°. Still, phase I does not permit switching on dipoles.

A similar technique is used to measure the energy but with a steerer to replace the dipole and a screen to measure beam displacement. The Fig. 6.14 shows the principle of this method.

The energy is given by Eq. (6.16) where l_B is the magnetic length of the steerer, L is the distance steerer-screen, B is the magnetic field, and d is the displacement of the beam centroid.

$$E = l_B \times L \times \frac{\Delta B}{\Delta d} \tag{6.16}$$

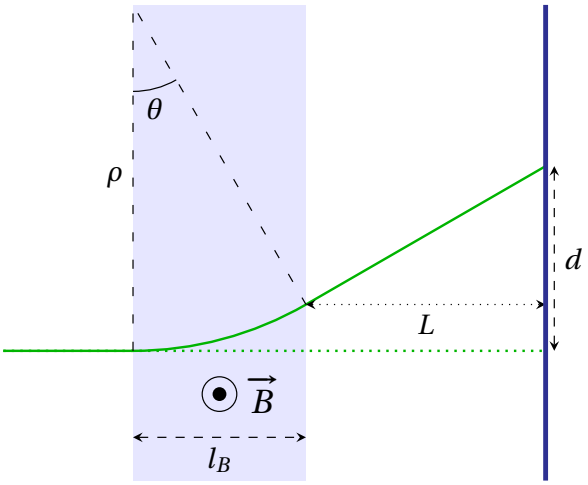

Figure 6.14: Drawing of the principle of the beam energy measurement using steerers (light blue rectangle) and screen station (dark blue line).

The measurement is done for several magnetic fields for a greater accuracy. The $\frac{\Delta d}{\Delta B}$ factor is then computed as the slope of the linear fit on the measured points of the beam displacement against the magnetic field. The fit error provides the energy error.

6.2.1.6.2 Measurement The method could be used at two locations. Before the accelerating section using the first steerer (LI/AE/STR.01) and the first screen station (LI/DG/SST.01) of the linac, or after it using the third steerer (TL/AE/STR.01) and the second screen station (TL/DG/SST.01). One energy measurement before the accelerating section is presented in Fig. 6.15.

The upper part shows three different beam positions at three magnetic fields corresponding to the extreme and the middle data, while the lower part shows the measured points and the linear fit.

At that time, the energy of the beam at the exit of the gun was $E = (3.6 \pm 0.3)\,\mathrm{MeV}$. Now, the nominal energy of $5\,\mathrm{MeV}$ before the section and $50\,\mathrm{MeV}$ after it has been reached.

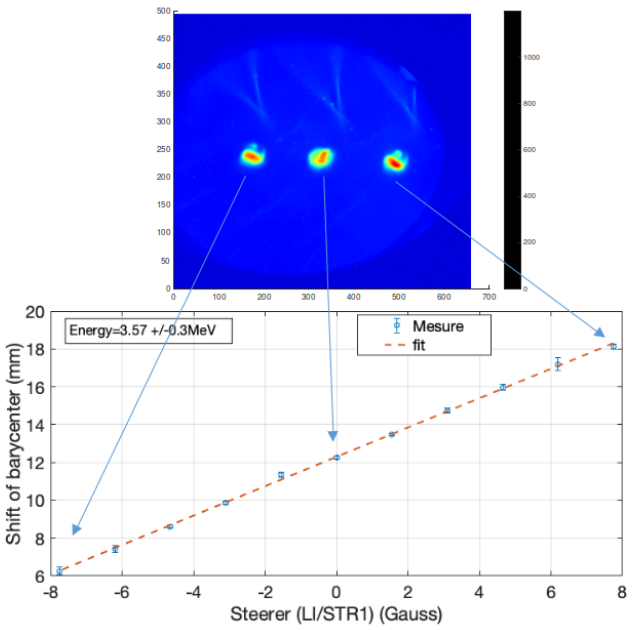

Figure 6.15: Beam energy measurement with the linac's first steerer (LI/AE/STR.01) and the first screen station (LI/DG/SST.01). Above is a superposition of three beams for three different magnetic strength values: $-8\,\mathrm{G}$, $0\,\mathrm{G}$ and $8\,\mathrm{G}$. Below is the curve of the displacement of the beam center against the steerer strength.

6.2.2 . Beam Position Monitors

Beam position monitors (BPMs) are devices using four electrodes to measure the transverse beam position. An example of the four electrodes signal of one beam on the TL/DG/BPM.01 BPM is shown Fig. 6.16.

The position calculation is done by the Libera brillance + electronic [34]. When the signal on one of the channel passes over the threshold - in red on the figure - at the Analog to Digital Converter (ADC) counts T, the Libera computes the sum of all ADC's values from $T - n_b$ to $T + n_a$ for each electrode. On ThomX the number of ADC's values before the threshold is $n_b = 10$ and the number of ADC's values after the threshold is $n_a = 50$. This sum corresponds to the voltage V_i delivered by electrodes A, B, C and D. Then, to compute the beam position, one must use Eq. (6.17).

$$\begin{cases} x = k_x \frac{(V_A+V_D)-(V_B+V_C)}{(V_A+V_B+V_C+V_D} - x_{\text{offset}} \\ y = k_y \frac{(V_A+V_C)-(V_B+V_D)}{(V_A+V_B+V_C+V_D} - y_{\text{offset}} \end{cases} \tag{6.17}$$

The offsets x_{offset} and y_{offset} are used to correct electrodes coupling, while the conversion factors k_x and k_y permit conversion of voltage ratios into meters. Those four values have been measured beforehand with a virtual network analyser

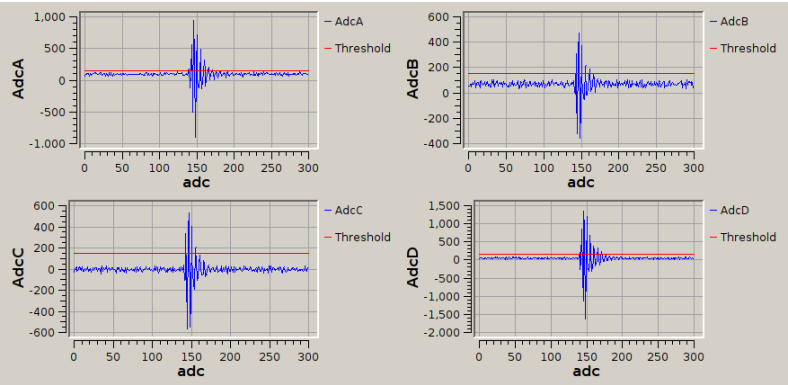

Figure 6.16: Signals from the 4 electrodes of the BPM TL/DG/BPM.01. If one look downstream, electrodes correspond to : A→top-right, B→top-left, C→bottom-left, D→bottom-right. The horizontal axis corresponds to the time, while the vertical corresponds to the measured voltage. The red line represents the threshold used to detect the beam.

for the offsets and on a test bench for the conversion factors.

Several preliminary measurements show a beam-to-beam fluctuation of hundreds of micrometres, corresponding to the theoretical BPM accuracy. The same comparison with screen stations shows a smaller fluctuation. Hence the beam-to-beam instability in the BPM is dominated by the BPM accuracy.

6.2.3 . Integrating current transformer

The integrating current transformer (ICT) is a solenoid wrapped around the beam. A current is induced in the solenoid when the beam passes through the ICT. The ratio $R_{i\to b}$ between the induced current and the beam current is approximately 10 for ThomX ICTs.

The induced current is measured by a WaveCatcher (WAC, see section 2.3.3). An example of the signal on both ICT in the linac is shown Fig. 6.17.

The beam signal corresponds to the negative peak on these curves, while the dark current is responsible for the global offset. The dark current is more prominent for the ICT after the gun than after the section, as a large part of the dark current does not match the accelerating section acceptance. The time delay between both beam signals corresponds to the synchronisation delay difference between the two WACs used. The after-section ICT is ahead to permit measurement of the Faraday cup on the same WAC.

The beam charge Q_{beam} can be computed using Eq. (6.18) where $R_{i\to b} \approx 10$ is the ICT efficiency, $f = 3.2\,\text{GHz}$ is the sampling frequency, $Z = 50\,\Omega$ the impedance of the WAC, $I(t)$ the ICT signal read by WAC and I_{dark} the average dark current.

$$Q_{\text{beam}} = R_{i\to b} \times Q_{\text{induce}} = R_{i\to b} \times \frac{1}{f \times Z} \sum_t (I(t) - I_{\text{dark}}) \tag{6.18}$$

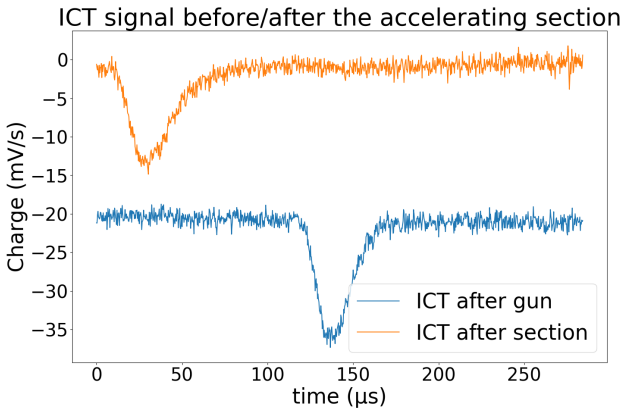

Figure 6.17: ICT's signals on LI/DG/ICT.01 and TL/DG/ICT.01, the two ICTs before and after the accelerating section. In both cases, the measured charge signal was around $100\,\mathrm{pC}$.

The average dark current is computed by taking the average of 100 repetitions of the mean of the ICT signal when a shutter stops the laser beam.

In the Fig. 6.17, both ICT signals give a beam charge of $100\,\mathrm{pC}$, which means a total transport of the nominal beam charge in the accelerating section.

6.3 . Conclusion

The commissioning is an important step for a machine and be able to actively participate to it permit to understand the challenge that it induce.

I have mostly participate to the commissioning of diagnostics - such as BPM, ICT, FC and SST - which are essential for characterising the beam and for which I had to operate the machine.

I have also developed some Graphical User Interface (GUI) to use theses diagnostics effectively. Creating those GUI have permit to understand the acquisition control system and obtained a global visualisation of ThomX

Eventually, in August 2022 ThomX has obtained is authorisation to start the phase II and about a month later - in September the 9^{th} - we obtained our first electron beam injected in the ring that had lead to the commissioning of all TL diagnostics and of ring's BPM.

Conclusion

This thesis takes place in a prototype of a new kind of high-intensity X-ray source named ThomX. This source aims at using a $50\,\mathrm{MeV}$ electron beam stored in a small storage ring to increase - by momentum transfer - the energy of photons stored in a Fabry-Perrot cavity. This phenomenon is the Compton backscattering effect.

Before the commissioning of the machine, some simulations of the accelerator's transfer line (TL) and ring injection were made. Those simulations have permitted the study of particle loss risks during the injection.

The risk of losses is null for nominal beam parameters on the perfect machine. Losses are unlikely for larger beam size or momentum but could occur, especially during the first half-ring turn after the injection. Those losses may diminish the X-ray flux and must be avoided as much as possible. For that purpose, particle tracking has been implemented and has permitted the creation of maps of losses projected at diagnostic locations. The two first screen stations of the TL do not allow determining a free-losses region where the beam must be to avoid losses in the first ring turn, but the third can. On this station, the best location for the beam position seems to be x between $-7\,\mathrm{mm}$ and $10\,\mathrm{mm}$ and y between $\pm 2\,\mathrm{mm}$.

The maps of losses have also been projected in the ring's first beam position monitor (BPM), and they could also give a good evaluation of the acceptance window of the ring's first turn.

An injection feedback code has been developed to correct the beam injection in the ring using steerers of the TL. This code is based on two 6D propagation equations computed using a linear transfer matrix. It aims to quickly compute the steerers' strength as only a few calculations must be made. This feedback is not tested on the accelerator as the ring is not commissioned yet, but some simulation tests have been performed.

According to those simulations, the error on the beam position measurement seems to have the worse impact on the horizontal injection feedback correction as it induces some large beam oscillations in the ring for many iterations. Still, with the right choice of the correction coefficient to be applied from one beam to the next and of the beam position, a good injection correction may be obtained. For a $1\,\%$ correction coefficient and an off-axis beam, a $\pm 0.1\,\mathrm{mm}$ error on the BPM measurement lead to a horizontal oscillation of the order of $(0.15 \pm 0.11)\,\mathrm{mm}$ in the ring.

In every case, the injection feedback in the vertical plane is accurate, with the most prominent oscillations in the ring of less than $0.1\,\mathrm{mm}$.

The commissioning of the linear part of the accelerator started in June 2021. Some electron diagnostics results have been presented, such as beam position,

charge, energy and emittance. For the last two, a screen station is used to visualise the beam. The calibration of the screen station has been detailed. Thanks to those diagnostics, the nominal beam parameters were obtained soon after the first photo-emitted electron beam.

The authorisation of the French Nuclear Safety Authority (Autorité de Sûreté Nucléaire - ASN) to start the operations for phase II of the ThomX project was obtained in August 2022. Phase II started with the TL's commissioning and the beam's characterisation. Once a good beam's transport is obtained, the ring's commissioning has begun. The first beam is the ring has been obtained in September the 9^{th}, 2022. The injection feedback system will be tested soon to improve the injection and better understand what was obtained during the simulations. The first X-rays are expected towards the end of 2023.

A - Summary of injection feedback simulations

This annex is a summary of all simulation done for the injection feedback test (section 5.2 and section 5.3).

The principle of those simulations can be described in 6 steps:

1. **Selection**: Selection of one beam centroid represented by a particle
2. **Propagation**: Tracking of this particle from the beginning of the transfer line to the end of the first ring turn
3. **Estimation**:Computation of the estimator
4. **Computation**: Computation of the steerers' correction
5. **Correction**: Application of a fraction of the above correction
6. **Iterations**: Restart from 2. for a certain number of iterations

Some parameters can be tested for each step except for the estimation. Is there a list of all those parameters

- **Selection**:
  - Parameter: **Selection**:
    * Use the reference particule $\overrightarrow{0}$: denoted as $\overrightarrow{0}$
    * Select the particle within the 1-σ beam ellipse : denoted as **1-σ beam**
    * Select the particle within the 5-σ beam ellipse : denoted as **5-σ beam**
- **Propagation**:
  - Parameter: **Beam-to-beam fluctuation** shorted **B-to-B fluct.**
    * Use the same particle from one iteration to the next: denoted as **No fluct.**
    * Add some beam-to-beam fluctuation of :
      · 1 % of the 1-σ beam size and momentum : denoted as **1 % fluct.**
      · 10 % of the 1-σ beam size and momentum : denoted as **10 % fluct.**

- **Computation**:
  - Parameter: **BPM error** shorted **BPM**
    * Use exact values return by the MadX simulation : denoted as **perfect** BPM
    * Add some uniform random noise (within $\pm 0.1\,\mathrm{mm}$) to simulate BPM error : denoted as **realistic** BPM
- **Correction**:
  - Parameter: **Feedback coefficient** shorted as **Feedback coeff.**
    * Several values tested: 100 % (full correction), 50 %, 20 %, 10 %, 5 %, 1 %
- **Iterations**:
  - Parameter: **Number of iteration** shorted **# it.**
    * Two values tested: 100 and 1000

Using the above definitions, there is the table of parameters for all simulations made for the Chapter 5 :

Table A.1: Summary of parameters used for every simulation presented in chapter 5.

Section	*Selection*	*B-to-B fluct*	*BPM*	*Feedback coeff*	*# it.*
5.2.2	$\vec{0}$	No fluct.	Perfect	10 %	100
5.2.3	1-σ beam	No fluct.	Perfect	10 %	100
5.2.4.1	1-σ beam	1 %	Perfect	10 %	100
5.2.4.2	1-σ beam	10 %	Perfect	10 %	100
5.3.1.1	5-σ beam	No fluct.	Perfect	10 %	100
5.3.1.2	5-σ beam	1 %; 10 %	Perfect	10 %	100
5.3.2.1	1-σ beam	No fluct.	Perfect	100 %; 20 %; 10 %; 5 %; 2 %; 1 %	100
5.3.2.2.1	1-σ beam	1 %	Perfect	100 %; 20 %; 10 %; 5 %; 2 %; 1 %	100
5.3.2.2.2	1-σ beam	10 %	Perfect	100 %; 20 %; 10 %; 5 %; 2 %; 1 %	100
5.3.3.1	1-σ beam	No fluct.	Realistic	10 % 1 %	100 1000
5.3.3.2	1-σ beam	1 %	Realistic	1 %	1000

B - Résumé de la thèse en Français

ThomX est un prototype de source compacte de rayon X utilisant l'effet Compton inverse appelé CCS pour Compton Compact source. Son but est de démonter qu'il est possible de créer des machines de taille et coût financier raisonnable permettant de produire de haut flux de rayon X quasi-monochromatique. Pour ce faire, un faisceau d'électrons de $50\,\mathrm{MeV}$ rencontre un faisceau laser arrivant en sens inverse au point d'interaction Fig. 2.12 et il existe une certaine probabilité que certains électrons fournissent une partie de leur énergie cinétique au photons les faisant passé des infra-rouge proche au rayon X. C'est l'effet Compton inverse section 2.4.1.

Une machine telle que ThomX surpasse, théoriquement, les tubes à rayon X que ce soit en terme de flux produit, ou de qualité de faisceau Fig. 1.24. Actuellement les sources fournissant les meilleurs faisceaux et les plus gros flux de rayon X sont les synchrotrons et ils vont probablement le rester encore longtemps, mais les CCS tel que ThomX pourrait collaborer avec les synchrotrons afin de décharger ces derniers des taches pour lesquels ils sont sur-dimensionnés mais qui ne peuvent pas être réalisé avec des tubes à rayon X. En résumé ThomX et ces successeurs permettrons de combler le gouffre énorme entre les tubes à rayon X et les synchrotrons.

Mais ce n'est pas tous. Des projets de machine compacte dans des containers pourrait permettre de déplacé la source au près de l'objet à étudier et non l'inverse afin d'éviter de déplacer des statues fragiles et lourdes par exemple. De par son coût modéré et ça compacité des laboratoires, hôpitaux ou même musées pourraient s'équiper de répliquât de ThomX ce qui éviterait là encore de déplacer des échantillons, patients ou encore oeuvres d'art mais aussi permettrait à ces entité un accès plus simple et contrôlé à de tel sources de rayon X. Dans le cadre de la médecine par exemple, il existe une méthode de traitement de cancer par irradiation à une énergie bien spécifique (voir section 1.3.2.3) qui est testé sur synchrotron mais pourrait tout aussi bien l'être sur ThomX une fois qualifié pour de tels études.

Cet annexe résume les différents travaux réalisés lors de ma thèse sur ThomX et présentés dans ce document.

B.1 . Structure de la thèse

Cette thèse comporte 6 chapitres articulés comme suis :

1. **Accélérateur et rayon X** : Résumé historique de la découvert des électrons et des rayons X puis état de l'art en terme de physique des accélérateurs de particules et sources de rayon X.

2. **ThomX, une source de rayon X Compton** : Description des différents composant de ThomX et description de l'effet Compton dans ce cas précis.

3. **Simulations** : Description du formalisme des matrices de transfert dans le cadre de la physique des accélérateurs de particules puis présentation des deux codes utilisés dans cette thèse.

4. **Carte de perte** : Étude des pertes de particules dans la ligne de transfert et le premier tour dans l'anneau de ThomX avec deux visualisations des cartes de pertes, l'une selon l'axe de propagation, l'autre projeter à un endroit spécifique.

5. **Rétroaction sur l'injection** : Présentation d'un système de rétroaction sur l'injection du faisceau d'électron dans l'anneau de ThomX puis test de ce système grâce à des simulations.

6. **Démarrage de ThomX** : Présentation du démarrage de ThomX avec quelques résultats sur le démarrage des diagnostics du faisceau d'électrons.

Les deux premiers chapitres sont résumés dans l'introduction de ce résumé et la section suivante, puis à chaque chapitre correspond une section.

B.2 . ThomX

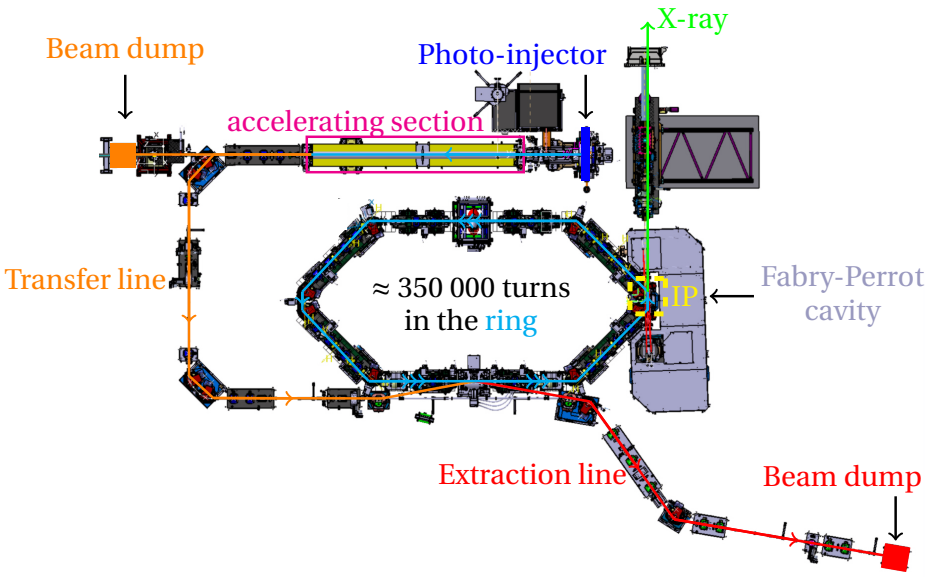

Figure B.1: Schéma mécanique de ThomX vue du dessus.

ThomX peut être décomposé en 7 morceaux principaux, 5 correspondants à l'accélérateur d'électrons (photo-injecteur, section accélératrice, ligne de transfert, anneau et ligne d'extraction) auxquels s'ajoute la cavité Fabry-Perot et la ligne de rayon X (voir Fig. B.1). Voici leurs rôles respectifs :

- **Photo-injecteur** : permet de générer un faisceau d'électron de $5\,\mathrm{MeV}$, a $50\,\mathrm{Hz}$
- **Section accélératrice** : permet d'accélérer les électrons jusqu'à $50\,\mathrm{MeV}$
- **Ligne de transfert** : permet la propagation, la caractérisation et l'adaptation du faisceau d'électrons
- **Anneau de stockage** : permet de stockage du faisceau d'électron pendant $20\,\mathrm{ms}$ avec une fréquence de répétition de $16.7\,\mathrm{MHz}$
- **Cavité Fabry-Perot** : permet de stocker le faisceau laser et d'accumuler une forte puissance laser
- **Ligne de rayon X** : permet de caractériser le faisceau de rayon X crée et de l'emmener jusqu'à la salle d'expérimentation hors du bunker de l'accélérateur
- **Ligne d'extraction** : permet d'arrêter proprement le faisceau d'électrons après avoir faire environ 350000 tours dans l'anneau

Le point d'interaction correspond à l'endroit où les électrons et les photons vont interagir. Pour augmenter au maximum le flux de rayon X produit, les deux faisceaux (électrons et laser) sont focalisés jusqu'à avoir une taille RMS d'environ $70\,\mu\mathrm{m}$. De plus, la petite taille de l'anneau permet d'avoir une haute fréquence de répétition c'est-à-dire plus d'interaction par seconde et donc un plus grand flux.

Cela dit, la petite taille de l'anneau induit aussi un système d'injection extrêmement rapide. L'injection est composée de deux éléments principaux : le septum et le kicker. Le septum est un élément composé de deux cavités, une sur l'axe de l'anneau où il n'y a jamais de champ magnétique, ce qui évite de perturber la propagation du faisceau une fois rentré dans l'anneau, et une seconde sur l'axe de l'injection (désaxé qu'une quinzaine de millimètres) ou un champ magnétique existe permettant une première correction de l'angle d'injection. Cela n'est pas suffisant puisque l'angle entre la trajectoire d'injection après le septum et la trajectoire optimale est toujours non nul. Le kicker situé un peu plus loin dans l'anneau permet justement de compenser cet angle et si le faisceau est bien au centre du tube au niveau de celui-ci et le kicker corrige correctement l'angle restant, alors le faisceau est stocké.

Pour vérifier les propriétés du faisceau d'électrons, différents diagnostics existent (voir section 2.2). Il y a, entre autre, les BPM (Beam Position Monitor ou moniteur de position) qui permettent de connaître la position du faisceau grâce au courant induit dans chacune de ces 4 électrodes qui est au premier ordre proportionelle à la distance à l'électrode. Pour ce qui est des mesures de charge, trois ICT (Integrating Current Transformer) et deux coupes de faraday (FC) sont utilisés sur ThomX. Les premières sont non destructives comme les BPM et utilise le courant induit dans une bobine autour de l'axe faisceau supposé proportionnel à

la charge du faisceau. Les secondes nécessitent d'arrêter complètement le faisceau et de mesurer le dépôt de charge dans une pièce en graphite, ce qui est plus précis puisqu'il s'agit d'une mesure directe, mais détruit complètement le faisceau. Les coupes de Faraday se trouvent donc dans les arrêtoirs permettant d'arrêter proprement le faisceau. Il existe aussi des mesureurs de pertes (Beam Loss Monitor ou BLM) utilisant l'effet Cherencov pour détecter les pertes le long de l'accélérateur. Un hublot au niveau d'un des aimants de l'anneau permet de récupérer le rayonnement synchrotron émit dans celui-ci afin de faire des mesures de longueur de paquet d'électron. Enfin, il y a aussi 5 stations à écran (screen station ou SST) permettant la visualisation du faisceau grâce à différents écrans pouvant être inséré sur la trajectoire du faisceau.

Afin de récupérer toutes les données générées par ces diagnostics et de contrôler les différents équipements de la machine, un système de contrôle doit être utilisé (voir section 2.3). Ce système est composé de différent niveau. Tout d'abord il y a l'équipement lui-même qui peut être une caméra, un moteur ou wavecatcher (sorte d'oscilloscope fait au laboratoire et permettant des mesures de courant) ou tout autre système. Ensuite, il existe un niveau permettant de normaliser les requêtes faites axu différents équipement en convertissant le langage de chaque équipement en un langage commun grâce à des DS (Device Server). Sur ThomX ce rôle est rempli par le logiciel Tango. Enfin, différent niveau supérieurs peuvent être ajouté pour permettre par exemple la création d'interface homme-machine et donc le contrôle de la machine.

B.3 . Simulations

Lors de cette thèse, deux codes de simulations ont été utilisés :

- **MadX** : (voir section 3.2)
  - Développé par le CERN
  - Permet :
    * La propagation de faisceau
    * L'optimisation de ligne
    * Le tracking de particules avec récupération des pertes si les ouvertures des éléments sont données (voir section 3.2.5)
  - Intérêts et utilisations :
    * Simulation non-linéaire de la machine
    * Réalisation des cartes de pertes
- **Mon code** : (voir section 3.3)
  - Code réalisé sous MatLab [45]

- Permet :
  * le calcul de l'équation de propagation d'une particules d'un point de la machine à un autre
  * la paramétrisation de n'importe quel paramètre des éléments de la ligne (longueur/position d'éléments, force des déviateur/quadrupôle, angle des dipôles ...)
- Intérêts et utilisations :
  * Donne l'équation analytique de l'impact des déviateurs (steerer) ou du kicker sur le faisceau

Ces deux codes sont basés sur du calcul linéaire de matrice de transfert, mais MadX prend aussi en compte des non-linéarité. Ce type de calcul est présenté dans la section 3.1.2.1 et toutes les matrices de transfert utilisées sont données dans la section 3.1.2.2. Les positions des particules calculées pas cette méthode sont données dans un référentiel cartésien mobile où l'origine correspond à une particule idéale ayant la bonne énergie et ce propageant dans un accélérateur sans défaut ni correcteur. Cette particules hypothétique est appelée particule de référence et sa trajectoire est dénotée $\vec{s}$. Le repère est tel que $\vec{z}$ est colinéaire à $\vec{s}$ et les directions traverses $\vec{x}$ et $\vec{y}$ sont respectivement horizontal orienté vers la gauche lorsque l'on regarde le faisceau s'éloigner et vertical orienté vers le haut.

Dans les deux cas, la partie injection dans l'anneau à nécessité une attention toute particulière puisque lors de l'injection, entre le septum et le kicker, le faisceau ne passe pas sur l'axe de l'anneau, mais sur l'axe d'injection décalé horizontalement (voir section 3.2.3). Hors, deux quadrupôles se trouvent sur cette ligne et une propagation hors axe dans ceux-ci induit une défection du faisceau qui doit être pris en compte. Pour cela, dans les deux codes, il a été décidé de réaliser un changement de référentiel à la fin du septum afin de passer du référentiel de la particules de référence à celui de l'anneau sur lequel sont centrés les quadrupôles. Ainsi, entre le septum est le kicker, les propagations sont bien calculées hors axe et après le septum les deux référentiels doivent coïncider dans le cas d'une injection parfaite ce qui permet de vérifier la cohérence de la méthode.

Enfin, dans ce chapitre 3, il est aussi décrit la méthode de sélection de particules (section 3.2.4). Celle-ci consiste en une sélection aléatoire uniforme à l'intérieur d'une ellipse décrite pas les propriétés théoriques du faisceau à la sortie de la section accélératrice. Pour réaliser des sélections plus réalistes, l'ellipse est agrandi d'un facteur k^2 (et donc la taille d'un facteur k) et le faisceau correspondant est dénoté par "faisceau k-σ".

B.4 . Carte de perte

MadX permettant d'enregistrer les pertes de particules lors du tracking, une étude de ces pertes du début de la ligne de transfert à la fin du premier tour

dans l'anneau a été réalisée. Pour ce faire des particules sont sélectionnées à l'intérieur de l'ellipse d'un faisceau, propagées en utilisant MadX puis les pertes sont représentées de deux façons différente.

Carte le long de l'accélérateur : (voir section 4.2.2)

- Permet :
  - La visualisation de l'enveloppe du faisceau
  - La visualisation de la localisation des pertes
- Observation :
  - Avec une sélection de particules dans un faisceau 5-σ :
    - * Jamais de pertes
    - ⇒ Pas ou très peu de perte dans le cas d'un faisceau parfait dans un accélérateur parfait
  - Avec une sélection de particules dans un faisceau 12-σ :
    - * Pertes localisées au début de la ligne de transfert dut à la sélection des particules très proche du tube faisceau
    - * Aucune perte après le premier dipôle
    - ⇒ Le faisceau peut être très large sans augmenter le risque de perte après le premier dipôle
  - Avec une sélection de particules dans un faisceau 20-σ :
    - * Pertes localisées au début de la ligne de transfert dut à la sélection des particules très proche du tube faisceau
    - * Quelques pertes localisées dans l'anneau
    - ⇒ Un grand moment transverse semble entraîné un plus grand risque de perte de particules
      Le risque reste néanmoins faible

Cartes projetées : (voir section 4.2.3)

- Permet :
  - La visualisation des positions transverses du faisceau à un endroit de la machine
  - La visualisation des particules qui seront perdus plus tard et la localisation (approximative) de ces pertes
- Étude du cas du "faisceau 20-σ" uniquement
- Observation :

- Projection au début de la ligne de transfert :
  - * Les pertes dans la ligne de transfert se font par les bords
  - ⇒ Défini une fenêtre d'acceptabilité de la ligne de transfert
  - * Les pertes dans l'anneau semblent aléatoirement dispersé dans une fenêtre d'acceptabilité si l'on regarde les plans (x,y) et (x',y'), mais pas dans les plans (x,x') et (y,y')
  - ⇒ Permettent de confirmer que ce sont les grands moments transverses par rapport à la position qui défini les potentielles pertes de particules
- Projection au niveau du première (Fig. 4.8) et du deuxième (Fig. 4.9a) écrans de la ligne de transfert :
  - * Permet d'obtenir la taille de la fenêtre d'acceptabilité de la ligne de transfert
  - * Ne permet pas de différencier les particules finissant le 1^{er} tour de celles perdues dans l'anneau
- Projection au niveau du troisième écran (Fig. 4.8) de la ligne de transfert :
  - * Permet d'obtenir la taille de la fenêtre d'acceptabilité de la ligne de transfert
  - * Une portion de la projection ne contient que des particules allant jusqu'à la fin du premier tour
  - ⇒ Permet de définir une fenêtre d'acceptabilité du premier tout de l'anneau

Les pertes dans la machine semble être très peu probable dans les conditions nominales, mais plus on s'en éloigne et moins ce constat est vrai. Cette étude à permit de créer un outil pouvant être utilisé pour évaluer le risque de perte dans la suite de la machine en comparant la position du faisceau sur les écrans ou dans les BPM avec la fenêtre d'acceptabilité. De plus, étant donné que MadX permet de prendre en compte des désalignements d'élément ou des déviateurs, il est possible de refaire très rapidement ces cartes de pertes dans ces différentes conditions et de comparer les résultats théoriques et expérimentaux pour avoir une meilleure compréhension de la propagation du faisceau dans la machine.

B.5 . Rétroaction lors de l'injection dans l'anneau

Le coeur de ma thèse correspond à l'étude de l'injection dans l'anneau de ThomX (voir section 3.2.3 et section 5.1.1), la création d'un code de rétroaction pour l'injection (voir section 5.1.2), et au test ce celui-ci grâce à MadX (voir section 5.2 et section 5.3).

Le principe de l'injection à déjà était décrit dans la section B.3 de ce résumé.

Le principe de la rétroaction est donné par la Fig. 5.2. En effet, le but est d'utiliser les mesures de la position du faisceau dans les deux premiers BPM de l'anneau (appelé BPM2 et BPM3) afin de calculer les corrections qu'il aurait fallu appliquer aux deux derniers déviateurs (STR3 et STR4 pour steerer) de la ligne de transfert pour avoir une injection parfaite. Ce calcul est réalisé grâce aux équations de propagations calculées à partir de mon code MatLab.

Après les premiers tests on a constaté que parfois les positions dans les BPM convergé effectivement vers les positions nominales, mais qu'entre les deux et dans le reste de l'anneau de large oscillation était visible. Pour réduire cela, une contrainte supplémentaire sur la position optimum a été donné : $x' = 0$ dans le BPM3 de l'anneau. Le kick du kicker a été choisie pour permettre de libérer un cinquième degrés de libertés et s'assurer la possibilité de respecter les cinq contraintes (les deux positions optimum dans les deux BPM plus la contrainte sur x').

L'injection dans l'anneau de ThomX n'étant pas encore possible, ce code de rétroaction a été testé sur des simulations MadX. Ces simulations suivent 6 étapes :

1. **Sélection** : Sélection d'une particules dans une ellipse du faisceau k-σ permettant de représenter le centroïde d'un faisceau
2. **Propagation** : Tracking de cette particule le long de la ligne de transfert et du premier tour dans l'anneau
3. **Estimation** : Calcul d'un estimateur de l'injection
4. **Calcul** : Calcul de la correction des déviateurs
5. **Correction** : Application d'une fraction de cette correction calculée
6. **Itérations** : Recommencé à partir de l'étape 2. pour un nombre fixe d'itérations

Á chacune de ces étapes, différents choix peuvent être faits. Voici la liste des différents choix fait et présenté ici :

1. **Sélection** :
   - Sélection de la particule de référence : $\overrightarrow{0}$
   - Sélection dans le faisceau 1-σ
   - Sélection dans le faisceau 5-σ
2. **Propagation** :

- Utiliser toujours la même particules d'une itération à la suivante : *Cas parfait*
- Utiliser la particule sélectionnée plus une fluctuation aléatoire tir à tir de :
  - $1\,\%$ de la taille et du moment transverse du faisceau 1-σ : *Cas fluctuation* $1\,\%$
  - $10\,\%$ de la taille et du moment transverse du faisceau 1-σ : *Cas fluctuation* $10\,\%$
- Le septum et le kicker son considéré parfait

  La reproductibilité tir à tir de ces éléments donne des oscillations sur les 20 premiers tours dans l'anneau de l'ordre de $\pm 0.2\,\mathrm{mm}$

3. **Estimation** :
   - $E_U = \sqrt{\frac{1}{\#BPM}\sum_{BPM} U^2}$
   - With $U = x,\ x',\ y$ or y'.
   - On considère une bonne injection lorsque :
     - E_x et $E_y < 0.1\,\mathrm{mm}$
     - $E_{x'}$ et $E_{y'} < 0.1\,\mathrm{mrad}$
4. **Calcul**:
   - Utilisé les "mesures" de BPM directement : *BPM parfait*
   - Ajouter in bruit de lecture aux "mesures" des BPM avec tirage aléatoire uniforme de l'ordre de grandeur de l'incertitude des BPM ($\pm 0.1\,\mathrm{mm}$) : *BPM réaliste*
5. **Correction** :
   - Différentes valeurs de coefficient de rétroaction ont été testées : $100\,\%$, $50\,\%$, $20\,\%$, $10\,\%$, $5\,\%$, $1\,\%$
6. **Itérations** : Deux valeurs d'itérations ont été testées : 100 ou 1000

Cette thèse présente, dans l'ordre, les cas suivants :

- **Cas de référence** (section 5.2.2) :

Sélection	*Fluctuation tir à tir*	*BPM*	*Rétroaction coeff.*	*Nb itérations*
$\vec{0}$	Non	Parfait	$10\,\%$	100

- **Cas parfait** (section 5.2.3) :

Sélection	*Fluctuation tir à tir*	*BPM*	*Rétroaction coeff.*	*Nb itérations*
faisceau 1-σ	Non	Parfait	10 %	100

- **Cas fluctuation** 1 % (section 5.2.4.1) :

Sélection	*Fluctuation tir à tir*	*BPM*	*Rétroaction coeff.*	*Nb itérations*
faisceau 1-σ	1 %	Parfait	10 %	100

- **Cas fluctuation** 10 % (section 5.2.4.2) :

Sélection	*Fluctuation tir à tir*	*BPM*	*Rétroaction coeff.*	*Nb itérations*
faisceau 1-σ	10 %	Parfait	10 %	100

- **Cas parfait avec un faisceau large** (section 5.3.1.1) :

Sélection	*Fluctuation tir à tir*	*BPM*	*Rétroaction coeff.*	*Nb itérations*
faisceau 5-σ	Non	Parfait	10 %	100

- **Cas fluctuant avec un faisceau large** (section 5.3.1.2) :

Sélection	*Fluctuation tir à tir*	*BPM*	*Rétroaction coeff.*	*Nb itérations*
faisceau 5-σ	1 % et 10 %	Parfait	10 %	100

- **Étude de l'impact du coefficient de rétroaction : cas parfait** (section 5.3.2.1) :

Sélection	*Fluctuation tir à tir*	*BPM*	*Rétroaction coeff.*	*Nb itérations*
faisceau 1-σ	Non	Parfait	100 %-20 %-10 %-5 %-2 %-1 %	100

- **Étude de l'impact du coefficient de rétroaction : cas fluctuation** 1 % (section 5.3.2.2.1) :

Sélection	*Fluctuation tir à tir*	*BPM*	*Rétroaction coeff.*	*Nb itérations*
faisceau 1-σ	1 %	Parfait	100 %-20 %-10 %-5 %-2 %-1 %	100

- **Étude de l'impact du coefficient de rétroaction : cas fluctuation** 10 % (section 5.3.2.2.2) :

Sélection	*Fluctuation tir à tir*	*BPM*	*Rétroaction coeff.*	*Nb itérations*
faisceau 1-σ	10 %	Parfait	100 %-20 %-10 %-5 %-2 %-1 %	100

- **Étude de l'erreur des BPM : cas parfait** (section 5.3.3.1) :

Sélection	*Fluctuation tir à tir*	*BPM*	*Rétroaction coeff.*	*Nb itérations*
faisceau 1-σ	Non	Réaliste	10 %-1 %	100-1000

- **Étude d'un cas réaliste** (section 5.3.3.2) :

Sélection	*Fluctuation tir à tir*	*BPM*	*Rétroaction coeff.*	*Nb itérations*
faisceau 1-σ	$1\,\%$	Réaliste	$1\,\%$	1000

A partir de toutes ces études il est possible de déduire que :

- La position et le moment transverse du faisceau au début de la ligne de transfert a relativement peu d'impact sur le système de correction
- Les fluctuations tir à tir de $1\,\%$ induise des fluctuations rapides de l'estimateur qui restent en dessous du seul de $0.1\,\mathrm{mm}$, ce qui est acceptable
- Les fluctuations tir à tir de $10\,\%$ induise des fluctuation plus amples mais ces fluctuations sont surestimées et le cas $1\,\%$ semble plus réaliste
- Les erreurs de mesure des BPM sont ce qui cause le plus de fluctuation et contrairement aux fluctuation tir à tir, celle-ci on tendance à durer pendant plus longtemps
- Pour tous les cas avec un BPM parfait, un coefficient de rétroaction de $10\,\%$ était suffisant, mais les erreurs de mesure des BPM implique la nécessité de descendre a $1\,\%$ au moins

Le tout dernier cas présenté est le cas le plus réaliste simulé et les résultats sont encourageant. Le système n'a malheureusement pas pu être testé sur la machine lors de cette thèse, mais pourrait l'être dans les prochains mois.

B.6 . Démarrage de l'accélérateur

En mai 2021 l'autorité de sûreté nucléaire (ASN) a donnée son autorisation pour lancer la phase I du démarrage, c'est-à-dire le démarrage de la partie linéaire de l'accélérateur. Le démarrage a commencé par le conditionnement du canon et de la section accélératrice. Cette étape se compose de répétition de monté douce de la puissance injecté dans le canon ou la section jusqu'à l'apparition de claquage, puis de décente jusqu'à ce que la puissance nominal puisse être injecté sans nouveau claquage. Le 4 octobre 2021, le premier faisceau photo-émit de la cathode à été observé sur le premier écran de la machine (Fig. 6.3). Un mois plus tard, les paramètres nominaux de la phase I était obtenus, à savoir :

- Énergie en sortie de photo-injecteur : $5\,\mathrm{MeV}$
- Énergie en sortie de section accélératrice : $50\,\mathrm{MeV}$
- Taux de répétition : $10\,\mathrm{Hz}$
- Charge à la fin de la ligne : $100\,\mathrm{pC}$

Les moins suivants ont été utilisés pour optimiser le transport, compenser ou supprimer des champs magnétiques parasites observés, étudier l'alignement et continuer la mise en place de certain diagnostics tel que les BLM, ou certains écrans des stations SST.

Ce dernier chapitre ce focalise plus particulièrement sur le démarrage de certains diagnostics et leurs utilisations. Il présente rapidement le fonctionnement et des mesures des BPM (section 6.2.2) et des ICT (section 6.2.3) mais surtout il détail les différentes applications des stations SST.

Les stations apportent en effet la possibilité de visualiser la projection transverse du faisceau grâce à deux types d'écrans : les YAG et les OTR. Le premier est un cristal (YAG:Ce pour Yttrium Aluminium Grenat dopé au cérium) dans lequel les électrons déposent de l'énergie ré-émis ensuite sous forme de photon. Le deuxième utilise l'émission de lumière dut au changement de milieux appelé aussi rayonnement de transition optique (ou Optical Transition Radiation (OTR) en anglais). L'écran YAG émet beaucoup plus de lumière que l'OTR (section 6.2.1.4), mais est aussi moins précis à cause de l'étalement de l'énergie déposée d'où la présence de ces deux écrans.

L'autre écran présent sur toutes les stations est un écran de calibration (section 6.2.1.1) permettant de mesurer le grandissement du système optique sur la caméra et d'obtenir la résolution du système.

Sur une station des stations, un quatrième écran en saphir permet la création de rayonnement Cherencov envoyé a une caméra à balayage afin d'obtenir une mesure de la longueur longitudinale du faisceau d'électron. Une première image de l'émission du rayonnement Cherencov à la sorti du bunker a été obtenue le 21 juillet 2022 (voir Fig. 6.5).

En utilisant un quadrupôle et un écran YAG, il est possible de réaliser des mesures de l'émittance du faisceau d'électron et, après quelque optimisation, il a été possible d'atteindre des émittances transverses normalisées de $2\pi.\mathrm{mm.mrad}$, ce qui correspond aux attentes théoriques dans le cas d'un faisceau de $100\,\mathrm{pC}$.

Enfin, grâce à un déviateur et toujours à l'écran YAG, il est possible de réaliser des mesures d'énergie (section 6.2.1.6). Cette méthode est la seule permettant les mesures d'énergie avant la section accélératrice et c'était aussi le cas après dans le cadre de la phase I où les dipôles ne pouvaient pas encore être allumés.

Conclusion

Cette thèse s'est passé sur ThomX, un prototype de nouvelle source de rayon X à haut flux utilisant l'effet Compton inverse. Pour cela, ce projet utilise un anneau de stockage d'électron à $50\,\mathrm{MeV}$ et une cavité Fabry-Perot.

Avant le démarrage de la machine, des simulations de l'accélérateur, principalement de la ligne de transfert et de l'anneau, ont été faites et ont permis de faire une étude des pertes de particules pendant l'injection.

Le risque de perte est nul pour les paramètres nominaux et peu probable dans le cas de faisceau plus large, néanmoins il existe, surtout dans la première moitié de l'anneau durant l'injection. Pour éviter ces pertes, des trackings de particules ont été faits et ont permis la création de cartes de pertes projetées au niveau des diagnostics. Les cartes de perte au niveau des deux premières stations diagnostics ne permettent pas de définir de zone sans aucune perte, mais la troisième le peu. Ainsi, la meilleure position pour le faisceau au niveau de cette dernière station d'écran semble être x compris entre $-7\,\mathrm{mm}$ et $10\,\mathrm{mm}$ et y compris entre $\pm 2\,\mathrm{mm}$.

Afin de contrôler l'injection dans l'anneau, un code de correction d'injection a été développé et testé grâce à des simulations MadX. Ce code utilise des équations de propagations entre différentes parties de l'accélérateur calculées à partir du formalise des matrices de transferts. Il permet de calculer les défections qu'il aurait fallu appliquer dans les deux derniers déviateurs de la ligne de transfert afin d'obtenir une injection parfaite en ce basant sur des mesures faites avec les deux premiers BPM de l'anneau.

Les résultats des simulations MadX sont prometteurs et dans le cas le plus réaliste des oscillations de l'ordre de $0.1\,\mathrm{mm}$ au niveau des BPM de l'anneau sont attendus. Le code n'a pas encore pu être testé sur la machine, il devrait bientôt l'être.

Le démarrage de la machine a commencé en juin 2021 ce qui m'a permis d'y participer. Ainsi je me suis occupé du démarrage de certain diagnostics présenté ici et utilisé pour caractériser le faisceau d'électron.

L'obtention l'autorisation de passage en phase II est prévu pour la deuxième moitié de 2022. Cette phase permettras le démarrage de la ligne de transfert, de la ligne d'extraction puis de l'anneau. Il est prévu de tester le code de correction d'injection dès que possible. Les premiers rayons X sont attendus fin 2023.

Bibliography

[1] J. J. THOMSON, "Carriers of negative electricity," *Nobel Lecture*, December 11, 1906. [Online]. Available: https://www.nobelprize.org/uploads/2018/06/thomson-lecture.pdf

[2] W. C. Röntgen, "On a new kind of rays," *Nature*, vol. 53, p. 274–276, 1896. [Online]. Available: https://doi.org/10.1038/053274b0

[3] Wikipedia contributors, "Crookes tube — Wikipedia, the free encyclopedia," https://en.wikipedia.org/w/index.php?title=Crookes_tube&oldid=1057836256, 2021, [Online; accessed 1-June-2022].

[4] W. Röntgen, "First medical x-ray by wilhelm röntgen of his wife anna bertha ludwig's hand," 1895, domaine public. [Online]. Available: https://commons.wikimedia.org/w/index.php?curid=5059748

[5] E. L. Murphy and J. R. H. Good, "Thermionic emission, field emission, and the transition region," *Physical review*, vol. 102, no. 1464, 1956. [Online]. Available: https://doi.org/10.1103/PhysRev.102.1464

[6] A. Einstein, "Über einen die erzeugung und verwandlung des lichtes betreffenden heuristischen gesichtspunkt," *Annalen der physik*, no. 322, pp. 132–148, 1905. [Online]. Available: https://doi.org/10.1002/andp.19053220607

[7] A. B. Arons and M. B. Peppard, "Einstein's proposal of the photon concept—a translation of the annalen der physik paper of 1905," *American Journal of Physics*, no. 33, pp. 367–374, 1965. [Online]. Available: https://doi.org/10.1119/1.1971542

[8] T. Thuillier, "Electron cyclotron resonance ion sources -1," CAS - CERN Accelerator School (2012). [Online]. Available: https://cas.web.cern.ch/sites/default/files/lectures/senec-2012/thuillieri.pdf

[9] R. Chehab, "French-ukrainian workshop - instrumentation developments for high energy physics (ijclab) : Positron sources at lal-orsay: a long story," 2021, slide 11. [Online]. Available: https://indico.ijclab.in2p3.fr/event/7323/

[10] F. Hinterberger, "Electrostatic accelerators," 2006. [Online]. Available: http://cds.cern.ch/record/1005042

[11] F. Rohrbach, "High voltage in vacuum," adapt from CERN Courier vol. 9, July 1969, pp208–210. [Online]. Available: https://cerncourier.com/a/high-voltage-in-vacuum/

[12] G. Kube, "Profile measurements with scintillators: Requirements and application at accelerator," join ARIES-ADA Workshop on "Scintillation Screens and Optical Technology for transverse Profile Measurements". [Online]. Available: https://indico.cern.ch/event/765975/contributions/3180703/

[13] L. Wartski, J. Marcou, and S. Roland, "Detection of optical transition radiation and its application to beam diagnostics," *IEEE Transactions on Nuclear Science*, vol. 20, no. 3, pp. 544–548, 1973.

[14] A. Bazzano, "Isotopic analysis of environmental samples using inductively coupled plasma mass spectrometry," https://www.researchgate.net/figure/schematic-diagram-of-a-Faraday-cup-and-its-amplifier-circuit_fig10_312494038, 2016, [Online; accessed 14-January-2022].

[15] N. Morange, "Analyse de données," École de la Physique au Détecteur (2021). [Online]. Available: https://indico.in2p3.fr/event/24934/contributions/102630/

[16] A. Collaboration, "Observation of a new particle in the search for the standard model higgs boson with the atlas detector at the lhc," *Physics Letters B*, vol. 716, no. 1, pp. 1–29, 2012. [Online]. Available: https://doi.org/10.1016/j.physletb.2012.08.020

[17] A. Abada, M. Abbrescia, S. AbdusSalam, and al., "Fcc-ee: The lepton collider," *Eur. Phys. J. Spec. Top.*, no. 228, pp. 261–623, 2019. [Online]. Available: https://doi.org/10.1140/epjst/e2019-900045-4

[18] A. A. Miller, "Wikipedia : Braggpeak.png," the dose produced by a native and by a modified proton beam in passing through tissue, compared to the absorption of a photon or X-ray beam. [Online]. Available: https://en.wikipedia.org/wiki/Bragg_peak#/media/File:BraggPeak.png

[19] "New aglae : le nouveau accélérateur grand louvre d'analyse Élémentaire," le journal, CNRS. [Online]. Available: https://lejournal.cnrs.fr/infographies/nouvel-aglae-lart-et-la-matiere

[20] W. Commons, "File:em spectrum properties edit.svg — wikimedia commons, the free media repository," 2022, [Online; accessed 23-June-2022]. [Online]. Available: https://commons.wikimedia.org/w/index.php?title=File:EM_Spectrum_Properties_edit.svg&oldid=654291941

[21] J. Clarke, "Insertion devices lecture 1 : Introduction to synchrotron radiation," aSTeC, Daresbury Laboratory. [Online]. Available: https://www.cockcroft.ac.uk/wp-content/uploads/2014/12/Lecture-1.pdf

[22] "Position along the storage ring," synchrotron SOLEIL. [Online]. Available: https://www.synchrotron-soleil.fr/en/position-along-storage-ring

[23] S. Miyamoto, Y. Asano, S. Amano, D. Ii, K. Imasaki, H. Kinugasa, Y. Shoji, T. Takagi, and T. Mochizuki, "Laser compton back-scattering gamma-ray beamline on newsubaru," *Radiation Measurements*, vol. 41, 12 2006.

[24] C. Sun, "Characterizations and diagnostics of compton light source." *Dissertation, Duke University*, 2009.

[25] "Munich compact light source web site," [Online; accessed 24-June-2022]. [Online]. Available: https://www.bioengineering.tum.de/en/central-building/munich-compact-light-source

[26] A. Variola, J. Haissinski, A. Loulergue, F. Zomer, and al.., "Thomx - technical design report," *in2p3-00971281*, p. 164, 2014.

[27] "Lyncean compact light source web site," [Online; accessed 24-June-2022]. [Online]. Available: https://lynceantech.com/products/#compact-light-source

[28] J. M., "Potential of compact compton sources in the medical field." *Phys Med.*, no. 32(12):1790-1794, 2016 Dec.

[29] Yue Ma, Jianfei Hua, Dexiang Liu, and al., "Region-of-interest micro-focus computed tomography based on an all-optical inverse compton scattering source," *Matter and Radiation at Extremes*, vol. 5, no. 064401, 2020. [Online]. Available: https://doi.org/10.1063/5.0016034

[30] R. Gradl, M. Dierolf, L. Hehn, and al., "Propagation-based phase-contrast x-ray imaging at a compact light source." *Scientific Reports*, vol. 7, no. 4908, 2017. [Online]. Available: https://doi.org/10.1038/s41598-017-04739-w

[31] J. Madsen, "Lep injector linac," *CERN PS 89-56 (LP)*, 1989. [Online]. Available: https://cds.cern.ch/record/2742719/files/CERN-PS-89-56-LP.pdf

[32] I. Drebot, "Electron beam dynamics with and without Compton back scattering," Theses, Université Paris Sud - Paris XI, Nov. 2013. [Online]. Available: https://tel.archives-ouvertes.fr/tel-00920424

[33] A. Gamelin, "Collective effects in a transient microbunching regime and ion cloud mitigation in ThomX," Theses, Université Paris-Saclay, Sep. 2018. [Online]. Available: https://tel.archives-ouvertes.fr/tel-01934906

[34] P. Leban, *Libera Brilliance+, Electron Beam Position Processor, User Manual*, August 2014, version 2.81.

[35] Crytur, "Yag:ce," 2022. [Online]. Available: https://www.crytur.cz/materials/yagce/

[36] G. Abeille and al., "Tango documentation," [Online; accessed 23-June-2022]. [Online]. Available: https://tango-controls.readthedocs.io/en/latest/contents.html

[37] J. collaboration, "Jive documentation," [Online; accessed 23-June-2022]. [Online]. Available: https://www.esrf.fr/computing/cs/tango/tango_doc/tools_doc/jive_doc/index.html

[38] D.Breton and J.Maalmi, *WaveCatcher Family User's Manual*, August 2014, https://www.hep.ucl.ac.uk/pbt/wikiData/manuals/WaveCatcher/WaveCatcherFamily_V1.2.pdf.

[39] K. R. Crandall and D. P. Rusthoi, *TRACE 3-D documentation (LA–11054-MS)*, 3rd ed. Los Alamos National Laboratory (Los Alamos, New Mexico, United States), may 1997.

[40] F. C. Iselin, *The MAD Program (Methodical Accelerator Design): Physical Methods Manual. Ver- sion 8.13*. CERN, Geneva, Switzerland. http://mad8.web.cern.ch/mad8/doc/phys_guide.pdf, 1994.

[41] L. Deniau, H. Grote, G. Roy, and F. Schmidt, *The MAD-X Program (Methodical Accelerator Design): User's Reference Manual. Version 5.06.01*. CERN, Geneva, Switzerland., 1994. [Online]. Available: http://madx.web.cern.ch/madx/

[42] L. Garolfi, "High-gradient S-band electron Linac for ThomX," Theses, Université Paris-Saclay, Jan. 2018. [Online]. Available: https://tel.archives-ouvertes.fr/tel-01779739

[43] G. Van Rossum and F. L. Drake Jr, *Python reference manual*. Centrum voor Wiskunde en Informatica Amsterdam, 1995.

[44] B. Holzer, *Introduction to Transverse Beam Dynamics*. CAS - CERN Accelerator School: Course on Superconductivity for Accelerators, 2014. [Online]. Available: http://dx.doi.org/10.5170/CERN-2014-005

[45] MATLAB, *version 9.7.0.1216025 (R2019b)*. Natick, Massachusetts: The MathWorks Inc., 2019.

[46] N. Mokhov and F. Cerutti, "Beam–material interactions," *CERN, Joint International Accelerator School: Beam Loss and Accelerator Protection*, vol. 2, 2016. [Online]. Available: https://doi.org/10.5170/CERN-2016-002.83

[47] G. J. Lockwood, L. B. Bishop, and M. M. Selph, "Measurements of pulsed radiation-induced fiber fluorescence and darkenin," *Proc. SPIE 2290, Fiber Optic Materials and Components*, 1994. [Online]. Available: https://doi.org/10.1117/12.187423

[48] H.Purwar and al., "Random error propagation on electron beam dynamics for a 50 MeV S-band linac," unpublished.

[49] A. Moutardier *et al.*, "Characterization of the Electron Beam Visualization Stations of the ThomX Accelerator," presented at IPAC'22, Bangkok, Thailand, Jun. 2022, paper MOPOPT006, unpublished.

[50] U. air force", "Photographic lenses," 1951, document ID : MIL-STD-150. [Online]. Available: https://quicksearch.dla.mil/qsDocDetails.aspx?ident_number=35531

[51] B. company, *Basler scout : USER'S MANUAL FOR GigE VISION CAMERAS*, 24 August, 2018, aW000119, Version 19.

[52] TAMRON Europe GmbH, "Tamron : 18-400mm f/3.5-6.3 di ii vc hld," https://www.tamron.eu/lenses/18-400mm-f35-63-di-ii-vc-hld/, 2022, [Online; accessed 4-June-2022].

[53] S. D. Williams *et al.*, "Lens Calibration for Beam Size Monitors at ThomX," in *Proc. IBIC'20*. JACoW Publishing, Geneva, Switzerland, 2020, paper THPP35, pp. 281–284. [Online]. Available: http://accelconf.web.cern.ch/ibic2020/papers/THPP35.pdf

[54] N. Delerue, "Talk : Profiles transverses - nicolas," 2018. [Online]. Available: https://indico.ijclab.in2p3.fr/event/5002/

[55] H. Wiedemann, *Particle Accelerator Physics, chapter 8, Measurement of the Beam Emittance p.224-227*, 4th ed. Springer, 2004, https://library.oapen.org/bitstream/id/2d14822b-7fda-40ee-92fc-22b3cdf2e1f4/1006502.pdf.

[56] A. Terebilo, "Accelerator toolbox for matlab," *SLAC Publication*, 2001.

[57] C. Bruni *et al.*, "First Electron Beam of the ThomX Project," presented at IPAC'22, Bangkok, Thailand, Jun. 2022, paper WEOYSP2, unpublished.